

Hydrodynamics of Ducted and Open-Centre Tidal Turbines



Clarissa Belloni

Balliol College

University of Oxford

A thesis submitted for the degree of

Doctor of Philosophy

Trinity 2013

Acknowledgements

First and foremost, I would like to thank my supervisors Dr Richard Willden and Professor Guy Houlby for their support of my dissertation and their guidance over the past four years. I further extend this thank you to all members, past and present, of the Oxford Tidal Energy Research Group, for valuable advice throughout the course of my research project.

I would like to express my gratitude to the Engineering and Physical Sciences Research Council, the German Academic Exchange Service, the Oxford Martin School, and the Bracken Fund, which have partially funded this work. Thank you also to Balliol College and the New England Marine Renewable Energy Center for enabling me to present my work at the 4th Annual Marine Renewable Energy Technical Conference.

On a personal note, I would like to thank all of my colleagues at the Oxford Engineering Department, in particular, but not limited to, Jenkin Room 11, for a great working atmosphere. Thank you also to everybody at Balliol College for making the past four years an unforgettable experience.

A heartfelt thank you to my family and my friends back home, who have supported me throughout the past years, and a particularly big thank you to Alex, for giving me the confidence to pursue this degree.

Abstract

This study presents a numerical investigation of ducted tidal turbines, employing three-dimensional Reynolds-averaged Navier-Stokes simulations. Bidirectional ducted turbines are modelled with and without aperture, referred to as ducted and open-centre turbines respectively.

The work consists of two investigations. In the first, the turbine rotors are represented by actuator discs, a simplification which captures changes in linear momentum and thus the primary interaction of the turbine with the flow through and around the duct, while greatly reducing computational complexity. In the second investigation, the turbine rotors are represented through a CFD-integrated blade element momentum model, employing realistic rotor data, capturing swirl and blade drag in addition to the extraction of linear momentum.

Both modelling techniques were employed to investigate the performances of bare, ducted, and open-centre turbines, relating these to the flow fields exhibited. For axial flow, substantial decreases in power generated by the ducted and open-centre turbines were found, relative to a bare turbine of equal total device diameter. For open-centre turbines, an increase in aperture size leads to a further reduction in power generated. Increased blockage was shown to positively affect the performance of all devices.

Two further measures of performance were employed: power density, normalising the power by the rotor area, and basin efficiency, relating the power generated to the overall power removed from the flow. Moderate increases in power density can be achieved for the ducted and open-centre devices, while their basin efficiencies are of similar value to that of the bare turbine.

For yawed inflow, the performance of the bare turbine decreases, whilst that of the ducted and open-centre turbines increases. This is due to an increased flow velocity following flow acceleration around the inlet lip of the duct and also an increase in effective blockage as ducts present greater projected frontal area when approached non-axially.

Contents

| | | |
|----------|--|-----------|
| 1 | Introduction and objectives | 1 |
| 1.1 | The tidal resource | 1 |
| 1.2 | Tidal turbine concepts | 3 |
| 1.3 | Thesis outline | 6 |
| 2 | Ducted turbines | 8 |
| 2.1 | Ducted and open-centre tidal turbines proposed by the industry | 9 |
| 2.1.1 | Bidirectional ducted tidal turbines | 10 |
| 2.1.2 | Unidirectional ducted tidal turbines | 13 |
| 2.1.3 | Devices chosen for analysis | 14 |
| 2.2 | Previous analyses of ducted turbines | 16 |
| 2.2.1 | Analytical studies of ducted turbines | 16 |
| 2.2.2 | Analysis parameters for ducted turbines | 17 |
| 2.2.3 | Analyses of ducted axial-flow wind turbines | 19 |
| 2.2.4 | Analyses of ducted axial-flow tidal turbines | 22 |
| 2.2.5 | Recent analyses of ducted axial-flow tidal turbines | 24 |
| 3 | Modelling tidal turbines | 31 |
| 3.1 | Overview of computational turbine models | 32 |
| 3.2 | Computational fluid dynamics and RANS modelling | 35 |
| 3.2.1 | Governing equations | 35 |
| 3.2.2 | Reynolds-averaged Navier-Stokes (RANS) equations | 37 |
| 3.2.3 | Turbulence closure | 39 |
| 3.2.4 | ANSYS FLUENT solver | 44 |
| 4 | Actuator disc simulations | 49 |
| 4.1 | Actuator disc modelling | 50 |
| 4.1.1 | Linear momentum actuator disc theory and the Betz limit | 50 |
| 4.1.2 | Actuator disc representation of tidal turbines in numerical and physical experiments | 55 |

| | | |
|----------|--|------------|
| 4.2 | Modelling free surface effects for tidal turbines | 59 |
| 4.2.1 | Open channel flow | 59 |
| 4.2.2 | Theoretical modelling of the free surface | 61 |
| 4.2.3 | Numerical modelling of the free surface | 63 |
| 4.3 | Model setup | 65 |
| 4.3.1 | Actuator disc implementation and model setup | 65 |
| 4.3.2 | Investigation of unsteady flow features | 67 |
| 4.3.3 | Grid resolution study | 69 |
| 4.3.4 | Turbulence parameter sensitivity analysis | 72 |
| 4.4 | Bare turbine model validation | 76 |
| 4.4.1 | Data extraction | 76 |
| 4.4.2 | Flow field analysis | 77 |
| 4.4.3 | Thrust analysis | 79 |
| 4.4.4 | Performance analysis | 80 |
| 4.5 | Analysis of a bidirectional ducted turbine in axial flow | 88 |
| 4.5.1 | Flow field of the ducted turbine | 90 |
| 4.5.2 | Thrust of the ducted turbine | 93 |
| 4.5.3 | Performance of the ducted turbine | 95 |
| 4.6 | Analysis of an open-centre ducted turbine in axial flow | 98 |
| 4.6.1 | Flow field of the open-centre turbine | 100 |
| 4.6.2 | Thrust of the open-centre turbine | 105 |
| 4.6.3 | Performance of the open-centre turbine | 106 |
| 4.7 | Yawed inflow | 108 |
| 4.7.1 | Model setup for yawed inflow | 108 |
| 4.7.2 | Comparison of steady and unsteady simulations | 109 |
| 4.7.3 | Flow field analysis in yawed inflow | 110 |
| 4.7.4 | Thrust analysis in yawed inflow | 115 |
| 4.7.5 | Performance analysis in yawed inflow | 117 |
| 4.7.6 | Alternative domain setup | 122 |
| 4.8 | Summary of results of the actuator disc simulations | 123 |
| 5 | RANS-BEM simulations | 126 |
| 5.1 | Blade element momentum (BEM) theory | 127 |
| 5.1.1 | Introduction to BEM | 127 |
| 5.1.2 | Corrections to BEM | 133 |
| 5.1.3 | Analytical BEM rotor design | 135 |

| | | |
|----------|--|------------|
| 5.1.4 | BEM application in wind and tidal turbine research | 137 |
| 5.2 | RANS-BEM model implementation | 141 |
| 5.3 | Hydrofoil selection | 143 |
| 5.4 | Bare turbine model validation | 148 |
| 5.5 | Rotor design | 152 |
| 5.5.1 | Design criteria | 152 |
| 5.5.2 | RANS-BEM rotor design tool | 155 |
| 5.5.3 | Results of rotor design | 157 |
| 5.6 | Axial inflow | 164 |
| 5.6.1 | Comparison of steady and unsteady simulations | 164 |
| 5.6.2 | Bare turbine in axial inflow | 167 |
| 5.6.3 | Ducted turbine in axial inflow | 172 |
| 5.6.4 | Open-centre turbine in axial inflow | 177 |
| 5.6.5 | Comparison of RANS-BEM and actuator disc simulations | 182 |
| 5.7 | Yawed inflow | 185 |
| 5.7.1 | Bare turbine in yawed inflow | 186 |
| 5.7.2 | Ducted turbine in yawed inflow | 192 |
| 5.7.3 | Open-centre turbine in yawed inflow | 201 |
| 5.8 | Summary of results of the RANS-BEM simulations | 209 |
| 6 | Conclusions and future work | 212 |
| 6.1 | Conclusions | 212 |
| 6.2 | Future work | 216 |
| 6.3 | Contribution of thesis | 217 |
| A | Publications | 218 |
| | Bibliography | 219 |

Nomenclature

Latin alphabet

| | |
|--------------|--|
| A | area |
| a | axial induction factor |
| a' | circumferential (swirl) induction factor |
| \mathbf{a} | acceleration |
| B | area blockage ratio |
| C_0 | baseline target local thrust |
| C_d | sectional drag coefficient |
| C_l | sectional lift coefficient |
| C_P | power coefficient |
| C_{PD} | power density coefficient |
| C_T | thrust coefficient |
| C_{TD} | thrust density coefficient |
| C_θ | circumferential blade force coefficient |
| C_x | axial blade force coefficient |
| c | chord length |
| D | turbine/device diameter |
| D | drag of an aerofoil |
| d | drag of an aerofoil per unit span |
| F | force |
| F | tip-loss correction factor |
| f | cell face |
| f | variation factor |
| Fr | Froude number |
| G | energy flux |
| H | total head |
| h | depth of flow |
| h_c | critical depth |

| | |
|-----------|-----------------------------------|
| I | turbulence intensity |
| k | turbulent kinetic energy |
| L | characteristic length |
| L | lift of an aerofoil |
| l | turbulent length scale |
| l | lift of an aerofoil per unit span |
| m | mass |
| \dot{m} | mass flow |
| N_B | number of blades |
| p | pressure |
| P | power |
| Q | rotor torque |
| R | turbine/disc radius |
| r | local radius |
| Re | Reynolds number |
| S | source term |
| T | thrust |
| t | time |
| t | aerofoil thickness |
| U | velocity modulus |
| u_i | local velocity in i -coordinate |
| V | volume |

Greek alphabet

| | |
|-----------------------|-----------------------------|
| α | angle of attack |
| β | blade twist angle |
| Γ | diffusion coefficient |
| γ | yaw angle |
| ϵ | turbulence dissipation rate |
| ϵ | error |
| η_{basin} | basin efficiency |
| θ | circumferential velocity |
| λ | tip-speed ratio |
| μ | dynamic viscosity |

| | |
|------------|--|
| μ_t | eddy viscosity |
| ξ | axis in inflow direction |
| ρ | fluid density |
| σ_r | local blade solidity |
| τ | stress on fluid element |
| ϕ | angle between blade inflow and plane of rotation |
| Ω | angular velocity of turbine |
| ω | specific turbulence dissipation rate |

Subscripts

| | |
|----------|--|
| ∞ | condition upstream of the turbine |
| ap | aperture |
| d | condition at the duct |
| dyn | dynamic |
| fw | condition in the far wake of the turbine |
| hub | hub |
| loc | local |
| max | maximum |
| ref | reference |
| rel | relative to the blade |
| stat | static |
| tot | total |
| t | condition at the turbine |
| ta | turbine annulus |
| w | condition in the wake of the turbine |

Acronyms

| | |
|--------------|---|
| 1D / 2D / 3D | one- / two- / three-dimensional |
| ABEM | analytical blade element momentum |
| BEM | blade element momentum |
| CFD | computational fluid dynamics |
| DNS | direct numerical simulation |
| EMEC | European Marine Energy Centre |
| LMADT | linear momentum actuator disc theory |
| NACA | National Advisory Committee for Aeronautics |
| NREL | National Renewable Energy Laboratory |
| PFA | projected frontal area |
| PIV | particle image velocimetry |
| RANS | Reynolds-averaged Navier-Stokes equations |
| SERI | Solar Energy Research Institute |
| SST | shear-stress transport |
| THAWT | Transversal Horizontal Axis Water Turbine |
| VOF | volume of fluid |

Chapter 1

Introduction and objectives

This chapter introduces the research by presenting an overview of the tidal resource in section 1.1 and an introduction to tidal turbine concepts proposed by the industry in section 1.2. An outline of the remainder of this thesis is presented in section 1.3.

1.1 The tidal resource

As the search for novel and economical renewable energy sources continues, tidal energy has seen a strong increase in interest over recent years. Tidal power can be harvested in two ways: by extracting the energy directly from the tidal stream, or by storing the tidal flow behind a barrage. To capture the energy of a tidal stream, the flow can be used to turn a turbine, in much the same manner that wind energy is captured by a wind turbine. Alternatively, to use the energy potential between ebb and flood the tidal flow is stored behind a barrage and its potential energy is converted to usable electricity as it exits through the barrage. Whilst a small number of tidal barrage energy plants have been in operation since the 1960s, tidal stream devices have recently become a focus of research institutes and energy companies.

Although the energy density in most marine currents is relatively low, certain flow conditions, such as flows past headlands, around islands and through straits and shallows, can give rise to current flow speeds, typically of 2 to 3 m/s, yielding high energy densities and making economical energy extraction a viable possibility. The predictability of ocean and tidal currents makes this energy source particularly attractive compared to many other renewable energy sources.

Both ocean and tidal marine currents offer an energy resource that could make a significant contribution to future energy requirements. A report published in 1996 by the European Commission (1996) estimated that the marine current resources of the most promising sites in Europe could collectively contribute up to 50 TWh/year, with approximately half of this available resource lying within the UK's coastal waters. A more recent report published by the Carbon Trust (2011*b*) gives a more conservative estimate of the technically extractable resource for the UK's coastal waters of 20.6 TWh/year, with roughly a third of the resource around the Pentland Firth and another third located around the channel islands (Carbon Trust, 2011*a*). At this level, the technically extractable resource represents around 5-6 % of the UK's electricity demand.

A tidal stream turbine, often also referred to as a marine current turbine, can be best described as a set of hydrofoil blades that are arranged such that, when the flow passes them, the blades rotate about an axis and can be used to produce electricity. Though the tidal energy industry can partially build on experience gained in the wind energy industry, and indeed some tidal turbine designs look very similar to wind turbines, there is a considerable difference between the maturity of wind turbine technology and that of tidal stream turbines. Whilst wind energy is a rapidly expanding market with a fairly uniform design approach taken by the various suppliers (three blades, horizontal axis, pitch control) marine current energy is still in its infancy. A broad range of technologies are currently under investigation, as possible candidates and a final solution (or several) is yet to emerge. As one might expect, a number of concepts have been imported from the wind energy field and it may be that design concepts which failed to make an impact in the wind market may be better suited for the marine application.

1.2 Tidal turbine concepts

The UK, Ireland and Canada are currently leading the way on marine renewable energy research and development with a broad range of local device developers and research facilities conducting extensive research on the topic. A wide array of universities have active research projects in this area. On the manufacturing side there are currently around 25 developers, some of which are OpenHydro Group Ltd. (2013), Marine Current Turbines Ltd. (2013) and Ocean Renewable Power Company (2013), all of which are pursuing different turbine concepts.

A comprehensive overview of currently developed tidal turbine concepts is given by the European Marine Energy Centre Ltd. (2013*b*). Most commonly the devices are classified into the following three general groups: Axial-flow turbines, cross-flow turbines, and oscillating hydrofoils. Figure 1.1 illustrates these three groups.

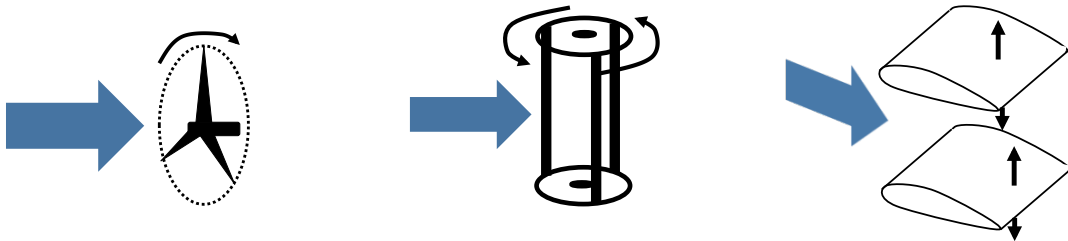


Figure 1.1: Overview of types of tidal turbine devices: Axial-flow turbine (left), cross-flow turbine (middle), oscillating hydrofoil (right), adapted from Savage (2007).

Cross-flow turbines exist in the form of horizontal axis as well as vertical axis turbines and are based on the Darrieus turbine concept. The rotational axis of this type of device is perpendicular to the flow, and as the rotor turns the blades move with and against the flow as they complete a full rotation. Examples of such devices are the THAWT concept (horizontal axis) developed at the University of Oxford (McAdam *et al.*, 2013), the TidGen device by Ocean Renewable Power Company (2013), the

Kobold (vertical axis) turbine developed by Ponte di Archimede S.p.A. (2013) and experimentally analysed by Kracht *et al.* (2012), and the Edinburgh vertical axis turbine (Salter and Taylor, 2007). Vertical axis cross-flow turbines encased by ducts have also been suggested, see for instance the device designed by Tidal Energy Pty Ltd. (2013).

In the case of the oscillating hydrofoil, a hydrofoil is attached to a mechanical arm, the motion of which is used to generate electricity, for instance by driving a reciprocating hydraulic pump. As the symmetric hydrofoil moves up and down within the water column it drives the pump, which in turn pressurises oil. This oil then passes through a hydraulic generator to produce electricity. Examples of oscillating hydrofoil devices include Stingray, proposed by Engineering Business Ltd. (2005), and a device developed by Pulse Tidal Ltd. (2013) and tested in the Humber estuary.

At present, the concepts based on an axial-flow turbine – looking much like a wind turbine design – are the closest to commercialisation. A range of prototype plants have been installed in the past decade, such as the 1.2 MW SeaGen turbine developed by Marine Current Turbines Ltd. (2013) and tested in Strangford Lough, Northern Ireland and the Free Flow by Verdant Power (2013), installed in the East River in New York, USA. More recently the AR-1000 designed by Atlantis Resources Corporation Pte Ltd (2013) and the HS1000 designed by Andritz Hydro Hammerfest (2013) have been installed at the European Marine Energy Centre Ltd. (2013a) (EMEC) in Orkney, Scotland, with the HyTide by Voith Ocean Current Technologies (2013) to follow soon. All three of these designs are rated at 1 MW and feature a 3-bladed rotor in the range of 16-21 m diameter. Though the general designs look similar at first glance, the rotor designs and control are very different. The HyTide follows the approach of a fixed pitch, bidirectional rotor, thus eliminating both yaw and pitch mechanisms. The HS1000 operates with a variable pitch system which eliminates any

nacelle yawing mechanism as the blades can be fully rotated by 180° . In contrast, the AR-1000 has fixed pitch blades, but implements a nacelle yawing mechanism.

As the maturity of tidal turbine technologies progresses, large tidal farm projects are coming into view. The project pursued by MeyGen Ltd. (2013) in the Pentland Firth foresees a tidal farm of nearly 400 MW installed capacity, of which 86 MW have been recently approved by the Scottish government. The proposed technology is a new turbine development, although based on the experience of the AR-1000 and the HS1000 turbines.

The free-stream axial-flow devices introduced above are currently at the forefront of tidal energy development. However, over the past decade, several turbine concepts have also been proposed involving ducts surrounding the axial-flow rotor. Examples of such turbine concepts are the ducted turbines proposed by both Lunar Energy Ltd. (2013) and Clean Current Power Systems Inc. (2013), as well as the open-centre turbine developed by OpenHydro Group Ltd. (2013). Several of these concepts have attracted the support of industry partners, both energy utilities and turbomachinery manufacturers, and have therefore gained considerable investment and publicity, particularly during the period 2007-2009 (E.ON UK, 2007). Though claims of superior hydrodynamic efficiency of these designs have often been voiced by the developers, at the start of this research project no studies were publicly available confirming these claims. Based on the strong industry support as well as the unconfirmed claims of superior efficiency, ducted turbine concepts were chosen as the focus of this research. The goal of this study is to understand the behaviour of the fluid flow through these axial-flow ducted tidal turbines, as well as their hydrodynamic efficiency, and to compare this to that achieved by free-stream (bare) axial-flow turbines.

1.3 Thesis outline

The goal of this research study is to determine through numerical simulation the fluid mechanical behaviour and performance of various marine current turbine concepts in particular that of bidirectional ducted and open-centre turbines. This thesis is divided into the following chapters:

Chapter 2: Ducted turbines

This chapter introduces the ducted tidal devices proposed by the industry and concludes with a literature review of studies analysing ducted turbines, operating in both wind and tidal currents.

Chapter 3: Modelling tidal turbines

This chapter presents a short overview of computational turbine models used in tidal turbine research, both those employed in this study and other popular modelling approaches. It introduces the numerical method, the Reynolds-averaged Navier-Stokes (RANS) equations, as well as the solver employed in this study, ANSYS FLUENT.

Chapter 4: Actuator disc simulations

In this chapter, linear momentum actuator disc theory (LMADT) is introduced together with applications of this theory in wind and tidal energy. The model setup of the actuator disc within the solver is presented. A validation of the model is performed for the bare turbine.

Bare, ducted, and open-centre turbines are introduced and simulated using first axial inflow and then yawed inflow. The discussion of the analyses in both cases addresses the flow field, the forces on the turbine, and its performance, and compares these between the different devices.

Chapter 5: RANS-BEM simulations

Blade element momentum (BEM) theory is introduced and the application of this method in wind and tidal energy research is discussed. The implementation of BEM in the RANS solver (RANS-BEM) is presented and validated using a bare turbine in low blockage.

BEM theory introduces rotation and real rotor geometry to the flow problem, therefore requiring a rotor design. Turbine rotors are designed for each of the devices analysed, using a RANS-BEM-integrated rotor design algorithm. The three devices analysed using actuator disc theory in chapter 4 are simulated using RANS-BEM. Both axial and yawed inflow cases are investigated in detail with regards to flow features, forces on rotor and device, as well as performance.

Chapter 6: Conclusions

The conclusions drawn from chapters 4 and 5 are discussed in the final chapter. In particular, the results of the two different simulation methods are compared to each other. The contribution of the body of work is presented and future work suggested.

Chapter 2

Ducted turbines

The use of diffusers or ducts for enhancing the performance of wind and tidal turbines has been in discussion for a many years (Foreman *et al.*, 1978; van Bussel, 2007). In general there are two types of ducts that have been proposed for wind and tidal turbines: unidirectional ducts (diffusers) and bidirectional ducts. The former is often made up of an aerofoil-shaped cross-section that induces a circulation and thus lifting force toward the duct axis. The bidirectional duct is designed to provide an increase of the flow velocity at the throat of the duct where the rotor is placed. Figure 2.1 shows an example of each of these duct types.

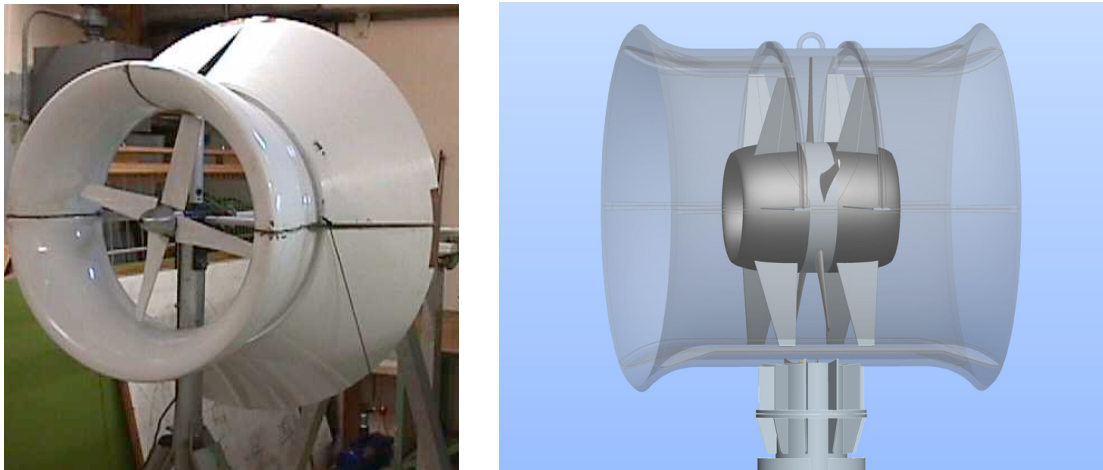


Figure 2.1: Examples of uni- and bidirectional ducts. Left: Vortec unidirectional duct for wind energy application (Phillips *et al.*, 2005). Right: CleanCurrent bidirectional duct for tidal energy application (Clean Current Power Systems Inc., 2013).

Ducts proposed for the wind industry are of the unidirectional type, which need to be yawed into the flow together with the turbine rotor. Although the rotor itself can be smaller compared to a bare turbine extracting the same amount of energy from

the air flow, the added weight of the duct, together with the requirement to allow to rotate, and thus the cost of the complete structure, normally outweighs the benefits of flow speed augmentation for these type of devices.

Whilst the concept of encasing the turbine blades in a shroud has not proven viable for wind turbines, a wide range of ducted tidal devices have been suggested, see section 2.1. Studies commissioned by manufacturers of these devices claim a substantial increase in power in comparison to bare devices (Thorpe, 2005), as well as other advantages such as better performance in yawed flow conditions and lower maintenance costs. However, the details of the analyses are not always fully available in the public domain. Section 2.2 gives an overview of the available publications concerning ducted turbines for both wind and tidal applications.

2.1 Ducted and open-centre tidal turbines proposed by the industry

This section aims to present a comprehensive overview of proposed axial-flow tidal turbine devices that make use of a duct structure. Ducted cross-flow turbines are omitted, as cross-flow devices are outside the scope of this study. The focus is on bidirectional ducted axial-flow devices. However, a brief overview of unidirectional ducted axial-flow concepts is given as well. Since the start of this study, some of the proposed devices have apparently been abandoned commercially by the developers, which will be noted where this information is available.

2.1.1 Bidirectional ducted tidal turbines

Rotech Tidal Turbine by Lunar Energy Ltd. (2013):

The Rotech Tidal Turbine, see figure 2.2, is a conventional horizontal axis turbine that is located midway along a venturi shaped duct. The main feature of this concept is the bidirectional duct, which the developers believe to accelerate the flow that passes through the turbine. As the flow passes from the inlet to the duct throat, its velocity is increased inversely proportional to the decrease in area, $U_{\text{throat}}/U_{\text{inlet}} = A_{\text{inlet}}/A_{\text{throat}}$, assuming mass flow is conserved. Since power generated is proportional to the cube of the flow velocity, the duct is believed to increase the energy that can be captured by a rotor of a given diameter (Shields, 2008). Additionally the developers argue that the modular setup should reduce maintenance costs and that the bidirectional duct should provide a flow straightening effect, allowing modest yaw angles to be readily accommodated. In 2007 Lunar Energy received the support of the energy utility E.ON, and plans for large scale applications were made (E.ON UK, 2007). However, these plans never materialised and the most up-to-date press-release by Lunar Energy was published in 2008.



Figure 2.2: The Rotech Tidal Turbine by Lunar Energy Ltd. (2013).

Open-Centre Turbine by OpenHydro Group Ltd. (2013):

The design of the Open-Centre Turbine, see figure 2.3, focusses on few moving parts, except the turbine rotor itself. This turbine has an aperture at its centre and turns with low rotational speeds. In a similar way to the Rotech Tidal Turbine, the open-centre turbine is enclosed by a duct, though in the case of the Open-Centre Turbine this duct is short and designed to house the generator parts, rather than designed for a large flow acceleration. The central opening produces a jet and thus a low pressure region, providing a suction effect to accelerate the flow through the turbine, increasing the power take off.

The OpenHydro turbine has been tested extensively at the EMEC facility since 2006, while the testing of a 10 m diameter turbine (rated at 1 MW) installed 2009 in the Bay of Fundy, Canada, had to be aborted after a few months due to structural failures. OpenHydro has tested their 16 m diameter 2.2 MW device over a three month period at Paimpol-Bréhat, France, where a tidal farm consisting of six turbines is planned. OpenHydro has further been awarded a license to develop a 100 MW tidal farm off the coast of Northern Ireland.



Figure 2.3: The Open-Centre Turbine by OpenHydro Group Ltd. (2013).

Clean Current tidal turbine by Clean Current Power Systems Inc. (2013):

In 2006, the Clean Current tidal turbine (see figure 2.4 and patent by Davis *et al.* (2011)) became the first ducted bidirectional tidal turbine to be deployed, measuring 5 m in diameter and rated at 65 kW. The design is similar to that proposed by Lunar Energy. However, similar to the turbine proposed by OpenHydro, the hub is ring shaped, providing a small central aperture. CleanCurrent gained the support of Alstom in 2009, a collaboration which was terminated in late 2012. CleanCurrent has since abandoned its bidirectional ducted design and is now developing unidirectional ducts for river applications and unidirectional ducts with a passive yaw mechanism for tidal applications.

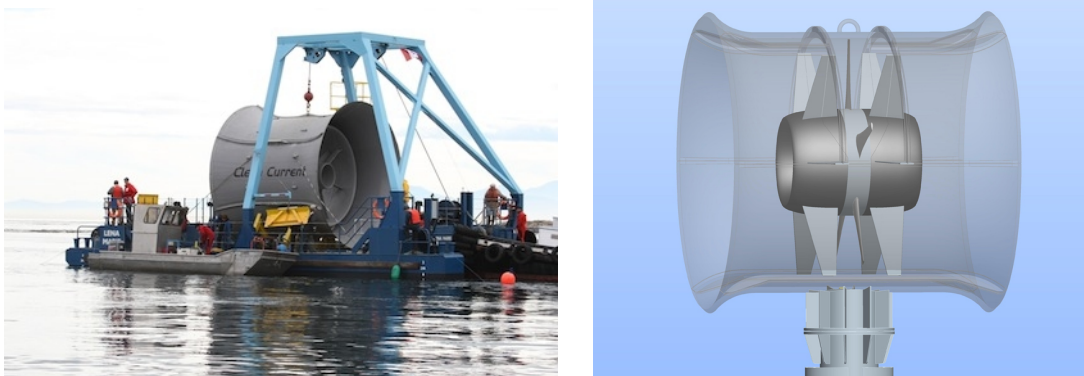


Figure 2.4: A 2006 (left) and 2010 (right) design version of the Clean Current tidal turbine by Clean Current Power Systems Inc. (2013).

Solon turbine by Atlantis Resources Corporation Pte Ltd (2013):

The duct design of the Solon turbine, see figure 2.5, is very similar to that proposed by Clean Current, however, like the device by Lunar Energy, it does not feature an aperture at its centre. In 2008, Atlantis tested the 500 kW version of the Solon turbine, the AS-500, through offshore tow-tests in Singapore. Rated at 2.4m/s, it produced up to 500 kW of power for a rotor diameter of circa 5 m and a total device diameter of around 7 m. After completing the tow-tests, the turbine was advertised commercially at three different power ratings, 100 kW, 500 kW, and 1 MW (Mehmood

et al., 2012b). Atlantis progressed to develop free-stream (unducted) turbine concepts and has not pursued or advertised the Solon turbine further.



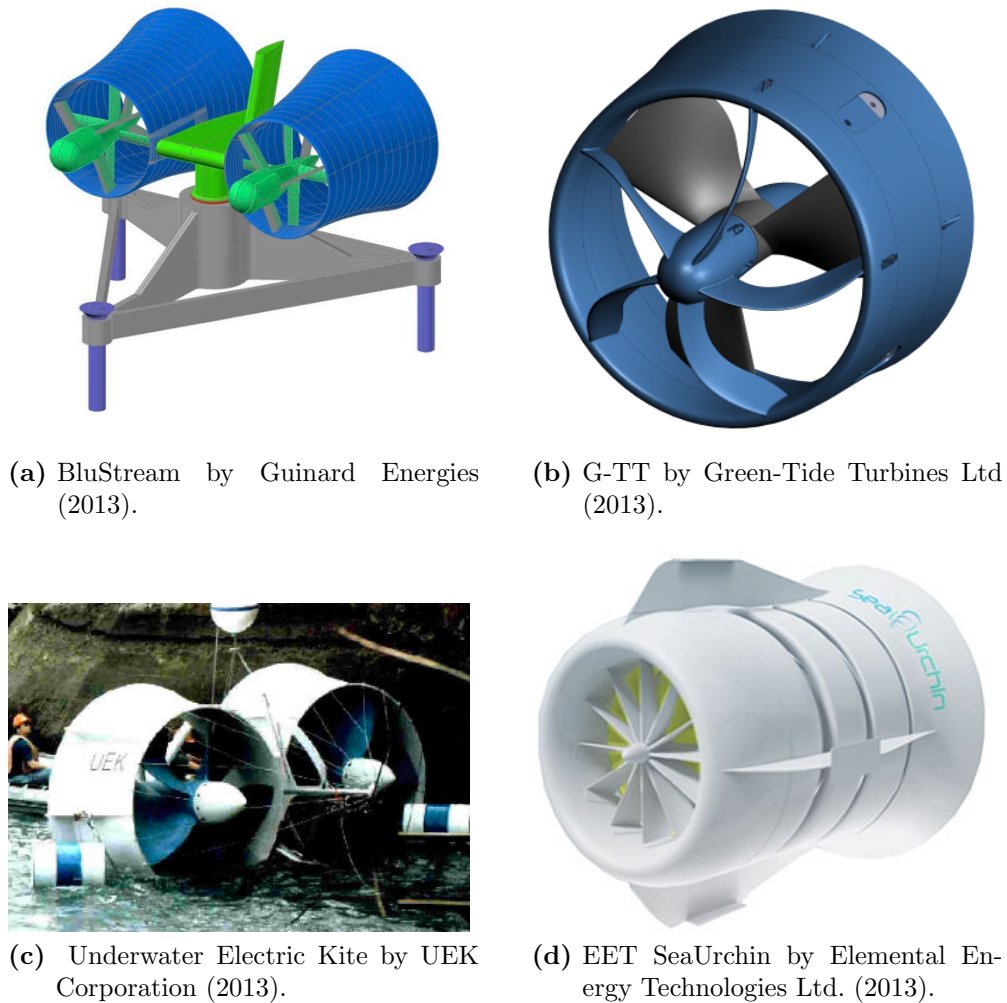
Figure 2.5: The Solon turbine by Atlantis Resources Corporation Pte Ltd (2013).

2.1.2 Unidirectional ducted tidal turbines

Unidirectional ducted tidal turbines

Unidirectional ducted turbines make use of a diffuser in order to increase the mass flow through the rotor compared to the same rotor without a duct. This mass flow increase can be explained as a result of the duct acting as an annular wing. The wing produces a lift force acting towards the centre of the duct, which, due to bound circulation, draws flow towards the duct centreline, thereby augmenting the velocity through the rotor (Shives, 2011). A range of unidirectional ducted turbines have been suggested for tidal applications, see figure 2.6, though many more have been suggested at smaller scale for river applications.

All of the devices presented in figure 2.6 are designed with passive yawing mechanisms in order to align the rotor with the tidal flow, noting that for riverine or ocean current applications the same devices may be installed without a yawing mechanism. Based on the energy density of water and the typical tidal flow velocities of 2-3 m/s,



(a) BluStream by Guinard Energies (2013).

(b) G-TT by Green-Tide Turbines Ltd (2013).



(c) Underwater Electric Kite by UEK Corporation (2013).



(d) EET SeaUrchin by Elemental Energy Technologies Ltd. (2013).

Figure 2.6: Unidirectional ducted tidal turbine concepts.

commercial scale tidal devices in the MW range will need to exhibit device diameters of 10-20 m. Hence, the overall mass of material to be yawed is extremely large and the feasibility of such devices remains questionable.

2.1.3 Devices chosen for analysis

Apart from the SeaGen Turbine (Marine Current Turbines Ltd., 2013) which was commercially installed in Strangford Lough, Northern Ireland, in 2008, bidirectional ducted turbines (with and without aperture) received the lion's share of media atten-

tion and industrial support at the time of planning of this research project (2009). This was the case, even though no scientific publications on bidirectional ducts or open-centre turbines were available.

Manufacturers of bidirectional ducted turbines claimed a significant flow acceleration effect through the duct. However, there remained a lack of basic understanding of how effective this and other similar flow accelerators are in practice. As the turbine presents a greater resistance to the free passage of the flow through the device, some of the flow must be diverted to pass around the outside of the duct. Hence, the full flow acceleration effect, that the duct might be expected to provide, cannot be achieved in practice. In order to mitigate the effect of turbine resistance, some manufacturers have proposed to incorporate an aperture at the centre of the turbine. While this does reduce the resistance to the flow and increase the mass flow through the duct, the rotor area, and hence power generating device area, is significantly reduced.

Since the only existing analyses of these devices have been performed by the manufacturers themselves, the details of the analyses are commercially confidential. It is believed that previous studies of these devices, both experimental and numerical, have been carried out at high blockage (ratio of device to flow passage cross-sectional areas), and have therefore resulted in unrepresentative power predictions for low blockage conditions. Further, as will be shown in this study, the reference area for comparison is crucial when discussing performance increases.

It is therefore of importance to the industry to conduct unbiased independent research using theoretical, computational and, where appropriate, experimental modelling. In the present study, numerical modelling (computational fluid dynamics, CFD) was employed to gain a thorough understanding of the flow through bidirectional ducted tidal turbines with and without apertures and conduct a comparative analysis of various tidal turbine concepts.

2.2 Previous analyses of ducted turbines

This section presents an overview of past studies performed on ducted turbines. Developments of analytical models are presented, as well as studies aimed specifically at wind and tidal turbine applications.

2.2.1 Analytical studies of ducted turbines

Several publications present discussions of ducted horizontal wind or water turbines using analytical modelling. These analytical models treat the flow as inviscid uniform flow, applying momentum conservation to a stream-tube passing through a ducted actuator disc. As these models assume inviscid flow they require additional empirical parameters to capture the effects of flow separation and other viscous flow effects.

In the work by Lawn (2003), similar to that of Foreman *et al.* (1978), the performance of ducted turbines is investigated by treating the ducts upstream and downstream of the turbine as contractions or expansions having specified diffuser efficiencies. Lawn concludes that, for given diffuser efficiencies, there is an optimum turbine resistance for generating maximum power, as the swallowing capacity of the duct is increased as the resistance decreases. This theory has been tested only using unidirectional ducts with aerofoil cross-sections and smooth inlet profiles. However, due to the empirical parameters of inlet and diffuser efficiency, it may also be applicable to bidirectional ducts with large scale separation, for which no results have been presented so far.

Linear momentum actuator disc theory (see chapter 4) has been extended by both van Bussel (2007) and Jamieson (2009) to account for the influence of ducts on the flow field in which a turbine operates. Van Bussel identifies ideal duct performance based on two parameters: the area ratio between duct exit and throat as well as

the back pressure at the diffuser exit. However, the model neglects viscous loss and flow separation effects. Introduced in Jamieson (2008) and in a more general form in Jamieson (2009), Jamieson’s model describes the ideal limiting performance for ducted devices. Within this theory, the Betz limit emerges as the special case of energy extraction in unconstrained flow. Further, the theory states that, in an ideal system, the universal limit of energy extraction is found at 8/9 of the upstream kinetic energy, in the stream-tube associated with the energy extraction. Thus this theory suggests that, from a given source stream-tube, a ducted turbine cannot extract more energy than a bare rotor, but that the same energy can be extracted using a smaller rotor. However, since this theory only analyses systems where the duct modifies the flow field but does not in itself extract energy, it will not be applicable to systems where strong separation effects (and thus energy loss) occur, such as for bidirectional ducts with all but shallow diffuser sections.

2.2.2 Analysis parameters for ducted turbines

When discussing studies of ducted turbines, it is crucial to understand the boundary conditions employed and the methods used for analysing performance. As shown in chapter 4, the blockage ratio, B , of an experimental or numerical domain has a substantial impact on the performance of a tidal device. It is defined as

$$B = \frac{\text{blocked area}}{\text{channel cross-sectional area}} = \frac{A_{\text{device}}}{A_{\text{domain}}} \quad (2.1)$$

where A is the cross-sectional area. While for a bare turbine $A_{\text{device}} = A_{\text{rotor}}$, for a ducted turbine $A_{\text{device}} > A_{\text{rotor}}$, as illustrated in figure 2.7. Analogous to the studies presented hereafter, A_{domain} and A_{rotor} are fixed, such that the blockage ratio is larger for the ducted turbine, compared to the bare turbine.

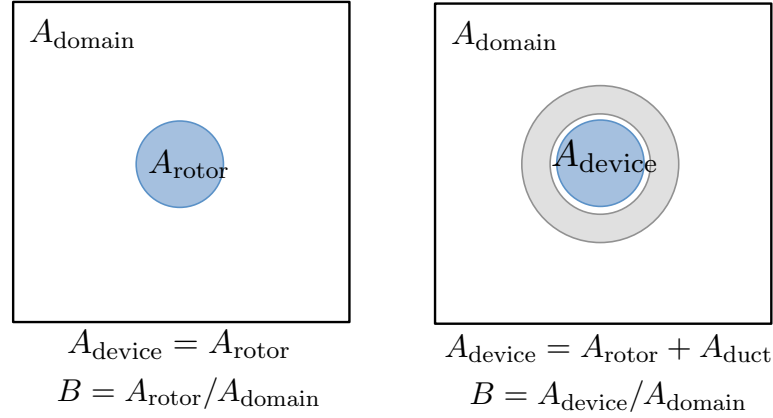


Figure 2.7: Blockage ratio of the bare and ducted devices when turbine rotor and domain cross-section are constant.

The diffuser area ratio is defined as $A_{\text{device}}/A_{\text{rotor}}$ and is therefore the factor by which blockage is increased for the ducted turbine compared to the bare turbine, $B_{\text{duct}}/B_{\text{bare}} = A_{\text{device}}/A_{\text{rotor}}$. Maximum performance of a device (measured in power coefficient, C_P) increases with blockage,

$$C_{P,\text{max}} \propto 1/(1 - B)^2, \quad (2.2)$$

as derived by (Garrett and Cummins, 2007), and as further supported in chapter 4. Therefore, using fixed rotor and domain dimensions when comparing bare and ducted devices, generates a performance bias in favour of the ducted turbine, purely based on the increase in blockage. In order to quantify this effect, the parameter blockage bias is introduced

$$B_{\text{bias}} = \frac{1}{\frac{(1 - B_{\text{duct}})^2}{1}} = \left(\frac{1 - B_{\text{bare}}}{1 - B_{\text{duct}}} \right)^2, \quad (2.3)$$

which is a ratio of the blockage enhancement for the ducted turbine, based on relation (2.2).

The conventional method of quantifying the efficiency of a turbine is given by the nondimensional power coefficient,

$$C_P = \frac{P}{1/2 \rho A_{\text{ref}} U_{\infty}^3} \quad (2.4)$$

where P is the power generated by the turbine, A_{ref} the reference area, and U_{∞} the free-stream flow velocity. An early study into ducted wind turbines by Lilley and Rainbird (1956) analyses the performance of the ducted turbine based on the device area, therefore employing A_{device} as A_{ref} . However, nearly all other authors investigating the performance augmentation by ducts, solely present their results through A_{rotor} as the reference area. It is clear that as $A_{\text{device}} > A_{\text{rotor}}$, normalising power on A_{rotor} leads to the reporting of much higher power coefficients.

As shown by McIntosh *et al.* (2011), rotors designed for application in bare turbines perform poorly in ducts and vice versa, concluding that tailored rotor designs are needed to fairly compare bare and ducted devices. Employing the same rotor for both devices fails to acknowledge this fact, and thus further performance bias may be introduced into comparison of rotor operation with and without duct augmentation.

2.2.3 Analyses of ducted axial-flow wind turbines

From time to time, ducted wind turbines have been discussed in the literature, though so far none have proven commercially viable. As similar modelling techniques (with the exception of the free surface) are used for ducted wind turbine studies, tentative conclusions for modelling ducted tidal turbines can be drawn. Table 2.1 gives an overview of the studies presented hereafter, all of which investigate unidirectional ducts. Where the information is available, the diffuser area ratio is presented as well

Table 2.1: Analyses of ducted axial-flow wind turbines

| Study | method | $A_{\text{device}}/A_{\text{rotor}}$ | $C_P(\text{rotor})$ | $C_P(\text{device})$ | $C_P(\text{bare})$ |
|--|----------------|--------------------------------------|---------------------|----------------------|--------------------|
| Phillips <i>et al.</i> (2005) | wind tunnel | 2.22 | 0.81 | 0.37 | n.a. |
| Visser (2009) | field test | n.a. | 0.6-0.8 | n.a. | n.a. |
| Hansen <i>et al.</i> (2000) | numerical disc | 1.84 | 0.94 | 0.51 | 0.59 |
| Ohya <i>et al.</i> (2008) | wind tunnel | 6.68 | 1.40 | 0.21 | 0.25 |
| Grassmann, Bet, Ceschia and Ganis (2003) | numerical | 2.25 | 0.64 | 0.28 | 0.40 |

as the maximum achieved power coefficient, based on A_{rotor} , and calculated for A_{device} . Where applicable, the performance of the bare turbine, $C_P(\text{bare})$, is also stated.

An extensive study was performed by Phillips (2003) on a ducted axial-flow wind turbine developed by (then commercially still active) Vortec Energy. Over the years, several diffuser designs were developed through numerical simulation and are presented in Phillips (2003) and Phillips *et al.* (2005), with the most recent design displayed in figure 2.1. This design was analysed experimentally in a wind tunnel. The results were compared to CFD simulations, showing good agreement in general with regards to velocity increase and pressure. However, the power predicted by the CFD simulations was significantly higher than that reached in the experiment. This discrepancy was attributed to separation occurring in the physical diffuser which was not captured numerically through the use of the $k - \epsilon$ turbulence model.

In a similar way to Phillips (2003), Visser (2009) analysed a design of a ducted axial-flow wind turbine as part of a commissioned report, which was promoted by WindTamer Corporation (now further developed by Skywolf Wind Turbine Corporation (2013)). The design is similar to that by Vortec Energy, consisting of a straight duct section and a diffuser section, with a slot for boundary layer control separating

the two. Results from field tests, using a 1.3 m rotor diameter indicate a performance slightly higher than the Betz limit ($C_{P,\text{Betz}} = 0.59$, theoretical performance limit of turbines in unconfined flow, see section 4.1.1 for a definition).

Hansen *et al.* (2000) have developed an actuator disc CFD model of the flow through a wind turbine in a diffuser. The shape of the unidirectional diffuser for this study is based on a deformed NACA 0015 aerofoil. A 10° section of the disc and diffuser were modelled and periodic boundary conditions employed. The domain blockage ratio was low, representing nearly unconfined conditions, and therefore the blockage effect may be assumed minimal.

Ohya *et al.* (2008) have tested a turbine shrouded by a flanged diffuser in wind tunnel tests as well as in the field. First the optimal duct shape – a diffuser shape – was established. This was then further enhanced by a flange placed at the diffuser exit. The flange generates a low-pressure region at the exit of the diffuser by vortex formation and draws increased mass flow through the diffuser tube. Field experiments support the results obtained through wind tunnel tests, hence the authors believe that the wind tunnel experiments are free from blockage effects. The diffuser area ratio is reported as 2.35, however, the total frontal area of the device including the flanges leads to a much higher value of $A_{\text{device}}/A_{\text{rotor}} = 6.68$.

Grassmann, Bet, Ceschia and Ganis (2003) studied a short diffuser consisting of two aerofoil sections separated by a slot, which they analysed both numerically as well as experimentally in field tests (Grassmann, Bet, Cabras, Ceschia, Cobai and DelPapa, 2003) and compared to a bare turbine of same rotor diameter. For the experiments Grassmann *et al.* employ two commercially available residential wind turbines of the same model, of which they fit one with a diffuser. As power coefficients are not reported for the experiments, the results in table 2.1 refer to the numerical simulation.

All of the above studies have reported power augmentation due to the employed diffusers. The reported performance coefficient, $C_P(\text{rotor})$, employs A_{rotor} as the reference area. When renormalising the performance results on A_{device} , see table 2.1, all of the above results lie below those achievable by a bare turbine ($C_{P,\text{Betz}} = 0.59$), and, where a direct comparison was conducted, below those of the bare turbine compared to.

2.2.4 Analyses of ducted axial-flow tidal turbines

Manufacturers of ducted tidal devices claim substantial increases in power, through the use of a bidirectional duct. However, no publication of substantial data is available. This section will therefore present the few (mostly academic) publications available on ducted axial-flow tidal turbines. Most of the following studies focus on unidirectional ducts, and only that by Setoguchi *et al.* (2004) investigates the bidirectional duct. As for the studies of ducted wind turbines, it is of importance to understand which reference area was used in the performance analyses and how domain blockage was treated.

A number of studies have been performed on ducted vertical axis tidal turbines, many of which include flume and open water tow tests, see Kirke (2005), Klapotocz *et al.* (2007), and Alidadi (2009). However, since the hydrodynamics of vertical cross-flow turbines are rather different to those of horizontal axial-flow tidal turbines, these results will not be further discussed here.

Münch *et al.* (2009) modelled the full rotor of the unidirectional ducted tidal turbine proposed by Guinard Energies (2013) using three-dimensional (3D) CFD simulation. The four bladed rotor is placed in a rotating mesh embedded within a stationary mesh containing the aerofoil shaped diffuser and outer flow domain. The optimisation of rotor geometry and duct geometry are performed separately, while the authors

believe further performance enhancements should be feasible through a coupled design approach. For the optimised configuration a maximum power coefficient of $C_P(\text{rotor}) = 0.55$ was found, however, no direct comparison to a bare turbine is given.

A numerical and experimental study by Gaden (2007), later published as a summary by Gaden and Bibeau (2010), investigates the use of diffusers in a parametric study. As further discussed in section 4.1.2, the turbine is modelled as a momentum source region, extracting axial momentum. In this methodical study of diffuser geometries, key features of unidirectional diffusers (opening angle, area ratio) were varied. The best diffuser configuration was found to produce twice the amount of power of the bare turbine, even after renormalising based on A_{device} . This result contrasts those presented in table 2.1, suggesting real power augmentation.

Two additional factors introduced in section 2.2.2 are the source of this considerable power augmentation: Rotor design tailored for ducted operation and blockage bias. Though domain dimensions are not stated, the blockage appears to be of the order of $B_{\text{duct}} = 0.04$ for the ducted turbine and correspondingly $B_{\text{bare}} = 0.025$ for the bare turbine, thus resulting in a moderate blockage bias of $B_{\text{bias}} = 1.048$. This suggests a performance overestimate of 4.8% stemming from the difference in blockage. However, the main factor contributing to the power augmentation is the application of the momentum source model. The axial thrust was chosen at a level close to ideal for ducted operation, but was applied to both the bare and ducted device. This is considerably lower than the optimal thrust level for bare turbine operation. Therefore the bare turbine Gaden *et al.* compared to is operated far off its design point.

Setoguchi *et al.* (2004) analyse the exterior shapes of bidirectional empty ducts, while keeping the inside shape (converging + straight + diverging section) the same. Though the experiments are performed in a wind tunnel, the study is aimed at

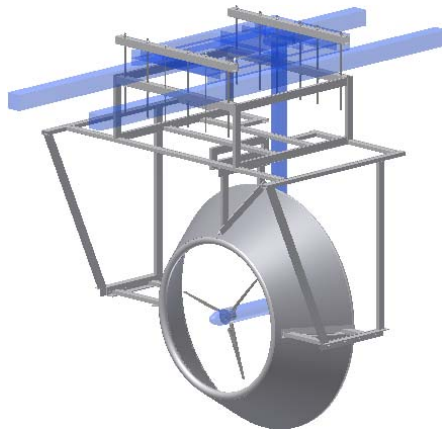
studying ducts for tidal turbines. It was found that the best results are obtained with a cylindrical exterior duct shape. In general a significant effect of the outside shape of the duct on the flow within the duct is reported. However, this study neglects to model the turbine and its effects on the flow field.

Though some conclusions can be drawn from the literature presented above, for the most relevant configuration – a bidirectional ducted turbine – no scientific publications were available at the start of this project. While the analyses of unidirectional ducts and their potential for power augmentation are of general interest, the application of unidirectional ducts for large tidal turbine devices remains questionable. As the flow of a bidirectional duct differs considerably from that of a unidirectional duct, only limited conclusions can be drawn from these studies. Further, analysing the duct without a turbine, as Setoguchi *et al.* (2004) have, disregards the influence of the turbine resistance on the flow and the resulting interaction with the internal and external duct flow fields. Coupled analyses, modelling both duct and turbine are thus needed to understand this interaction.

2.2.5 Recent analyses of ducted axial-flow tidal turbines

Since the start of this research project, a number of new studies on ducted turbines have been published, that will be summarised here. However, despite the industry’s bias towards bidirectional devices, of the studies presented here, the study conducted by Fleming *et al.* (2011) remains the only other investigation concerned with bidirectional ducts. Figure 2.8 presents an overview of some of the ducted designs studied experimentally.

As for the previous publications of diffuser augmented turbines, most of the publications discussed below fail to acknowledge the change in blockage when testing a rotor of fixed diameter both with and without the duct in a fixed constrained domain

(a) Reinecke *et al.* (2011).

(b) Sun and Kyojuka (2012).

(c) Luquet *et al.* (2013).

(d) Lokocz (2012).

Figure 2.8: Ducted tidal turbines studied experimentally.

(numerically or experimentally), see Reinecke *et al.* (2011) and Lokocz (2012), Sun and Kyojuka (2012). A few investigators of unidirectional ducts for tidal applications acknowledge the importance of reference area and state the performance both in terms of rotor and outer diffuser diameter, see Luquet *et al.* (2013) and Shives (2011). For each study, table 2.2 summarises the performance results and calculates the performance based on total device area where possible.

Two recent studies investigate the velocity increase through diffusers, conducting parametric studies of diffuser design parameters. However, neither study considers the effect of the turbine through the duct. Mehmood *et al.* (2012a) model an empty unidirectional duct of aerofoil cross-section employing CFD, varying both chord length and angle of attack. Khunthongjan and Janyalertadun (2012) numerically and

Table 2.2: Recent analyses of ducted axial-flow tidal turbines

| Study | method | $A_{\text{device}}/$ A_{rotor} | $C_P(\text{rotor})$ | $C_P(\text{device})$ | $C_P(\text{bare})$ | B_{bias} |
|-------------------------------|---------------------|--|---------------------|----------------------|--------------------|-------------------|
| Gaden and Bibeau (2010) | numerical | 1.56 | 0.87 | 0.56 | 0.28 | 1.048 |
| Reinecke <i>et al.</i> (2011) | towing tank | 3.29 | 1.72 | 1.10 | 0.46 | 1.260 |
| Sun and Kyozuka (2012) | flume | ≈ 1.96 | 0.88 | 0.45 | 0.36 | 1.063 |
| Luquet <i>et al.</i> (2013) | towing tank | 2.16 | 0.64 | 0.30 | n.a. | n.a. |
| Lokocz (2012) | towing tank | ≈ 1.07 | 0.40 | 0.37 | 0.44 | 1.013 |
| Shives and Crawford (2010) | numerical modelling | 2.87 | 1.1 | 0.38 | 0.59 | 1.000 |
| Fleming <i>et al.</i> (2011) | numerical modelling | 1.31 | 0.55 | 0.42 | 0.72 | 1.000 |

experimentally investigate an empty unidirectional duct consisting of a straight pipe and a cone-shaped flanged diffuser of varying opening angles.

Reinecke *et al.* (2011) studied a unidirectional duct intended for ocean current applications, employing two-dimensional (2D) axisymmetric numerical analysis and towing tank tests. First the curved-plate diffuser shape was optimised and modelled numerically in low flow blockage. The optimised diffuser shape was then tested in a highly blocked towing tank using a rotor designed by the University of Southampton (Bahaj, Batten and McCann, 2007). The ducted tests exhibited a higher performance than the bare rotor, which was also tested in the towing tank. Although a blockage correction was discussed, this correction was not applied to the experimental data.

The data shows a power augmentation of a factor of roughly 4 compared to the bare turbine, which is larger than the area ratio of the diffuser. Changes in blockage between the bare ($B_{\text{bare}} = 0.046$) and ducted rotor ($B_{\text{duct}} = 0.15$) result in a blockage bias of $B_{\text{bias}} = 1.260$, thus accounting for 26% of the power augmentation compared

to the bare turbine. However, as in the study by Gaden and Bibeau (2010), the bulk of the reported power augmentation is likely to derive from the fact that the bare turbine is operated significantly off its design point. The rotor employed by Reinecke *et al.*, though designed for bare turbines, was employed using a high blade pitch angle, suited for ducted turbine operation, but 10° off the bare rotor design point (Bahaj, Batten and McCann, 2007).

It should be noted, that the investigation by Reinecke *et al.* (2011) is the only study to present a $C_P(\text{device})$ larger than the theoretical limit of $C_{P,\text{Betz}} = 0.59$. Correcting the ducted turbine performance for blockage by employing relation (2.2) reduces the power coefficient to $C_P(\text{device, corrected}) = 0.79$, which is still higher than $C_{P,\text{Betz}}$.

In a similar study, Sun and Kyozuka (2012) propose a short, flanged unidirectional duct in their comparative experimental flume analysis. Only one rotor and duct geometry are tested, with the rotor employed being the same for both the bare and ducted test cases. Though not all dimensions are given the diffuser area ratio is estimated at 1.96. The results show an increase in power by a factor of 2.5 for the ducted turbine when compared to the same bare rotor. The results are further supported by CFD simulations. As for Reinecke *et al.* (2011), changes in blockage and in reference area are not discussed, though significant blockage bias also exists in this case. Further, the poor performance of the bare turbine ($C_P(\text{bare}) = 0.36$ at $B = 0.03$) suggests that the rotor is not optimised for bare operation.

A recent numerical and experimental study by Luquet *et al.* (2013) builds on the work by Münch *et al.* (2009), investigating an updated duct design. Experiments of the ducted turbine were conducted in a large towing tank facility of 105 m^2 cross-section, thereby minimising influence of blockage ($B < 1\%$). The results obtained experimentally confirm those obtained numerically. A bare turbine was not tested for comparison.

Lokocz (2012) investigated a ducted turbine, using the NACA 4412 aerofoil profile for the diffuser cross-section. The aerofoil profile is applied with zero degree angle of attack and hence the rotor to diffuser area ratio is close to 1. The exact duct dimensions are not given and are estimated. The investigation was performed experimentally in a towing tank at moderate blockage ($B_{\text{duct}} = 0.089$). Two three-bladed rotors were designed for duct and free-stream application using the same rotor diameter. Due to the low diffuser area ratio, the blockage bias is minimal. No power augmentation was reported for the ducted compared to the bare turbine rotor.

Shives (2011) studied a unidirectional duct of aerofoil cross-section using analytical and numerical modelling. As for the studies by Münch *et al.* (2009) and Gaden and Bibeau (2010), an optimisation of the duct shape was carried out, modelling the turbine as an actuator disc. Ducted and bare turbines were compared using actuator disc simulation in nearly unblocked conditions. Apart from stating the performance of the devices in terms of power coefficients, Shives and Crawford (2010) further define the term “overall efficiency”, $\eta = P/P_E$, where P is the power produced by the device and P_E the power extracted from the flow. This measure of efficiency is also employed in the present study, where it is referred to as basin efficiency. The ducted devices analysed exhibit a poorer performance than the bare turbine when compared on this measure, due to the increased drag presented by the duct.

In addition to the duct optimisation, Shives developed a semi-empirical coupled Duct-BEM model. The strategy employed was to parameterise the effect of the duct on the flow and to then determine these parameters through modelling a range of duct geometries using CFD. The resulting parameterised duct model was then combined with BEM in order to form the coupled Duct-BEM model. When comparing CFD and the Duct-BEM model good agreement was found. The application of this model was considered limited as a large number of CFD simulations would be needed in order to

cover a significant duct design-space. Further, the Duct-BEM model was derived for unbounded flow, while blockage effects play a significant role in tidal turbines.

Fleming *et al.* (2011) conducted an analysis of various bidirectional duct shapes, including the case of a straight-walled pipe. The effects of internal and external duct surface curvature on various performance parameters were analysed using CFD with the turbine modelled as an actuator disc. Contrary to the studies introduced above, Fleming *et al.* maintain a constant blockage throughout the analysis, comparing devices of equal outer diameter. All the ducted turbines considered yield lower power coefficients compared to a bare turbine. The results of the highest performing duct are included in table 2.2.

Fleming *et al.* also model the ducted turbine using higher-order modelling techniques, such as a blade-resolved model and a coupled CFD-BEM model developed by McIntosh *et al.* (2011). The authors note the lack of tip-vortex generation by the rotor of the ducted turbine. As expected, the performance results using higher-order modelling lie significantly below those generated with the actuator disc, which represents an ideal rotor. The results presented by Fleming *et al.* (2011) are in line with the findings of the present study and deliver confirmation that the results presented in Belloni and Willden (2011) are also applicable for more arbitrary duct shapes.

While nearly all of the studies presented in this chapter report power augmentation through the use of a diffuser, in most cases renormalising performance on the total device area leads to a lower performance than for the bare turbine. For the studies where blockage bias was negligible, the power per device area was lower than for the bare turbine. Of the studies presented in tables 2.1 and 2.2, only three, Gaden and Bibeau (2010), Reinecke *et al.* (2011), and Sun and Kyojuka (2012), report performance augmentation after renormalising on A_{device} . These results would indicate real

power augmentation by a diffuser. However, as discussed above, all three studies exhibit significant blockage bias and compare to bare turbines operating in off-design conditions. Considering that no other studies of ducted wind or tidal turbine have indicated real power augmentation, it is believed that correcting for these factors would lead to a power reduction compared to the bare turbine. Note that the study (Reinecke *et al.*, 2011) presents a performance result higher than the Betz limit after correcting for both blockage and diffuser area ratio.

Chapter 3

Modelling tidal turbines

For this study, numerical simulation, solving the Reynolds-averaged Navier-Stokes equations, was selected as the method of choice. This method was chosen over an experimental analysis in a flume for various reasons. The quality of experimental results depends greatly on whether hydrodynamic similarity of Reynolds and Froude numbers (see sections 3.2.2 and 4.2.1 for definitions) can be achieved. At the same time, the blockage of the channel cross-section should be kept low (or at least to values representative of a tidal channel) in order to analyse the tidal devices without introducing significant blockage effects. For a given flume cross-section, the requirement of Reynolds similarity and low blockage are conflicting, as both are directly linked to the dimensions of the device to be analysed.

Numerical modelling produces high resolution flow field data at full scale. Such data can be analysed to gain insight into the fluid mechanics of ducted tidal turbines. This chapter gives a short overview of computational turbine models used in tidal turbine research, see section 3.1. The two models used in this study, as well as other computational turbine models are presented. In section 3.2 the Reynolds-averaged Navier-Stokes (RANS) equations and the numerical method are introduced, together with the solver employed in this study, ANSYS FLUENT.

3.1 Overview of computational turbine models

This section introduces relevant computational methods for modelling wind and tidal turbines. There are various levels of detail in which a turbine rotor might be represented in a CFD model, ranging from a simple actuator disc model to full rotor representation through a moving mesh in a rotating reference frame. The computational costs can increase significantly when moving from simple to detailed modelling techniques. The study of Fleming *et al.* (2011) compares various of the simulation methods described below in terms of their computational efficiency.

A popular approach to modelling turbines is to represent the turbine as an actuator disc, implemented using a numerical porous disc. This method assumes steady flow, neglects effects caused by discrete blades and angular momentum, and solely models the reduction of linear momentum through the turbine rotor. The actuator disc approach is independent of the rotor design, as the turbine is modelled as an ideal energy extractor. Embedded in a numerical solver, it is a widely used tool for modelling wind (Sørensen and Myken, 1992; Mikkelsen, 2003) and tidal turbines (MacLeod *et al.*, 2002; Batten *et al.*, 2013). The method has been employed in the first part of this study and will therefore be discussed in detail in chapter 4.

An increasingly popular method for numerical modelling of turbines is to employ a CFD-embedded blade element momentum (BEM) model (Turnock *et al.*, 2011; Masters *et al.*, 2013). In BEM theory the rotor is modelled by applying force data to the flow based on actual rotor characteristics. Using tabulated blade coefficient data, both linear momentum extraction as well as angular momentum effects can be captured. The blades are not modelled discretely, but are divided into radial blade sections. The discrete blade forces at a given radial location are evenly distributed over a rotor revolution, resulting in a set of concentric annuli acting essentially as

separate actuator rings. Due to the smearing of the blade forces across one revolution, discrete blade effects (such as tip vortices) are not captured in this approach. The benefits of this approach are that, as for the actuator disc method, the blades need not be modelled in the mesh and that the model is a steady flow model, leading to a computationally efficient solution (though it is noted that unsteady simulations may be required to capture unsteady flow effects generated by the support ducts and support structure). At the same time, real rotor data may be applied yielding more realistic flow field and performance data compared to the actuator disc method. A CFD-embedded BEM model has been used in this study and will be introduced in chapter 5.

A method offering both the simplicity of not requiring rotor meshing, at the same time delivering results of discrete blade effects, is the actuator line method. Rather than resolving the rotor in the mesh, each blade is represented by an actuator line, for which tabulated blade data is applied across the span according to the simulated flow field. This actuator line rotates around the turbine axis at the given rotational speed and applies the blade forces to the current blade location only. Actuator line methods were first developed for wind turbines (Sørensen and Shen, 2002) and have recently been adapted for tidal turbine applications (Schluntz and Willden, 2012; Churchfield *et al.*, 2013).

If all details of the flow through a turbine need to be captured, a full 3D rotor model must be employed. This type of model includes fully meshed rotor blades incorporated in a sliding mesh which rotates within a fixed inertial outer domain mesh. Using this modelling approach, discrete unsteady blade effects can be studied. The forces on the blade are extracted directly from the simulation data and are a direct result of the flow and rotational velocities, as well as the rotor design. Hence, no external forces or assumptions need to be applied in order to model the rotor and its forces on

the flow field. Several studies employ full 3D rotor modelling, including Afgan *et al.* (2013); Fleming *et al.* (2013), however the high computational effort of this approach is substantial.

The objective of the present study is to fairly compare the performance of ducted, open-centre and bare devices. In the first part of this analysis (chapter 4) the devices are compared using the actuator disc approach, in order to investigate the impact of the duct and aperture itself, without introducing rotor design effects. In the second part of the analysis (chapter 5) rotors are designed for each of the three device types and are compared using a CFD-embedded BEM model. Together with the inclusion of hub structures, this second analysis delivers more realistic performance results to support the results obtained using the actuator disc simulations.

3.2 Computational fluid dynamics and RANS modelling

This section gives a brief overview of the governing equations of fluid flow as well as those variations of the equations implemented in the numerical solver used for the present analysis. An overview of CFD methods can be found in Anderson (1995), Pope (2000), Versteeg and Malalasekera (1995) and Wilcox (1993).

3.2.1 Governing equations

The motion and properties of fluid flow can be described by the governing fundamental equations of fluid dynamics which are mathematical statements of the three fundamental conservation laws:

- Mass conservation
- Momentum conservation
- Energy conservation

These equations can be written in various forms, and a detailed explanation and derivation can be found in many texts, see for instance Anderson (1995). Only a brief description of the parts relevant to this thesis will be given in this section.

The momentum equations for viscous flow are usually summarised under the term of “Navier-Stokes equations”. The continuity equation is based on the physical principle of mass conservation, the momentum equation on Newton’s second law ($\mathbf{F} = m\mathbf{a}$), and the energy equation on the principle of energy conservation.

A viscous flow is one in which transport phenomena of friction are included. Friction plays an important role close to fluid boundaries, and in general in flows of strong variation within the velocity field. A viscous flow is further defined as a flow where

viscous forces are important when compared to inertial forces and hence at modest Reynolds numbers (ratio of inertial to viscous forces) the full Navier-Stokes equations must be solved. In the present problem heat transfer is negligible and the flow can be regarded as incompressible. Hence, the equation for energy conservation does not need to be solved, reducing the problem to the solution of the continuity and momentum equations.

The momentum equation is a statement of Newton's second law when applied to a fluid element (Anderson, 1995):

$$\begin{array}{c}
 \mathbf{F} = m\mathbf{a} \\
 \hline
 \underbrace{\hspace{10em}}_{\text{body forces}} \qquad \underbrace{\hspace{10em}}_{\text{surface forces}} \\
 \hline
 \underbrace{\text{weight (gravity)} \quad \text{Coriolis force} \quad \text{centrifugal force} \quad \text{electromagnetic force}}_{\text{body forces}} \quad \underbrace{\text{pressure forces} \quad \text{viscous forces}}_{\text{surface forces}} \\
 \hspace{15em} \underbrace{\hspace{4em}}_{\text{normal}} \quad \underbrace{\hspace{4em}}_{\text{shear}} \\
 \hspace{15em} (\tau_{xx}, \dots) \quad (\tau_{xy}, \dots)
 \end{array}$$

In the momentum equations it is common to highlight the contributions due to surface forces as separate terms, while including the effects of body forces as source terms (Versteeg and Malalasekera, 1995).

The continuity and momentum equations in tensor notation for an incompressible Newtonian fluid are given by equations (3.1) and (3.2) respectively. These equations are a coupled system of non-linear partial differential equations that are difficult to solve analytically. For all but few special cases there is no closed-form solution to these equations (Anderson, 1995) and thus they must be solved numerically.

$$\text{Continuity for incompressible fluid:} \quad \frac{\partial u_i}{\partial x_i} = 0 \quad (3.1)$$

$$\text{Momentum :} \quad \rho \frac{\partial u_i}{\partial t} + \rho \frac{\partial (u_i u_j)}{\partial x_j} = -\frac{\partial p}{\partial x_i} + \mu \left(\frac{\partial^2 u_i}{\partial x_j^2} + \frac{\partial^2 u_j}{\partial x_j \partial x_i} \right) + S_{M,i} \quad (3.2)$$

where x_i the i -th spatial dimension, u_i is the i -th component of velocity, ρ the fluid density, t is time, μ dynamic viscosity and $S_{M,i}$ the momentum source in the i -th direction. Note that for steady cases the first term in the momentum equation is identically zero.

3.2.2 Reynolds-averaged Navier-Stokes (RANS) equations

Two distinctly different flow regimes exist, laminar and turbulent flow. In the laminar flow state the velocity field varies smoothly and the streamlines do not mix, but move parallel to one another. In the turbulent flow state large velocity and pressure fluctuations occur in both space and time. Whether a flow is laminar or turbulent is a function of the ratio of inertial to viscous forces, i.e. for laminar flow the fluid viscosity is large enough to damp out perturbations introduced to the flow, while for turbulent flows the inertial forces are much larger than the viscous forces (Ray *et al.*, 2012). The non-dimensional Reynolds number represents this ratio of inertial to viscous forces,

$$\text{Re} = \frac{\rho u L}{\mu} \quad (3.3)$$

where L is a characteristic length scale of the flow, e.g. turbine diameter or a fraction thereof. Thus, for low Reynolds numbers the flow is characterised as laminar and for high Reynolds numbers turbulent.

The flows at typical sites for tidal turbine installations are highly turbulent, as discussed in Gerber *et al.* (2013) and thus the flow equations must be solved for a turbulent flow field. Direct numerical simulation (DNS) resolves all spatial and temporal fluctuations without need for modelling, however it is computationally extremely expensive and is limited to simple geometries. The most commonly used approach to model turbulent flows, is through solution of the Reynolds-averaged

Navier-Stokes (RANS) equations, for which the simulation time frames, and therefore computational expenses, are much reduced.

In order to transform the Navier-Stokes equations into the RANS equations, it is assumed that time varying (turbulent) velocity fluctuations can be separated from the mean velocity. This split of a variable into a mean (time-averaged) component (\bar{u}_i) and a fluctuating component (u'_i) is generally termed the ‘‘Reynolds decomposition’’. As an example the Reynolds decomposition of the u_i velocity component is:

$$u_i(\mathbf{x}, t) = \bar{u}_i(\mathbf{x}) + u'_i(\mathbf{x}, t) \quad (3.4)$$

Applying the Reynolds decomposition to the velocity and pressure followed by time averaging (indicated by an overbar) yields the Reynolds-averaged Navier-Stokes equations (RANS):

$$\text{Continuity :} \quad \frac{\partial \bar{u}_i}{\partial x_i} = 0 \quad (3.5)$$

$$\text{Momentum :} \quad \rho \left(\frac{\partial \bar{u}_i}{\partial t} + \frac{\partial (\bar{u}_i \bar{u}_j)}{\partial x_j} \right) = \rho \bar{f}_i + \frac{\partial}{\partial x_j} (-\bar{p} \delta_{ij} + 2\mu \bar{S}_{ij} - \overline{\rho u'_i u'_j}) \quad (3.6)$$

where \bar{f}_i is the time mean external force tensor and \bar{S}_{ij} is the mean rate of strain tensor:

$$\bar{S}_{ij} = \frac{1}{2} \left(\frac{\partial \bar{u}_i}{\partial x_j} + \frac{\partial \bar{u}_j}{\partial x_i} \right) \quad (3.7)$$

Note that the time derivative of a time-averaged quantity (see first term of equation (3.6)) is zero, but is retained in the RANS momentum equation. The basis for this is the assumption of a separation of time scales: that the averaging time is higher than the time scale of small turbulent fluctuations, but much smaller than the time scales of the bulk flow activities in the flow (e.g. vortex shedding or rotor rotation). On this basis, the RANS method may be applied to unsteady flow simulations, referred to as the unsteady Reynolds-averaged Navier-Stokes (URANS) method.

As can be seen in equation (3.6), the right hand side of the momentum equation now contains a term which is defined as the Reynolds stress tensor, $-\overline{\rho u'_i u'_j}$. As there are now more unknowns than equations a further equation is necessary to provide the Reynolds stress tensor. The absence of this additional equation is often referred to as the turbulence closure problem. An approximation allowing a solution for the Reynolds stresses and thus providing closure to the RANS equations is given by use of a turbulence model, to represent the velocity fluctuations or their effects on the flow. With the use of RANS with a turbulence closure model the resources required to numerically solve the Navier-Stokes equations are greatly reduced, to the extent that present day computers can tractably perform meaningful calculations.

3.2.3 Turbulence closure

As discussed in the previous section, a model is necessary to close the equations, expressing the Reynolds stress tensor using time-averaged quantities. In the following an introduction to turbulence modelling and some of the most commonly used models is given.

Turbulence models of various complexity have been developed and can generally be classified in two groups: eddy viscosity models and Reynolds stress models. Reynolds stress models model the stresses directly through a set of transport equations, one for each stress, thus requiring the solution of six additional transport equations. The key advantage of the Reynolds stress models is that they do not require isotropy in the stresses, as all stresses are computed directly. However, the additional complexity renders these models expensive to solve, and they are therefore not widely used. In comparison, eddy viscosity models only require one or two additional transport equations. Various eddy viscosity models are implemented in commercial flow solvers

such as ANSYS FLUENT and are usually the first choice for modelling turbulence in an engineering application.

The underlying assumption employed in all eddy viscosity models is the Boussinesq hypothesis (Boussinesq, 1878), which provides the results of the Reynolds stress tensor using the gradient of the time-mean velocity field (Schmitt, 2007):

$$-\overline{\rho u'_i u'_j} = -\frac{2}{3}\rho k \delta_{ij} + \mu_t \left(\frac{\partial u_i}{\partial x_j} + \frac{\partial u_j}{\partial x_i} \right) \quad (3.8)$$

where μ_t is the eddy viscosity (also referred to as turbulent viscosity) and k the turbulent kinetic energy. It should be noted that the Boussinesq hypothesis assumes the eddy viscosity to be isotropic.

Three categories of turbulence models, based on the Boussinesq hypothesis, are in use to date:

- **Algebraic (zero-equation) models:**

For this type of model an algebraic relation is used to close the problem, and no additional equations describing the transport of turbulent quantities, stresses and fluxes are introduced. Not modelling the transport of turbulence, the zero-equation models cannot accurately predict any flows which have non-local mechanisms such as the history effect, i.e. the influence of flow processes downstream of the event. Numerical simulations employing this type of model are thus usually restricted to attached boundary-layer flows, which can be modelled using only local relations (Bredberg, 2001). The two most widely used zero-equation models are the Cebeci-Smith and Baldwin-Lomax models, which are discussed in detail by Wilcox (1993). As separated flows are expected in the simulations of ducted tidal turbines analysed in this study, zero-equation models were not considered.

- **One-equation models:**

In one-equation models an equation is derived for one turbulent quantity, i.e. the turbulent kinetic energy or the eddy viscosity. The turbulent length scale, however, is simply related to a typical flow dimension and not modelled, and the model therefore cannot accommodate changes in length scale or dissipation rate occurring in the flow. Due to the requirement of supplying the length scale, one-equation models do not convey a significant advantage over zero-equation models, therefore few of this type of model exist. A one-equation model available within ANSYS FLUENT is the Spalart-Allmaras model (Spalart and Allmaras, 1992). The model solves a transport equation for the working variable $\tilde{\nu}$, which is related to the turbulent kinematic viscosity, ν_t . The Spalart-Allmaras model has been analysed for the application of modelling cross-flow tidal turbines in Consul (2011).

- **Two-equation models:**

Two-equation models make up the category of the most widely developed turbulence models. In addition to modelling the turbulent kinetic energy, these models also allow modelling of the turbulent length scale. They are therefore considered complete models, which can predict turbulent flow properties without prior knowledge of the turbulence structure (compared to one-equation models which are considered incomplete), see Wilcox (1993).

Commonly, the first variable, determining the level of energy in the turbulence, is the turbulent kinetic energy, k . The second variable, determining the scale of the turbulence, varies according to the turbulence model used. Two of the most popular models employ, in one case, the dissipation rate of the turbulent kinetic energy ϵ , and in the other, the specific dissipation rate of turbulent

kinetic energy ω . Named after the variables they model, these turbulence closure models are specified as the $k - \epsilon$ and $k - \omega$ models respectively.

Detailed discussions on turbulence modelling in CFD can be found in Pope (2000) and Wilcox (1993) and an overview of the available turbulence models in ANSYS FLUENT is given in ANSYS Inc. (2009a). In the following the turbulence model chosen for this study is presented in more detail.

The turbulence model chosen for this study is the $k - \omega$ shear-stress transport (SST) model, an adaptation of the $k - \omega$ model introduced by Wilcox (1993). It was chosen for its ability to model boundary layer separation in adverse pressure gradients, as are known to occur for ducted tidal turbine devices (Gaden and Bibeau, 2010; Fleming *et al.*, 2011). The $k - \omega$ SST model was developed by Menter (1993) to blend the formulation of the $k - \omega$ model in the near-wall region with the $k - \epsilon$ model in the far field. This model is widely used (Menter *et al.*, 2003) and has been the model of choice for several ducted tidal turbine studies (Shives and Crawford, 2011; Fleming *et al.*, 2011) and full rotor studies (McIntosh *et al.*, 2011; McNaughton *et al.*, 2013).

The $k - \omega$ SST model is described through a set of transport equations that include terms for the generation, effective diffusivity, and dissipation of k and ω , as well as a cross-diffusion term to blend the $k - \omega$ and $k - \epsilon$ models together. The transport equations for the $k - \omega$ SST model are given as

$$\frac{\partial}{\partial t}(\rho k) + \frac{\partial}{\partial x_i}(\rho k u_i) = \frac{\partial}{\partial x_j} \left(\Gamma_k \frac{\partial k}{\partial x_j} \right) + \tilde{G}_k - Y_k + S_k \quad (3.9)$$

and

$$\frac{\partial}{\partial t}(\rho \omega) + \frac{\partial}{\partial x_i}(\rho \omega u_i) = \frac{\partial}{\partial x_j} \left(\Gamma_\omega \frac{\partial \omega}{\partial x_j} \right) + G_\omega - Y_\omega + D_\omega + S_\omega \quad (3.10)$$

where \tilde{G}_k and G_ω respectively represent generation of k and ω , Γ_k and Γ_ω the effective diffusivity, Y_k and Y_ω the dissipation, and S_k and S_ω are user-defined source terms.

D_ω is the cross-diffusion term. The introduced terms of generation, diffusivity and dissipation are closed by a system of equations that rely on multiple empirically evaluated coefficients.

Using the solution of the transport equations, the turbulent viscosity, μ_t , can be obtained through

$$\mu_t = \frac{\rho k}{\omega} \frac{1}{\max[\frac{1}{\alpha^*}, \frac{SF_2}{a_1\omega}]} \quad (3.11)$$

where S is the strain rate magnitude, F_2 a blending function, α^* a damping coefficient, and a_1 a model constant.

The application of this particular turbulence model to ducted tidal flows has been thoroughly discussed by Shives and Crawford (2011). It was concluded, that for complex flows the $k - \omega$ SST turbulence model outperforms other commonly used models, such as the $k - \epsilon$, $k - \omega$, and the Spalart-Allmaras model. Further, Aplsey and Leschzinger (1999) investigated the ability of various two-equation turbulence models to predict separated flow in a diffuser by comparing them to experimental data. The results show that the $k - \omega$ SST outperforms all other two-equation models with regards to modelling reversed flow in the velocity profile of the diffuser.

Some of the designs presented in this study feature large scale exterior separation, and in some cases reattachment downstream. As the flow field on the turbine exterior crucially influences the flow through the turbine and hence the performance, it is essential to capture this flow separation and reattachment. Labroquère *et al.* (2013) investigated the performance of various turbulence models when applied to a backward facing step and report that the $k - \omega$ SST best models the point of reattachment. This result therefore further supports the choice of this turbulence model for use in the present study.

3.2.4 ANSYS FLUENT solver

The solver employed for this study, is the commercial software ANSYS FLUENT 12.0 (ANSYS Inc., 2009a) solving the RANS equations using the finite volume method. In this study, it is employed as a three-dimensional, pressure-based, segregated, implicit, incompressible flow solver.

In the pressure-based solver, the constraint of mass conservation of the velocity field is achieved by solving a pressure correction equation. The pressure equation is derived by manipulating the continuity and momentum equations such that the velocity field, corrected by the pressure, satisfies mass conservation.

The pressure-based segregated algorithm solves the individual governing equations sequentially. While being solved, each governing equation is decoupled from other equations. As the governing equations are nonlinear and coupled to one another, the solution loop is carried out iteratively in order to obtain a converged numerical solution.

3.2.4.1 Spatial discretisation

In order for the RANS equations to be solved, the continuous flow problem needs to be discretised spatially on a computational grid or mesh. For this study, the meshes employed within ANSYS FLUENT have been generated using the commercial software ANSYS ICEM CFD (ANSYS Inc., 2009c), while the imported device geometries have been generated in Autodesk AutoCAD (Autodesk, 2012). Once a computational mesh exists, the governing equations need to be approximated for the discrete domain, for which ANSYS FLUENT employs a cell-centred finite volume method. This method is described in detail in the textbooks by Versteeg and Malalasekera (1995) and

Feistauer *et al.* (2004) with a concise summary given by Ray *et al.* (2012). A short introduction to the finite volume method follows below.

Using the finite volume method, the solution domain is subdivided into a finite number of small control volumes in which the variables are evaluated at the centroid of the control volume. The integral form of the conservation equations are then applied to the control volume defined by a cell to obtain the discrete equations for that cell.

The discretisation of the governing equations may be illustrated by considering the unsteady conservation equation for transport of a scalar quantity ϕ , written in integral form for an arbitrary control volume V :

$$\int_V \frac{\partial \rho \phi}{\partial t} dV + \oint \rho \phi \vec{u} \cdot d\vec{A} = \oint \Gamma_\phi \nabla \phi \cdot d\vec{A} + \int_V S_\phi dV \quad (3.12)$$

where \vec{u} is the velocity vector, \vec{A} the surface area vector around the control volume V , Γ_ϕ the diffusion coefficient for ϕ , and S_ϕ the source of ϕ per unit volume. Applying equation (3.12) to each control volume yields the discretised form:

$$\frac{\partial \rho \phi}{\partial t} V + \sum_f^{N_{\text{faces}}} \rho_f \phi_f \vec{u}_f \cdot \vec{A}_f = \sum_f^{N_{\text{faces}}} \Gamma_\phi \nabla \phi_f \cdot \vec{A}_f + S_\phi V \quad (3.13)$$

where V is the cell volume, N_{faces} the number of faces enclosing the cell, ϕ_f the value of ϕ convected through face f , and $\rho_f \vec{u}_f \cdot \vec{A}_f$ the mass flux through a face. $\vec{A}_f = |A_f| \vec{n}_f$ where $|A_f|$ is the value of the area and \vec{n}_f the outward unit normal vector of face f . The discretised equations solved by ANSYS FLUENT follow the general form presented in equation (3.13).

Discrete values of the scalar ϕ are stored at the cell centres, however, face values, ϕ_f are required in equation (3.13) and therefore must be interpolated from the cell centre values. For this interpolation ANSYS FLUENT employs an upwind scheme, which means that the face value is derived from quantities in the cell upstream, relative

to the direction of the normal velocity. Several upwind schemes are available within the software package and are detailed in ANSYS Inc. (2009a). For example, first-order accuracy is achieved when the face value of ϕ_f is set equal to the cell centre value in the upstream cell, referred to as the first-order upwind scheme. In the second-order upwind scheme, second-order accuracy is achieved at cell faces through a Taylor series expansion of the cell-centred solution about the cell centroid. In this study the second-order upwind scheme has been employed.

3.2.4.2 Temporal discretisation

The flow field may be solved in either steady or unsteady form. A steady solution may be achieved if the flow problem does not exhibit time-varying flow features, while for unsteady flow, the evolution of the flow field must be solved employing time-marching. Both methods have been applied in this study.

When conducting unsteady simulations, the governing equations are discretised both in space and time. The temporal discretisation involves the integration of each term in the differential equations over a given time-step Δt .

The time evolution of a variable ϕ is given by

$$\frac{\partial \phi}{\partial t} = F(\phi) \quad (3.14)$$

where the function F incorporates any spatial discretisation. Using backward differences, the first and second-order accurate temporal discretisation are given as

$$\frac{\phi^{n+1} - \phi^n}{\Delta t} = F(\phi^{n+1}) \quad (3.15)$$

and

$$\frac{3\phi^{n+1} - 4\phi^n + \phi^{n-1}}{2\Delta t} = F(\phi^{n+1}) \quad (3.16)$$

where n is the value at the current time level (t), $n + 1$ the value at the next time level ($t + \Delta t$), and $n - 1$ the value at the previous time level ($t - \Delta t$). Depending on which level of accuracy is chosen, equation (3.15) or (3.16) is solved iteratively at each time level for ϕ^{n+1} (implicit time integration).

The time-step, Δt , applied for the time-marching is the determining parameter of stability and convergence of the solution. The Courant-Friedrichs-Levy (CFL) condition states the following stability condition

$$C = \Delta t \sum_{i=1}^n \frac{u_{x_i}}{\Delta x_i} \leq 1 \quad (3.17)$$

where C is the Courant number, Δx_i the length interval (e.g. of the cell), and u_{x_i} the velocity in x_i -direction. While the CFL condition is a requirement for explicit schemes, this is not the case for implicit schemes. However, it provides a suitable first estimate for the time-step. Equation (3.17) states that $\Delta t \leq \Delta x_i / u_{x_i}$. As the local flow velocities in the flow field are not known a priori, a range of time-steps need to be employed in order to find the appropriate value in terms of convergence and computational efficiency.

3.2.4.3 Convergence

In terms of convergence of the solution, both computational convergence as well as grid convergence should be achieved. Computational convergence was evaluated using the scaled residual, R^ϕ , quantifying the error of the approximated solution scaled using a scaling factor representative of the flow rate of ϕ through the domain. Further, where applicable, the force coefficients on wall surfaces were analysed in order to confirm convergence of integral quantities.

In order to achieve grid convergence, several mesh configurations were tested and evaluated. Grid convergence was deemed to be met, if the power coefficient did not change by more than 1% when further increasing mesh density by a factor of 2.

The simulations presented in this study have been performed on a 16-node computer cluster of 8 cores per node. For the simulations presented in this study, 2 to 8 cores have been employed, depending on mesh size. As an example, the steady computations of the ducted turbine presented in section 5.6.3 were conducted using 4 cores and typically converged within 8 hours, therefore leading to a total computation time of 32 core hours per simulation.

Chapter 4

Actuator disc simulations

This chapter presents a numerical actuator disc analysis of three tidal turbine devices: the bare, ducted, and open-centre turbines. Section 4.1 introduces the modelling approach employed here, linear momentum actuator disc theory. Relevant studies employing this method in wind and tidal energy are presented. In section 4.2 methods for modelling the free-surface of an open-channel are introduced and the approach chosen for this study is discussed.

The model setup of the actuator disc within the solver is presented in section 4.3. A validation of the model is performed using the bare turbine, introducing the analysis methods employed throughout the study (section 4.4).

The ducted and open-centre turbines are introduced in section 4.5 and section 4.6 respectively, and are simulated with axial inflow. The model modifications for yawed inflow are presented in section 4.7 and all three devices are simulated and analysed at various yaw angles. The chapter concludes with section 4.8, which contains a summary of the results.

4.1 Actuator disc modelling

This section presents the background theory and literature of the actuator disc turbine representation. A one-dimensional (1D) representation of the turbine – the linear momentum actuator disc theory (LMADT) – is introduced. Published work on turbine actuator disc models, both experimental, as well as embedded in Eulerian CFD models are presented.

4.1.1 Linear momentum actuator disc theory and the Betz limit

Linear momentum actuator disc theory (LMADT, often referred to as momentum theory or actuator disc theory) is the fundamental theory used in the analysis of rotors and propellers. It was introduced by Froude (1889) for propellers, further developed by Betz (1920), and has since been expanded and implemented in analyses of wind and tidal turbines (Burton *et al.* (2011)).

LMADT is based on Bernoulli's assumptions and therefore assumes steady, inviscid, incompressible and irrotational flow. The turbine is represented by a disc, whilst the fluid passing through the disc is described by a streamtube, in which non-axial flow is ignored. In this model the flow inside the streamtube does not mix with the surrounding fluid, which means that the mass flow rate of the fluid flowing along the streamtube is conserved for all positions upstream and downstream of the rotor disc. Far upstream and far downstream the pressure is assumed equal to the free-stream static pressure.

The rotor disc extracts kinetic energy from the fluid flow, thus the velocity of the fluid within the streamtube must decrease. As the fluid is assumed incompressible, the streamtube must expand to accommodate the slower moving fluid. The presence

of the turbine causes the approaching flow to slow down, such that when the flow arrives at the disc its velocity is already lower than the free-stream. As a result the upstream streamtube expands and its static pressure rises. When passing through the rotor disc, the static pressure of the flow drops, such that on leaving the disc the fluid is below the free-stream static pressure. This pressure difference is equalised far downstream resulting in a further reduction of kinetic energy in the flow and therefore further widening of the streamtube. It is important to stress that this is a purely 1D analysis with a uniform thrust loading and velocity across the disc. Figure 4.1 illustrates the expansion of the streamtube as it passes the actuator disc and names the relevant axial stations.

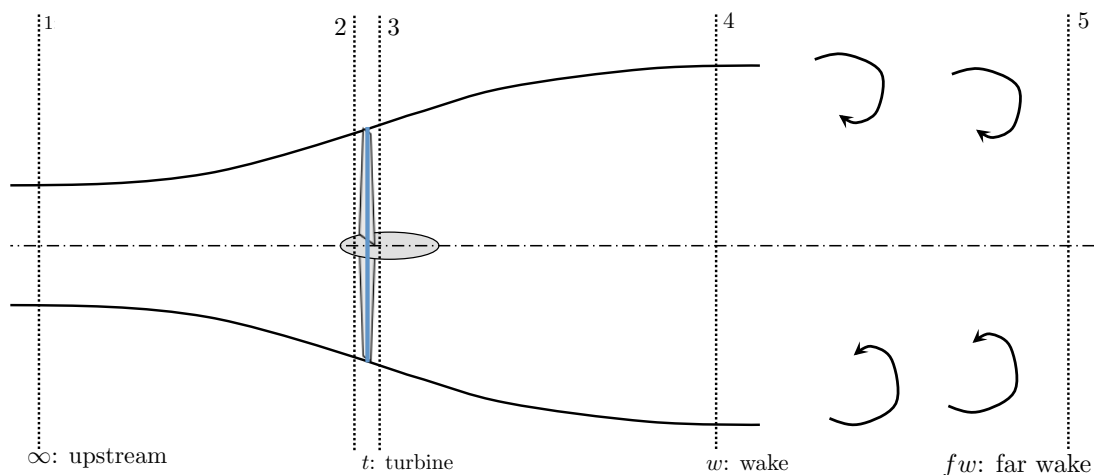


Figure 4.1: Turbine rotor represented by an actuator disc (marked in blue) and bounding streamtube. Relevant axial stations marked by numbers.

The axial stations are given as:

- station 1, the region far upstream where the flow is unaffected by the disc presence and flow parameters are at free-stream (∞) conditions: U_∞ , p_∞ , A_∞ ,
- station 2, the region just before the disc where the value of velocity is that through the turbine (t) plane and the area of the streamtube is equal to the turbine disc area: U_t , A_t , p_2 ,

- station 3, the region just behind the disc, where the values of velocity and area are equal to those of station 2: U_t, A_t, p_3 ,
- station 4, the region in the near wake (w) where free-stream pressure has been recovered, but the velocities in the turbine and bypass differ, p_∞, U_w, A_w ,
- station 5, the region in the far wake (fw) where after mixing the velocity is once again uniform p_∞, U_{fw}, A_{fw} .

In order to obtain a full description of velocity and pressure along the streamtube, three equations can be applied to the problem: continuity equation and a momentum-force balance applied across the length of the streamtube, as well as Bernoulli's equation, applied both upstream and downstream of the turbine disc.

As shown by Betz (1920), the continuity equation can be applied along the length of the streamtube, stating that the mass flow rate must remain constant,

$$\dot{m}_{\text{streamtube}} = \rho A_\infty U_\infty = \rho A_t U_t = \rho A_w U_w. \quad (4.1)$$

The subscripts follow the nomenclature of axial stations introduced above. A and U are respectively the cross-sectional area of the streamtube and the flow velocity, while ρ is the density of the fluid. An axial flow induction factor, a , is used to quantify the reduction in the axial flow velocity at the turbine disc,

$$U_t = U_\infty (1 - a). \quad (4.2)$$

A momentum-force balance on the control volume encompassed by the streamtube can be written as

$$\begin{aligned} -T &= \dot{m} (U_w - U_\infty) \\ (p_2 - p_3) A_t &= \rho A_t U_\infty (1 - a) (U_\infty - U_w) \end{aligned} \quad (4.3)$$

where the axial thrust of the turbine disc on the flow, T , is equal to the product of the pressure drop created by the presence of the disc and the turbine disc area, A_t .

Bernoulli's equation is applied in the upstream

$$p_\infty + \frac{1}{2} \rho U_\infty^2 = p_2 + \frac{1}{2} \rho U_t^2 \quad (4.4)$$

and downstream section of the streamtube

$$p_\infty + \frac{1}{2} \rho U_w^2 = p_3 + \frac{1}{2} \rho U_t^2. \quad (4.5)$$

Equation (4.5) may be subtracted from equation (4.4), yielding

$$\frac{1}{2} \rho (U_\infty^2 - U_w^2) = p_2 - p_3. \quad (4.6)$$

Combining equations (4.3) and (4.6) yields the result for the velocity in the wake,

$$U_w = U_\infty (1 - 2a). \quad (4.7)$$

From equations (4.2) and (4.7) it can be seen, that half of the overall reduction in axial velocity in the streamtube takes place upstream and the other half downstream of the turbine disc.

Two important non-dimensional parameters in the field of turbine hydrodynamics are the power coefficient C_P and the thrust coefficient C_T , which quantify the power extracted from the fluid and the streamwise force on the turbine disc, respectively.

Using the equations derived above the coefficients C_P and C_T are defined as

$$\begin{aligned}
 C_P &= \frac{\text{power extracted from fluid}}{\text{power available for extraction}} \\
 &= \frac{T U_t}{1/2 \rho A_t U_\infty^3} \\
 &= 4a(1-a)^2
 \end{aligned} \tag{4.8}$$

$$\begin{aligned}
 C_T &= \frac{\text{force acting on turbine}}{\text{kinetic pressure force upstream}} \\
 &= \frac{T}{1/2 \rho A_t U_\infty^2} \\
 &= 4a(1-a)
 \end{aligned} \tag{4.9}$$

Betz (1920), showed that by differentiating equation (4.8) the maximum attainable value of C_P can be determined: the so-called Betz limit, which occurs at $a = 1/3$ and yields a value of $C_{P,\max} = 16/27 = 0.59$ for $C_T = 8/9$. The relationships between C_P , C_T and a are illustrated in figure 4.2.

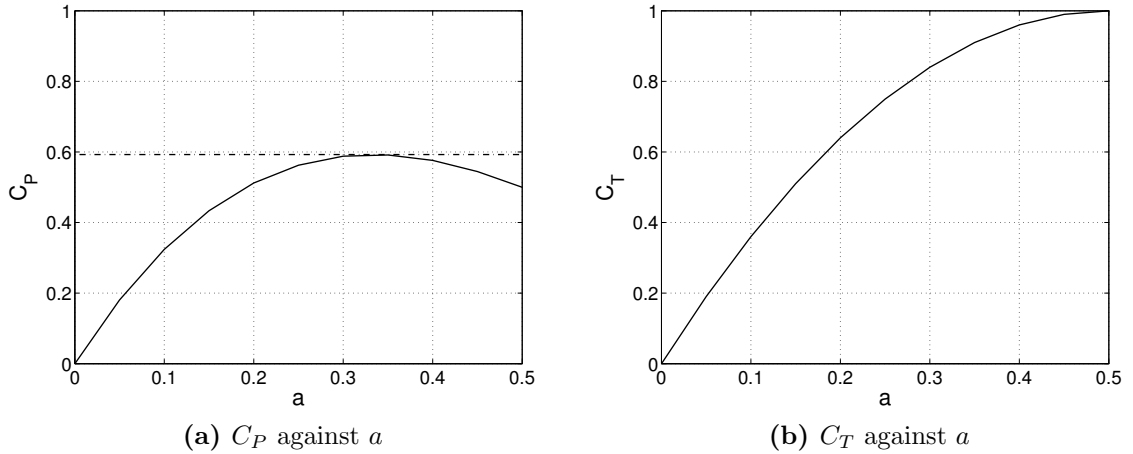


Figure 4.2: Relationship between C_T , C_P and the induction factor a for LMADT. Betz limit indicated by dashed line.

It is possible to further define a local thrust coefficient,

$$C_{T,\text{loc}} = \frac{T}{1/2 \rho A_t U_t^2} \tag{4.10}$$

which normalises the thrust by the velocity at the disc (rather than the free-stream velocity) and is used in numerical models in order to specify the disc thrust level.

4.1.2 Actuator disc representation of tidal turbines in numerical and physical experiments

In all the simulations presented in this chapter, the turbine is represented as an actuator disc, implemented using a numerical porous disc, a method widely used to model the principal effects of turbines in a simplified manner. Real rotors produce a complex flow consisting of discrete blade effects, swirled flow and decelerated flow through the rotor plane. Despite the complexities of these flows, they can be reasonably well represented through neglecting discrete blade effects, hence the success of blade element momentum theory in the wind industry (see chapter 5), and further through neglecting angular momentum effects, hence the success and accuracy of LMADT.

The principal influence of a rotor on the flow is to reduce its linear momentum. These characteristics are also displayed by both numerical and physical porous discs. The ability of actuator discs to mimic the linear momentum extraction of physical rotors has led to its wide use in modelling wind turbines (Mikkelsen, 2003), and its adoption in tidal energy research by many experimentalists (Whelan *et al.*, 2009; Harrison *et al.*, 2009) and numerical investigators (Gant and Stallard, 2008; Harrison *et al.*, 2009; Gaden and Bibeau, 2010; Fleming *et al.*, 2011; Nishino and Willden, 2012) in place of rotors with discrete blades. Further, actuator discs present a more general case than a physical rotor, as the actuator disc does not assume a specific rotor design. In comparison, the performance of the physical rotor is largely a function of choice of aerofoil, twist and taper etc. The actuator disc yields an upper limit on energy

extraction by an ideal rotor, for which the maximum achievable power is given by the product of thrust on the disc and flow velocity through the disc.

The objective of the present analysis is to fairly compare the performance of bare, ducted, and open-centre devices. Incorporating real turbine geometries, which would necessarily have to be different for ducted and bare operation, would confuse rotor and duct effects, preventing a proper analysis of the impact of the duct and aperture. Thus, the actuator disc approach is chosen deliberately for the first part of this investigation, so as to study the impact of ducts and apertures, and not the specific performance of a rotor within a duct. Rotor effects are studied in chapter 5 where real aerofoil and rotor data is employed in a RANS-BEM approach.

In both cases, CFD and experiment, the porous or actuator disc applies a similar thrust force on the moving fluid as a set of rotating blades and thus can model the energy extraction of a turbine. However, no swirl is introduced to the flow and the vortices generated by the bladed turbine are not captured. Actuator discs, represented by porous discs, have been in use for a long time to model wind turbines, in particular for studies concerning the wake of one or multiple turbines. In general the actuator disc approach is employed in studies where the interest lies in the overall momentum extraction by the turbine and not in the flow around blades or the rotation of the flow.

While in experiments a porous disc represents the actuator disc, in CFD analysis a momentum source model is implemented. Instead of modelling the turbine blades, the rotor is treated as a black box, where energy is removed from the flow by introducing a momentum source term to the governing momentum equations in the region enclosing the turbine.

Within ANSYS FLUENT the momentum source term can either be applied to a region of cells (porous zone), or in a further simplification, can be reduced to a porous jump

boundary, where the turbine rotor representation has no thickness (ANSYS Inc., 2009b). Both methods have been implemented in recent publications to model the flow through and around tidal turbines. While the porous zone has been implemented in studies by Sun (2008), Harrison *et al.* (2009), and Gaden and Bibeau (2010), the approach taken within this study is the simplification of the actuator disc to a plane (porous jump) which is also applied by Gant and Stallard (2008) and Fleming *et al.* (2011).

Sun (2008) presents results of both a computational study and two sets of experiments, using the actuator disc approach. In the numerical simulation the free surface is modelled using the volume of fluid (VOF) method (see section 4.2), thus allowing for surface deformation due to the presence of the disc. Two experimental tests were performed in moving water using a natural open channel and in still water using a towing tank. The numerical results compare favourably to the wake velocity profiles measured in the experiments, thus suggesting that the actuator disc numerical model can provide qualitative insight into the mechanism of wake development behind tidal current turbines. The comparison between the two experimental environments also support the validity of using a towing tank for the understanding of the physical processes governing the performance of rotors and turbine wake behaviour (providing blockage effects are not extreme).

Harrison *et al.* (2009) performed a series of experiments using porous discs of varying thrust coefficients in a circulating water channel, the results of which were then compared to actuator disc numerical simulations. The wake velocity results of the CFD model and the experimental results agree reasonably well, as was also found by Sun *et al.* (2008). The main factors affecting the wake structure were found to be the C_T value, the ambient turbulence levels, and to a lesser extent, the disc

induced turbulence. As to be expected the main differences between the models and experiments were in terms of the turbulence levels throughout the model.

Myers and Bahaj (2009) and Bahaj, Myers, Thomson and Jorge (2007) present further experimental work using porous disc models in a tilting flume. Both studies concentrate on the characterisation of the wake of a tidal turbine and the development of a model to describe this wake.

4.2 Modelling free surface effects for tidal turbines

The main difference when modelling tidal turbines in comparison to wind turbines is the proximity of the free surface. Whilst wind turbines are influenced by the Earth's atmospheric boundary layer, the flow may be regarded as unconfined. For tidal turbines not only the ocean floor boundary layer effects are to be taken into account, but also the free surface which confines the water flow at the top and is thought to create a substantial blockage effect on flows through tidal turbines.

Section 4.2.1 introduces the physics of open channel flow and numerical modelling techniques for a free surface. In section 4.2.2 theoretical models for dealing with the free surface and the effect on a turbine are presented, while numerical modelling techniques are presented in section 4.2.3.

4.2.1 Open channel flow

In order to understand the flow field of a turbine in proximity of a free surface one must first examine the physics of open channel flow without the turbine. Assuming steady flow, constant density and temperature, the mechanical energy divided by weight contained in the flow at any particular point is

$$\frac{p}{\rho g} + \frac{u^2}{2g} + z \quad (4.11)$$

where z is the height of the streamline above an arbitrary datum. For small slopes and low flow curvature the pressure at any point in the stream is governed only by its depth below the free surface (Massey, 1968). Thus the energy equation can be simplified to

$$H = h + \frac{u^2}{2g} \quad (4.12)$$

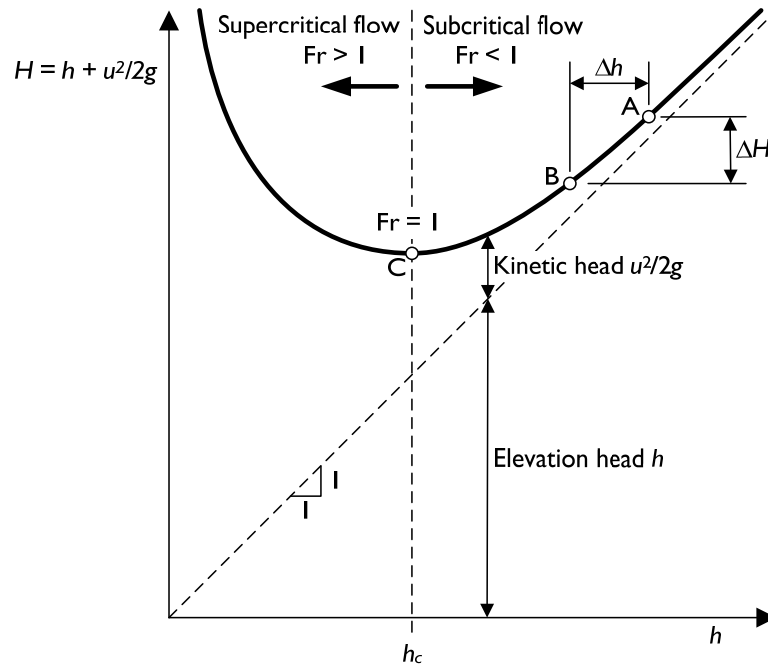


Figure 4.3: Variation of total head, H , with depth of flow, h , reproduced from Houlsby, Oldfield and Draper (2008).

where h is the static head and is the depth of the flow, and H is called the total head. Any change in energy such as the energy extraction through a turbine corresponds to a change in H . Plotting H against h (see figure 4.3) shows that shallow flows contain a high kinetic energy, while in deep flows the static head dominates (Houlsby, Oldfield and Draper, 2008). By differentiating H by h the critical depth h_c can be found, at which the specific energy is lowest for a given volumetric flow rate. A dimensionless number describing this relationship is the Froude number:

$$\text{Fr} = \frac{u}{\sqrt{gh}} \quad (4.13)$$

The minimum energy flow (critical flow) occurs at $\text{Fr} = 1$. Flows at $\text{Fr} < 1$ are termed subcritical or tranquil, at $\text{Fr} > 1$ supercritical, or rapid. Tidal flows relevant for energy extraction are generally subcritical with Froude number values of around $\text{Fr} = 0.2$. Returning to figure 4.3, an example of energy extraction through a tidal

turbine is illustrated through the change in H and h moving from point A to B. Energy extraction from subcritical tidal flows corresponds to a decrease in surface elevation, i.e. removal of static head and increase in dynamic head, and therefore flow velocity.

4.2.2 Theoretical modelling of the free surface

As introduced in equation (2.1), the blockage of a channel is typically defined as the ratio of blocked area to channel cross-sectional area. Garrett and Cummins (2007) have extended LMADT for turbines in a tidal channel for any given blockage ratio, but effectively neglecting free surface effects. In comparison to standard LMADT, the bypass flow, its interaction with the turbine flow, and wake mixing are taken into account, thus accounting for the geometric finiteness of the flow field. Garret and Cummins assume no height change in the channel, thus representing a turbine in a parallel-sided tube, which is the simulation approach employed within the present study.

A further expansion of this model, to include the height change of the free surface, is presented by Houlsby, Draper and Oldfield (2008). For the case of the parallel-sided tube Houlsby *et al.* introduce a formulation that defines the relationship between C_P and C_T based on the blockage ratio with the case of unconfined flow, $B = 0$, being equal to standard LMADT. Figure 4.4 is an extension of figure 4.2 and shows the results of the aforementioned formulation for three blockage ratios ($B = 0$, $B = 0.035$ and $B = 0.2$) as they are employed in this study.

Whelan *et al.* (2009) studied free surface proximity effects using 1D actuator disc theory and derived a theoretical description (see figure 4.5). Note that the model does not include the downstream mixing of the wake. The theoretical model has been validated for highly blocked and unblocked cases by comparison to open channel

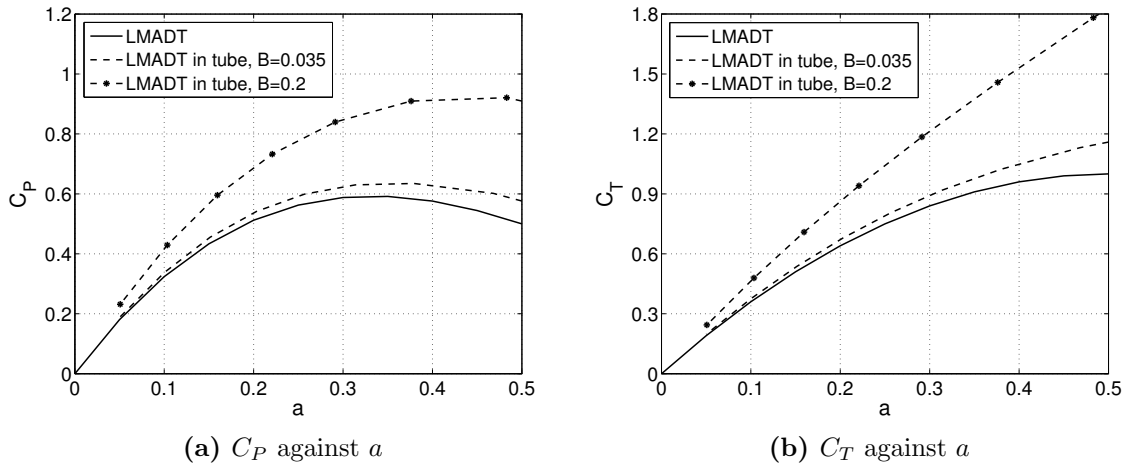


Figure 4.4: Relationship between C_T , C_P and the induction factor a for LMADT (unconfined flow, $B = 0$) and LMADT in a parallel-sided tube (confined flow) at two different blockage ratios ($B = 0.035$ and $B = 0.2$).

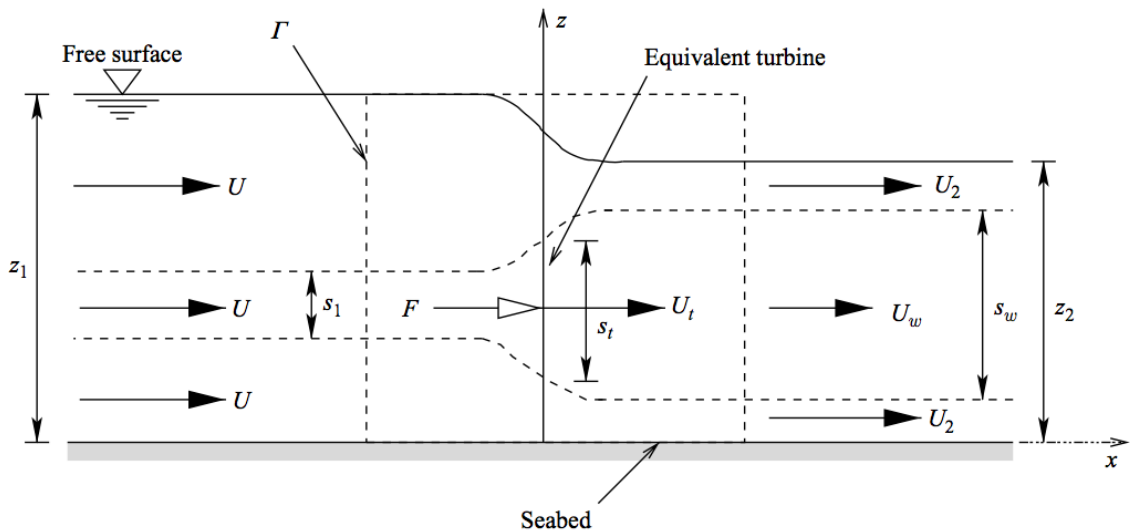


Figure 4.5: Free surface deformation for a highly blocked turbine. Reproduced from Whelan *et al.* (2009).

flow experiments with a porous disc as well as experiments with a model horizontal axis turbine. The proposed theoretical model of the effects of free surface proximity provides a blockage correction for axial induction that can be incorporated in blade element momentum codes. Validation with experimental results shows good agreement for C_P and C_T at low tip-speed ratios, while for high tip-speed ratios a further correction is needed to achieve better agreement.

The aforementioned studies indicate that even a small increases in blockage can have a visible influence on the power capture of a tidal turbine (power increase of 7.6 % for $B = 3.5\%$ compared to $B = 0\%$, see figure 4.4). Thus, it becomes obvious that results from studies performed in highly blocked conditions – in particular experimental – should be treated with care. Studying the effect of blockage forms a significant element within this research project and the importance of maintaining a constant blockage ratio when comparing different devices is stressed.

4.2.3 Numerical modelling of the free surface

As detailed above, the free surface has a substantial effect on the flow of an open channel, thus it is of interest to model this surface in numerical turbine models. As the free surface may vary both spatially and temporally this is not a trivial task. There are several methods of modelling or approximating the free surface.

The simplest method, applicable only to flows with insignificant variations in the free surface (low blockage), is to approximate the free surface using the rigid-lid approach. In this method the free surface is treated as an imaginary frictionless horizontal plane on which the velocity perpendicular to the plane is zero and the velocity tangential to the plane is non-zero (Sun, 2008). However, for problems where the free surface deforms substantially, a more detailed description of the free surface is needed.

A range of numerical methods that capture a deformable free surface are discussed by Hyman (1984). Two general strategies exist. In moving grid methods the Lagrangian computational grid is permitted to move with the free surface. The other strategy is to keep the Eulerian grid fixed and use a separate procedure to describe the position of the interface within the grid, either through surface-tracking or surface-capturing. In general, fixed grid methods are less computationally expensive than moving grid methods.

The most popular fixed grid surface-tracking method is the volume of fluid (VOF) approach. Within this model the surface is defined by calculating the volume fraction of each of the two phases, air and water, within each cell; with values for this fraction ranging from zero (i.e. air phase) to one (i.e. water phase). The interfaces of the free surface occur in the cells with fractional volumes (Hyman, 1984). A detailed description of the implementation of the VOF method in ANSYS FLUENT is given in ANSYS Inc. (2009a).

The VOF method has been employed in tidal turbine studies by Fleming *et al.* (2012) and Consul *et al.* (2013). Consul *et al.* analyse a transversal horizontal tidal turbine in 2D at blockages of up to $B = 0.5$. The power and thrust achieved at this very high blockage were shown to differ by a few percent only between modelling a deformable surface and using the rigid-lid method. Fleming *et al.* modelled an experimental tidal turbine setup in 3D featuring a blockage of $B = 0.24$. The overall reduction in free surface elevation using VOF was found to be less than 0.5%, resulting in only very slight variations of turbine power and thrust.

For this study the rigid-lid modelling approach was selected. The devices investigated are modelled at two blockage ratios, $B = 0.035$ and $B = 0.2$. Previous studies employing the VOF method have shown that both the free surface deformation for blockage ratios $B \leq 0.2$, as well as the effect on the turbine performance is very small (Fleming *et al.*, 2012; Consul *et al.*, 2013). Therefore the rigid-lid modelling approach was deemed sufficiently accurate while being computationally efficient.

4.3 Model setup

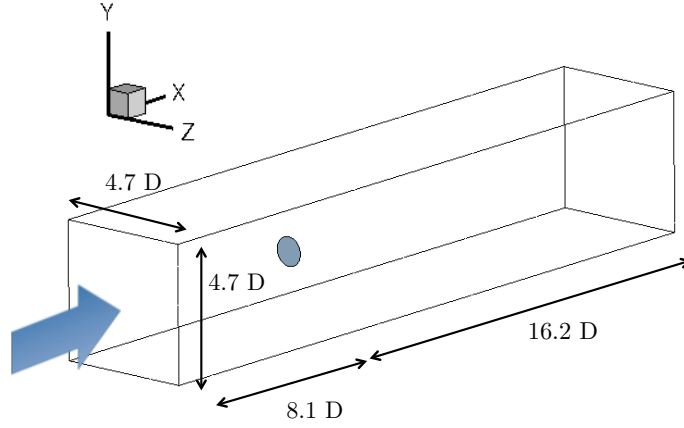
The following section presents the general model setup used for all of the actuator disc simulations. It describes the actuator disc model implementation within the CFD solver and presents a grid resolution study as well as a turbulence parameter sensitivity analysis.

4.3.1 Actuator disc implementation and model setup

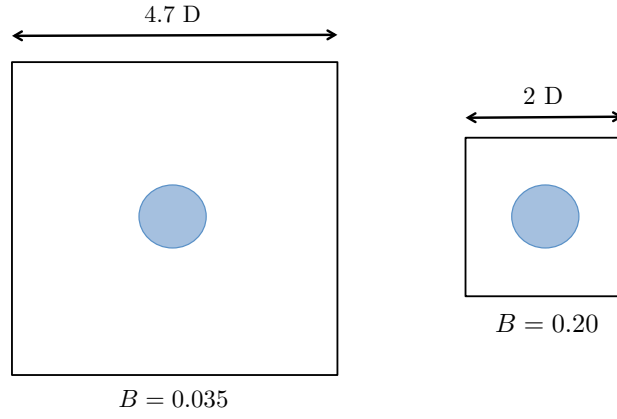
In order to evaluate the numerical model a bare disc is considered in nearly unconstrained flow (noting that fully unconstrained flow cannot be achieved numerically). The domain extends 8.1 diameters, D , (130 m) upstream of the 16 m diameter disc, 260 m (16.2 D) downstream and 75 m (4.7 D) in the cross-stream direction, resulting in a blockage ratio of $B = 0.035$. Figure 4.6a illustrates the simulation domain.

As a simple approximation to realistic flow conditions, a second simulation domain with a reduced cross-section is employed. This domain has the same upstream and downstream dimensions as the low blockage case, and a reduced cross-stream dimension of 32 m (2 D), in both width and height, yielding a blockage ratio of $B = 0.2$, see figure 4.6b. This simulation domain is considered representative of what might be a typical turbine installation as part of a turbine array. As the aim is to study turbines in axial flow as well as yawed flow, the full domain is modelled, while for purely axial flow, a quarter of the domain and disc would be sufficient.

The following boundary conditions were employed: uniform inlet velocity ($U_\infty = 2$ m/s), uniform outlet pressure ($p = 0$ Pa) and flow symmetry on the remaining boundaries. The resulting Reynolds number defined on the turbine diameter is $Re \approx 10^6$.



(a) Domain dimensions for low blockage, $B = 0.035$.



(b) Domain cross-section of the two domain blockage ratios analysed: left, low blockage, right, high blockage.

Figure 4.6: The simulation domain.

The presence of the turbine is modelled through an axial resistance provided by a numerical porous disc. The local pressure drop across the disc is defined using the local thrust coefficient, $C_{T,\text{loc}}$, introduced in equation (4.10):

$$\Delta p = C_{T,\text{loc}} \left(\frac{1}{2} \rho u_x^2 \right) \quad (4.14)$$

where u_x is the local axial flow velocity at the disc plane. From equations (4.9) and (4.14) and approximating u_x to be constant and equal to U_t over the disc plane, the

relationship between $C_{T,\text{loc}}$ and C_T follows as

$$C_{T,\text{loc}} = C_T \frac{U_\infty^2}{U_t^2}. \quad (4.15)$$

In order to cover the full range of expected C_T values, $C_{T,\text{loc}}$ is varied between $0.1 \leq C_{T,\text{loc}} \leq 3.5$.

The $k-\omega$ SST turbulence model was chosen as the turbulence closure for its ability to model separated flows as are known to occur for ducted devices, see section 3.2.3. Noting the wide range of turbulence levels at offshore sites, multiple levels of turbulence metrics are analysed in section 4.3.4.

As illustrated in figure 4.6, no support structure, such as hub or tower are modelled. It is acknowledged that a support structure can have a significant effect on the flow field as well as the performance of the turbine. A hub reduces the turbine area, thereby directly affecting the power generated. Further, a hub may exhibit flow separation, influencing the flow through the rotor. The tower, or any other support structure, is expected to cause interference with the rotor, depending on the relative location and the design of the structure. Adding structure to the flow increases the thrust, therefore affecting the channel dynamics and leading to increased energy removal from the flow. These points will be partially accounted for in chapter 5, where minimal support structure is accounted for by modelling the turbine hubs.

4.3.2 Investigation of unsteady flow features

As introduced in section 3.2.4, unsteady simulations discretise the simulation temporally using a time-stepping mechanism as well as retaining the unsteady term in the Navier-Stokes equations. The solution of the simulation is therefore extended by a further dimension and requires more computational resource than a steady simulation

(usually an order of magnitude depending on convergence rates). It is therefore of interest to investigate whether more computationally efficient steady simulations sufficiently capture all flow features present.

The turbine representations used in chapters 4 and 5 are steady flow models, thus no unsteady effects are introduced through the turbine disc. However, as structures are added to the flow in order to model the ducts, unsteady features could potentially form at the trailing edges.

In order to investigate the flow field for unsteady flow features, unsteady simulations are performed employing various time-step intervals. The time-step interval is gradually reduced until a converged solution is obtained. After obtaining the converged solution, the results of the flow field and the forces on wall structures are analysed for fluctuations. If fluctuations exist, the amplitude of these fluctuations indicates the intensity of the unsteady flow features present in the flow.

In case a converged steady simulation result can be obtained, the result can be compared to that of the converged unsteady simulation. Due to the fluctuations, the unsteady simulation results need to be averaged over one or more fluctuation periods. By comparing the steady and unsteady result, errors may be computed for the steady simulation result. If the errors of the steady result are small, steady simulations may be used to efficiently approximate the time-dependent solution resolving the fluctuations.

All flows simulated for this study were found to be steady, and thus the unsteady simulations did not exhibit any fluctuations. Very little difference was observed in the unsteady simulation results and hence only steady flow results are presented. For simulations of highly separated flows, several unsteady simulation checks were conducted, the results of which are presented in the respective sections (see sections 4.7.2 and 5.6.1).

4.3.3 Grid resolution study

In order to gain confidence in the simulation results, a grid convergence study was performed. From this study one can determine a converged solution and derive an optimal grid with regards to accuracy and computation time. A large number of mesh variations were tested. However, for simplicity only a few relevant examples will be presented in this section. The grid resolution study was performed for the three device types analysed: the bare turbine, the ducted turbine, and the open-centre turbine. The details of the grid convergence study are presented here at the example of the bare turbine in low blockage ($B = 0.035$). For the ducted and open-centre turbines, the results are given in the respective sections.

Unstructured tetrahedral grids are employed to discretise the domain. As introduced above, the bare turbine is modelled as a porous disc boundary condition, without the inclusion of hub or support structure, hence no wall zones needed to be modelled. The grid resolution study of the bare turbine was conducted considering meshes ranging from 2.1×10^5 to 2.2×10^6 elements, see table 4.1. In all cases regions of higher mesh density were placed on the disc, in the region immediately approaching the disc, as well as in the wake of the disc. The dimensions of the mesh densities are given in table 4.1. Figure 4.7 illustrates the converged mesh in the vicinity of the actuator disc.

Table 4.1: Mesh resolution overview for bare turbine

| Resolution: | low resolution | medium resolution | high resolution |
|---|-------------------|-------------------|-------------------|
| Cell count [n]: | 2.1×10^5 | 1.2×10^6 | 2.2×10^6 |
| Max. element dimension, far field [D] : | 1.25 | 0.94 | 0.625 |
| Max. element dimension, wake [D] : | 0.25 | 0.125 | 0.125 |
| Max. element dimension, disc [D] : | 0.031 | 0.013 | 0.006 |

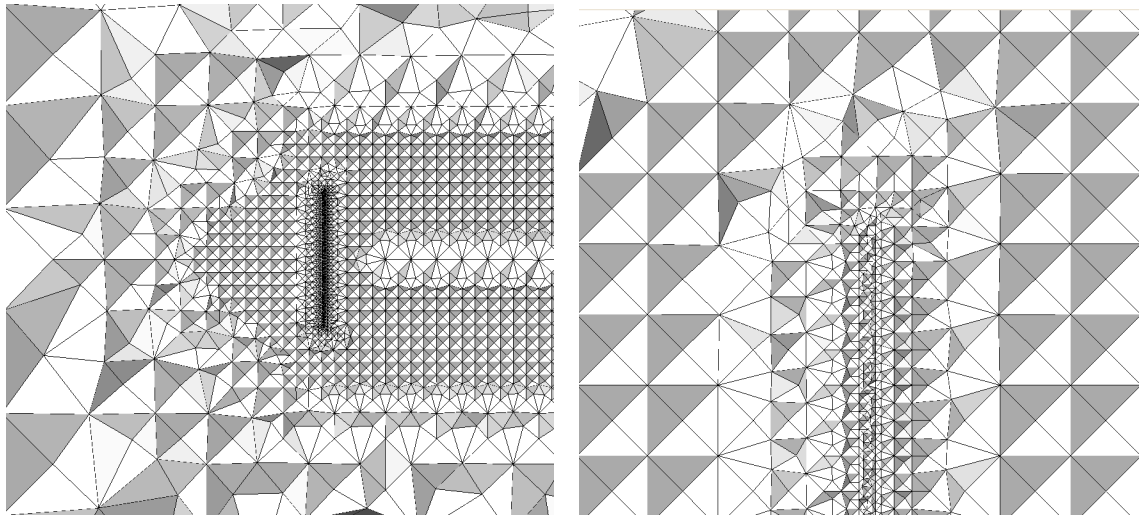
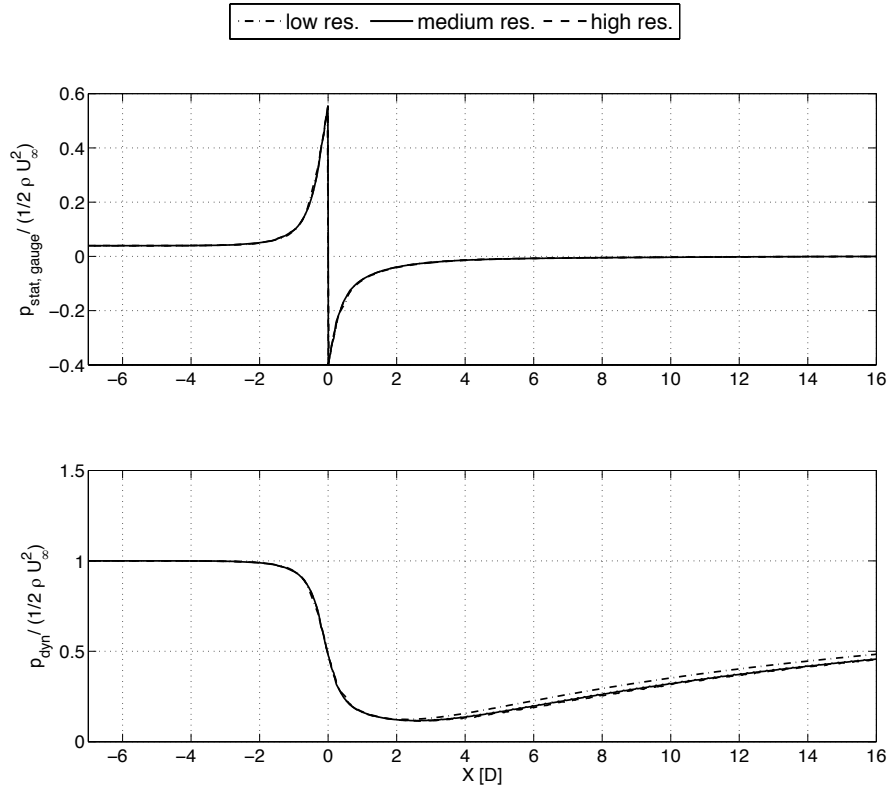


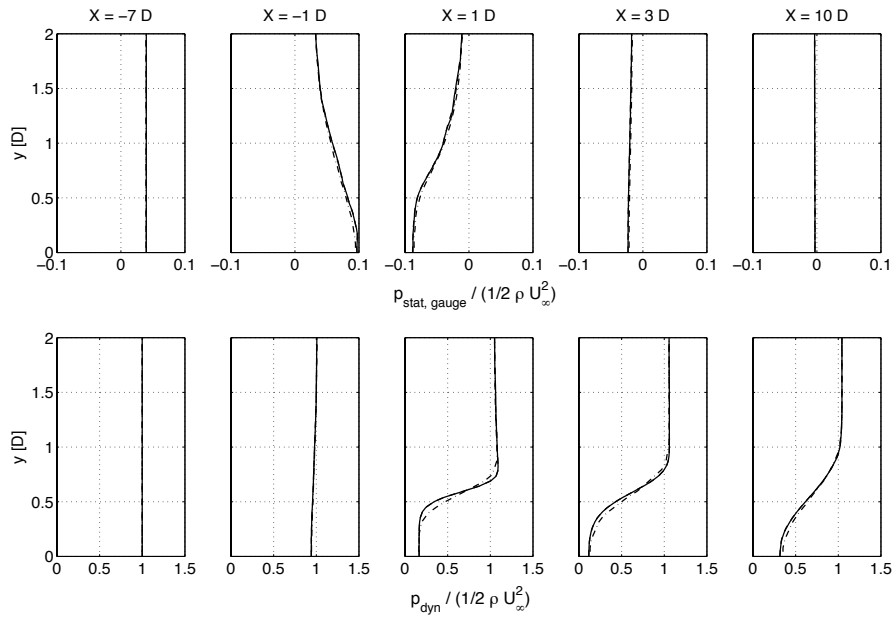
Figure 4.7: Mesh of the bare turbine in the vicinity of the actuator disc (left) and close-up of mesh on actuator disc (right).

The simulations were performed at a high thrust setting ($C_{T,loc} = 2.0$) as highly sheared flow conditions should be more sensitive to changes in mesh resolution. In order to examine the flow field around the turbine more closely, two types of plots are presented. Figure 4.8a illustrates the pressure distribution on the centreline of the simulation domain, which is also the turbine rotational axis. The second plot presents the transversal axial velocity and pressure profiles at various positions upstream and downstream of the turbine, see figure 4.8b.

Figure 4.8a shows an increase in static pressure, p_{stat} , and reduction in dynamic pressure, $p_{dyn} = 1/2 \rho U^2$, followed by wake expansion and recovery of p_{stat} followed by p_{dyn} . One can see a very good match between the simulation results for the high and the medium resolution mesh. It can therefore be concluded that with the medium resolution mesh one can achieve satisfactory accuracy with no further need for refinement. In order to reduce computation time, coarser meshes are tested to see at what resolution the results start to deteriorate. An example can be seen from the low resolution results also plotted in figure 4.8a. Especially far downstream, substantial differences for the dynamic pressure (and thus the velocity field) are



(a) Centreline pressure distribution.



(b) Transversal pressure distribution at five locations upstream and downstream of the turbine disc.

Figure 4.8: Pressure distribution (static gauge and dynamic pressure) of the turbine disc, plotted for high, medium, and low mesh resolution. Disc thrust of $C_{T, \text{loc}} = 2.0$.

observed, suggesting that the low resolution mesh lacks accuracy. For this comparison, an extremely low resolution case was selected, so that the changes in the results are more pronounced and thus easily visible. However, in the mesh analysis it was seen that, for meshes with lower resolution than the presented medium resolution mesh, the results diverge from the converged results.

The flow field dependency on resolution is further examined in figure 4.8b in which the transversal vertical pressure profiles for high, medium, and low mesh resolution are presented at various distances from the disc. The distance x to the disc given in turbine diameters is noted above each subplot, the transversal location, y , also given in turbine diameters, is noted on the vertical axis, and on the horizontal axis the pressure (normalised by the inflow dynamic pressure) is plotted. It is clear that the dynamic pressure far downstream is reduced for lower resolution analysis. Furthermore, differences at the wake boundary can be seen immediately behind the disc; whilst the shear layer between wake and bypass flow is seen to have the same strength (velocity difference) in both cases, the shear layer is clearly more diffuse in the low resolution case.

Power and thrust were observed to vary by less than 1% between the three meshes considered. The final mesh selected is that referred to as “medium resolution” in the discussion above. Though the differences in power and thrust were marginal between high and low resolution mesh, due to the differences in flow field as seen in figures 4.8a and 4.8b the medium resolution mesh was selected for subsequent analyses.

4.3.4 Turbulence parameter sensitivity analysis

As mentioned in section 3.2.3, the $k-\omega$ SST turbulence model was chosen for its ability to model separated flows. Within this model, one must set boundary conditions on the turbulence quantities: the turbulent intensity, I [%], and the turbulent length

scale, l [m]. In order to test the influence of ambient turbulence on the simulation result turbulence intensity was varied between $2\% < I < 10\%$, around the initial estimated value of 5% , which was also used as the “medium” level in the study by Gaden and Bibeau (2010). An empirical approximation is used to estimate the order of the turbulent length scale, l (ANSYS Inc., 2009b):

$$l = 0.07L \tag{4.16}$$

where L is the characteristic length of the obstruction in the flow. In this case this is the diameter of the porous disc, therefore $L = 16$ m and l is estimated at 1.12 m. Values of length scale between $0.7 \text{ m} < l < 16 \text{ m}$ are investigated. The results of this parameter study are given as the centreline pressure distribution, see figure 4.9.

Generally, the variation in results is mostly confined to the wake, as expected and reported in previous studies (Sun, 2008). It has been reported that turbulence intensity does not have a strong impact on power generated, but is of importance when regarding the turbine wake. Both the increase in ambient turbulence, as well as an increase in the turbulent length scale lead to increased velocity far downstream, due to enhanced wake mixing and therefore to a faster wake recovery. For the ranges analysed, the effect of variation in I is much larger than that of l . Note that for $I = 0.1\%$ there is virtually no mixing of the wake. For subsequent simulations $I = 5\%$ and $l = 1.6$ m are employed as representative of the turbulent environment.

As there is no ambient turbulence generating mechanism (i.e. seabed roughness) included in the simulation, the ambient turbulence introduced at the domain inlet dissipates along the length of the simulation domain. In order to quantify this turbulence dissipation, the domain is simulated with and without the disc and the turbulence intensity is measured along the domain centreline as a function of its value at the inlet, see figure 4.10.

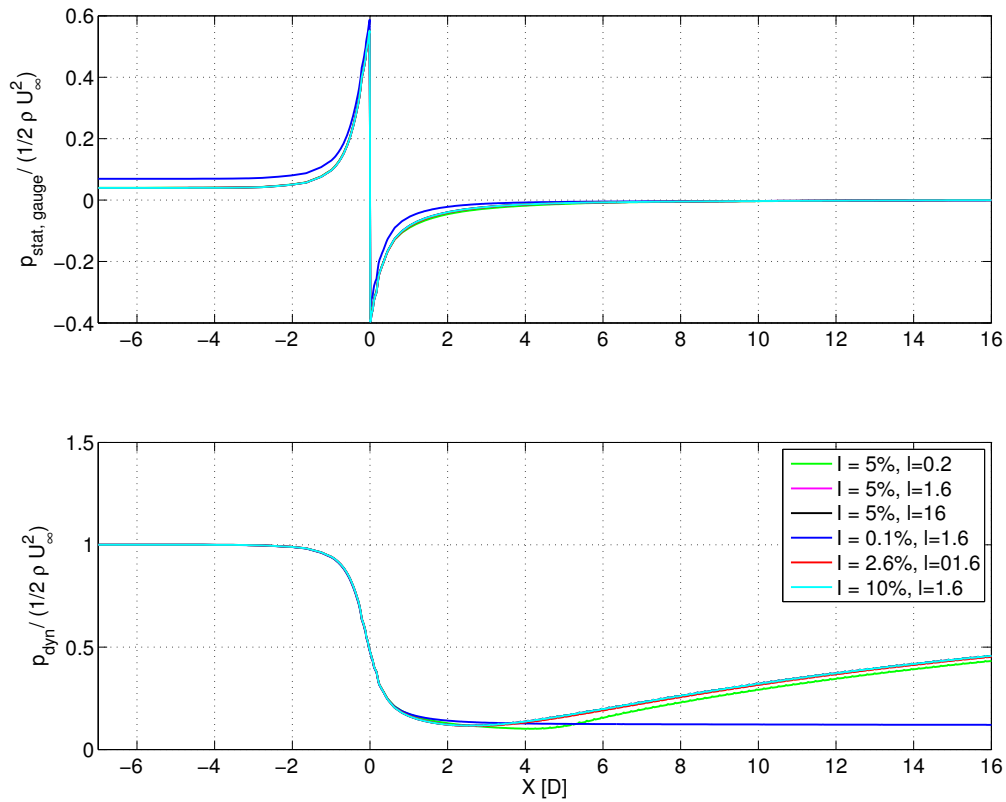


Figure 4.9: Centreline pressure distributions (static gauge and dynamic pressure) plotted for varying turbulence intensities and turbulent length scales.

For both the empty domain, as well as the domain with actuator disc, the ambient turbulence intensity drops steadily to about 75 % of its original value by the time it reaches the location of the disc, $x = 0$. This drop is purely a function of downstream distance, hence for a shorter domain inlet this effect would be less pronounced at the disc location. For the domain with the actuator disc, I increases just as the flow approaches the disc and is considerably increased in the turbine wake (wake added turbulence). The ambient turbulence dissipation seen here is a numerical feature of this type of simulation, which does not realistically model the turbulence intensity of a tidal flow. However, as the impact of I on turbine performance as modelled here is minimal, no effort has been made to sustain a constant ambient turbulence profile. Further, the approach of adding bed friction would introduce a shear profile,

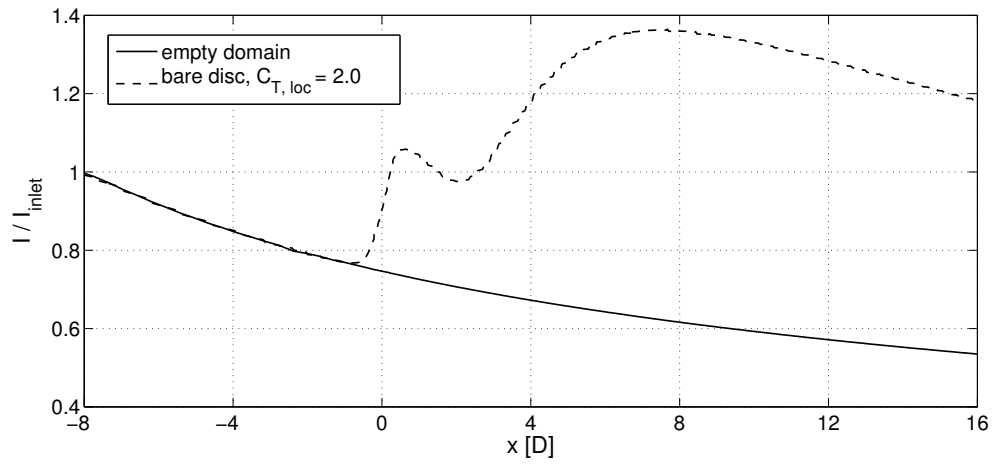


Figure 4.10: Dissipation of turbulence intensity measured along domain centreline.

a complication that is excluded from this investigation. The inlet turbulence intensity was adjusted accordingly, in order to obtain an ambient turbulence intensity of 5% at the device.

4.4 Bare turbine model validation

The following section describes the analysis methods used throughout this study for the example of the bare turbine. The data extraction process is introduced and the flow field visualised. Thrust and power are extracted and compared to LMADT in order to validate the CFD actuator disc method. The turbine performance is evaluated by introducing three measures of performance.

4.4.1 Data extraction

To compare the CFD results of the bare turbine to those of LMADT, power and thrust on the porous disc must be determined in an appropriate manner. Two methods of data extraction have been employed to obtain the force applied by the disc. The control volume method only uses the flow results, while the other, more simple, disc thrust method also uses the local thrust coefficient $C_{T,loc}$ specified on the disc.

For the control volume method the force acting on the disc is evaluated by considering conservation of linear momentum through a discretised set of control volumes encompassing the porous disc. Unlike actuator disc theory, the pressure field is continuous and hence the pressure drops across a small but finite distance normal to the plane of the disc. However, across this distance there can also be a significant change in streamwise momentum.

The disc thrust method uses the local thrust coefficient $C_{T,loc}$ specified on the disc, from which the pressure jump applied to the disc is immediately obtained, see equation (4.14). As the velocity at the disc varies across the disc radius, the area integral of the axial component of local velocity squared, u_x^2 , must be extracted from the simulation.

Both methods for data extraction have been applied to the bare turbine validation cases and the difference in pressure drop between the two methods was less than 1%. Thus we can be confident that the force applied by the numerical actuator disc corresponds to that defined in equation (4.14) and the simpler data extraction method can be applied. Hence, using equation (4.14) and the integral of the stream wise velocity at the disc, thrust and power follow as

$$T = \frac{1}{2} C_{T,\text{loc}} \rho \int_{A_t} u_x^2 dA \quad (4.17)$$

and

$$P = \frac{1}{2} C_{T,\text{loc}} \rho \int_{A_t} u_x^3 dA. \quad (4.18)$$

4.4.2 Flow field analysis

The flow field may be visualised in many ways. In the following, two ways of analysing the flow field are introduced. The first plot presents contours of gauge pressure and relative x -velocity of the horizontal cross-section, overlaid with velocity streamlines.

Figure 4.11 presents the pressure and velocity contours of the bare turbine at low and high disc thrust settings. The pressure jump generated by the presence of the disc is clearly visible in the left hand figures, as is the reduction in velocity with the accompanying widening of the streamtube on the right hand figures. For high disc thrust (figure 4.11b) the effects are significantly more pronounced than for low disc thrust (figure 4.11a).

The second plot type analyses the flow upstream and downstream of the turbine disc by presenting the static and dynamic pressure of the flow field, normalised by the

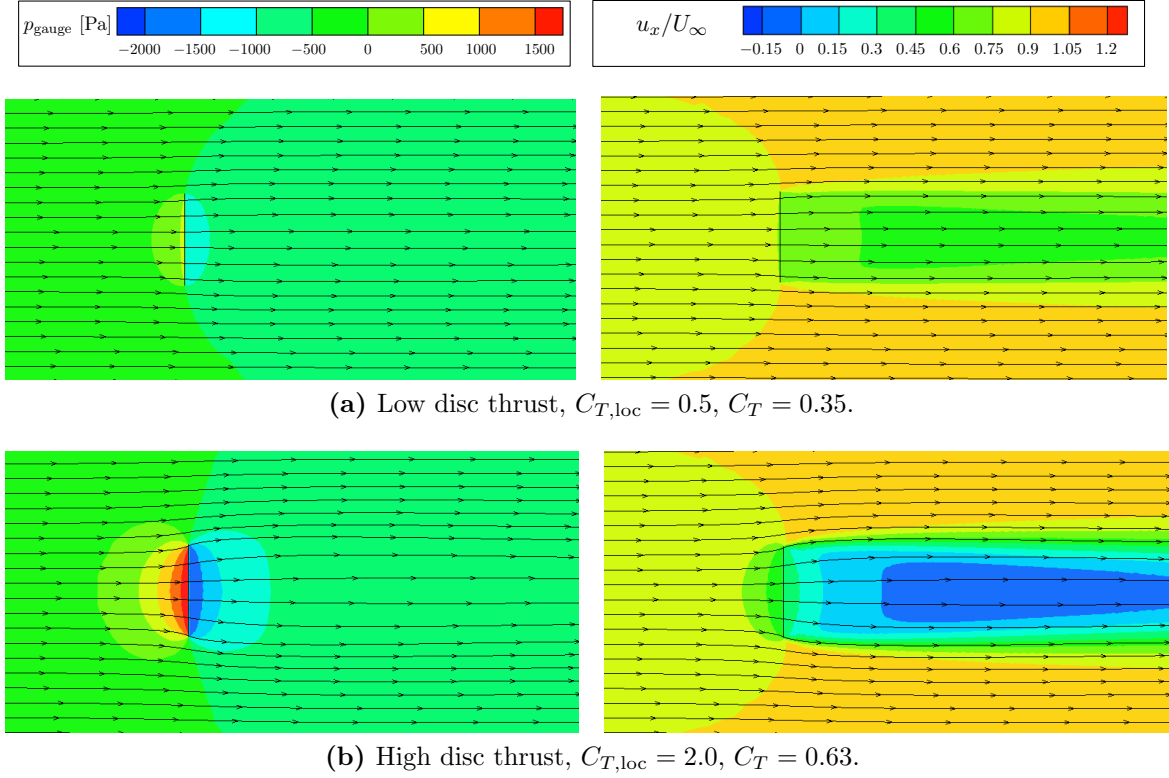


Figure 4.11: Contour plots of gauge pressure (left) and relative axial velocity (right) for the bare turbine, for low and high disc thrust.

free-stream dynamic pressure. Figure 4.12 shows the resulting transversal pressure profiles in the horizontal mid-plane for a medium disc thrust setting, $C_{T,loc} = 1.0$. Due to the symmetry of the problem, only half of the domain is presented here. The distance to the disc plane is noted above each profile. The static pressure is quantified as an offset to the gauge pressure. Upstream of the turbine disc (-1D) an increase in static pressure is present, coinciding with a reduction in dynamic pressure. In the wake of the disc (1D) the static pressure is decreased below the free-stream value and there is a distinct, hat shaped drop in dynamic pressure. Further downstream (3D, 10D) the static pressure quickly recovers, while the recovery of the dynamic pressure (and therefore the velocity) takes much longer. Close to the outlet of the simulation domain, a distinct wake profile is still visible in the dynamic pressure.

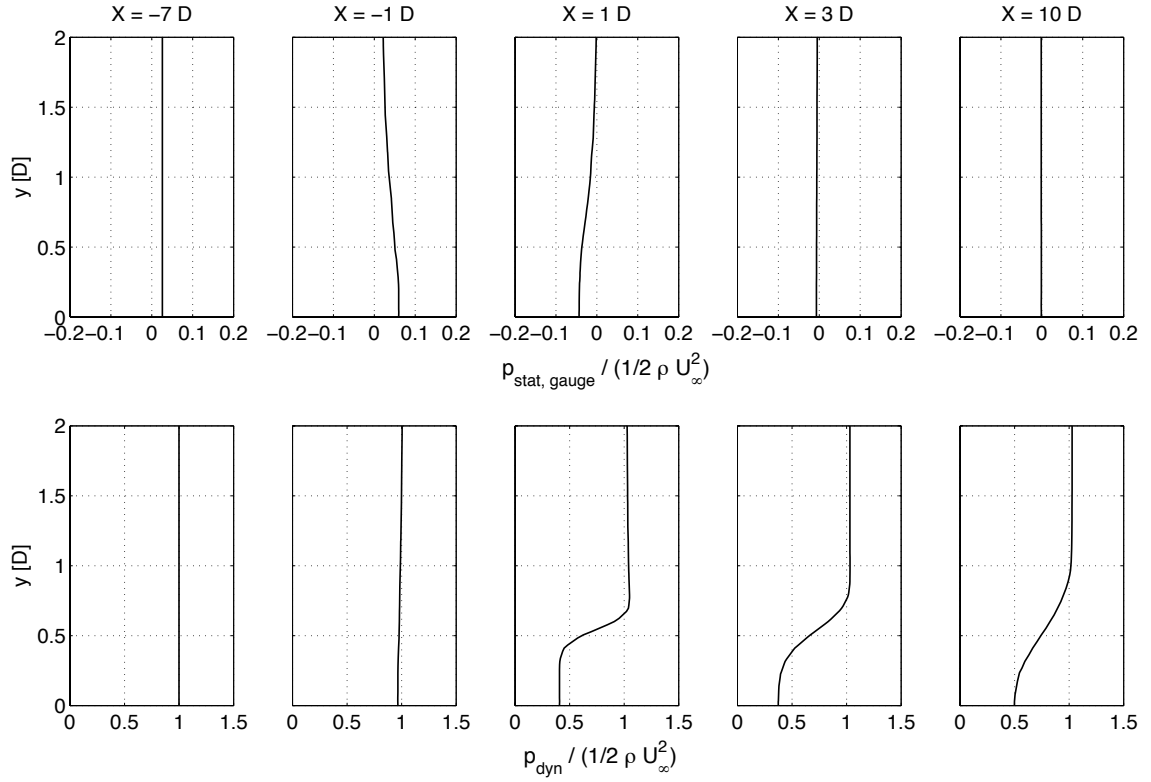


Figure 4.12: Transversal pressure profiles for the ducted turbine at five locations upstream and downstream of the turbine. $C_{T,loc} = 1.0$, $C_T = 0.65$, $B = 0.035$. Both streamwise and transversal location are given as a function of device diameters, D .

4.4.3 Thrust analysis

As the bare turbine represented by the actuator disc does not include any structural components, the only force exerted on the flow is that by the actuator disc. Therefore the device thrust analysis of the bare turbine only encompasses one component, the turbine disc. Figure 4.13 presents the results of the disc thrust dependent on the induction factor for low and high blockage. The simulation results compare well to those of extended LMADT (Houlsby, Draper and Oldfield, 2008), in particular at low blockage.

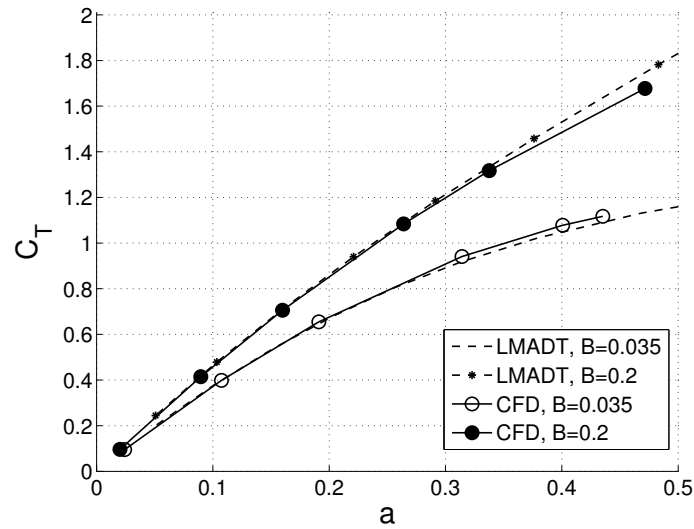


Figure 4.13: Thrust of the bare turbine, C_T against a , for blockage ratios of $B = 0.035$ and $B = 0.2$ for both CFD and LMADT for confined flow.

4.4.4 Performance analysis

The performance analysis of the devices under investigation is examined by multiple measures of performance:

- power: measured by the power coefficient, C_P
- power density : measured by the power density coefficient, C_{PD}
- efficiency: measured by the basin efficiency, η_{basin}

Each measure of performance is introduced in this section and compared to the results obtained employing LMADT.

4.4.4.1 Performance in terms of power

The first of the performance measures is the power coefficient introduced in section 4.1. It is important to note that the power coefficient for all of the results are defined in terms of the total frontal (blocked) area of the device (and not simply the disc area) as the reference area. For the bare turbine the total blocked area is the same

as the disc area, whilst for the ducted turbine the total blocked area is defined by the duct maximum outer diameter. This definition compares the devices using the actual stream area they occupy, not on the turbine swept area, and hence measures the performance of the whole device (rotor and duct where applicable) in extracting energy from the flow that would have otherwise passed through the space occupied by the device. When later comparing devices (i.e. bare, ducted, and open-centre turbines) using a constant blockage ratio and constant inflow, the denominators of equations (4.8) and (4.9) are the same for all devices. Comparison of the power coefficient is thus a direct comparison of the actual power extracted by devices of the same outer diameter.

Figure 4.14 presents the numerical simulation results of the bare turbine compared to LMADT for confined flow, as introduced in section 4.2.2. It is clear that the present CFD-embedded actuator disc model agrees well with extended LMADT and thus provides a valid tool for simulating simplified turbine flows in which discrete blade effects and wake rotation have been neglected.

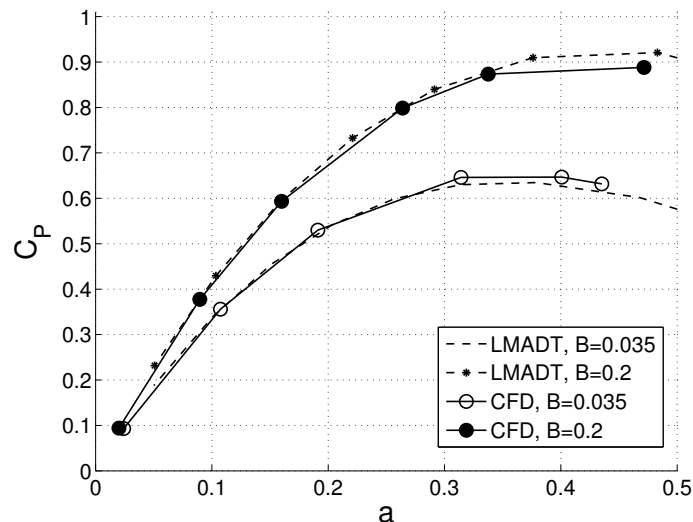


Figure 4.14: Performance of the bare turbine, C_P against a , for blockage ratios of $B = 0.035$ and $B = 0.2$ for both CFD and LMADT for confined flow.

4.4.4.2 Performance in terms of power density

Power density is measured using an alternative definition of the power coefficient,

$$C_{PD} = \frac{P}{1/2 \rho A_{\text{rotor}} U_{\infty}^3}. \quad (4.19)$$

In this alternative definition, the reference area employed in the denominator of equation (4.8) is that of the turbine (rotor) swept area. For the bare turbine both reference areas are the same, therefore C_{PD} and C_P provide the same result. Thus power density results for the bare turbine are not plotted here. For the ducted or open-centre turbine, however, the reference area may differ substantially depending on the device design, thus leading to significant differences in power and power density, as indicated in chapter 2 and further presented subsequent sections.

4.4.4.3 Performance in terms of basin efficiency

The third measure of performance employed is the basin efficiency, η_{basin} . Analysing the performance of a tidal turbine device simply through the power coefficient fails to portray the full picture. The wake behind the turbine must at some point remix with the bypass flow. The process introduces further, unavoidable energy removal from the flow. Additional energy removal is especially important when comparing bare and ducted devices. The presence of a duct within the flow exerts an additional thrust on the fluid. This added thrust can lead to significantly more energy being extracted from the flow than is converted into useful energy. As tidal flows must be considered as finite resources, the total energy removed from the flow represents an important feature of each device. Thus a device efficiency definition is introduced, which relates the useful power generated to the total power removed from the flow,

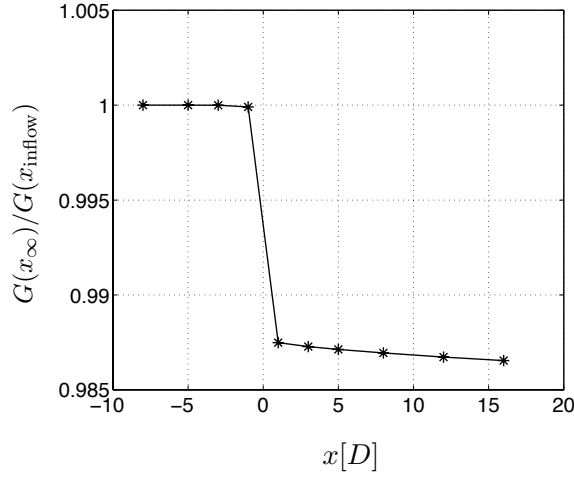


Figure 4.15: Streamwise variation of relative energy flux.

defined as the basin efficiency,

$$\eta_{\text{basin}} = \frac{\text{useful power}}{\text{total power removed from flow}}. \quad (4.20)$$

To retrieve the total power removed from the flow, two different methods have been applied. The energy flux method extracts data at the domain boundaries, while the simpler device thrust method extracts the thrust data from the device components. Both methods will be briefly described here.

For the energy flux method, the energy flux, G , is extracted at various stages upstream and downstream of the turbine. At each streamwise plane, the energy flux is calculated by integrating the product of the total pressure, p_0 , and the streamwise velocity, u_x , over the cross-sectional area, A_{yz} :

$$G(x) = \int_{A_{yz}} p_0 u_x dA. \quad (4.21)$$

Figure 4.15 presents the relative energy flux, $G(x)/G(x_{\text{inflow}})$ for a bare turbine as a function of streamwise distance, x/D , where $x = 0$ lies at the disc plane.

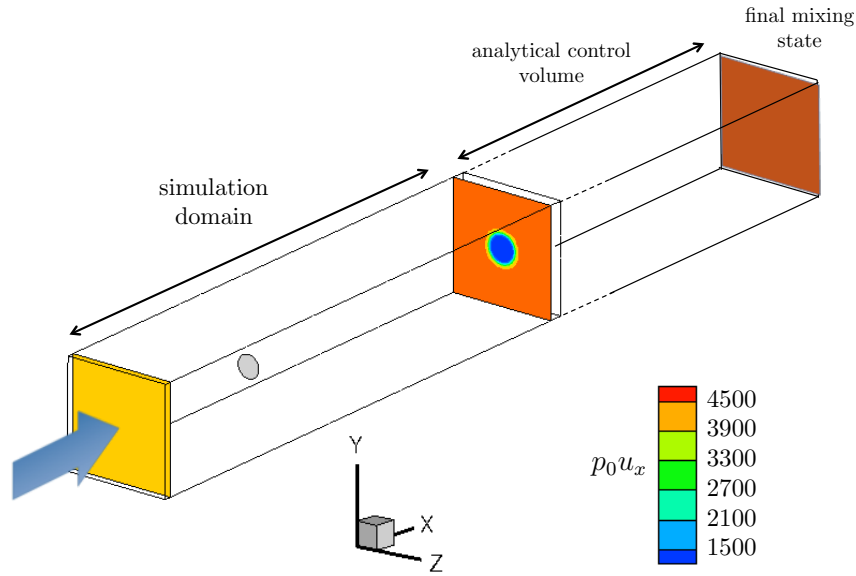


Figure 4.16: Contours of energy flux per unit area ($p_0 u_x$) over cross-stream planes upstream and downstream of the turbine disc.

Upstream of the disc ($-8D$ to $-1D$) the energy flux is constant and through the disc ($-1D$ to $1D$) a steep drop is observed, that is largely associated with useful power removed from the flow field. In the wake of the disc ($1D$ to $16D$) a further drop in the energy flux occurs due to wake mixing.

From figure 4.15 it can be seen that the final mixing state has not been achieved within the simulation domain, as the total power through the cross section has not reached equilibrium by the domain outlet. However, the final energy state can be calculated analytically by considering the flow passing through a control volume extending from the simulation domain outlet to a given cross-stream plane an undetermined downstream location through which the flow is fully mixed and uniform. The analytic control volume thus encompasses the full wake region of the turbine. Figure 4.16 illustrates the two control volumes as described above.

For the outlet of the analytical control volume (final mixing state) uniform outflow velocity and pressure are stipulated. Conservation of mass therefore directly results

in

$$\begin{aligned}\rho u_{x, \text{fms}} A &= \rho u_{\infty} A \\ u_{x, \text{fms}} &= u_{\infty}\end{aligned}\tag{4.22}$$

where the subscript ∞ refers to the conditions far upstream, “fms” to the final mixing state, and where A is the domain cross-section. A momentum force balance may then be employed on the analytical control volume, using integrated quantities from the simulation domain outlet as inlet parameters of pressure and velocities. As both pressure and velocity are uniform at the analytical control volume outlet, the pressure at this plane is the only remaining unknown which may be obtained from the momentum force balance:

$$p_{\text{fms}} = \text{constant} = \frac{1}{A} \int_A p_{\text{sdo}} dA + \frac{\rho}{A} \int_A u_{x, \text{sdo}}^2 dA - \rho u_{\infty}^2\tag{4.23}$$

where “sdo” refers to the simulation domain outlet. Using the pressure at the final mixing state the total pressure at this cross-section can be computed and from it the energy flux as given by equation 4.21.

In order to calculate the basin efficiency, η_{basin} , the useful power, is divided by the overall power removed. The overall power removed from the flow is given through the change in energy flux between the domain inflow and the final mixing state:

$$\eta_{\text{basin}} = \frac{P}{\left(\int_A p_0 u_x dA \right)_{\text{inflow}} - \left(\int_A p_0 u_x dA \right)_{\text{fms}}}\tag{4.24}$$

The alternative approach to computing the basin efficiency is by calculating the total power removed from the flow using the thrust on both the turbine disc and the structure if applicable (such as a duct). As shown in equation (4.25), the power removed from the flow can be calculated by multiplying the total thrust in streamwise

direction by the upstream velocity in streamwise direction:

$$\eta_{\text{basin}} = \frac{P}{(T_{\text{turbine}} + T_{\text{structure}})_{\xi} U_{\infty}} \quad (4.25)$$

The thrust and velocity directional component are those of the direction of the free-stream, ξ , in the case of axial flow this is the x -direction.

Both methods described above have been employed in order to compute the total power removed from the flow. The results differ by less than 1%, and therefore due to the simplicity of the approach, the device thrust method will be applied from hereon. This method is also employed by Shives and Crawford (2010) in their analysis of unidirectional ducted turbines.

As the bare actuator disc only encompasses a disc thrust component and no structural components, the basin efficiency may in this case be written as

$$\eta_{\text{basin, bare}} = \frac{U_t}{U_{\infty}} = 1 - a = \frac{C_P}{C_T} \quad (4.26)$$

where U_t is the spatial average of the streamwise velocity at the turbine disc. Therefore, for this particular case, η_{basin} is purely a function of the induction factor. For the Betz limit the basin efficiency is therefore $\eta_{\text{basin, Betz}} = 2/3$.

Figure 4.17 presents the basin efficiency of the bare turbine for both low and high blockage ratios and compares these to the theoretical results obtained using LMADT. All results lie on the same line defined by $1 - a$. However the results for one particular disc thrust will lead to different results of η_{basin} depending on the blockage ratio used (as indicated by the plot markers).

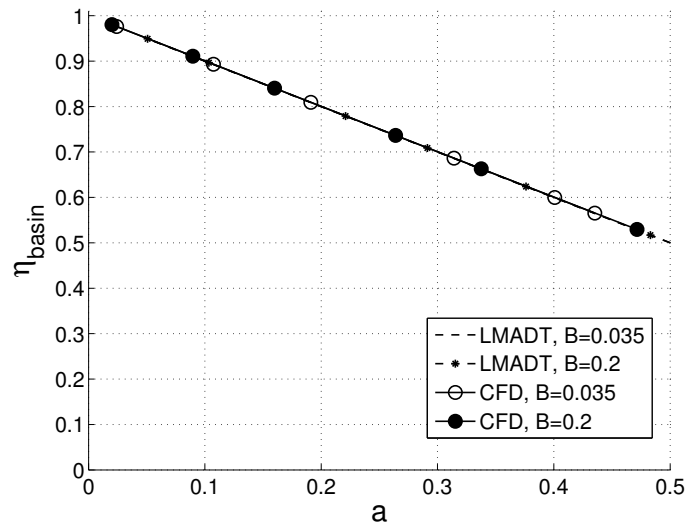


Figure 4.17: Performance of the bare turbine measured in basin efficiency.

4.5 Analysis of a bidirectional ducted turbine in axial flow

Following the validation of the numerical approach, a bidirectional ducted turbine (hereafter referred to simply as the ducted turbine) is investigated employing a porous disc embedded in a thin-walled convergent-divergent duct. Figure 4.18 illustrates the duct design. As for the bare turbine disc, two area blockage ratios of $B = 0.035$ and $B = 0.2$ are investigated, while for the high blockage ratio domain only performance data will be presented. The blockage ratio is based on the maximum outer diameter of the device, here the duct inlet area.

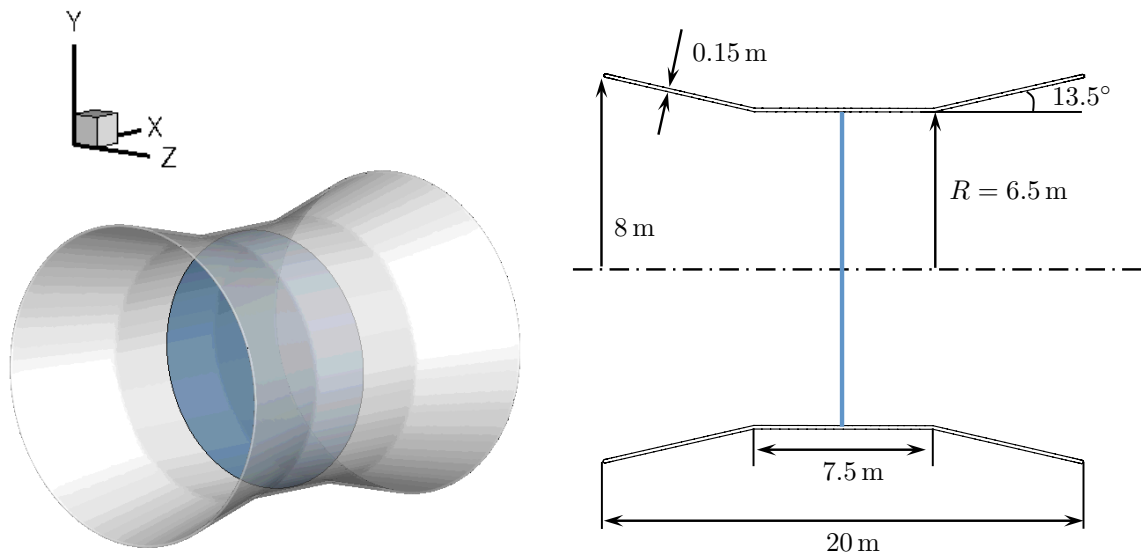


Figure 4.18: The ducted turbine (3D view and cross-section).

The duct wall has a thickness of 0.15 m and the leading and trailing edges of the duct wall are rounded. The nozzle contraction ratio – and due to symmetry also the diffuser opening ratio – is $A_{\text{inlet}}/A_{\text{throat}} = A_{\text{outlet}}/A_{\text{throat}} = 1.51$.

The grid consists of tetrahedral cells in the bulk of the domain and four prism layers on the duct surface in order to resolve the boundary layer. Figure 4.19 displays the mesh distribution in the domain, around the duct and on the leading edge of the

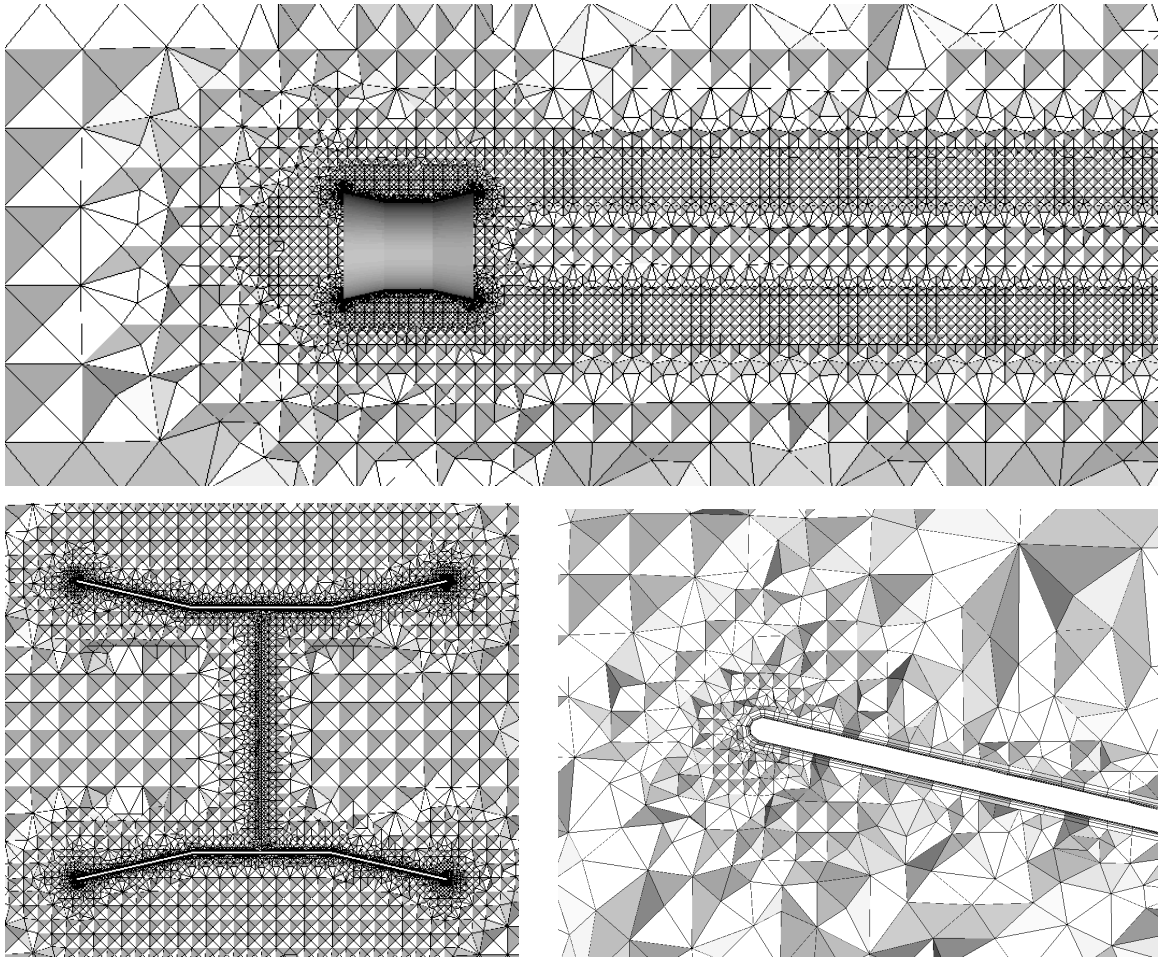


Figure 4.19: Mesh for the ducted turbine.

duct inlet. Density regions are placed in the immediate approach of the device, as well as the wake. A grid resolution study was performed, in accordance with the example given in section 4.3.3. Table 4.2 presents the details of the converged mesh solution.

In order to obtain the values of the dimensionless wall distance, y^+ , a sample simulation was conducted at high thrust setting ($C_{T,loc} = 2.0$). For the computationally efficient medium resolution mesh, the value for y^+ on the duct wall is located within the log-law layer as recommended in ANSYS Inc. (2009b). For all three meshes considered the performance coefficients varied by less than 1%.

Table 4.2: Mesh resolution overview for the ducted turbine

| Resolution | converged mesh |
|---|------------------------|
| Cell count [n]: | 4.5×10^6 |
| Max. element dimension, far field [D] : | 0.94 |
| Max. element dimension, wake [D] : | 0.125 |
| Max. element dimension, disc [D] : | 0.013 |
| Max. element dimension, duct [D] : | 0.013 |
| y^+ on duct wall: | $50 \leq y^+ \leq 200$ |

4.5.1 Flow field of the ducted turbine

Figure 4.20 presents the flow through the duct as pressure and velocity fields in the vertical xy -planes for four levels of turbine thrust ($C_{T,loc} = 0.1, 0.3, 0.5, 3.0$). As for the bare turbine, the contour plots are overlaid with streamlines, in order to better observe the widening of the streamtube and to better identify areas of flow separation.

From these flow fields we identify two distinct flow regimes, which relate to the variation of thrust applied on the turbine disc:

- at low disc thrust: nozzle-contoured, attached flow
- at medium to high disc thrust: separation dominated flow

Note that the turbine thrust reported here is only the thrust on the disc; thrust on the duct is considered separately in section 4.5.2.

For very low turbine thrust levels the disc inside the duct poses little resistance and the flow streamlines approach the duct nearly parallel to the turbine axis; see figure 4.20a. On the outer as well as the inner walls of the duct the flow remains fully attached, a flow regime denoted above as nozzle-contoured flow.

Increasing the thrust on the turbine results in increased resistance to the flow and hence to a widening of the streamtube as it approaches the device. The widening

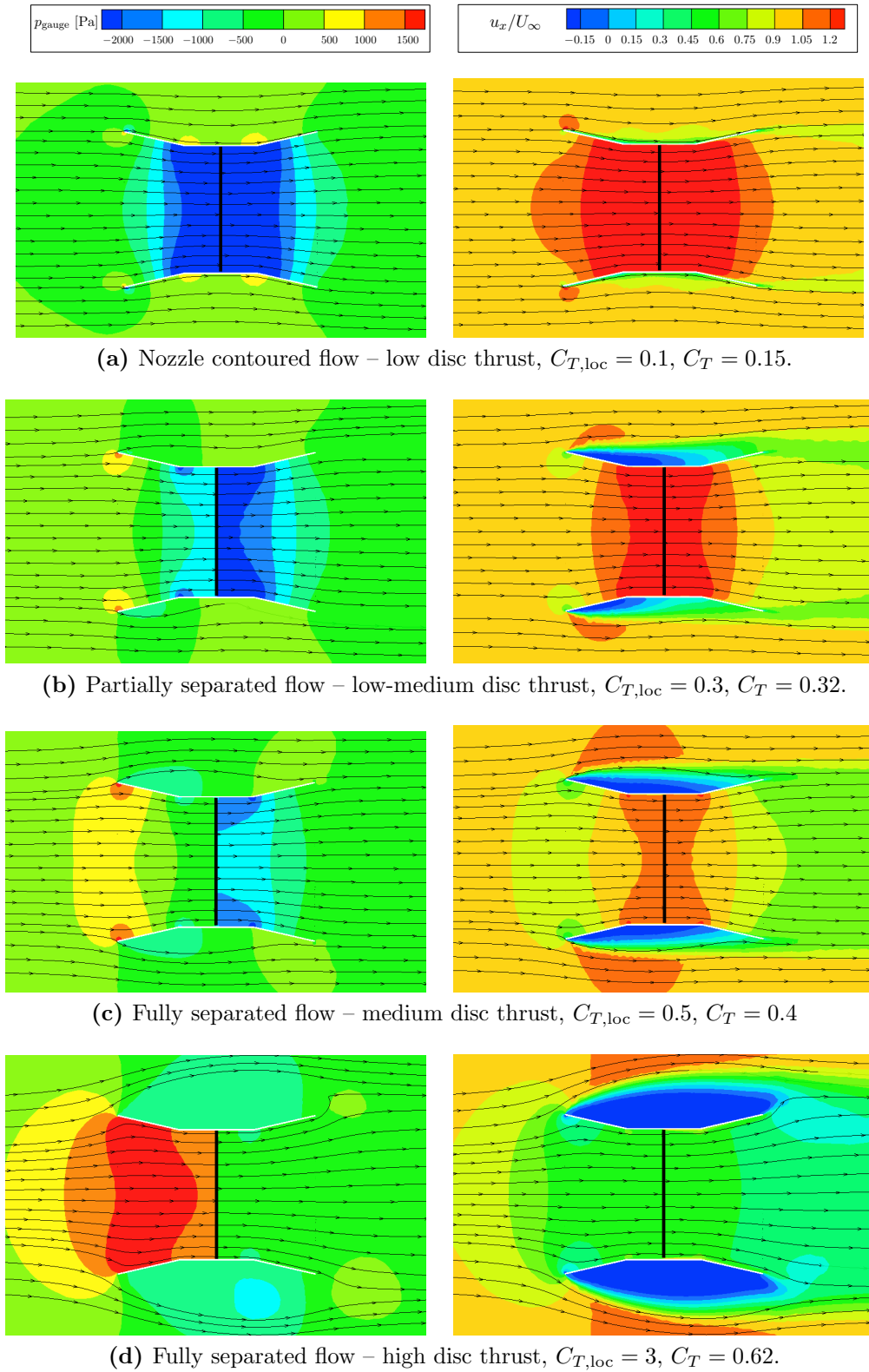


Figure 4.20: Contour plots of pressure and velocity distribution for the ducted turbine, for $B = 0.035$.

streamtube results in an increased angle between the incident flow and the duct inlet, resulting in flow separation on the outer surface of the duct, see figure 4.20b. The leading edge separation creates a recirculation zone on the outer surface of the duct which stretches from the leading edge to a flow reattachment point, somewhere along the duct length. As the thrust on the disc is increased further, the separation becomes more pronounced and the reattachment point moves progressively downstream, see figures 4.20b and 4.20c. For moderate disc thrust levels the flow separation on the outer duct surface covers the full duct length, see figure 4.20c. Although the streamtube widening is accompanied by a velocity reduction, the flow accelerates within the duct due to the contraction and even for this fully separated flow case, figure 4.20c, the flow passes the disc at higher velocity than free-stream. Increasing the thrust level further increases the resistance of the turbine in the duct leading to a stronger widening of the streamtube as it approaches the duct and therefore to a further decrease in flow rate through the duct, see figure 4.20d.

To investigate the energy removal from the flow, figure 4.21 examines the transversal pressure profiles of the ducted device, which may be compared to those of the bare device in figure 4.12. The unit D corresponds to the device diameter, which is the same as for the bare turbine, $D = 16$ m. The disc thrust level was chosen as $C_{T,loc} = 0.3$ in order to match the energy extraction from the domain in figure 4.12. The total thrust of the devices (which in case of figure 4.21 includes both disc and the duct, see section 4.5.2) is roughly of the same value: $C_{T,tot} = 0.68$ in figure 4.21, $C_{T,tot} = 0.65$ in figure 4.12.

In general the transversal pressure profiles for the ducted and the bare turbine are rather similar, especially when regarding the profiles at planes at a significant distance downstream from the device. A more pronounced drop in dynamic pressure and build up in static pressure is seen just upstream of the ducted device ($-1D$) when compared

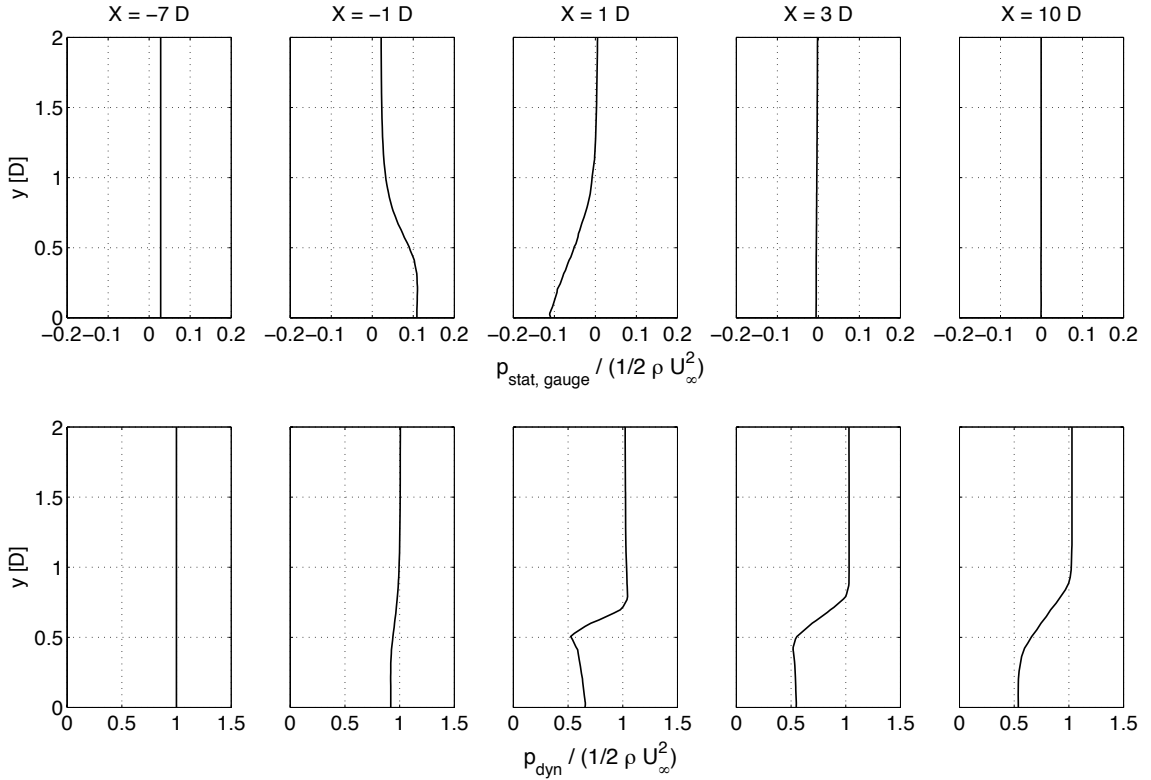


Figure 4.21: Transversal pressure profiles for the ducted turbine at five locations upstream and downstream of the turbine. $C_{T,loc} = 0.3$, $C_T = 0.32$, $C_{T,tot} = 0.68$, $B = 0.035$. Both streamwise and transversal location are given as a function of device diameters, D .

to the bare disc, as for the ducted device the maximum static pressure is reached close to the opening of the duct. Immediately behind the device (1D) the ducted device exhibits a smaller drop in both dynamic and static pressure compared to the bare turbine, however, the width of the wake is slightly larger. Far downstream (10D) virtually no difference is visible between the two flow fields.

4.5.2 Thrust of the ducted turbine

To assess the thrust effect of large scale separation on the duct and on the device overall, as well as to quantify the power removal from the flow, the thrust on the duct must be considered in addition to the thrust on the turbine disc. The thrust on the duct is obtained by computing the total force component along a specified

force vector (in this case the x -axis) by summing the dot product of the pressure and viscous forces on each face with the specified force vector (ANSYS Inc., 2009a). This is performed by the force report function supplied by ANSYS FLUENT.

Figure 4.22 presents the thrust coefficient plotted as a function of the spatial mean of the induction factor. Three thrust coefficients are plotted: $C_T = C_{T, \text{turbine}}$, the thrust coefficient for the turbine disc (the standard thrust coefficient), $C_{T, \text{duct}}$, coefficient for the thrust on the duct, and $C_{T, \text{tot}} = C_{T, \text{turbine}} + C_{T, \text{duct}}$. Note that A_{device} is used as the reference area in defining all three coefficients.

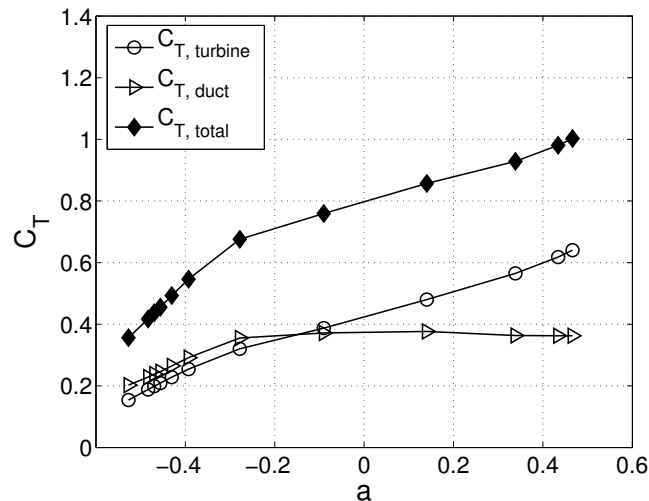


Figure 4.22: Thrust coefficients for the bidirectional ducted turbine. $B = 0.035$.

From figure 4.22 it is apparent that, for this type of duct geometry, the turbine and duct thrust are of similar magnitude and only diverge for high induction factors, where the turbine thrust steadily increases, whereas the duct thrust stays roughly constant. This can be explained by considering the flow regimes described in the previous section. The thrust on the duct increases as the separation region grows with increasing disc thrust. However, once the flow on the outside of the duct is fully separated (see figure 4.20c) no further increase in the thrust on the duct occurs. Overall, the total device thrust for the design point ($C_{T, \text{loc}} = 0.5$, $a = -0.1$) is

$C_{T,tot} = 0.77$, which is lower than that of the bare turbine at design point ($C_{T,tot, bare} = 0.95$).

4.5.3 Performance of the ducted turbine

Following the methods described in section 4.4.4 the performance of the ducted turbine is analysed: in terms of power coefficient C_P , power density, C_{PD} , and basin efficiency, η_{basin} . Figure 4.23b presents the performance results of the ducted turbine for both low and high flow blockage. In order to facilitate comparison, the results of the bare turbine are presented here as well.

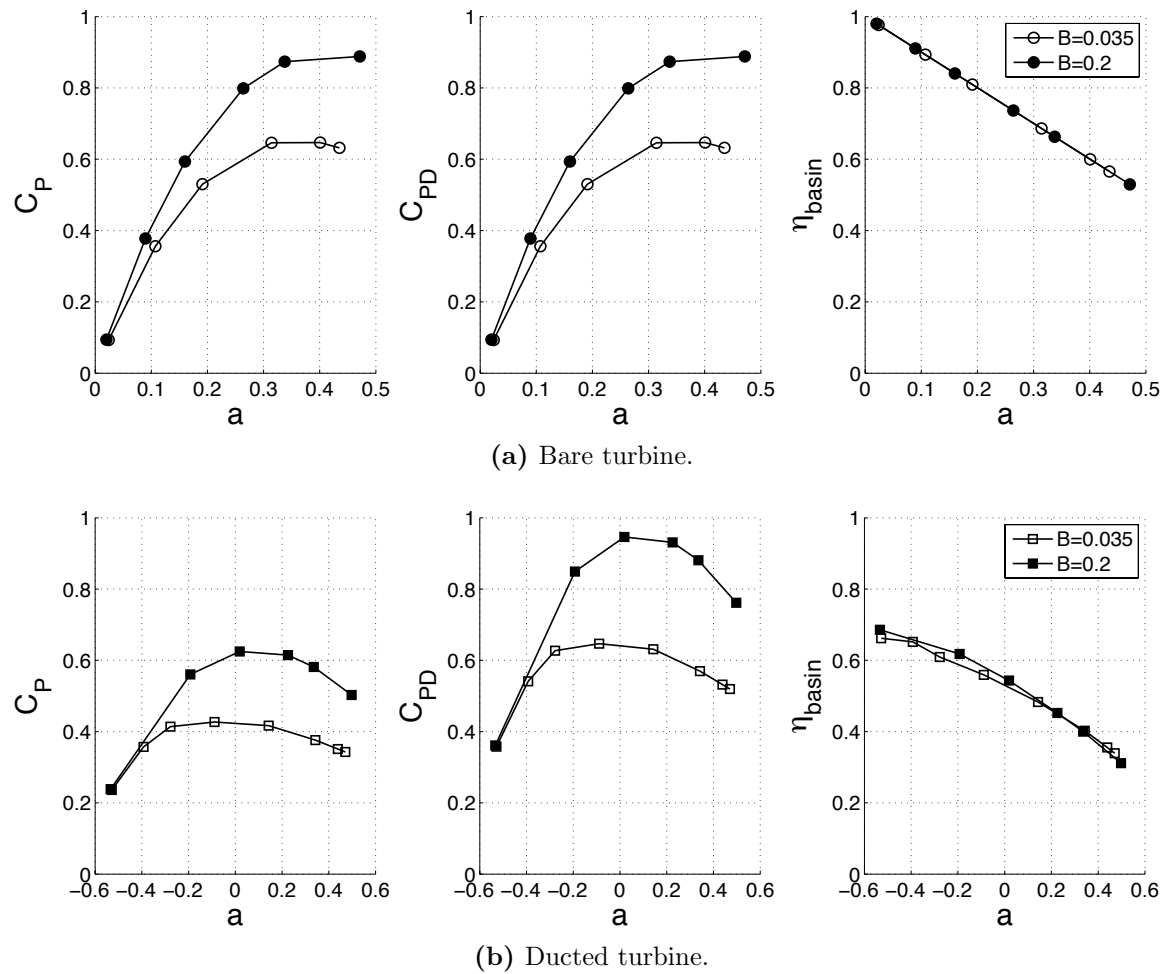


Figure 4.23: Performance of the bare and ducted turbines for low and high flow blockage.

First, the performance in terms of the power coefficient, C_P , is considered, given in the left hand plots of figure 4.23. In figure 4.23b it is seen that for the low blockage case the power coefficient of the ducted turbine takes a maximum value of $C_P = 0.42$ at $a = -0.1$, which is considerably less than that achieved for the bare turbine, $C_P = 0.63$, at the same blockage ratio, $B = 0.035$, as presented in figure 4.23a. The maximum power for the ducted turbine occurs when the flow is fully separated, at $C_{T,loc} = 0.5$ and $C_T = 0.4$, see figure 4.20c. At the maximum power point the significant external flow separation leads to an increase in the effective frontal cross section, and hence effective blockage, presented by the ducted turbine, with resultant increase in power relative to lesser separated cases. However, further increasing the disc thrust, and hence separation-enhanced effective blockage, leads to a reduction in mass flux through the turbine that offsets the performance improvement arising from the separation. Note, that the speed-up effect through the duct is evident in the negative induction factor which can be observed for low to medium disc thrust levels.

Figure 4.23 further presents the resulting power coefficients for the increased blockage ratio of $B = 0.2$, for both the bare turbine and the ducted turbine. In both cases power increases substantially due to the increase in blockage. Comparing the device at the maximum power point, the power coefficient is increased by 41 – 44% for both device types. Hence it may be concluded that the bare and ducted turbine are affected roughly to the same extent by an increase in blockage. Note that maximum power occurs at higher a for increased B .

While for the bare turbine the coefficient of power density is the same as the coefficient of power, for the ducted turbine the reference area of C_{PD} is significantly reduced compared to C_P , thus leading to substantial differences in the results. The reduction in reference area leads to an increase in C_{PD} compared to C_P as shown in figure 4.23b.

It can be seen that bare and ducted turbine exhibit a similar maximum power density at their respective maximum power points. Power density is affected by increased blockage to the same extent as the power coefficient. Hence C_{PD} of the bare and ducted turbine exhibit the same increase for high blockage as discussed for C_P (41 – 44%).

Considering the basin efficiency, η_{basin} , the bare turbine outperforms the ducted turbine, as can be seen in the right hand plots of figure 4.23. The results suggest that the ducted turbine is more wasteful of the underlying resource, dissipating more of the energy in the flow for a given level of useful energy extraction, compared to a bare turbine. For a fair comparison, the devices need to be analysed at their respective design points. For the induction factor leading to maximum power ($a_{\text{bare}} = 0.35$, $a_{\text{ducted}} = -0.1$) the penalty in basin efficiency for the ducted turbine is 25 % compared to the bare turbine.

Analysing the high blockage performance results in figure 4.23, it can be seen that while blockage has a substantial effect on the power, the basin efficiency remains almost unaffected by a change in blockage for both device types considered. However, as the maximum power point is shifted to higher values of a , the basin efficiency at the design point is decreased at higher blockage ratios.

4.6 Analysis of an open-centre ducted turbine in axial flow

This section investigates a generic open-centre ducted turbine (hereafter referred to as open-centre turbine), as illustrated in figure 4.24. The main features of this type of device are the bidirectional duct and central aperture. The outer duct wall of the chosen open-centre turbine design is parallel to the instream flow direction, thus inhibiting large scale flow separation previously observed for concave outer duct surfaces as presented in section 4.5. The interior of the duct cross-section is the shape of a circular segment yielding the same contraction ratio as the ducted turbine of $A_{\text{inlet}}/A_{\text{throat}} = 1.51$. The duct length is shorter than that of the ducted turbine in order to reflect industry proposals of this device type.

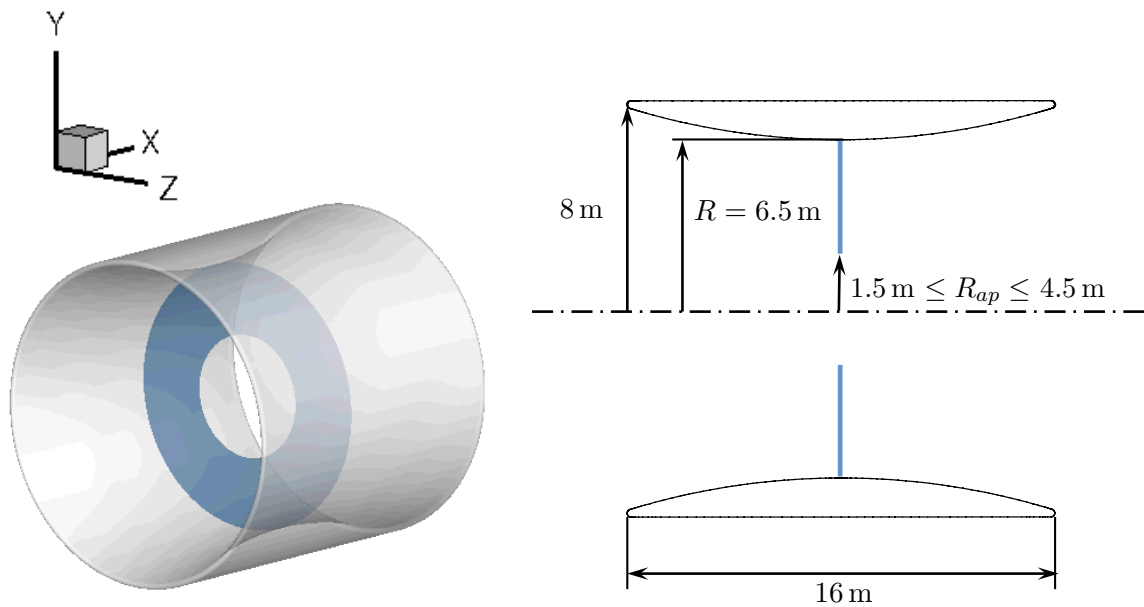


Figure 4.24: The open-centre turbine (3D view and cross-section).

In order to examine the influence of the central aperture of the turbine, the diameter of the aperture is varied, yielding four turbine configurations:

- OC-0: $R_{\text{ap}} = 0$ m, full disc
- OC-1.5: $R_{\text{ap}} = 1.5$ m
- OC-3.0: $R_{\text{ap}} = 3.0$ m
- OC-4.5: $R_{\text{ap}} = 4.5$ m

The configuration OC-0 essentially presents the analysis of a bidirectional ducted turbine of different duct geometry to that introduced in section 4.5. Also examined is the effect of varying disc thrust levels for one fixed aperture diameter, $R_{\text{ap}} = 3$ m. All domain dimensions are kept constant, yielding a blockage ratio of $B = 0.035$, based on the outer device diameter.

As for the ducted turbine, the grid consists of tetrahedral cells in the bulk of the domain and four prism layers on the duct surface. Figure 4.25 displays the mesh distribution around the duct and on the leading edge of the duct inlet. The details of the converged mesh are given in table 4.3.

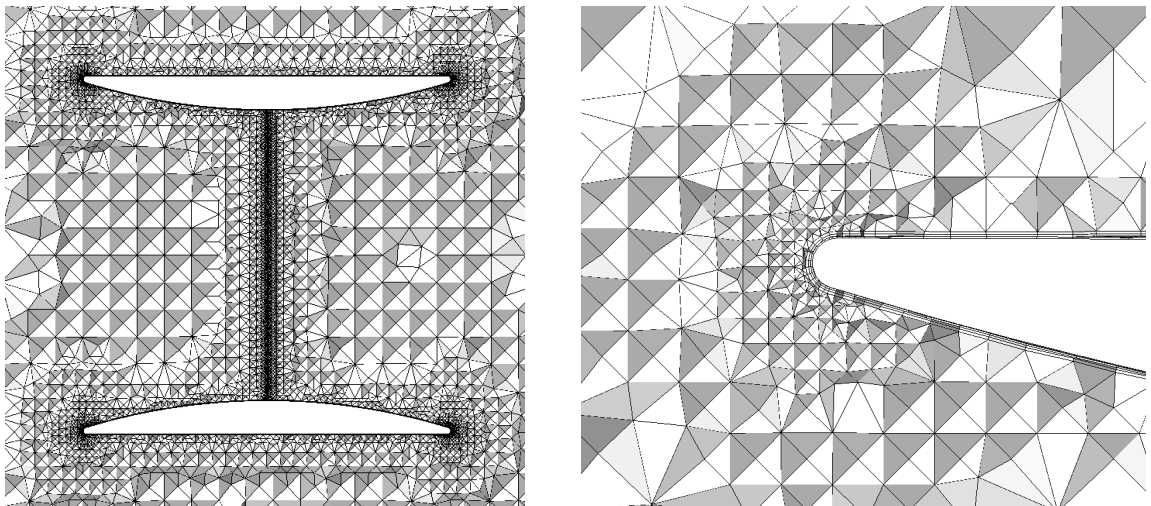


Figure 4.25: Mesh of the ducted turbine.

Table 4.3: Mesh resolution overview for the open-centre turbine

| | |
|---|------------------------|
| Resolution: | converged mesh |
| Cell count [n]: | 3.8×10^6 |
| Max. element dimension, far field [D] : | 0.94 |
| Max. element dimension, wake [D] : | 0.125 |
| Max. element dimension, disc [D] : | 0.006 |
| Max. element dimension, duct [D] : | 0.025 |
| y^+ on duct wall: | $15 \leq y^+ \leq 210$ |

4.6.1 Flow field of the open-centre turbine

First the variation of disc thrust is studied for an aperture diameter of $R_{\text{ap}} = 3$. Figure 4.26 presents the results for this size of aperture for four disc thrust levels, from low disc thrust, figure 4.26a, to high disc thrust, figure 4.26d. For low disc thrust, virtually no widening of the streamtube is observed, whereas a velocity increase through the duct interior is visible. As the turbine ring poses very little resistance to the flow, the pressure jump across the turbine ring is small and the impact of the aperture on the flow negligible.

Moving to medium disc thrust, see figures 4.26b and 4.26c, the effect of the aperture becomes visible. One can observe a distinct jet flow through the aperture, which is also visible in the near wake flow behind the device. At higher thrust levels on the turbine ring, figure 4.26d, the aperture effect becomes more pronounced. Further the streamtube widens leading to higher angles of attack on the duct inlet. Though the duct shape at the inlet seems to reduce the pressure gradient around the leading edge, the flow still eventually separates around the thickened inlet lip.

The effect of aperture size on the flow field is investigated by comparing each configuration at the respective maximum power points, thus figure 4.27c corresponds to figure 4.26c. When gradually moving from a full disc to an aperture of up to $R_{\text{ap}} = 4.5$ m (figure 4.27a to 4.27d) it can be seen that a jet flow develops through the

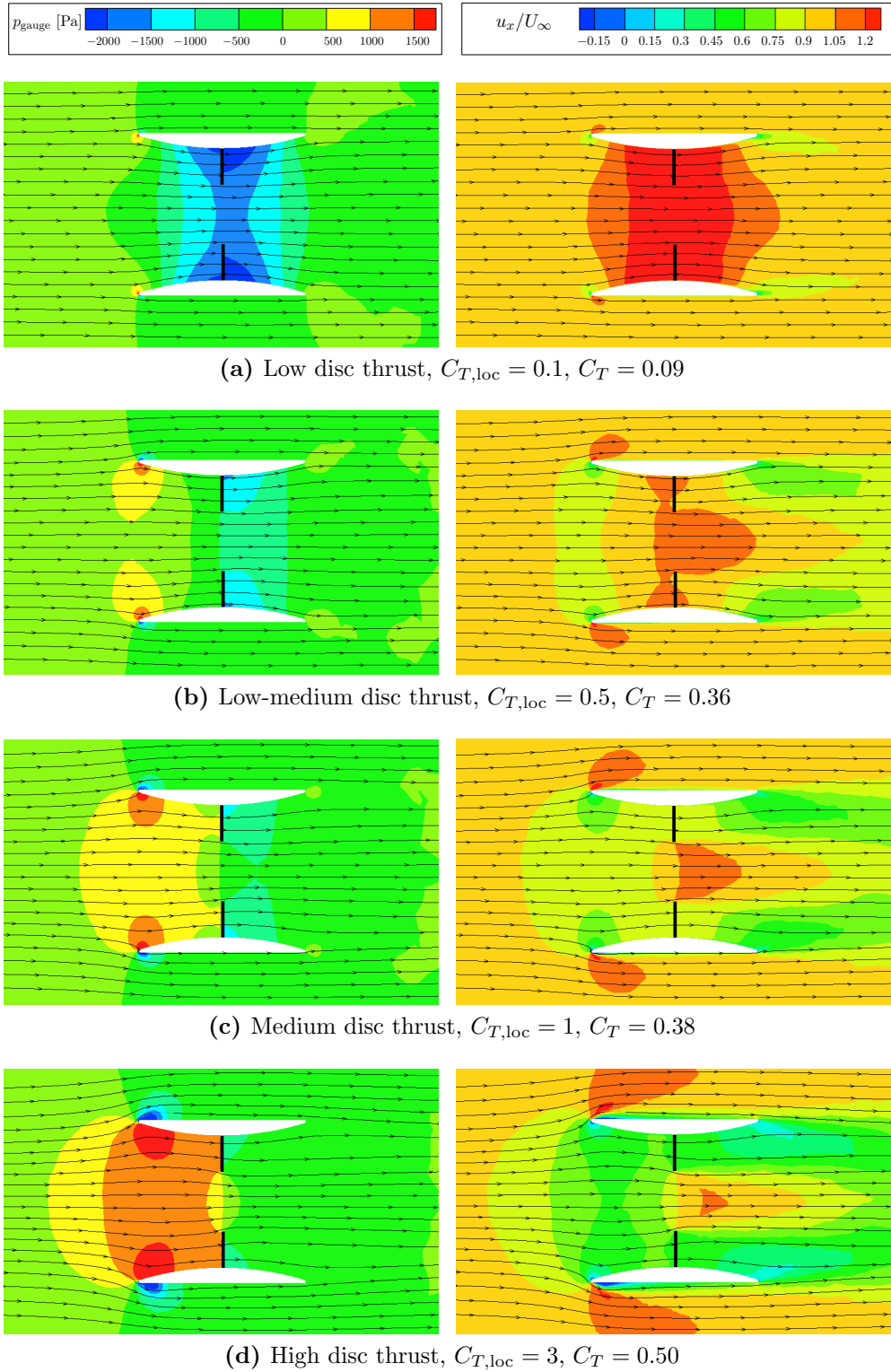


Figure 4.26: Contour plots of pressure and velocity distribution for open-centre turbine with an aperture of $R_{ap} = 3$ m, at various turbine thrust settings.

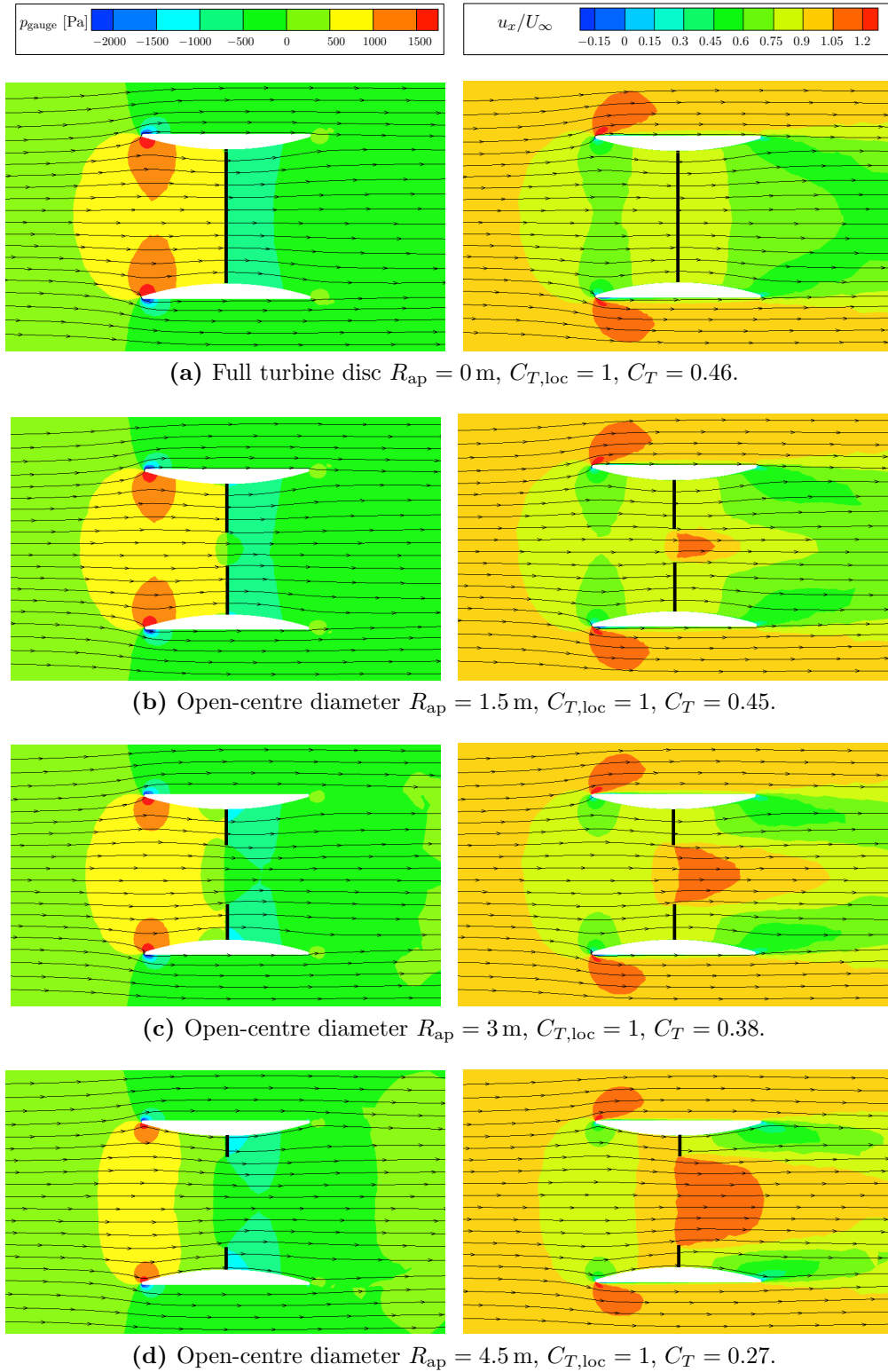
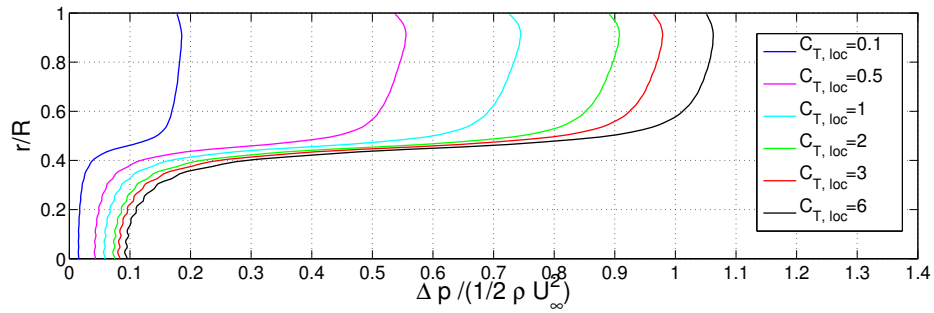
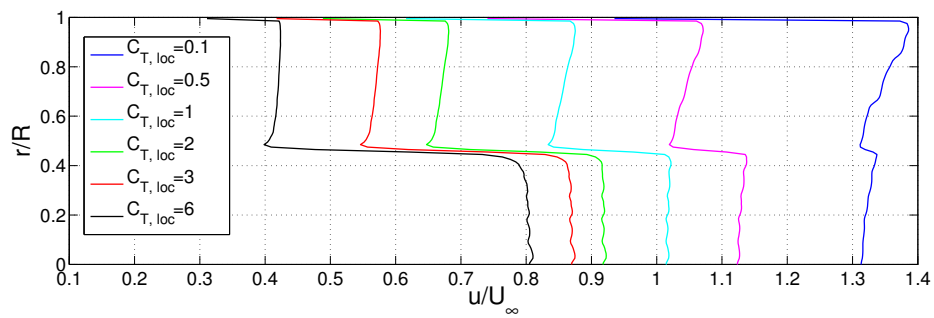


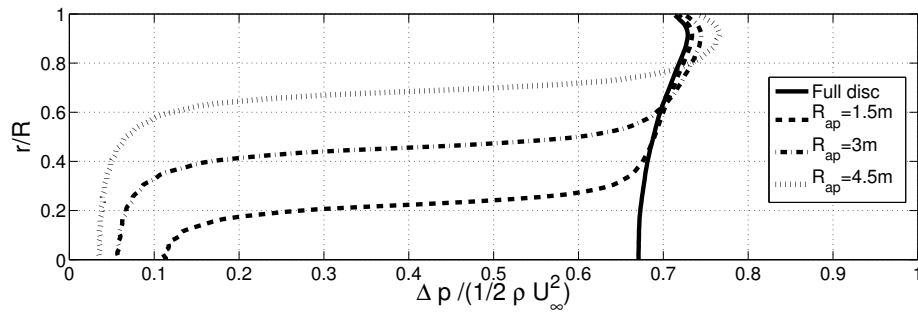
Figure 4.27: Contour plots of pressure and velocity distribution for open-centre turbine for $1.5 \text{ m} \leq R_{ap} \leq 4.5 \text{ m}$. All contours are taken at the device maximum power point, which uniformly corresponds to $C_{T,loc} = 1.0$.



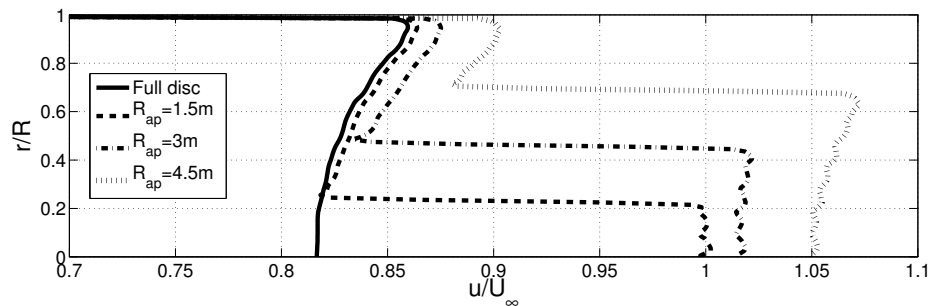
(a) Pressure jump profiles for $R_{ap} = 3$ m for varying thrust setting.



(b) Velocity profiles for $R_{ap} = 3$ m for varying thrust setting.



(c) Pressure jump profiles for varying aperture at the maximum power point.



(d) Velocity profiles for varying aperture at the maximum power point.

Figure 4.28: Velocity and pressure jump profiles plotted against the radial position (as a fraction of disc radius, R) for the open-centre turbine.

aperture of the turbine. Further, the velocity in this jet increases with aperture size, as does total mass flux through the turbine, as indicated by the modest reduction in the external flow speed.

The subsequent graphs focus on the flow field at the turbine plane. Figure 4.28 examines the pressure drop across the turbine disc and the velocity at the disc, as a function of radial position. Figures 4.28a and 4.28b present the results for one particular aperture diameter ($R_{\text{ap}} = 3\text{ m}$) for various thrust settings. As expected by the definition of the porous disc approach, we observe an increasing pressure drop across the turbine disc as $C_{T,\text{loc}}$ is increased. This is accompanied by a reduction in the velocity through the turbine disc annulus and also, to a lesser extent, by a reduction in the central jet velocity. Hence, as Δp increases, a step in streamwise velocity develops between the turbine annulus and the central jet flow.

In figures 4.28c and 4.28d the results for the maximum power point ($C_{T,\text{loc}} = 1$) are presented for the four open-centre turbine configurations considered. It can be seen that both the pressure jump and velocity through the turbine annulus increase as the central aperture is enlarged. This implies that power generated per unit turbine annulus area (i.e. power density) increases with increasing aperture size, results of which are presented in section 4.6.3.

The final part of the flow field analysis presents the transversal pressure profile of the open-centre turbine ($R_{\text{ap}} = 3\text{ m}$) for a disc thrust of $C_{T,\text{loc}} = 2.0$, see figure 4.29. The total thrust for the case presented here corresponds to a total thrust of $C_{T,\text{tot}} = 0.63$, which is moderately lower than for both ducted and bare devices presented in figures 4.21 and 4.12 respectively.

The resulting transversal profiles presented for the open-centre turbine show a distinctly different flow field from that observed for the bare and ducted devices in the immediate wake of the device. In particular the first downstream station (1D) clearly

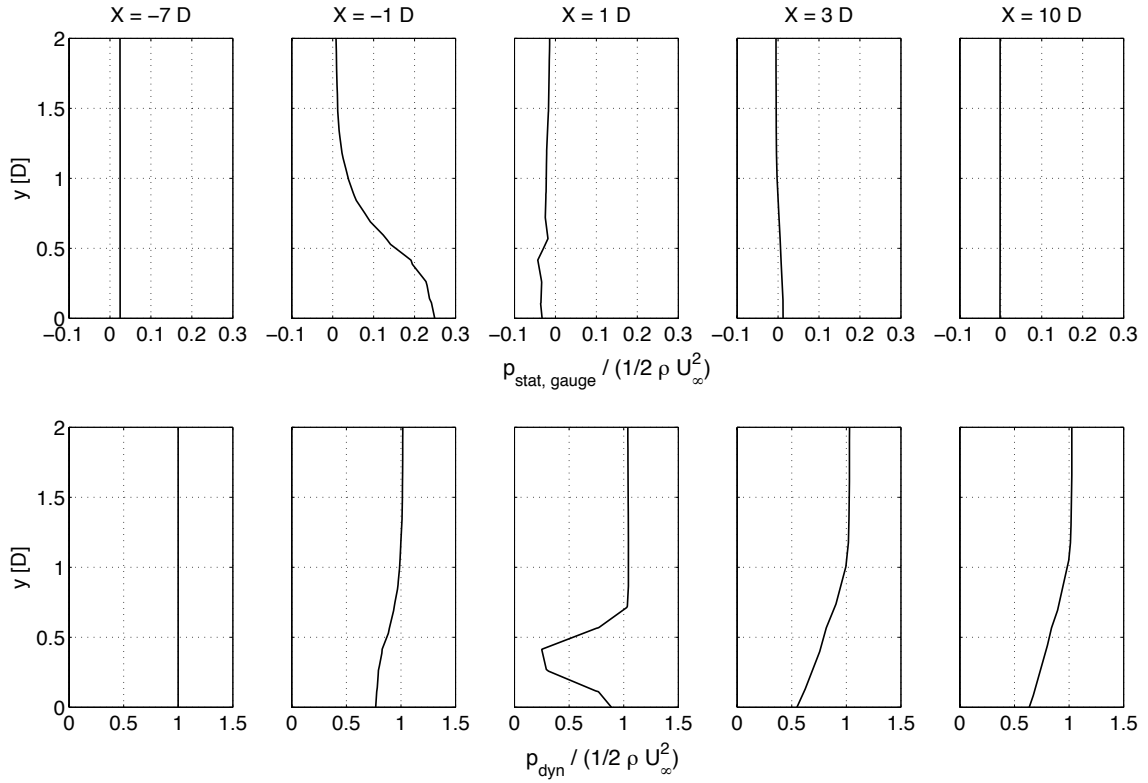


Figure 4.29: Transversal pressure profiles for the open-centre turbine of medium aperture ($R_{\text{ap}} = 3\text{m}$) at five locations upstream and downstream of the turbine. $C_{T,\text{loc}} = 2.0$, $C_T = 0.47$, $C_{T,\text{tot}} = 0.63$.

shows the central jet, whereas this jet is not visible further downstream ($\geq 3D$). The shape of the dynamic pressure profile at $x \geq 3D$ is distinctly different to that of the bare and ducted turbines, exhibiting a significantly faster wake recovery attributed to the internal shear layer.

4.6.2 Thrust of the open-centre turbine

Figure 4.30 presents the thrust coefficient for both turbine annulus and duct. For this analysis only one turbine configuration is investigated, the case of medium aperture, $R_{\text{ap}} = 3\text{m}$. For very low induction factors, thrust on duct and disc are of similar value. With increasing induction factor, the disc thrust, $C_{T,\text{turbine}}$, increases roughly linearly. While there is a small overall increase, the thrust on the duct, $C_{T,\text{duct}}$,

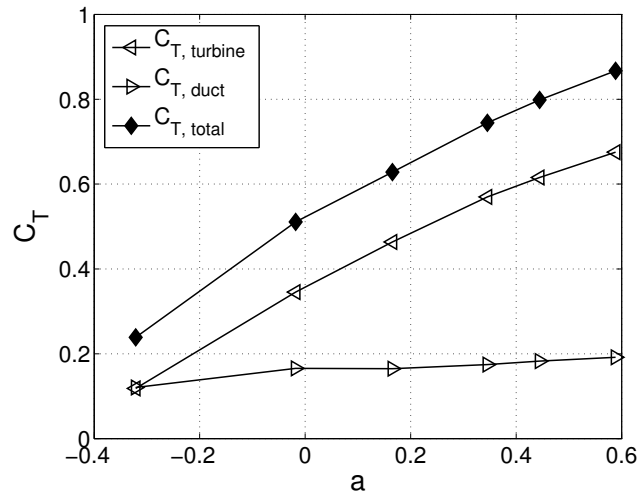


Figure 4.30: Thrust coefficients for the open-centre turbine, $R_{ap} = 3$ m.

remains roughly constant over a broad range of induction factors. At high induction factors the thrust on the duct is therefore significantly smaller than the disc thrust. The flat thrust curve of the duct can be attributed to the streamlined duct exterior which leads to minimal separation on the duct surface as presented in section 4.6.1. In contrast, as seen for figure 4.22, formation of large scale separation on the duct exterior leads to significantly higher value of thrust. The resulting total device thrust at design point ($a = -0.02$) is $C_{T,tot} = 0.53$, which is significantly lower than that of the bare or ducted device.

4.6.3 Performance of the open-centre turbine

Figure 4.31 presents the performance results of the open-centre turbine at various apertures. First the power coefficient of the configuration OC-0 (without aperture) is considered and compared to the bare turbine (figure 4.23a). The power coefficient of configuration OC-0 takes a maximum value of $C_P = 0.39$ at $a = 0.15$, which is considerably less than that for the bare turbine, $C_P = 0.63$, at the same blockage ratio, $B = 0.035$. This performance result is similar to that achieved by the ducted turbine presented in section 4.5, though considerable differences in duct shape exist.

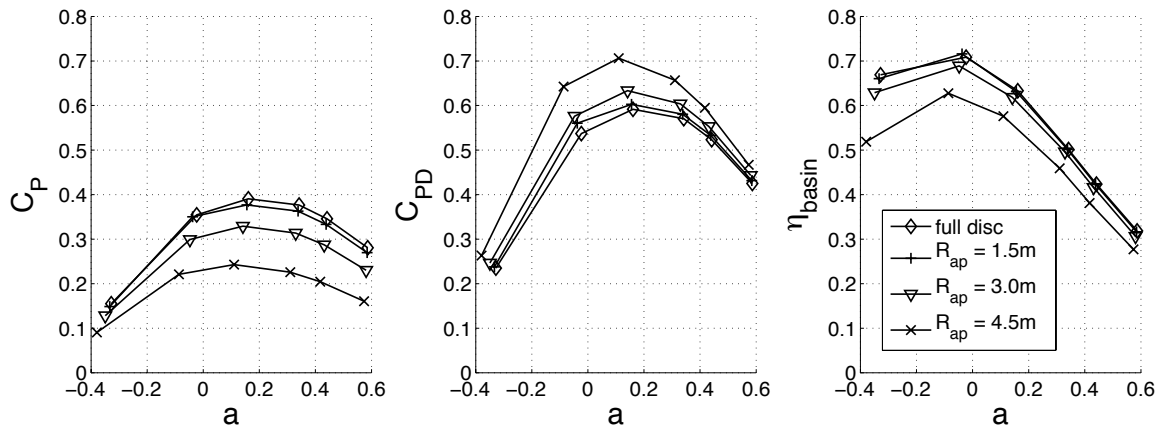


Figure 4.31: Performance of open-centre turbines for various apertures.

As the aperture diameter is increased, the maximum power coefficient of the configuration drops dramatically. This decrease occurs with increasing aperture, due to the steep drop in turbine annulus area. Despite the increase in power density that occurs as the aperture is increased, the overall area from which power can be extracted from the flow is significantly reduced.

The middle plot in figure 4.31 presents the results for power density. Though the power density of configuration OC-0 is significantly higher than the power, it does not reach the level of power density of the bare turbine. An increase in aperture leads to a visible increase in power density, which is in line with the flow field analysis presented in figure 4.28. As the aperture is increased to $R_{ap} = 4.5$ m, a power density higher than that of the bare turbine is achieved.

A moderate increase in the maximum basin efficiency is observed for small aperture diameters (OC-1.5), compared to the full disc configuration (OC-0). However, overall the basin efficiency for all of the open-centre turbine configurations, including OC-0, are of similar magnitude and remain below those of the bare turbine. Comparing the basin efficiency at the maximum power points of the bare ($\eta_{basin} = 0.71$) and open-centre turbine ($\eta_{basin} = 0.59$), a difference of about 12% can be observed.

4.7 Yawed inflow

Developers of ducted tidal turbines argue that the duct should provide a flow straightening effect allowing modest yaw angles to be readily accommodated. The following section presents a comparison of the bare, ducted and open-centre turbine performances in yawed inflow.

4.7.1 Model setup for yawed inflow

To study yaw effects there are two options of how to conduct the simulation. One option is to yaw the device within the simulation domain. A second option is to yaw the inflow and keep domain and the device fixed in position. The benefit of yawing the flow instead of the device is that only one mesh is needed to test various yaw angles. The only change to the mesh presented in the previous sections is the need for periodic boundaries at the side walls of the domain, see figure 4.32, and a broader application of mesh densities in the wake.

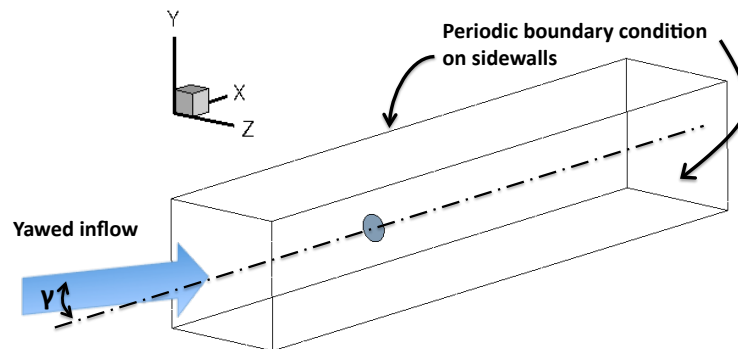


Figure 4.32: The simulation domain with yawed inflow.

The two approaches for achieving yawed inflow do not represent the same problem. Due to the periodic boundary condition the model represents an array of turbines. When yawing the device (or the domain, which is the same) the simulation represents a row of yawed devices, aligned on a line perpendicular to the flow. In contrast,

yawing the inflow simulates a staggered row of yawed devices. Since the latter is a more accurate representation of a likely turbine configuration, this is the approach employed in the following sections. In terms of nomenclature, the yaw angle is given as γ and the axis of inflow direction as ξ .

4.7.2 Comparison of steady and unsteady simulations

Large flow separation regions are expected for the ducted and open-centre turbines when placed in yawed flow. Therefore a comparison of steady and unsteady simulations was performed for the test case of the ducted turbine. The operating points chosen were $\gamma = 20^\circ$ and $C_{T,loc} = 2.0$, providing high degrees of separation and thrust. The results for a time-step interval of $\Delta t = 0.01s$ are presented (though larger time-steps were also analysed).

Figure 4.33 presents the time history of the thrust on the duct in ξ -direction, normalised by the converged result. Convergence was reached after approximately 400 s. No fluctuations of the thrust force are visible in the converged solution.

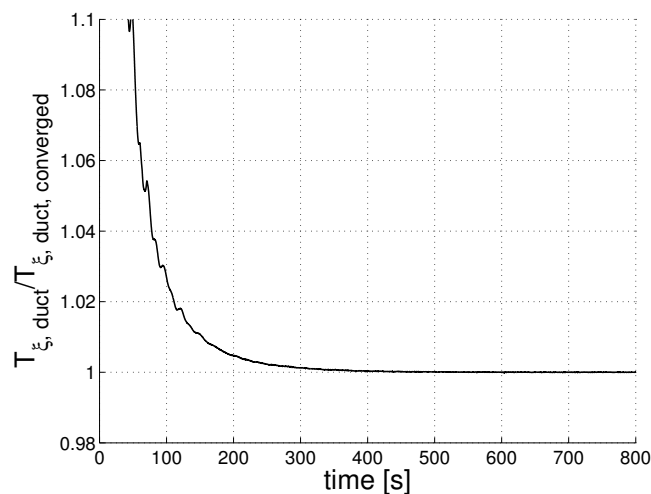


Figure 4.33: Time convergence of duct thrust.

The converged unsteady solution was then compared to the converged steady solution by regarding the flow field, the thrust on the duct, and the power extracted. Figure 4.34 presents the transversal flow field by presenting the dynamic pressure at various upstream and downstream locations. As no fluctuations were present for the unsteady case, the unsteady result did not require time averaging. Comparing the two results, no variations between the simulations are observed in the flow field.

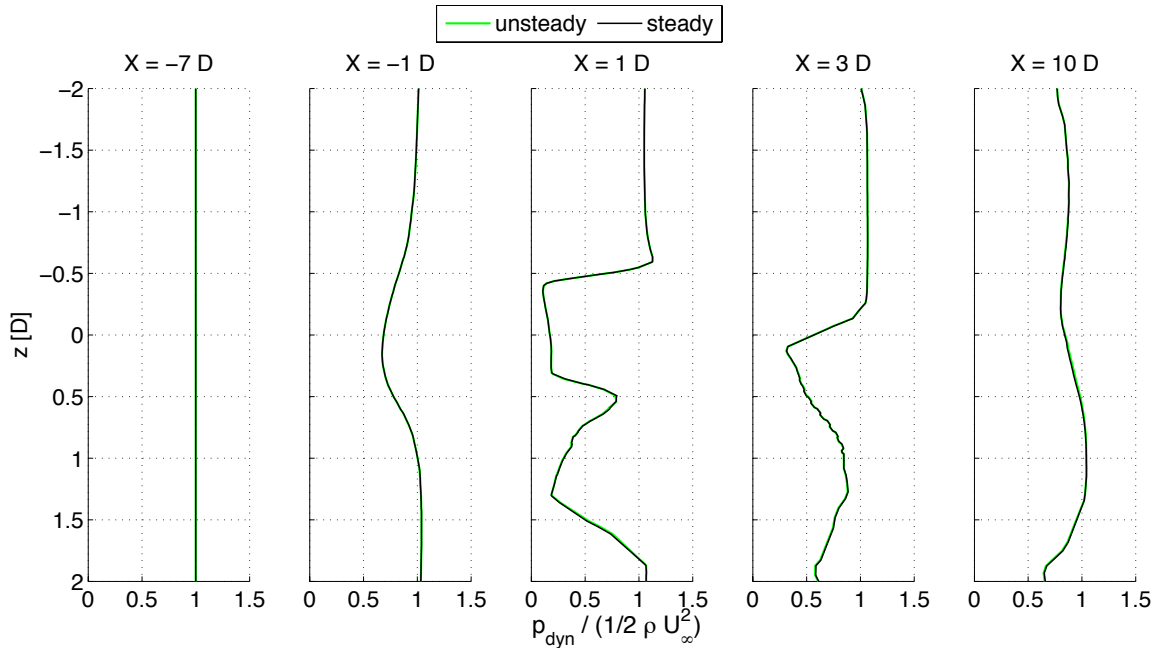


Figure 4.34: Transversal profiles of dynamic pressure for unsteady and steady simulations. Ducted turbine, $\gamma = 20^\circ$, $C_{T,\text{loc}} = 2.0$.

Comparing the thrust on the duct in ξ -direction an error of $\epsilon(T_{\xi,\text{duct}}) = 0.25\%$ was found for the steady simulation. In terms of power, the error was $\epsilon(C_P) < 0.1\%$. Therefore it was concluded that steady simulations were sufficiently capturing the flow effects in the yawed flow field.

4.7.3 Flow field analysis in yawed inflow

Using the approach of yawing the inflow, slices of the horizontal midplane in top view are presented, for all three device types, see figure 4.35. For the open-centre

turbine an aperture of $R_{\text{ap}} = 3 \text{ m}$ was selected. The yaw angle in this figure is $\gamma = 20^\circ$, though a range of yaw angles has been tested and analysed. The contour lines present the magnitude of relative velocity in inflow direction, ξ , and are overlaid with streamlines.

As can be seen in figure 4.35a the bare turbine creates little disturbance to the oncoming flow and behaves similarly to the bare turbine in axial flow. Naturally the wake develops with the flow direction, so the wake is now located at an angle to the turbine disc. However, a considerable difference to axial flow can be seen for both the ducted and open-centre turbines in figure 4.35b and 4.35c. The flow around and through the devices is no longer axisymmetric, thus while part of the flow stays attached to the duct exterior, some areas are now highly separated, creating large areas of separation that extend well past the duct trailing edge. For both devices, part of the duct inlet is now aligned with the flow in such a way, that it acts as a cambered aerfoil, accelerating and turning the incoming flow towards the turbine disc.

A change in the effective projected frontal area is observed, marked by the red lines in figure 4.35. While for the bare turbine the projected frontal area is smaller than the disc area, the projected frontal area of the ducted and the open-centre turbines is increased compared to the device outer diameter.

Note that due to the periodic boundary condition on the domain walls, the wake leaves and re-enters the domain on the opposite side. As figure 4.35 does not present the full domain cross-section, this effect is only partially visible here. While the re-entering wake is visible for the bare turbine in figure 4.35a, the straightening effect of the duct leads to a moderate straightening of the wake for both the ducted and open-centre turbines. Therefore, figures 4.35b and 4.35c do not capture the wake, which only re-enters the domain further downstream.

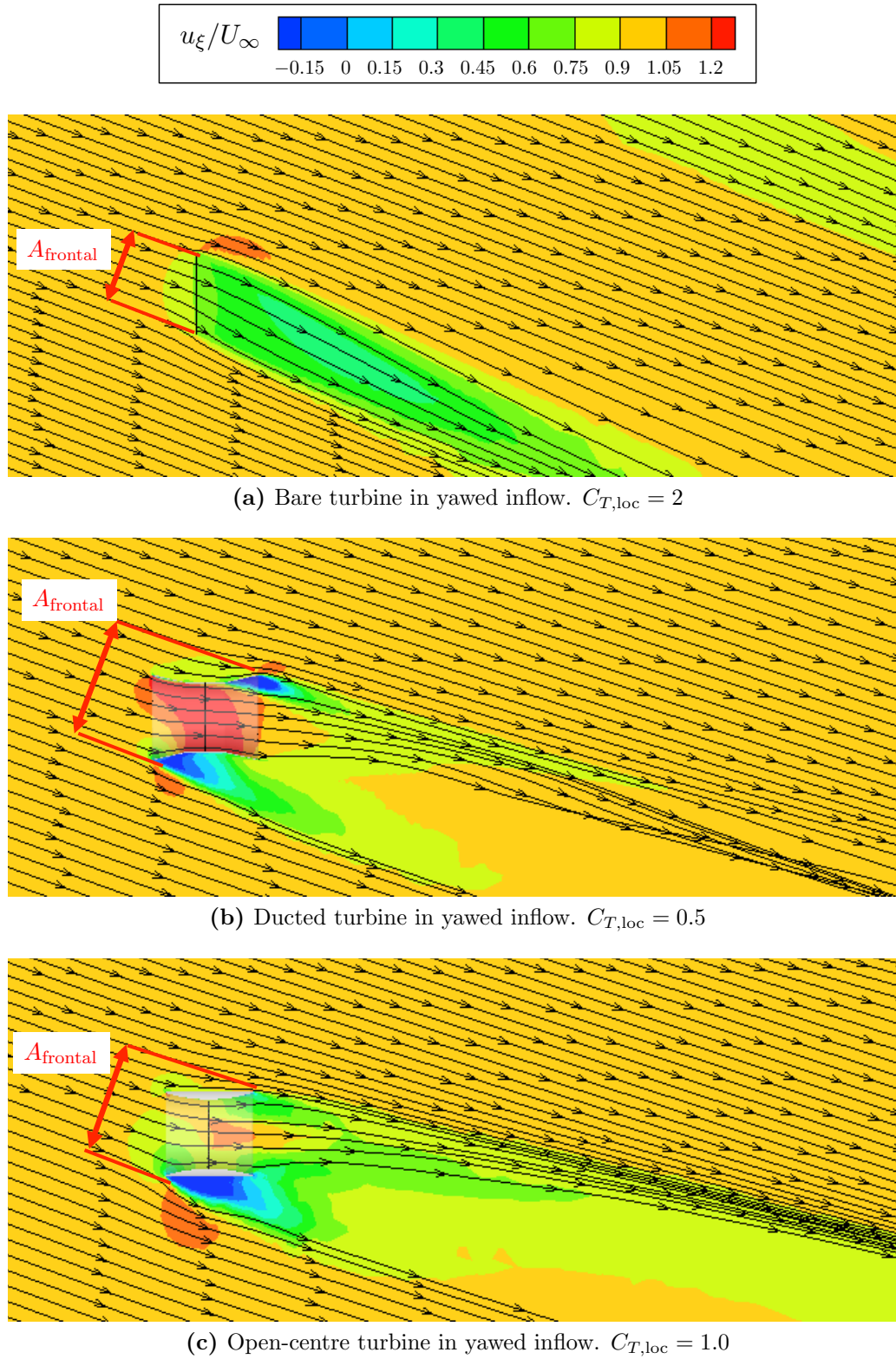
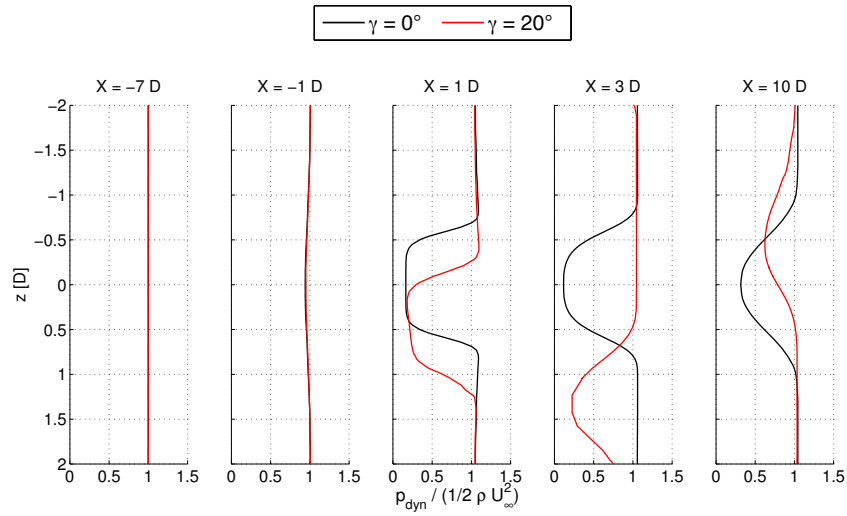


Figure 4.35: Streamlines and contour plots of velocity distribution in yawed flow conditions.

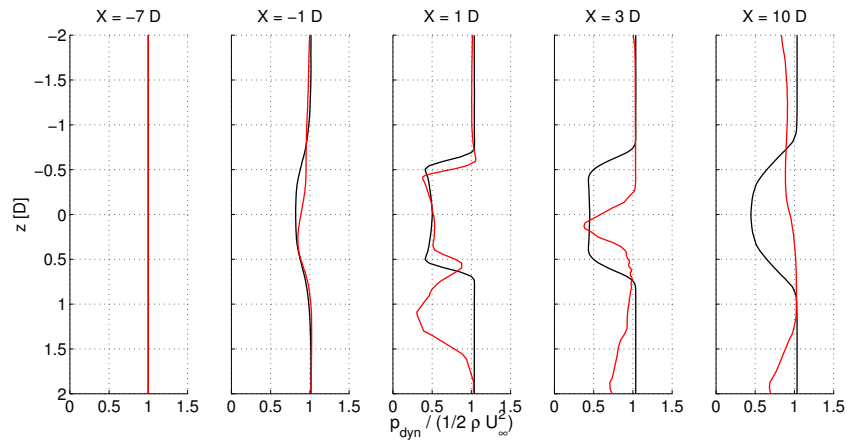
Analogous to the flow field analysis for axial flow, the dynamic pressure of the flow field is examined by plotting the transversal pressure profiles. Figure 4.36a presents the dynamic pressure profiles for the bare turbine, figure 4.36b for the ducted turbine, and figure 4.36c for the open-centre turbine. For comparison, the profiles for axial flow are added in black, while the results for yawed flow, taken at $\gamma = 20^\circ$ yaw, are marked in red. All cases are taken at the respective design point. Note that the orientation of the z -axis is plotted in reverse, in order to coincide with the the top view of the flow field plots in figure 4.35.

Comparing the axial and yawed inflow cases of the bare turbine in figure 4.36a, a similar development of the pressure profiles in both yawed and axial flow may be observed for the bare turbine. The wake develops along the direction of the inflow which can be seen from the downstream pressure profiles of the yawed flow case. There is a significant difference in velocity deficit at 10D downstream (i.e. the last transversal profile in the plot) with the yawed case showing a higher recovery of the wake. However, this can be attributed to two sources. The wake travels with the direction of the flow - for a yaw angle of $\gamma = 20^\circ$ the downstream distance at 10D in x -direction is actually 10.6D in inflow, ξ -direction. Further, due to the bare turbine posing less thrust on the flow (see next two subsections) the initial wake deficit is smaller than for the axial flow case.

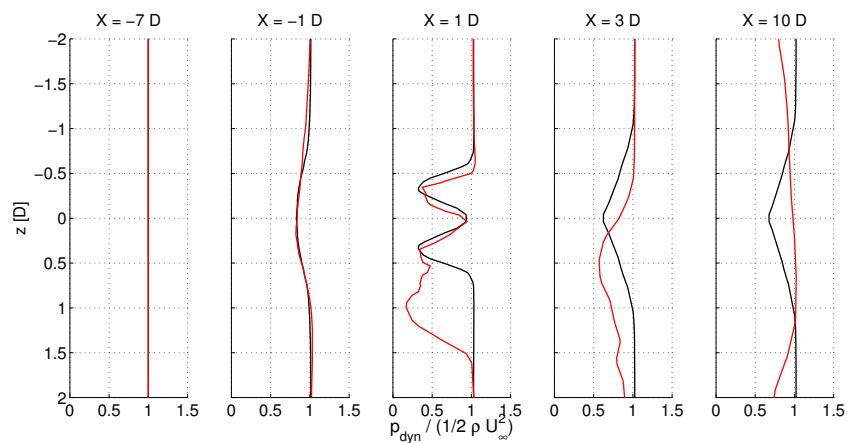
Figure 4.36b presents the ducted turbine in yawed and axial inflow. The first feature evident from the yawed inflow case, is the asymmetric nature of the wake flow, which is even more pronounced for the ducted turbine. The large separation zone in figure 4.35 is clearly visible in the transversal pressure profile (1D) as a second wake dip next to that of the duct itself. The two wake dips can still be seen further downstream (3D) with the wake of the interior duct flow well-aligned with the duct and the wake of the separation region propagating with the flow direction. Somewhat surprising is the



(a) Bare turbine. $C_{T,loc} = 2.0$.



(b) Ducted turbine. $C_{T,loc} = 0.5$.



(c) Open-centre turbine. $C_{T,loc} = 1.0$.

Figure 4.36: Transversal dynamic pressure profiles for axial and yawed inflow, taken at five upstream and downstream locations.

wake profile in yawed flow when examined further downstream (10D). It appears that the wake recovers much quicker for the yawed case than for the axial flow case. However, the wake deficit is more distributed over the domain cross-section in the yawed inflow case, due to the two aforementioned wake dips. When integrating the energy flux across over the domain cross-sectional area, it becomes evident that the ducted device extracts more energy from the flow when placed in yawed inflow compared to axial flow, see section 4.7.5.

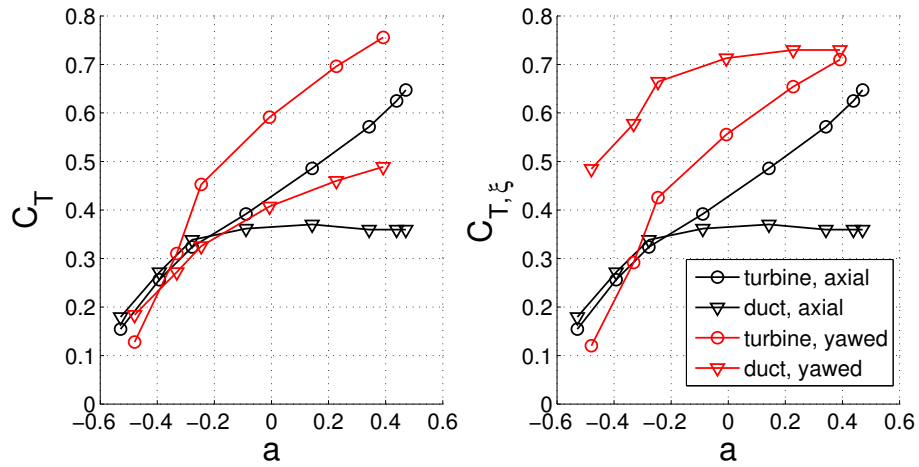
Figure 4.36c presents the results for the open-centre turbine. For yawed inflow, the open-centre turbine exhibits a similar transversal flow field to that of the ducted turbine. The main differences between the two are visible at 1D downstream, where for the open-centre turbine the central jet flow is visible, and at 3D, where for the open-centre turbine the two wake dips have already merged.

4.7.4 Thrust analysis in yawed inflow

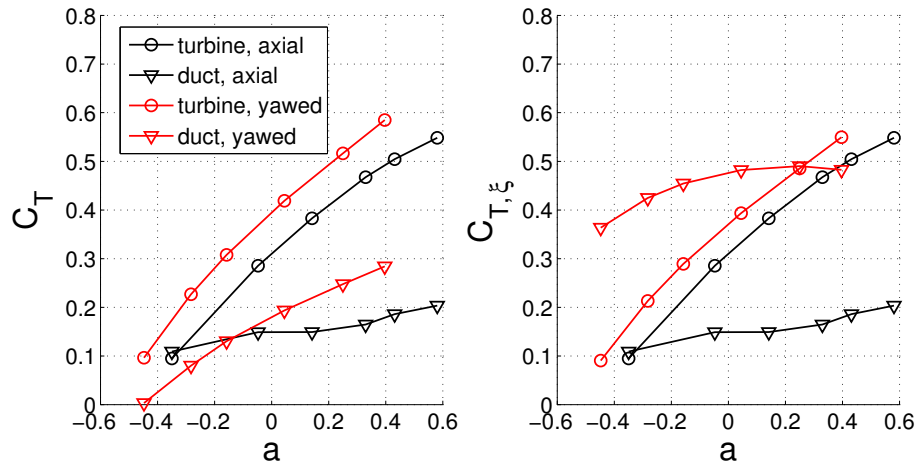
As for the case of axial inflow, the thrust on the device components, turbine disc and duct, are extracted and analysed for both the ducted and open-centre turbine. Figure 4.37 presents the results of the thrust coefficients in x -direction (left plots) and in inflow direction, ξ -direction (right plots) for the yaw angle of $\gamma = 20^\circ$. Note that, for the axial flow case x - and ξ -directions are the same. In order to compare the results quantitatively, the same denominator is used to non-dimensionalise all thrust coefficients,

$$C_{T,\text{component}} = \frac{F_{x,\text{component}}}{1/2 \rho U_\infty^2 A_{\text{ref}}}, \quad (4.27)$$

$$C_{T,\xi,\text{component}} = \frac{F_{\xi,\text{component}}}{1/2 \rho U_\infty^2 A_{\text{ref}}}, \quad (4.28)$$



(a) Thrust coefficients for the ducted turbine.



(b) Thrust coefficients for the open-centre turbine.

Figure 4.37: Thrust coefficients in yawed flow ($\gamma = 20^\circ$). Coefficients are presented for axial thrust (aligned with turbine axis) and thrust in ξ -direction.

where $A_{\text{ref}} = A_{\text{device}}$. Alternative approaches of defining the thrust coefficients could be employed, i.e. using free-stream velocity component in x - and ξ -directions, or normalising by the respective projected frontal area.

First the axial thrust coefficient of the ducted turbine is analysed. For low induction factors, duct and turbine thrust in yawed flow are of a similar order of magnitude. In contrast to the axial flow case, the thrust on the duct in yaw continues to increase steadily with increasing induction factor and does not reach a maximum. This is due

to the fact that for the yawed flow case the flow does not separate in a symmetric form around the duct and full separation around the outside of the duct is not reached. The thrust on the disc is increased for the yawed inflow case, which can be attributed to an increased mass flow through the turbine disc. This increase in mass flow in turn is caused by both the ducted device posing a higher effective blockage to the incoming flow when operated in yaw, as well as the alignment of the inlet section.

As expected from the flow field in figure 4.35b, the main thrust force on the duct does not act in axial direction, which is clearly visible when regarding $C_{T,\xi}$ for the ducted turbine. The thrust acting on the duct in inflow direction is roughly double that of the axial flow case. As the thrust level in inflow direction is the defining parameter of the overall energy extraction of the flow, this high level of thrust has a negative impact on the basin efficiency of the ducted turbine in yawed inflow (see section 4.7.5).

For the open-centre turbine a similar trend may be observed. In yawed flow the axial thrust on the duct increases more rapidly with increased induction factors, while the disc thrust is moderately higher than for axial flow. When analysed in ξ -direction the thrust on the duct is almost three times higher than for the axial flow case. This may be attributed to the design of this particular duct, which poses little thrust in the axial direction due to a hydrodynamically efficient duct shape.

4.7.5 Performance analysis in yawed inflow

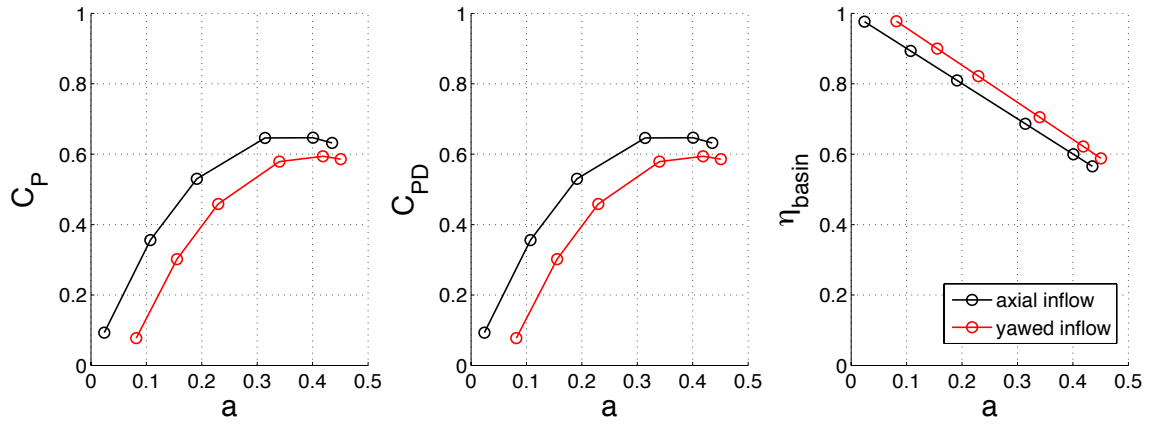
In the following the results for a inflow yaw angle of $\gamma = 20^\circ$ are presented. When analysing the performance of devices in yawed inflow, several effects have to be taken into account: change in projected frontal area, change in effective blockage, and flow straightening. All of these effects will be discussed in this section.

As has been shown in section 4.4.4 the choice of reference area can significantly alter the apparent performance results of a device. One option is to use the frontal area of the device, as employed for axial flow analysis, or alternatively to use the projected frontal area perpendicular to the flow. For axial flow both of these areas are the same, but this is not the case for yawed inflow. When using the projected frontal area perpendicular to the flow as reference, the reference area of the bare disc is reduced and that of the ducted device increased, thus significantly affecting the results. First, the performance results are presented using the device frontal area based on axial flow and then the results using the projected frontal area perpendicular to the yawed inflow.

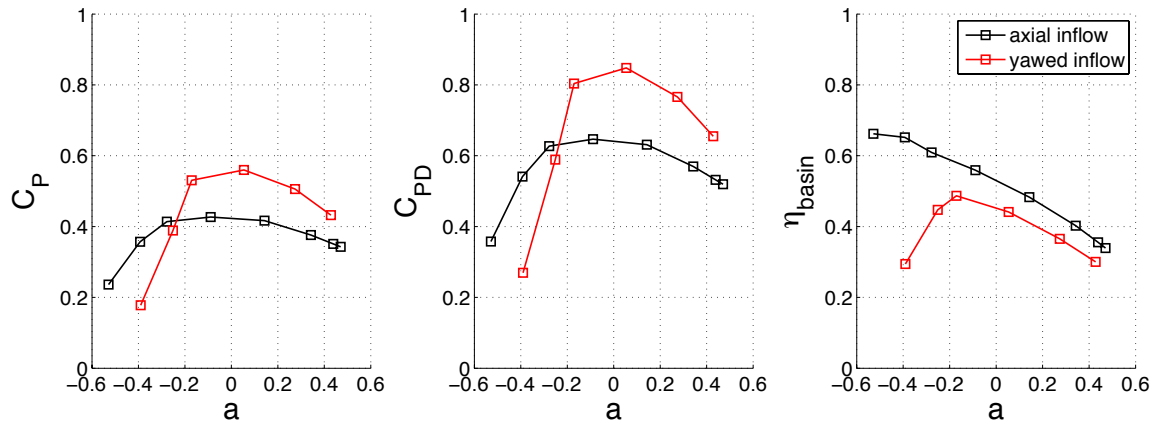
4.7.5.1 Performance based on device outer diameter

Figure 4.38 presents the performance of the yawed bare, ducted, and open-centre turbines and compares it to the results obtained for axial flow. The reference area used for the power coefficient is that of the device outer diameter, the same as applied to the axial flow performance analyses.

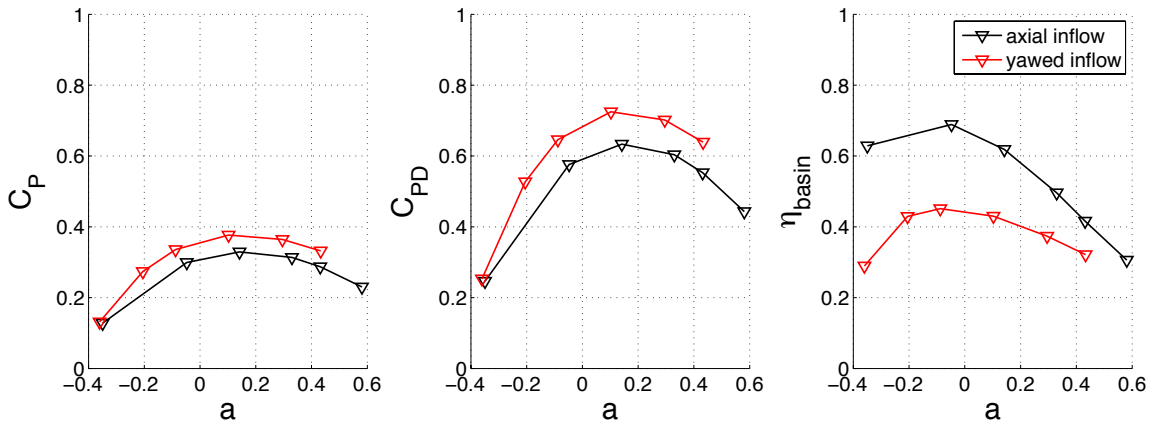
For the bare turbine a small reduction in power is observed when placed in yawed inflow conditions, while the ducted turbine shows a significant increase in power coefficient. This change is attributed mainly to a change in effective blockage as well as efficient flow-duct-inlet alignment for a portion of the duct, leading to flow acceleration. While the ducted turbine now poses a larger projected frontal area perpendicular to the flow and thus a higher effective blockage (see figure 4.35b), in this part of the analysis the same reference area as for the axial flow case is employed. The inverse is the case for the bare turbine - the projected frontal area is now smaller than the reference area used. The effect on the open-centre turbine is similar to that



(a) Performance of the bare turbine.



(b) Performance of the ducted turbine



(c) Performance of the open-centre turbine ($R_{\text{ap}} = 3\text{m}$)

Figure 4.38: Performance of bare, ducted and open-centre turbines for yawed and axial inflow. Based on the reference area of the device outer diameter.

of the ducted turbine, as it also poses a larger projected frontal area and presents a moderate increase in power coefficient for the given yaw angle of $\gamma = 20^\circ$.

The flow straightening effect, as often promoted by ducted device manufacturers, is indeed visible, see figure 4.35b. This flow straightening works to the advantage of both ducted and open-centre turbines, as the disc as modelled in this simulation setup (and rather similar to a real turbine) only extracts energy from flow perpendicular to the disc. Thus, while for the bare device less energy is available for extraction in yawed flow, the ducted and open-centre turbines recover from this reduction by aligning the flow perpendicular to the disc. Note that the maximum power increase due to yawed inflow was observed close to $\gamma = 20^\circ$, the yaw angle employed in all figures of this section.

As expected from the large separations visible on the ducts in figure 4.35b, the amount of energy removed from the domain is increased for the both ducted and open-centre devices in yawed inflow. This results in a substantial drop of basin efficiency compared to the axial flow case, as presented in the right hand plots of figure 4.38. At the same time, there is virtually no change in basin efficiency for the bare turbine in yawed flow.

4.7.5.2 Performance based on projected frontal area

Figure 4.39 shows the performance of the yawed bare, ducted, and open-centre turbines, using the projected frontal area perpendicular to the flow as the reference area. The use of the alternative reference area is denoted by “PFA” (projected frontal area) in $C_{P,PFA}$. Using this alternative reference area, essentially corrects for the change in effective blockage, which arises due to the geometry of the problem in yawed inflow.

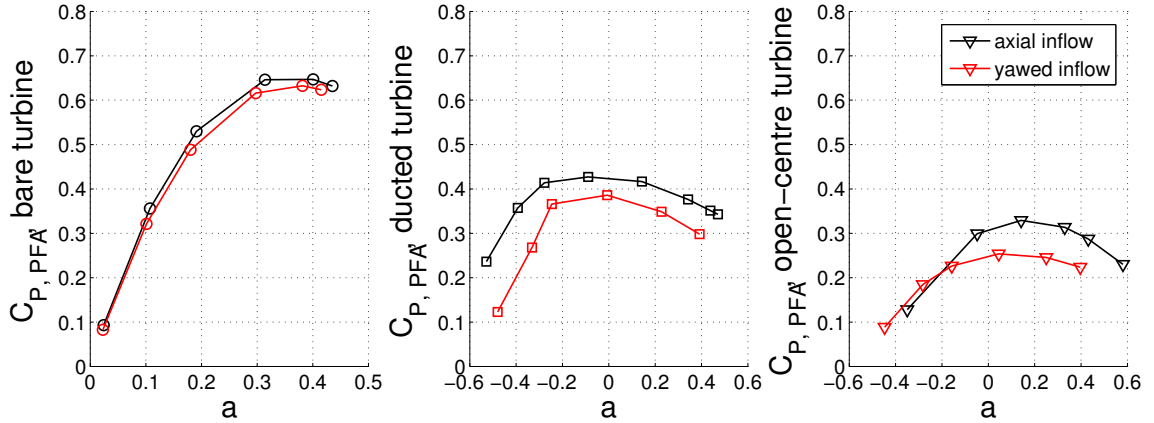


Figure 4.39: Alternative power coefficient ($C_{P,PFA}$) of bare, ducted and open-centre turbines for yawed and axial inflow. Yawed results noted in red. Based on the projected frontal area perpendicular to the flow as reference area.

When analysing the performance of the devices in yawed flow based on this alternative reference area, the results for power coefficient differ substantially from those presented in figure 4.38, see figure 4.39. Instead of a power increase, both ducted and open-centre turbines now exhibit a reduction in power. For the bare turbine, the power decrease for yawed flow, as seen in figure 4.38a, can be attributed to the reduction in area perpendicular to the flow. Thus, when based on this reduced reference area, the power decrease for yawed flow almost disappears and only marginal differences in terms of power coefficient remain.

4.7.5.3 Variation of yaw angle

Various yaw angles have been tested between $0^\circ < \gamma < 30^\circ$. The maximum increase in C_P for both ducted and open-centre devices in yaw is found close to $\gamma = 20^\circ$. Figure 4.40 presents the results of yaw variation for the bare and ducted turbines. The values of maximum power per device area, $C_{P,max}$, are presented here.

At the yaw angle of maximum power increase the duct manages to align the flow adequately while the frontal area of the yawed turbine provides a significant increase in blockage. When moving to higher yaw angles ($\gamma > 20^\circ$) the duct is not able to

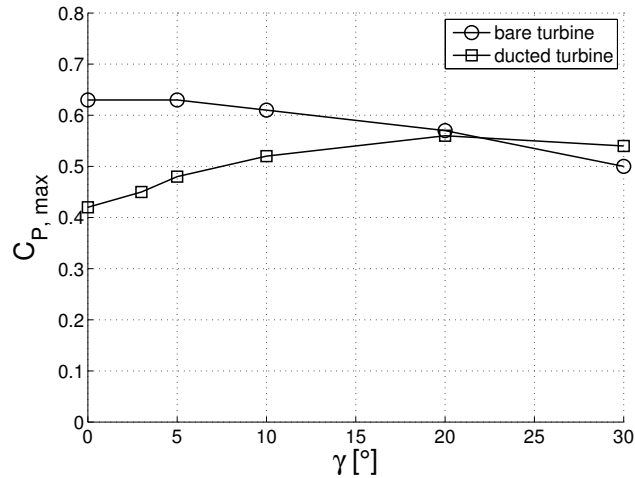


Figure 4.40: Performance variation of the bare and ducted turbine with γ . Values of maximum power presented.

align the flow as well as for the smaller yaw angles such that less mass flow reaches the turbine disc, leading to a reduction in power.

4.7.6 Alternative domain setup

As discussed in section 4.7.1, as an alternative to yawing the inflow, one can also yaw the domain around the device in order to study yawed flow conditions. This method is more time consuming as re-meshing of the simulation domain is needed for each yaw angle. Thus a test case has been performed employing the ducted turbine at a yaw angle of $\gamma = 20^\circ$ in order to compare this alternative method to the method used in the previous sections. Though representing a slightly different problem, as mentioned in section 4.7.1, the resulting flow field using the yawed domain is almost identical to that shown in figure 4.35b. The differences in performance of the ducted device are marginal. For sake of brevity the results for this alternative domain setup are therefore not presented.

4.8 Summary of results of the actuator disc simulations

A computational actuator disc study has been performed on three tidal turbine devices: a bare turbine, a bidirectional ducted turbine, and an open-centre ducted turbine. In this study the turbine rotor has been modelled as a computational porous disc that imposes a resistance to the passage of the flow. The computational method compares favourably to linear momentum actuator disc theory corrected for blocked flows.

Flow fields of all three device types have been presented. The convergent-divergent shape of the ducted turbine was found to yield two flow regimes; a nozzle-contoured flow regime at low turbine thrusts, and a separation dominated flow regime at higher thrust levels. The outer separation was seen to increase the effective device blockage leading to maximum power within this flow regime. Nevertheless the power developed by the ducted turbine was found to be significantly less than that for a bare turbine of the same total device diameter.

For the open-centre turbine flow simulations and analyses for varying central aperture sizes have been presented. In all cases with central aperture, a flow jetting effect develops through the aperture of the turbine. The effect of this jetting is to marginally increase the flow velocity and pressure drop across the turbine annulus. However, by markedly reducing the area available for energy generation from the flow, open-centre turbines are shown to have inferior performance which worsens with increasing aperture size.

Three measures of performance have been considered: power, measured in C_P , power density, measured in C_{PD} , and efficiency, measured in η_{basin} . Both the ducted and the open-centre turbines perform significantly inferior to the bare turbine, for both

power and basin efficiency. In terms of power density, the ducted and bare devices show similar performance, while that of the open-centre turbine varies according to aperture size. For large apertures of the open-centre turbine the power density exceeds that of the bare turbine.

All three devices have been analysed in yawed inflow, with the open-centre turbine modelled using a single aperture. Flow field analysis shows a large asymmetric separation area appearing for the ducted and open-centre turbines in yawed inflow. Depending on the reference area used in the performance analysis for yawed flow, different performance results are obtained. Using the device outer diameter, it is shown that, when placed in yawed flow, the power of the ducted and open-centre devices increases (with a maximum found close to $\gamma = 20^\circ$), while that of the bare turbine decreases. This change can be attributed to three factors: a change in effective blockage for the three devices, a flow straightening effect created by the duct, as well as favourable flow alignment at the duct inlet. However, due to large-scale asymmetric separation on the exterior duct surface, the basin efficiency of the ducted and open-centre turbines drops significantly in yawed flow, while that of the bare turbine remains the same.

Using the projected frontal area perpendicular to the flow as the reference area, it is possible to correct for the change in effective blockage. When compared on this measure, it is shown that the changes in power coefficient observed when using the device outer diameter as reference area are reversed.

Some comparisons can be drawn between the axial flow results presented here and those obtained by Fleming *et al.* (2011). Fleming *et al.* conducted a design study of a bidirectional duct and evaluated the performance of various duct shapes. The duct achieving the highest power is similar in shape to the ducted turbine presented here, achieving roughly the same value of power, $C_P = 0.42$. Further, the exterior

duct shape was varied. The results suggest that, for a given internal duct shape, increasing effective blockage through external separation will yield more power than that obtainable with a streamlined duct exterior.

Comparisons can also be made to the studies of unidirectional ducts presented in section 2.2. Generally, it has been shown that while power density can be increased for a ducted turbine, the power in terms of device area is reduced compared to a bare turbine. As presented in section 2.2, the studies reporting very large power augmentation are actually reporting power density values. Once all boundary conditions are taken into account, nearly all studies showed a decrease in power per device area. A study by Shives (2011), investigating an actuator disc placed inside a diffuser of aerofoil cross-section, reported an increase in power density, a decrease in power when compared on equal device area, and a reduction in basin efficiency for the ducted device. Therefore, it can be concluded, that although the flow field of unidirectional and bidirectional ducts differs, similar trends in performance exist.

Chapter 5

RANS-BEM simulations

This chapter presents RANS-BEM analysis of bare, ducted, and open-centre turbines. Section 5.1 introduces blade element momentum theory and its implementation in wind and tidal turbine simulations. The RANS-BEM model implementation as used in this study is described in section 5.2, and validated against an analytical BEM model in section 5.4 employing the aerofoil introduced in section 5.3.

Moving from porous disc simulations to RANS-BEM simulations, the results are no longer independent of rotor and aerofoil shape or tip-speed ratio. The advantage is a more realistic turbine representation with the ability to model the rotor at varying rotational velocities (and the resulting swirling flow field) and the ability to extract performance data based on realistic aerofoil and rotor data. While representing a more realistic modelling approach, it is important to note, that a turbine design must be chosen and that results will vary dependent on the design. The rotor design method used in this study and the resulting rotors for the bare, ducted and open-centre turbines are presented in section 5.5,. Using these rotors, the three device types are simulated for both axial (section 5.6) and yawed (section 5.7) flow. A summary of the RANS-BEM simulation results is given in section 5.8. In order to study a more realistic turbine representation a hub geometry is included for all simulations presented in this chapter.

5.1 Blade element momentum (BEM) theory

This section gives a summary of the blade element momentum (BEM) theory and introduces relevant literature implementing this turbine modelling technique. The analytical model was introduced by Glauert (1935) as a combination of momentum theory and blade element theory. BEM has been applied extensively in the design and analysis of wind turbines (Burton *et al.*, 2011; Moriarty and Hansen, 2005) and more recently also to tidal turbines (Lawn, 2003; Batten *et al.*, 2008). The reason for the widespread use of BEM can be attributed to its relatively high accuracy while being computationally inexpensive.

Recently, integration of BEM in RANS solvers has become increasingly popular, for both wind and tidal turbines (Hallanger and Sand, 2013; Masters *et al.*, 2013). This approach, here termed RANS-BEM is also employed for this study. A full discussion and derivation of BEM theory can be found in Burton *et al.* (2011). A summary of the method is discussed in the following.

5.1.1 Introduction to BEM

In BEM the rotor is modelled through a series of concentric annuli of radial increment δr , see figure 5.1. BEM assumes that all of these annular sections along the blade span are independent and can be treated separately, thus assuming radial velocity components can be neglected. Further, three-dimensional effects of individual blades are ignored as the forces of a blade element are evenly distributed around the annulus, corresponding to a rotor with an infinite number of blades. Note that the nomenclature of indices used hereafter follows that introduced for the actuator disc in figure 4.1.

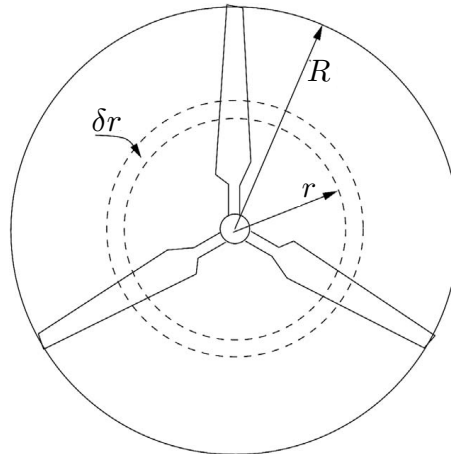


Figure 5.1: Illustration of blade element. Reproduced from Hansen *et al.* (2000).

BEM is a combination of two theories: blade element theory and momentum theory. Blade element theory is used to model the blade section drag and lift by dividing the rotor blade into a finite number of ring sections, while momentum theory is used to derive the equations for the axial and swirl induction factors at the rotor. Combining blade element and momentum theory leads to two force balance equations:

- axial (linear) momentum-force balance
- angular momentum-force balance

which can be solved iteratively to give the results of flow velocities and forces at the rotor.

In *blade element theory* the flow around the blade elements is assumed to be two-dimensional. Based on this assumption, the forces on each blade element are calculated using two-dimensional aerofoil characteristics, lift, L , and drag, D , given by dimensionless sectional lift and drag coefficients, C_l and C_d , defined as

$$C_l = \frac{l}{1/2 \rho U_{\text{rel}}^2 c} \quad (5.1)$$

and

$$C_d = \frac{d}{1/2 \rho U_{\text{rel}}^2 c} \quad (5.2)$$

where l and d are the lift and drag forces per unit span ($l = \delta L / \delta r$, $d = \delta D / \delta r$), U_{rel} is the relative blade inflow velocity and c the chord length. Figure 5.2 illustrates the velocity and angle terminology used in the discussion of the blade element. C_l and C_d are commonly available as tabulated aerofoil data obtained through experiments conducted in wind tunnels, see for instance Abbott and von Doenhoff (1959), or from numerical analysis using software such as XFOIL (Drela, 1989). The data is usually presented as a function of the angle of attack, α , the Reynolds number the experiments were performed at, and the surface roughness of the aerofoil.

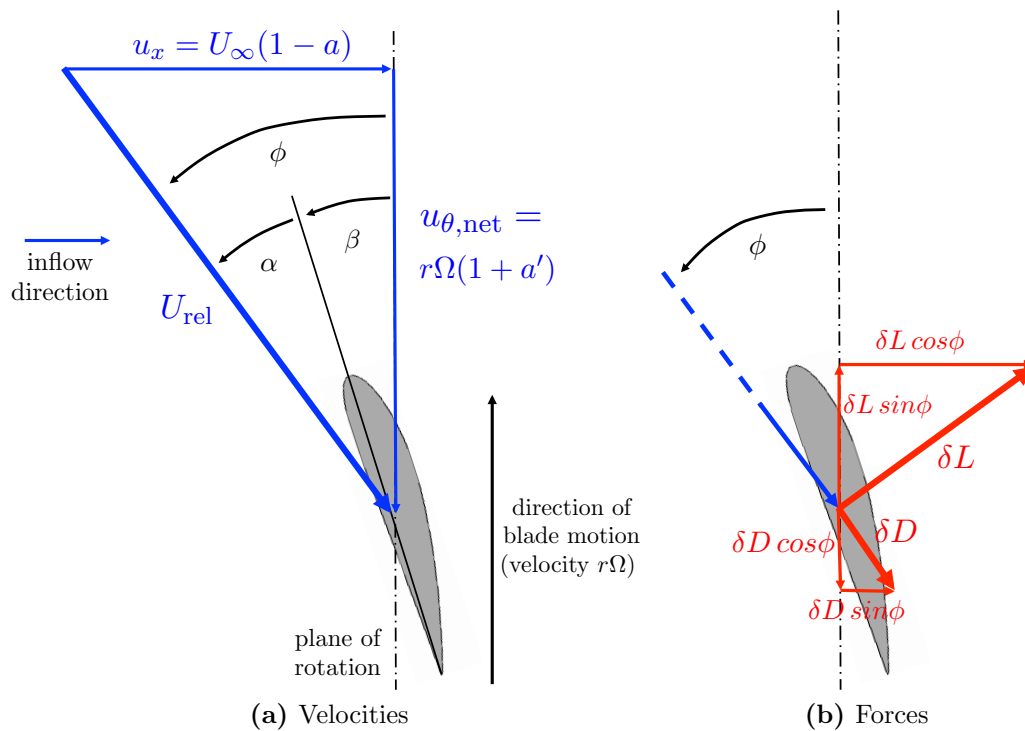


Figure 5.2: Illustration of velocities and forces acting on a blade section.

Given C_l and C_d from tabulated aerofoil data and U_{rel} , the lift force on a blade element of chord length, c , and span-wise length, δr , may be calculated using equations (5.1) and (5.2).

As illustrated in figure 5.2b, the lift force acts perpendicular, while the drag force acts parallel to U_{rel} . Given ϕ , the angle between incident velocity, U_{rel} , and the rotor plane, the axial and circumferential force components on each blade element are therefore

$$\delta F_x = \delta L \cos\phi + \delta D \sin\phi \quad (5.3)$$

and

$$\delta F_\theta = \delta L \sin\phi - \delta D \cos\phi. \quad (5.4)$$

For an annular ring of the rotor disc of span-wise length δr , located at radius r with N_B number of blades the axial thrust is thus

$$\begin{aligned} \delta T &= \delta F_x N_B \\ &= \frac{1}{2} \rho U_{\text{rel}}^2 c N_B (C_l \cos\phi + C_d \sin\phi) \delta r \end{aligned} \quad (5.5)$$

and the torque

$$\begin{aligned} \delta Q &= \delta F_\theta r N_B \\ &= \frac{1}{2} \rho U_{\text{rel}}^2 c r N_B (C_l \sin\phi - C_d \cos\phi) \delta r. \end{aligned} \quad (5.6)$$

In the next step, *momentum theory* is applied on the streamtube passing through each annulus. Both a balance of axial force and momentum as well as the balance of rotor torque and angular momentum need to be considered. The notation of streamtube stations follows that introduced in figure 4.1.

Applying Bernoulli's equation upstream and downstream of the turbine annulus and an axial momentum-force balance across the turbine annulus yields the velocity in the wake,

$$u_w = U_\infty (1 - 2a). \quad (5.7)$$

where U_∞ is the free-stream velocity and a the axial induction factor defined as the relative velocity deficit at the turbine plane. Equation (5.7) may be applied to the momentum-force balance across the turbine annulus,

$$\begin{aligned}\delta T &= -\delta\dot{m}(u_w - U_\infty) \\ &= -\rho A_{ta} U_\infty(1-a)(U_\infty(1-2a) - U_\infty) \\ &= 4\rho U_\infty^2 r \pi \delta r a(1-a)\end{aligned}\tag{5.8}$$

where δT is the force exerted on the flow by the turbine annulus, $\delta\dot{m} = \rho A_{ta} U_\infty(1-a)$ the mass flow through the streamtube, and $A_{ta} = 2r\pi\delta r$ the area of the turbine annulus.

Analogous to the axial induction factor, and consistent with many analytical BEM models, the swirl (or circumferential) induction factor, a' , is defined such that the circumferential velocity at the rotor plane is

$$u_{\theta,t} = r\Omega a'\tag{5.9}$$

and in the wake immediately behind the rotor plane is

$$u_{\theta,3} = 2r\Omega a'\tag{5.10}$$

where Ω is the angular velocity. Thus, the circumferential velocity component at the disc plane is assumed to reach half its downstream value. While for axial momentum an even split in upstream and downstream momentum loss can be derived analytically, for angular momentum such a derivation does not exist. Therefore $u_{\theta,t} = \frac{u_{\theta,3}}{2}$ is one of the core assumptions employed within BEM theory.

Combined with the circumferential velocity of the blade element, $r\Omega$, the net circumferential flow velocity experienced by the blade element, as illustrated in Fig. 5.2,

is

$$u_{\theta,\text{net}} = (1 + a') r \Omega. \quad (5.11)$$

The rate of change in angular momentum of the fluid passing through the annulus is equal to the rotor torque, Q ,

$$\begin{aligned} \delta Q &= \dot{m} \Delta u_{\theta} r \\ &= \rho A_{ta} U_{\infty} (1 - a) (2 r \Omega a') r \\ &= 4 \pi \rho U_{\infty} \Omega a' (1 - a) r^3 \delta r. \end{aligned} \quad (5.12)$$

At this stage two equations for both axial thrust and rotor torque have been derived from blade element theory and momentum theory. Combining equations (5.5) and (5.8) results in the *axial momentum-force balance*,

$$\frac{1}{2} \rho U_{\text{rel}}^2 c N_B (C_l \cos \phi + C_d \sin \phi) \delta r = 4 \rho U_{\infty}^2 r \pi \delta r a (1 - a) \quad (5.13)$$

and equations (5.6) and (5.12) in the *angular momentum-force balance*,

$$\frac{1}{2} \rho U_{\text{rel}}^2 c r N_B (C_l \sin \phi - C_d \cos \phi) \delta r = 4 \rho \pi U_{\infty} (\Omega r) a' (1 - a) r^2 \delta r. \quad (5.14)$$

Equations (5.15) and (5.16) have been derived from the momentum-force balance equations (5.13) and (5.14) and provide more convenient equations for iteratively solving the axial and swirl induction factors:

$$\frac{a}{1 - a} = \frac{\sigma_r C_x}{4 \sin^2 \phi} \quad (5.15)$$

$$\frac{a'}{1 + a'} = \frac{\sigma_r C_{\theta}}{4 \sin \phi \cos \phi} \quad (5.16)$$

with the local blade solidity defined as

$$\sigma_r = \frac{N_B c}{2 r \pi} \quad (5.17)$$

and the axial and circumferential blade section force coefficients, C_x and C_θ , defined as

$$C_x = C_l \cos\phi + C_d \sin\phi, \quad (5.18)$$

$$C_\theta = C_l \sin\phi - C_d \cos\phi. \quad (5.19)$$

The iteration process is started using a fixed rotor geometry with given β and σ_r and by supplying initial guess values for a and a' . Given the rotor geometry and induction factors, the flow velocities at the rotor plane are calculated and both ϕ and α are obtained. Using α , the blade force coefficients can be extracted from tabulated aerofoil data and the right hand side of equations (5.15) and (5.16) may now be solved. The iteration process is repeated using the new results for a and a' until a converged solution for a and a' is found. Once the solution has converged, the power produced by each annulus can be obtained from the product of torque (see equation (5.6)) and angular velocity:

$$\delta P = \delta Q \Omega = \delta F_\theta r N_B \Omega. \quad (5.20)$$

The performance coefficients may then be calculated using the same definitions as introduced previously.

5.1.2 Corrections to BEM

The BEM method has its limitations, some of which may be corrected for using empirical correction factors. A comprehensive list of correction models to BEM may be found in Burton *et al.* (2011) and Moriarty and Hansen (2005).

One of the assumptions is equilibrium of the rotor flow field, where the passing flow changes instantaneously to adjust to new operating conditions. However, aerofoil response to the changes of the wake flow is not instantaneous, an issue addressed by the generalised dynamic wake model described in Moriarty and Hansen (2005). Another limitation of BEM is the assumption of two-dimensionality when calculating the blade forces, thus neglecting any radial (spanwise) flow. Hence the theory is less accurate for heavily loaded rotors with large spanwise pressure gradients.

A major limitation of the original BEM theory is the inability to model tip vortices generated at the blade tips. The helical tip vortices influence the induced velocity field at the rotor, particularly near the tips of the blade, the area where the most power is produced. Hence, modelling this effect is critical for increasing the accuracy of rotor performance predictions. A model originally developed by Prandtl (Prandtl and Betz, 1927) can be summarised by a tip correction factor,

$$F = \frac{2}{\pi} \cos^{-1} \left[\exp \left(\frac{N_B (1 - \frac{R}{r})}{2 \sin \phi} \right) \right] \quad (5.21)$$

which is applied in the current model as a multiplication factor to the local induction factor. Figure 5.3 presents the results for F for an example rotor.

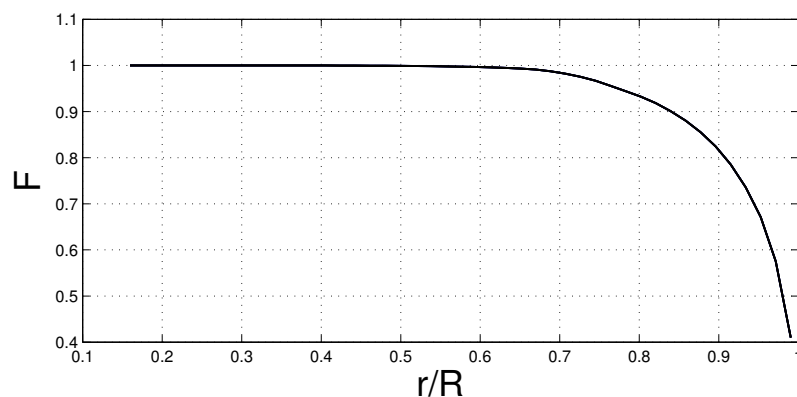


Figure 5.3: Example tip correction factor.

The effect of the tip correction factor is to decrease the local induction factor and hence increase the axial velocity near the blade tips, in order to account for flow entrainment at the blade tips. This increase in axial velocity leads to an increase in angle of attack in this region. Depending on the rotor geometry and the operating point of the rotor, this increase in α can lead to either an increase or decrease in power compared to a turbine where tip vortex effects have been neglected. Figure 5.4 shows an example of a rotor simulated with and without tip correction. Note that the tip correction factor is often applied incorrectly, as discussed in detail by Schluntz (2014). A typical error is the application of the factor to the velocity rather than the axial induction factor, thereby leading to a loss in axial flow velocity rather than an increase.

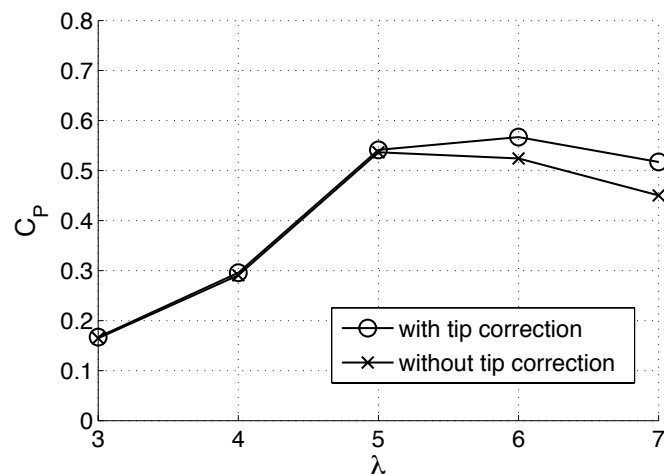


Figure 5.4: Example power coefficient for rotor modelled with and without tip correction.

5.1.3 Analytical BEM rotor design

An analytical BEM (ABEM) model is the implementation of BEM as introduced in section 5.1.1 in a purely analytical code. For a given rotor design, equations (5.15)

and (5.16) are solved iteratively until the results for the axial and circumferential induction factors, a and a' , converge.

Through a simple addition of a rotor design loop, the rotor may be adjusted in order to maximise performance. Power is maximised by adjusting the twist, β , of the rotor, in order to reach the target value of the angle of attack, α_{target} , which is given by the angle of attack resulting in maximum lift over drag, $(L/D)_{\text{max}}$.

The variation of chord length with radius is typically calculated using

$$c_r = \frac{16 \pi R}{9 C_{l,\text{design}} N_B \lambda^2 \frac{r}{R}}, \quad (5.22)$$

where $C_{l,\text{design}}$ is the lift coefficient at α_{design} . The chord distribution in equation (5.22) is that of a blade optimised to give maximum power at a particular tip-speed ratio, ignoring drag and tip-loss, see Burton *et al.* (2011) for details.

The BEM routine is embedded within the design routine, such that for each design a fully converged BEM result exists. After each converged BEM solution the resultant value of α is compared to the target value, α_{target} . If a difference above a certain threshold (e.g. 0.1 %) exists, the blade twist is adjusted by a fraction of the α -offset and the BEM simulation is repeated. Figure 5.5 illustrates the design and BEM iteration loops.

Such an ABEM rotor design code has been developed within this study and has been used for analytical rotor design exercises and for validation purposes, see section 5.4. The tip-loss model introduced in section 5.1.2 has been included in the implementation of this code.

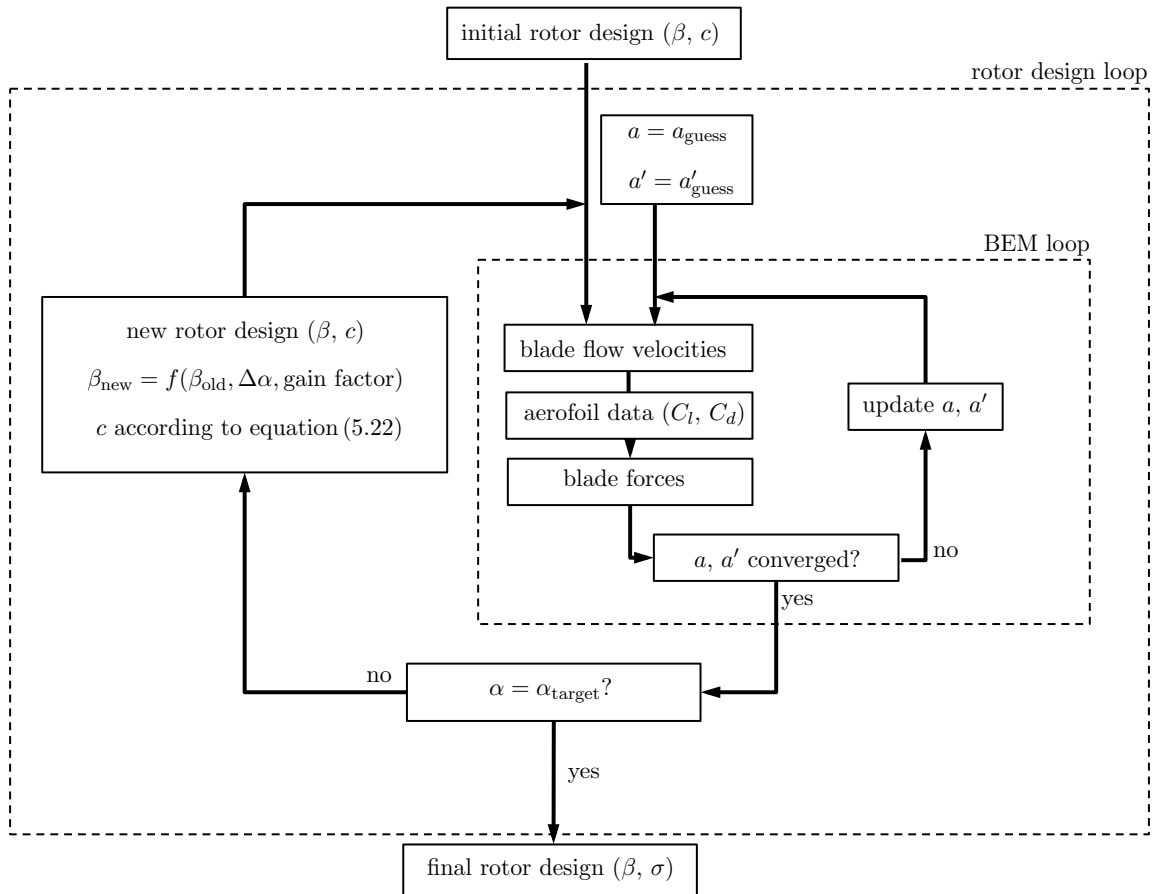


Figure 5.5: Flow chart of the analytical rotor design procedure.

5.1.4 BEM application in wind and tidal turbine research

BEM is a popular rotor modelling tool which has been applied to wind turbines for many decades and more recently to tidal turbines. It can be applied analytically (as described in the previous section), analytically with corrections (such as blockage corrections), or be embedded in a RANS solver, with or without corrections. BEM is implemented in many wind turbine design codes such as AeroDyn developed by the National Renewable Energy Laboratory (NREL), see Moriarty and Hansen (2005).

As discussed in section 5.1.2, several corrections need to be applied to BEM to deliver realistic results for both wind and tidal turbines. Many studies present further

corrections for wind turbines (Lanzafame and Messina, 2007; Masters *et al.*, 2007; Hansen, 2008; Sant, 2007), to account for secondary flow effects, such as radial flow along the blade span, or unsteady or yawed inflow.

When applying BEM to tidal flows, the assumption of unbounded flow is inappropriate. Turner and Owen (2009) present three analytical BEM models and compare them for finite domain tidal turbine applications. Classic, unbounded BEM, is compared to BEM which has been extended to account for a finite domain cross-section. The finite domain is modelled using two methods; a rigid boundary and a free-surface boundary. The findings show the boundary conditions have a very significant effect on the performance of a tidal turbine, as also presented in section 4.4.4 of the current study. The results further show no significant difference between the rigid lid BEM and the free-surface BEM model analysed (blockage of $B \leq 0.20$), therefore supporting the decision to use the rigid lid approach in the present study.

Shives (2011) combines an analytical duct performance model (adapted from Lawn (2003)) with BEM to form a combined analytical-empirical DuctBEM model. For the development of this model various duct geometries were simulated in CFD in order to determine duct efficiency terms. These terms are then used in determining the flow at the turbine plane, which in turn is used as input for the BEM model. The model is intended as a preliminary ducted turbine design tool as it does not require any further CFD simulation.

While other applications of analytical BEM models for tidal turbines exist (Batten *et al.*, 2008), RANS-embedded BEM methods (RANS-BEM) are becoming increasingly popular for tidal turbines (Turnock *et al.*, 2011; McIntosh *et al.*, 2011; Masters *et al.*, 2013; Batten *et al.*, 2013) as well as wind turbines (Hallanger and Sand, 2013). In RANS-BEM the blade element method is applied either as a boundary condition (analogous to the actuator disc approach) or across a region of cells, for instance a

thin cylindrical volume. The velocity field is calculated by the RANS solver, while the resulting blade forces are obtained from blade element theory and aerofoil performance data. These blade forces are then fed back into the RANS solver and the RANS equations solved. The process is repeated until convergence.

A main benefit of using RANS-BEM is that through the nature of its implementation the method accounts for finite domain effects, including those induced by any boundary or structure affecting the rotor flow, such as a duct. Depending on how BEM is integrated within RANS, non-uniform rotor inflow can be analysed. The RANS-BEM implementations by Turnock *et al.* (2011) and Batten *et al.* (2013) apply averaged velocity and force values across the annuli, thus assuming an axisymmetric distribution. In contrast, the model developed by McIntosh *et al.* (2011) computes the BEM values for each disc cell separately, yielding a model that can easily handle non-uniform rotor inflow without any further modifications. Compared to full blade-resolved simulations, the rotor blades do not need to be meshed and different rotors may easily be tested without altering the mesh. This substantially reduces the meshing effort as well as the overall number of cells in the simulation domain. Compared to the actuator disc simulations where the disc force only acts in the axial flow direction, the rotor in RANS-BEM exerts both axial and circumferential forces on the flow field, therefore leading to a swirling wake flow. As the power is calculated from the circumferential force component, a more realistic turbine performance result can be obtained.

Due to the computationally efficient approach of RANS-BEM, it has recently become a popular tool for predicting the wake flow in tidal arrays (Turnock *et al.*, 2011; Masters *et al.*, 2013; Batten *et al.*, 2013). When modelling an array of tidal turbines, the representation of the wake is of high importance. As the swirling motion of the wake is an essential component, a model that imparts swirl on the flow is

needed. At the same time multiple turbines need to be modelled. Modelling the turbine array with multiple fully blade resolved rotors is usually not an option due to computational constraints. As RANS-BEM provides both swirling wake flow while being computational efficient, it is being employed in several wake studies.

In the current study bare, ducted, and open-centre devices are analysed in axial, as well as yawed flow. An extended analytical BEM model has been developed for bare rotors in yawed flow, which compares favourably to wind tunnel tests (Hansen, 1992). For ducted turbines in axial flow, an extended BEM model has been suggested by Shives (2011). This model, however, requires extensive prior CFD analysis of the duct itself in order to characterise the duct flow for a given geometry. In the present study an interaction of non-axial flow with the duct (flow straightening, flow separation) is expected and hence a three-dimensional model is needed which is able to model the rotor in an azimuthally independent fashion. The RANS-BEM model developed by McIntosh *et al.* (2011) delivers this capability and is thus employed for this investigation.

5.2 RANS-BEM model implementation

The RANS-BEM model employed in this study, developed by Simon McIntosh of the Oxford Tidal Energy Research Group, has been described in McIntosh *et al.* (2011) and applied to bare and ducted turbines in Fleming *et al.* (2011). The model combines BEM theory as introduced in section 5.1.1 with RANS simulations by implementing the BEM method as a boundary condition in ANSYS FLUENT.

The RANS-BEM model applies the BEM method as a boundary condition within FLUENT (ANSYS Inc., 2009a), with the rotor represented as a thin disc, as in the actuator disc simulations. The axial blade forces acting on the flow are reproduced by applying a jump in static pressure Δp across the disc,

$$\begin{aligned}\Delta p &= \frac{1}{2} \rho U_{\text{rel}}^2 \sigma_r (C_l \cos \phi + C_d \sin \phi) \\ &= \frac{1}{2} \rho U_{\text{rel}}^2 \sigma_r C_x,\end{aligned}\tag{5.23}$$

where C_x is defined as per equation (5.18). The circumferential blade forces can be implemented through the specification of a circumferential velocity component downstream of the disc,

$$\begin{aligned}u_{\theta,3} &= -\frac{1/2 \rho U_{\text{rel}}^2 \sigma_r (C_l \sin \phi - C_d \cos \phi)}{\Delta p u_x} \\ &= -\frac{1/2 \rho U_{\text{rel}}^2 \sigma_r C_\theta}{\Delta p u_x},\end{aligned}\tag{5.24}$$

where C_θ is defined as in equation (5.19). As discussed in section 5.1.1, the circumferential velocity component at the turbine plane is assumed to reach half of its downstream value, $u_{\theta,t} = \frac{u_{\theta,3}}{2}$. As illustrated in figure 5.2, $u_{\theta,\text{net}}$ is defined as the resultant of the blade rotational velocity, $r \Omega$ and the circumferential flow velocity at the turbine plane, $u_{\theta,t}$,

$$u_{\theta,\text{net}} = r \Omega - u_{\theta,t}.\tag{5.25}$$

The incident blade velocity, U_{rel} , is defined as the resultant of the streamwise, u_x , and the net circumferential, $u_{\theta,\text{net}}$, velocity components,

$$U_{\text{rel}} = \sqrt{u_{\theta,\text{net}}^2 + u_x^2}. \quad (5.26)$$

The Prandtl tip-loss model as described in section 5.1.2 is implemented in the RANS-BEM code and may be enabled when required. As shown by Fleming *et al.* (2011) the tip-loss mechanism is not as severe in ducted rotor flows, therefore in the present study the tip-loss factor is set equal to unity for all ducted rotor simulations.

Note that, in the present model, in contrast to the standard approach used in CFD-embedded BEM models (see for instance Malki *et al.* (2013)), the rotor forces are not applied uniformly across an annulus, but instead are applied to each cell independently, according to the local flow conditions. This method can be best visualised as a large number of thin streamtubes of cell-sized cross-section (at the rotor plane), passing through the disc (“spaghetti” approach). This model can thus account for azimuthal variations in the rotor flow field, as are expected for non-axial flow cases.

5.3 Hydrofoil selection

The hydrofoil selection forms a central part of the design process as the lift to drag characteristics of the chosen hydrofoil limit the maximum performance of the rotor. Much of the foil development of the past century has been focussed on aerospace and wind turbine applications, hence the foils are usually referred to as aerofoils and will be referred to as such in this study.

The main performance characteristics of an aerofoil are given by the lift and drag coefficient, C_l and C_d , over a range of angles of attack, α . The performance is dependent not only on the shape of the aerofoil, but also on the operational Reynolds number and whether the aerofoil surface is smooth or rough. As the aerofoil aerodynamic data is directly used within the RANS-BEM model without a physical modelling of the aerofoil, it is important to not only choose a suitable aerofoil but also to source reliable data of its performance.

An extensive list of aerofoil catalogues exist, with those aerofoils produced by National Advisory Committee for Aeronautics (NACA) being the most widely used. However, having been developed for the aviation industry, the performance of these aviation class aerofoils is suboptimal when applied to wind turbines or tidal turbines (Ahmed, 2012). Thus in more recent decades many aerofoils have been developed particularly for wind turbine applications. Examples are the SERI S8xx aerofoils developed by the Solar Energy Research Institute (SERI, now the National Renewable Energy Laboratory, NREL), the DU yy-Wxxx aerofoil family developed by Delft University and the Risø-A and Risø-B aerofoil families developed by the Danish research organisation Risø which since has merged with the Danish Technical University (DTU).

When moving from wind to tidal turbine applications further constraints are placed on the aerofoils employed. The loads per unit area are larger for a tidal turbine

than a wind turbine as they are proportional to the product of density and velocity squared,

$$T/A_{turbine} \propto \rho U^2. \quad (5.27)$$

While the flow velocities are lower for tidal turbine applications (1-4 m/s) compared to wind turbine applications (3.5-25 m/s), the density is increased by a factor of $\rho_{seawater}/\rho_{air} = 837$, thus outweighing the contribution of velocity and leading to an overall increase in thrust loading per unit area. Hence, due to the structural requirements for tidal current turbines generally, aerofoils with a minimum thickness to chord ratio of $t/c > 20\%$ are employed. A range of suitable choices of aerofoils for hydrokinetic turbine applications are discussed in Ahmed (2012).

Apart from their suitability the main other criteria in the aerofoil selection process is the availability of reliable experimental or numerical data. While a large amount of data is available for the NACA aerofoils (Miley, 1982; Abbott and von Doenhoff, 1959), for thicker aerofoils, e.g. NACA 63-425, lift and drag data is limited to low angles of attack. The current study strives to investigate the turbines at various tip-speed ratios, which thus includes simulations at off-design conditions, away from the optimal tip-speed ratio. This off-design operation leads to a large variation in the angle of attack of up to $\Delta\alpha \approx 40^\circ$ (in the present study) when analysing a turbine.

While stall-regulated, fixed pitch wind and tidal turbines exist, all large scale wind turbine designs, as well as several tidal turbine developments are using a pitch-regulated approach. This method of turbine-regulation uses an adjustment of the blade pitch angle (and thus β) in order to operate at the optimal tip-speed ratio and to move to lower α at high flow velocities. Therefore this type of regulated turbine only encounters a small variation in angle of attack of $\Delta\alpha \approx 10^\circ$, compared to fixed-pitch devices, which operate at high α in stalled flow conditions.

The data available for the Risø-A1-24 aerofoil covers a broad range of incidence angles (Fuglsang *et al.*, 1999). In Ahmed (2012) this aerofoil is suggested as a popular choice within the tidal turbine industry. This claim is further supported by Sale *et al.* (2009) where tidal turbine blade design is conducted using the Risø-A1 aerofoil family.

Table 5.1 summarises the principal characteristics of the Risø-A1-24 aerofoil while figure 5.6 presents the profile geometry. The lift and drag characteristics, presented in figure 5.7, were recorded through wind tunnel tests in an open jet wind tunnel at a Reynolds number of 1.6×10^6 , a background turbulence intensity of 1%, and a flow velocity of 42 m/s. The aerofoil sections employed a chord length of 0.60 m and a span of 1.9 m. The aerofoil was simulated both with a smooth surface as well as with leading edge roughness. A trip tape was mounted on the surface of the leading edge in order to simulate the effects from leading edge roughness, which may occur in non-clean environments. The marine environment in which tidal turbines are placed is expected to lead to a certain level of marine fouling and corrosion on the turbine blades. The aerofoil is thus assumed to exhibit a non-clean surface and therefore only the aerofoil data with leading edge roughness is presented and used in this study.

The measurement data ranges from $-5^\circ < \alpha < 35^\circ$ and is expected to cover the majority of simulation cases investigated in this chapter. For $\alpha > 35^\circ$ the model described in 5.2 uses the C_l and C_d values of $\alpha = 35^\circ$. In realistic conditions, the lift will continue to drop and the drag will continue to increase. A method commonly used to predict aerofoil data for high angles of attack, is to employ a post-stall model. Post-stall models compute missing aerofoil data for the post-stall region based on pre-stall aerodynamic data as well as blade geometry characteristics (Spera, 2008; Tangler and Kocurek, 2005). Popular models include flat plate theory, where the turbine blade is approximated as a flat plate, the Viterna-Corrigan model (Viterna and Corrigan, 1981), as well as a model suggested by Tangler (1987). The approach of

Table 5.1: Risø-A1-24 aerofoil characteristics for aerofoil with leading edge roughness. Reproduced from Burton *et al.* (2011).

| Aerofoil | max. t/c [%] | x/c at max. t/c | Design α | max. C_l/C_d |
|------------|----------------|---------------------|-----------------|----------------|
| Risø-A1-24 | 24 | 0.302 | 7° | 58 |

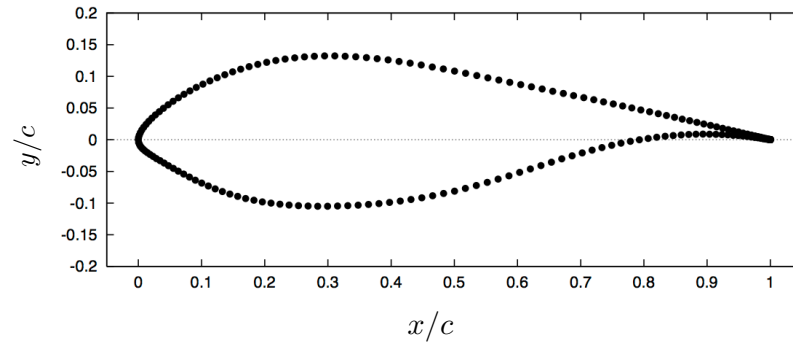


Figure 5.6: Geometry of the Risø-A1-24 aerofoil. Reproduced from Bertagnolio *et al.* (2001).

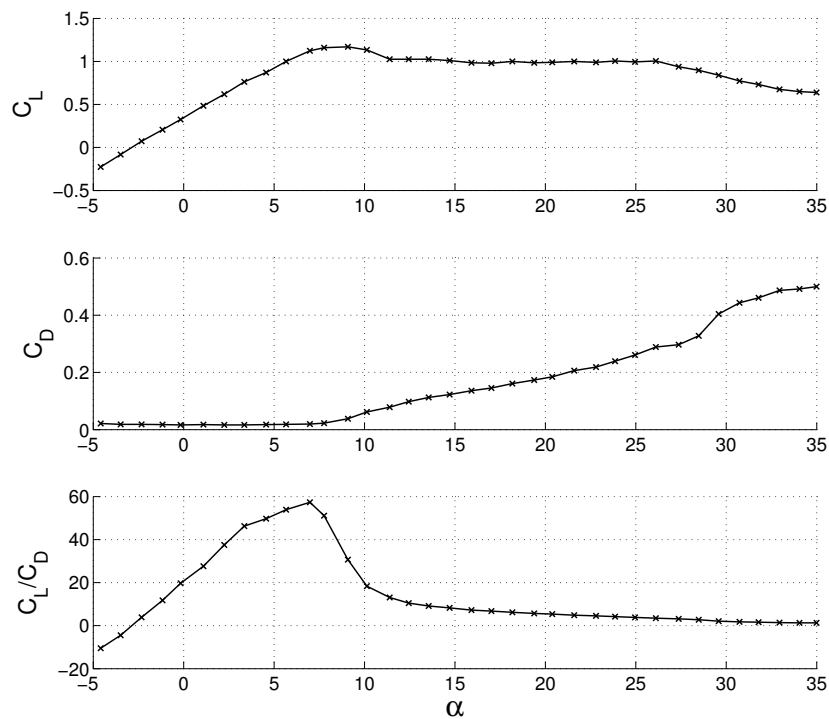


Figure 5.7: Risø-A1-24 lift and drag coefficients for aerofoil investigated with leading edge roughness. Data reproduced from Fuglsang *et al.* (1999).

using fixed value lift and drag coefficient rather than implementing a post-stall model was deemed sufficient as the occurrences of $\alpha \geq 35^\circ$ were very sparse (two instances), reaching in one case $\alpha_{\max} = 37^\circ$ and in the other $\alpha_{\max} = 47^\circ$. Further, these extreme angles of attack occurred at extreme off-design conditions, at very low λ . As the lift on the aerofoil would be lower and the drag higher, realistically the performance of these off-design conditions would be slightly lower when simulated using a post-stall model.

It is noted that hydrofoil development specifically for tidal turbine applications has been performed by Grasso (2011) using numerical optimisation. However, since the performance of the resulting hydrofoils has not been validated through experiments, these customised hydrofoils were not considered for this study.

5.4 Bare turbine model validation

In order to validate the RANS-BEM model the results for a bare turbine are compared to an analytical BEM (ABEM) implementation. In McIntosh *et al.* (2011) the RANS-BEM model has been shown to compare favourably to an analytical BEM model and to a lesser extent to fully blade-resolved simulations.

When validating the model with an ABEM model it must be noted that standard ABEM theory assumes a blockage of $B = 0$. Thus for the validation of the RANS-BEM model a very low domain blockage is chosen to model closely an unbounded rotor. The domain cross-section is of square shape as in the porous disc simulations, with the area blockage in this case set to $B = 0.00025$. Inside the first radial station a slip wall boundary represents a cylindrical frictionless hub, that stretches infinitely far up- and downstream, thus replicating the analytical BEM model, in which no flow is modelled inboard of the first annulus. Figure 5.8 illustrates the simulation domain used in the validation process. The tip radius of the turbine is $R = 8$ m and the hub radius is $R_{\text{hub}} = 1.2$ m.

Two rotor geometries were employed for the validation process, rotors V1 and V2. The rotors were generated using the RANS-BEM rotor design tool described in section 5.5. Both rotor geometries were paired with the aerofoil geometry introduced in section 5.3. The main difference between the two rotors is given in a variation in solidity σ_r , with rotor V1 having a solidity of $0.03 \leq \sigma_{r,V1} \leq 0.64$ and rotor V2 of $0.05 \leq \sigma_{r,V2} \leq 0.90$. Rotor V1 thus exerts a lower thrust on the flow than rotor V2. The validation analysis presented in McIntosh *et al.* (2011) was conducted using a rotor with lower solidity than either of the rotors presented in this study. However, early tests of the design routine indicated that for some devices a higher σ_r may lead to higher performance and therefore in this validation study higher levels of rotor solidity are analysed.

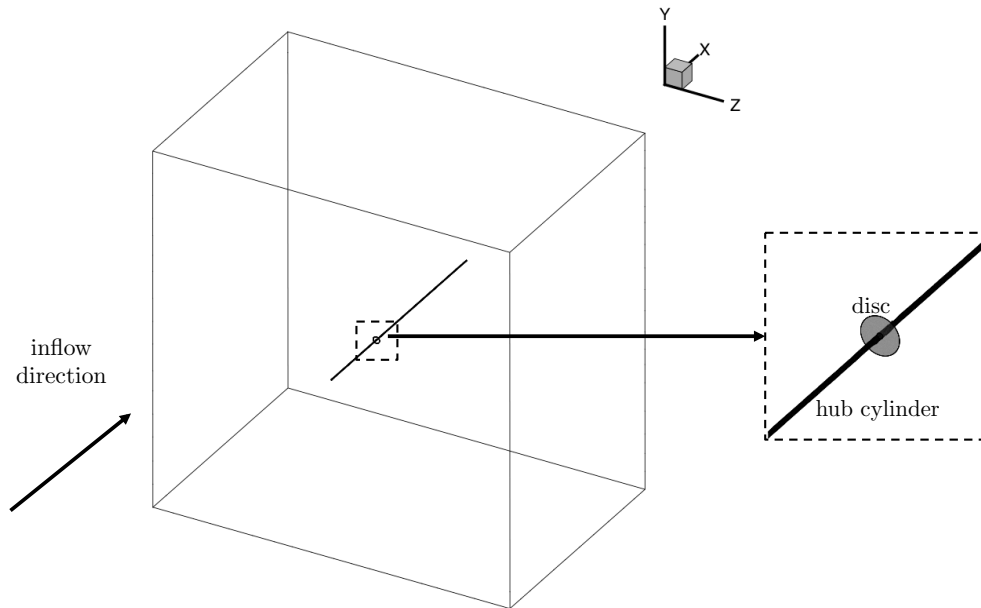
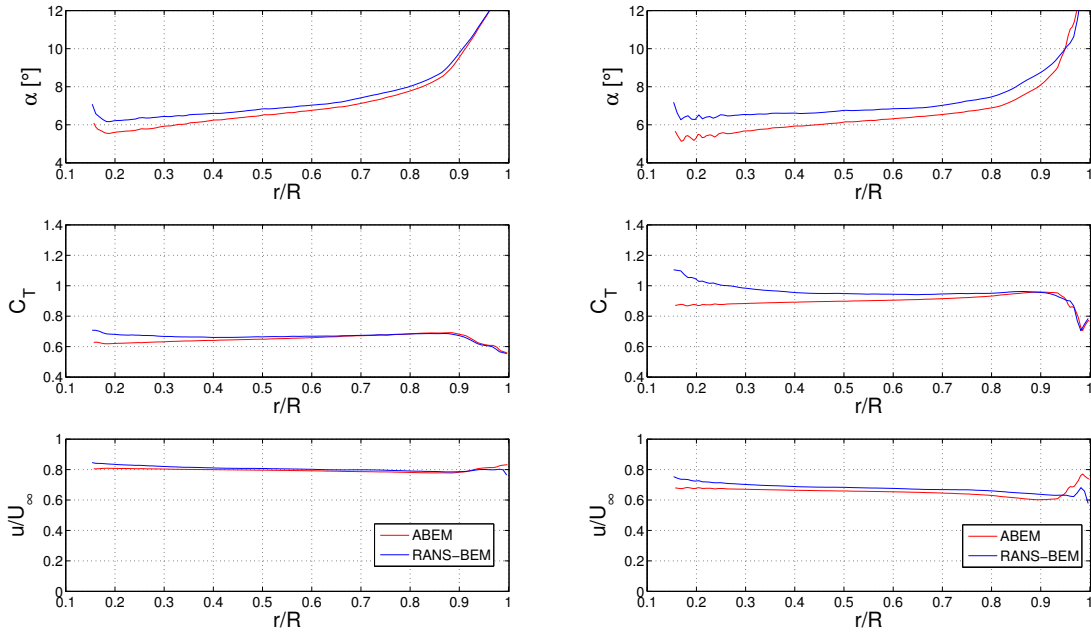


Figure 5.8: Simulation domain for RANS-BEM validation test

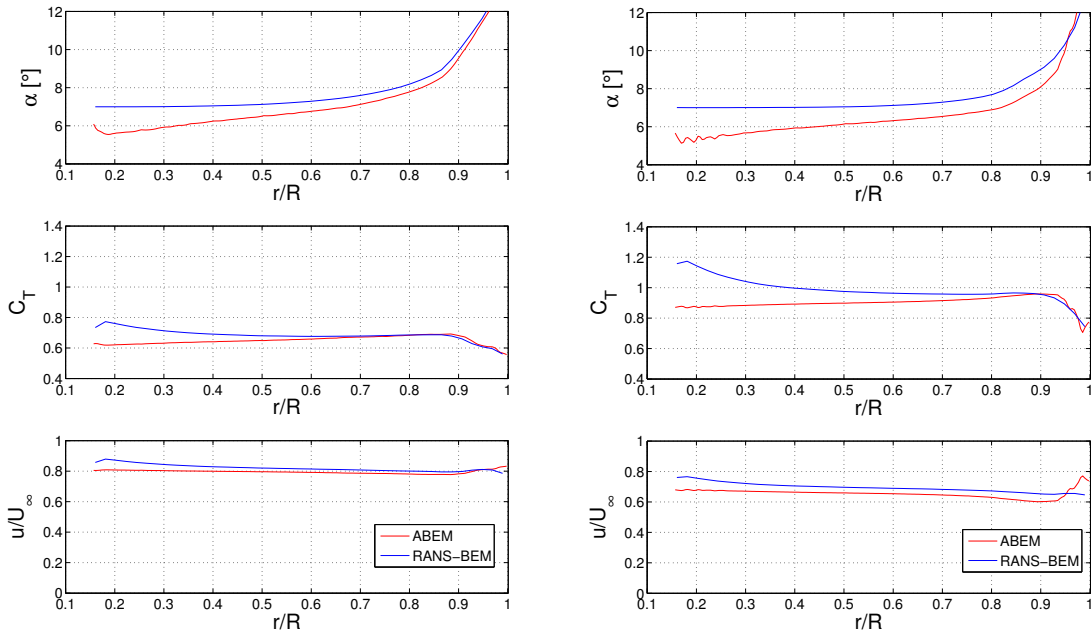
Figures 5.9a and 5.9b present the simulation results (performed at $\lambda = 4$) for angle of attack, α , thrust coefficient, C_T , and the velocity ratio of local velocity to upstream velocity, u_x/U_∞ , along the rotor span. For rotor V1 very good agreement is achieved between ABEM and the RANS-BEM across the whole rotor span with minor differences close to the hub. These differences are more pronounced for the high solidity rotor V2. The high rotor solidity in the vicinity of the hub creates a local blockage that induces a spanwise flow. While the RANS-BEM model captures this spanwise flow, ABEM assumes no radial flow along the span of the rotor blade. (Note that while spanwise flow is captured by RANS-BEM, the spanwise flow effect on C_l and C_d is not).

As a change in solidity and thus local blockage has a considerable effect on the flow close to the hub, further analysis is conducted at higher domain blockage. The blockage ratio used in the previous chapter, $B = 0.035$, is applied in the RANS-BEM investigations following in this chapter, thus both rotor V1 and V2 are analysed at this blockage. Figures 5.9c and 5.9d present the results for both rotors simulated at



(a) Rotor V1, medium solidity. $B = 0.00025$.

(b) Rotor V2, high solidity. $B = 0.00025$.



(c) Rotor V1, medium solidity. $B = 0.035$.

(d) Rotor V2, high solidity. $B = 0.035$.

Figure 5.9: RANS-BEM comparison to analytic BEM results for rotors of varying solidity simulated in low and moderate domain blockage.

$\lambda = 4$. As for the results at low domain blockage the differences between ABEM and RANS-BEM are most pronounced close to the hub. The effect of increasing domain blockage is very similar to that of increasing rotor solidity as can be clearly seen when comparing figure 5.9b with figure 5.9c.

In conclusion, when used in low blockage with a low to medium solidity rotor the results of RANS-BEM are in agreement with those of ABEM. As expected, for higher blockages and rotor solidity the results of the two BEM methods diverge as the assumptions of ABEM become invalid. As tidal turbine designs approach high solidity rotors operating in highly blocked flows, simple ABEM is not suitable for capturing the effects of these flows.

5.5 Rotor design

As discussed above, when employing RANS-BEM simulations, a rotor design must be introduced. As the goal is a fair comparison of different tidal turbine devices, it is of importance to tailor the rotor design to the environment. A rotor designed for a bare turbine will likely not yield the best results in ducted operation, see McIntosh *et al.* (2011). Similarly, a rotor designed for low blockage flow will operate sub-optimally in high flow blockage, see Schluntz and Willden (2013).

This section introduces the rotor design criteria and tool used to design three turbine rotors: bare, ducted and open-centre turbines. The rotor designs are then employed in subsequent investigations.

5.5.1 Design criteria

A rotor design is given by the blade twist, β , and the blade solidity, σ_r , for each radial station. Once the number of rotor blades is chosen the chord length, c , can be derived, using equation (5.17). The blade twist is the predominant rotor variable that determines the local angle of attack, α , while the solidity is the predominant variable in defining the local thrust, $C_{T,loc}$, that the blade section exerts on the flow. In the design process it is thus necessary to set a design angle of attack and a design local thrust in order to define the rotor geometry.

By choosing an aerofoil, the optimal angle of attack is necessarily inferred. This optimum is found at the maximum ratio of lift over drag, $(C_l/C_d)_{max}$. For the aerofoil introduced in section 5.3 $(C_l/C_d)_{max} = 58$ is found at $\alpha_{target} = 7^\circ$, see figure 5.7.

The optimal design local thrust is less straightforward. From LMADT the optimal local thrust coefficient in unblocked flow is known ($C_{T,loc} = 2$). For blocked flow,

however, this number is observed to be higher and must be found iteratively. Further, as the velocity of the flow changes across the radial disc position there is a valid question of whether a design approach given a constant $C_{T,loc}$ in fact leads to maximum power.

In order to validate the constant local thrust design approach a set of actuator ring simulations were performed. These simulations use the actuator disc model described in chapter 4, with a rotor disc divided into 8 equally radially spaced ring sections, see figure 5.10. A hub with semi-spherical ends is included in the simulation.

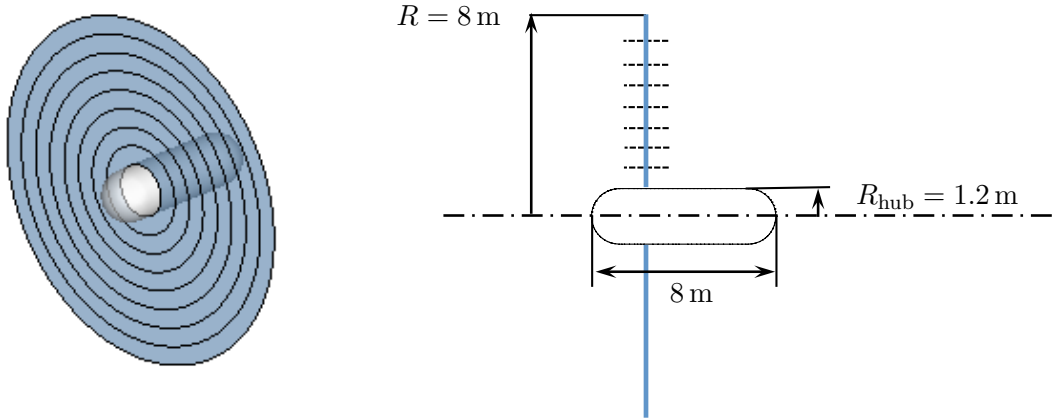


Figure 5.10: The rotor disc divided into 8 equally spaced rings.

$C_{T,loc}$ is varied radially across the eight rings according to the following equation:

$$C_{T,loc} = C_0(1 + f(r/R_{tip})) \quad (5.28)$$

where C_0 is the baseline target local thrust coefficient, f the radial variation factor and r the radial position of the ring. To cover a broad simulation space, C_0 was varied between $0.5 \leq C_0 \leq 5$ and f between $-1 \leq f \leq 1$. This variation results in an area-averaged disc thrust coefficient as presented in figure 5.11a. The total disc C_P is computed and presented in figure 5.11b. A maximum power plateau is found along an average local thrust of roughly $C_{T,loc} = 2.5$. This region of maximum power

extends from $0 \leq f \leq 0.8$, thus for uniformly loaded turbine discs ($f = 0$) as well as discs with increasing loading towards the tip ($f > 0$). Within this maximum power plateau the differences in power coefficient are small and lie within 1 %.

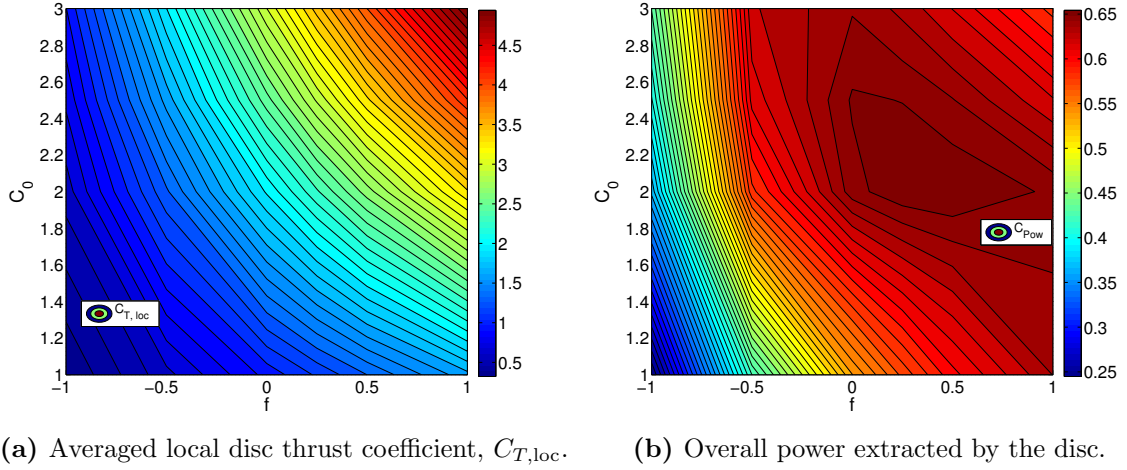


Figure 5.11: Contour plots of area averaged $C_{T,loc}$ and power extracted by the disc based on control variables C_0 and f .

A detailed representation of the performance coefficients dependent on radial position is given in figure 5.12 for $C_0 = 2$. The performance coefficients presented here use the turbine ring area, A_{ring} , as the reference area and are therefore referred to as density coefficients, C_{TD} , C_{PD} .

While $C_{T,loc}$ increases with increasing f as per equation (5.28), C_{TD} remains approximately constant for $0 \leq f \leq 1$ with just small increases in C_{TD} for high levels of f . The power produced per ring element is nearly constant across the seven inboard ring elements for $0 \leq f \leq 1$. For the outermost ring element the effect of the rotor edge (tip leakage) results in an observable in a drop in power. This can be attributed to the increased radial flow (and thus reduced axial flow component) at the disc edges. From a structural perspective it is not desirable to load the tips of a turbine blade. As the undesirable loading of the blade tips only leads to small increases in overall disc power compared to the constant thrust loading case ($f = 0$), it has been decided

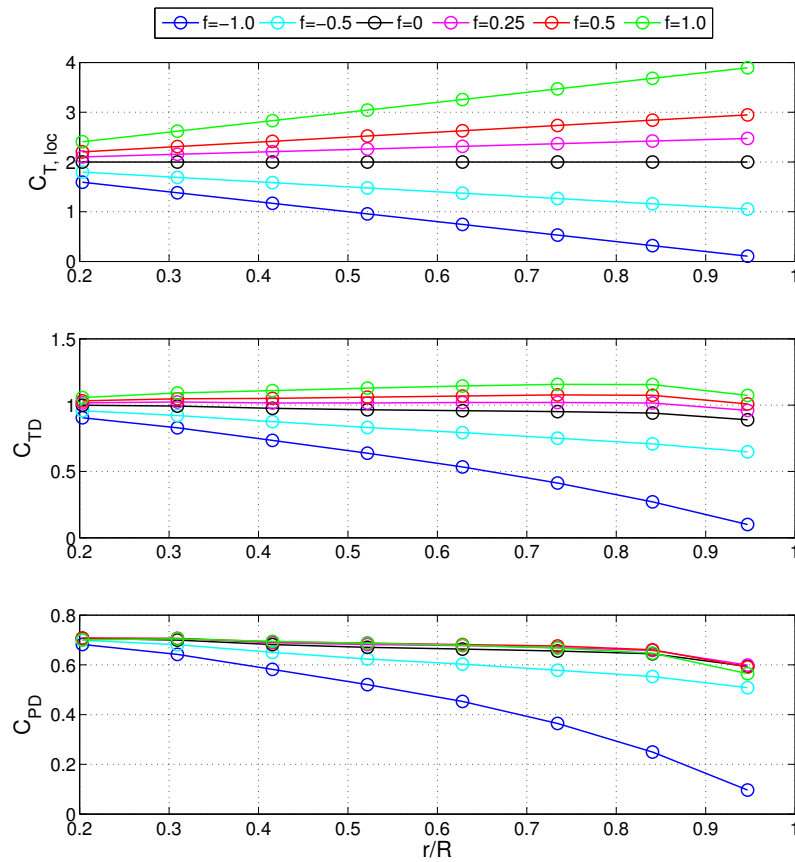


Figure 5.12: Performance of each disc ring for $C_0 = 2$ and varying f .

for this study to follow the constant $C_{T,loc}$ approach (i.e. $C_{T,loc} = C_0$ and $f = 0$) in the following rotor design exercise.

5.5.2 RANS-BEM rotor design tool

A rotor design tool is included in the RANS-BEM code described in section 5.2. It is coded as an add-on tool that may be turned on and off based on the type of simulation performed.

Given two target design values (α_{target} and $C_{T,loc}$) the tool adjusts the blade parameters β and σ_r until the target values are met at each solution point along the blade. This design adjustment is performed at each RANS iteration step. As the steady

simulation converges towards a solution, so does the rotor design in parallel, thus averting the need for any additional design iterations. The rotor design follows the pattern illustrated in figure 5.13.

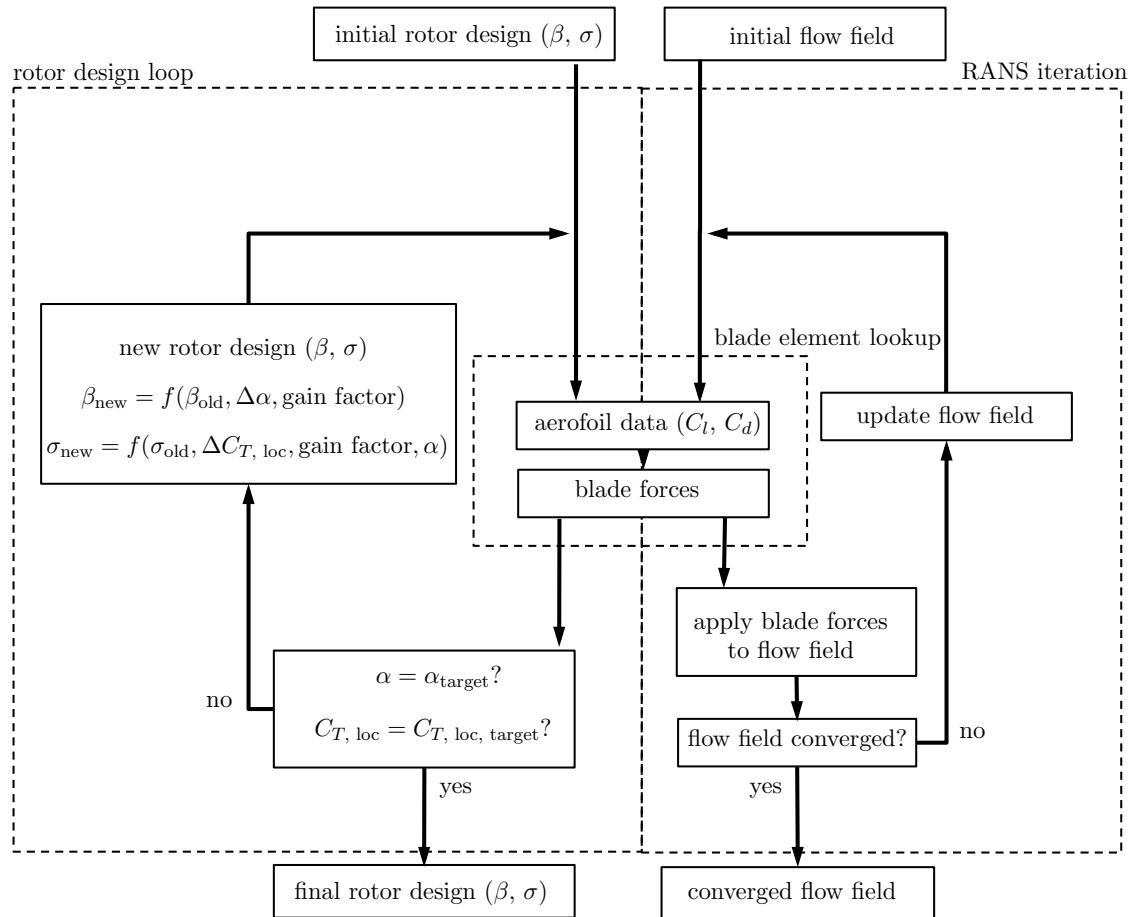


Figure 5.13: Flow chart of the RANS-BEM rotor design procedure.

The input values required for the design iteration are the aerofoil data (immediately resulting in the target angle of attack, α_{target}), initial rotor geometry and a target value for local thrust, $C_{T,\text{loc}}$. After each RANS iteration the current values of α and $C_{T,\text{loc}}$ are compared to the respective target values. The difference between target values and actual values is computed and multiplied by a gain factor (e.g. 0.05) which may be adjusted manually. The resulting incremental change is then applied to the design until the solution converges and the target values are met.

There are certain physical limitations which result in the target values not being reached. One such limitation is the solidity limit applied to the rotor, which has been set to $\sigma_{\text{imit}} = 0.95$. This limit prevents the rotor design tool from generating unrealistic rotor designs close to the hub.

5.5.3 Results of rotor design

The initial rotor geometry employed for the design iteration is rotor V1, which was previously used in the validation study. For the ducted and open-centre turbines the initial rotor geometry has been cropped at the inboard section in order to match the overall rotor dimensions. All design simulations for the three types of devices have been performed on a device diameter of $D_{\text{device}} = 16$ m in a domain of blockage ratio $B = 3.5\%$. Hubs and ducts have been included where applicable. However, further support structures have been omitted here. Duct shapes and dimensions are the same as for the actuator disc simulations. As discussed previously, the typical tip-loss mechanism is not present in ducted turbines, hence the tip-loss model was used only in the design simulation of the bare turbine. Table 5.2 lists the simulation inputs for the flow conditions, rotor and aerofoil characteristics.

Table 5.2: Inputs for rotor design

| Device type | bare | ducted | open-centre |
|------------------------|----------------------------|----------------------------|----------------------------|
| Upstream flow velocity | $U_{\infty} = 2\text{m/s}$ | $U_{\infty} = 2\text{m/s}$ | $U_{\infty} = 2\text{m/s}$ |
| Tip-speed ratio | $3 < \lambda < 7$ | $2 < \lambda < 6$ | $2 < \lambda < 5$ |
| Aerofoil | Risø-A1-24 | Risø-A1-24 | Risø-A1-24 |
| Number of blades | $N_B = 3$ | $N_B = 3$ | $N_B = 3$ |
| Initial rotor geometry | rotor V1 | rotor V1 (red.) | rotor V1 (red.) |
| Tip-loss model | on | off | off |
| Target design thrust | $1.8 < C_{T,loc} < 2.6$ | $0.5 < C_{T,loc} < 1.0$ | $0.7 < C_{T,loc} < 1.3$ |

As U_{∞} is kept constant, λ is varied through rotational velocity of the rotor, Ω . In a real world application, the rotor speed may vary according to the inflow velocity, in order for the turbine to operate close to optimal λ .

The design routine is performed multiple times for a range of $C_{T,loc, target}$ and λ , resulting in a matrix of rotor designs. The designs are then compared based on their performance and the design with maximum performance is chosen as the device rotor design. The rotor design process uses the power coefficient as defined in equation (4.8) as the performance criteria to be maximised. Thus the rotors are designed for maximum power for a given device frontal area. Details of how power and hence the power coefficient are extracted from the results of the RANS-BEM simulations are discussed in section 5.6.

5.5.3.1 Bare turbine rotor design

Dimensions of the bare turbine including both disc and hub were chosen after the review of current designs used in industry and are presented in figure 5.14. The ratio of hub radius to tip radius is $R_{hub}/R_{tip} = 1.2\text{m}/8\text{m} = 15\%$, and the disc is located at 22% of the nacelle length from the nose. The ends of the hub are modelled as cones with rounded tips.

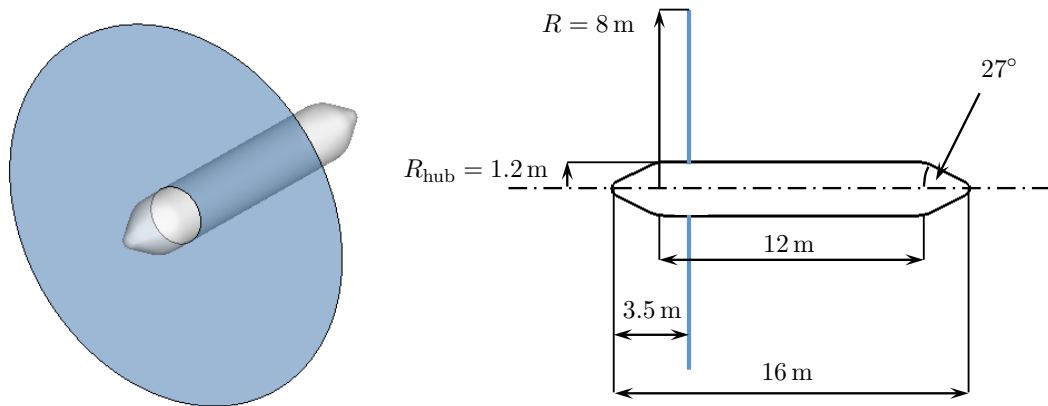


Figure 5.14: Bare rotor design.

Figure 5.15 presents a contour plot of the performance results for a design space of $2.2 < C_{T,loc, target} < 2.5$ and $5 < \lambda < 7$, and parameter increments of $\Delta C_{T,loc, target} = 0.1$ and $\Delta\lambda = 1$. Maximum power is found at $C_P = 0.60$ for $C_{T,loc, target} = 2.4$ and

$\lambda = 5$ (at $C_T = 0.98$ similar to porous disc simulations). Lower tip speed ratios of $\lambda < 5$ lead to unphysical rotor designs featuring too high solidities, hence these results were excluded. Note that while a maximum is found, the difference in C_P for the results shown remains small.

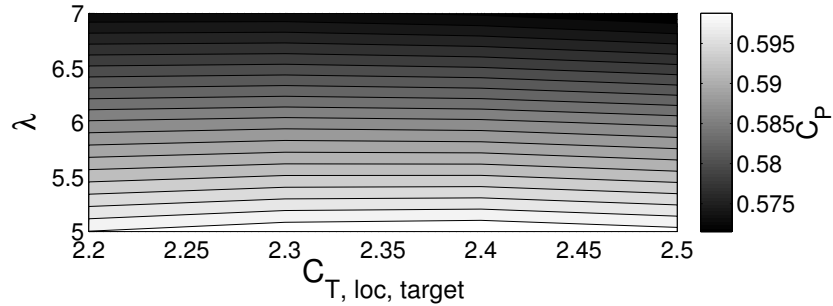


Figure 5.15: Bare rotor performance over $C_{T,loc} - \lambda$ design space.

5.5.3.2 Ducted turbine rotor design

Figure 5.16 illustrates the ducted device dimensions. The geometry of the duct corresponds to that used in chapter 4, apart from the inclusion of the hub. The hub is placed symmetrically within the disc and duct and follows a typical design proposed by the industry (van Drentham Susman *et al.*, 2011).

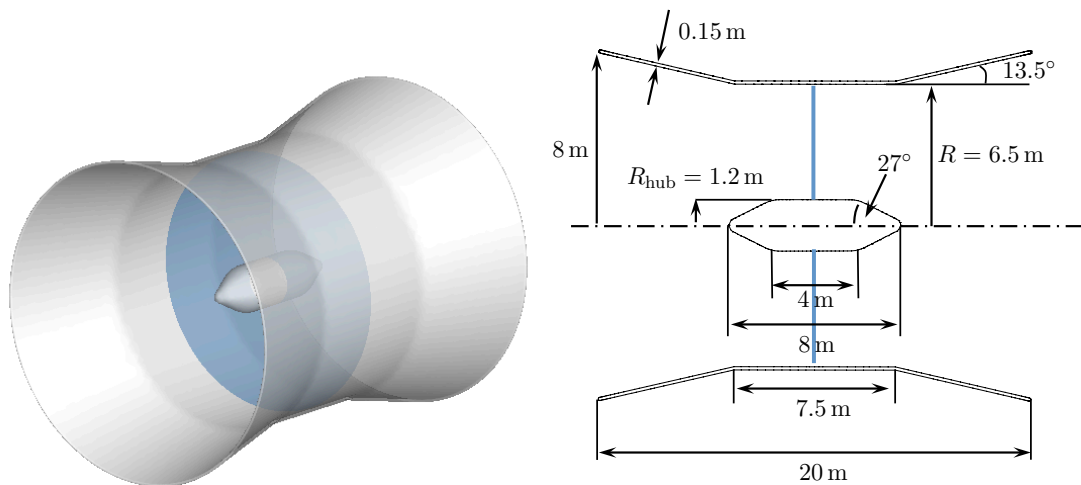


Figure 5.16: Ducted device design.

Figure 5.17 presents the performance results for the ducted rotor design space of $0.5 < C_{T,loc, target} < 0.7$ and $2 < \lambda < 5$, and parameter increments of $\Delta C_{T,loc, target} = 0.1$ and $\Delta\lambda = 1$. Maximum power is found at $C_P = 0.378$ for $C_{T,loc, target} = 0.6$ and $\lambda = 4$.

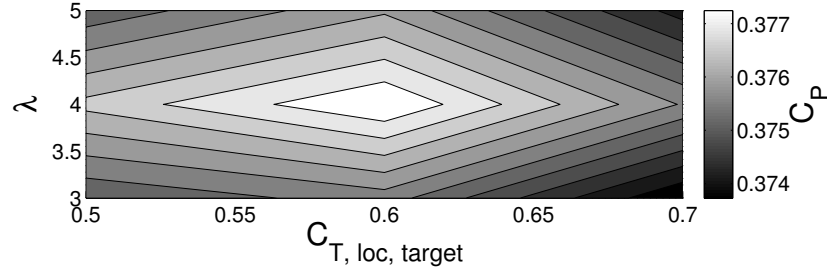


Figure 5.17: Ducted rotor performance over $C_{T,loc} - \lambda$ design space.

5.5.3.3 Open-centre turbine rotor design

As for the ducted turbine, the geometry of the open-centre outer duct remains unchanged except for the inclusion of a hub. In the case of the open-centre turbine, the hub is in the shape of an axially extruded ring with rounded leading and trailing edges, see Fig 5.18. Due to the nature of this design, the assumption is that the generator is housed within the outer duct and that the rotor blades are attached to a rotating ring section within that duct. A single aperture size is investigated, $R_{ap} = 1.65$ m.

Figure 5.19 presents the results for the design iteration of the open-centre turbine for a target variation of $0.8 < C_{T,loc, target} < 1.1$ and $2 < \lambda < 4$, and parameter increments of $\Delta C_{T,loc, target} = 0.1$ and $\Delta\lambda = 1$. Maximum power is found at $C_P = 0.333$ for $C_{T,loc, target} = 1.0$ and $\lambda = 3$. Table 5.3 summarises the results of the rotor design for all three device types.

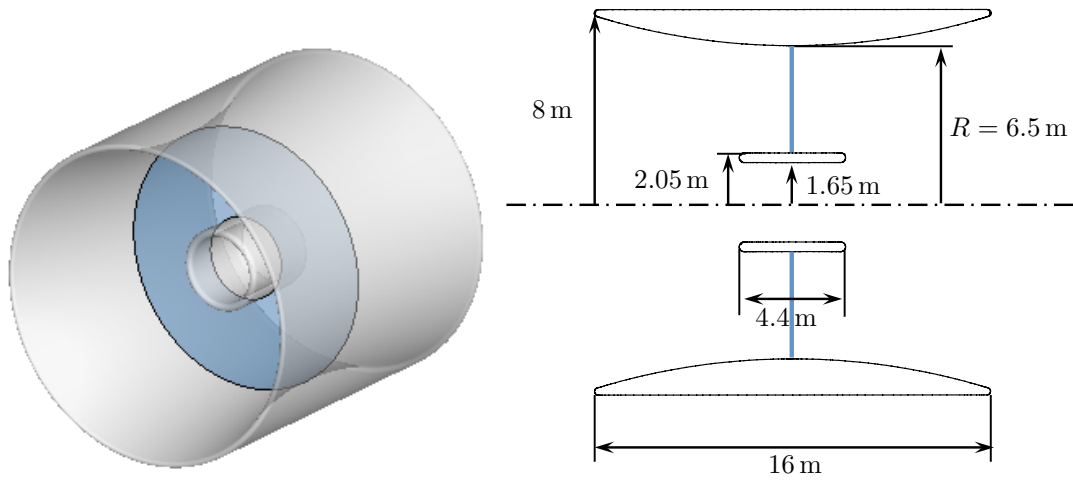


Figure 5.18: Open-centre device design.

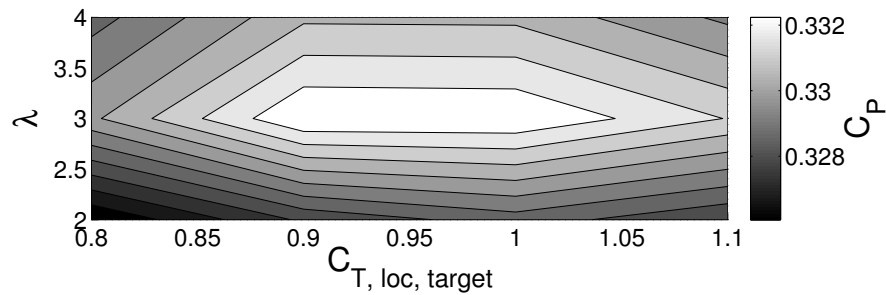


Figure 5.19: Open-centre rotor performance over $C_{T,loc} - \lambda$ design space.

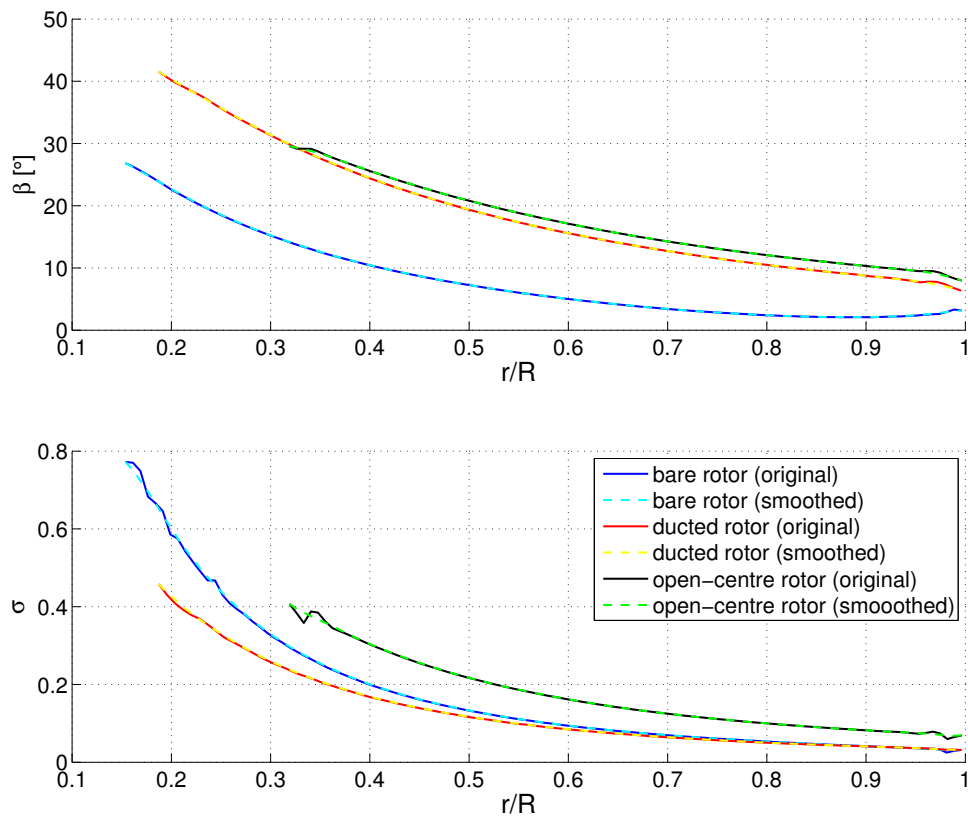
5.5.3.4 Rotor design comparison

The three rotor designs for which maximum power is achieved have been selected. The rotor designs obtained through the RANS-BEM design tool exhibit anomalies near the root and the tips, see figure 5.20. These anomalies stem from the rotor design process which adjusts the rotor design during each iteration. In areas of highly sheared flow, such as near the tips and the hub, the iteration process does not fully converge on a design solution, creating these anomalies in the design. As it was determined that these discretisation anomalies were of numerical nature, data smoothing was applied. Following data smoothing using a moving average function, the data for these rotors is plotted in figure 5.20. Note that the radial position is plotted as a function of tip

Table 5.3: Results of the rotor design iteration

| Device type | bare | ducted | open-centre |
|------------------------|-------------------|-------------------|-------------------|
| Design thrust | $C_{T,loc} = 2.3$ | $C_{T,loc} = 0.6$ | $C_{T,loc} = 1.0$ |
| Design tip-speed ratio | $\lambda = 5$ | $\lambda = 4$ | $\lambda = 3$ |
| Power at design point | $C_P = 0.505$ | $C_P = 0.378$ | $C_P = 0.333$ |

radius, R . Due to the changes in tip radius between bare and ducted turbine the relative position of the blade root changes, even though R_{hub} is of equal size for both designs.

**Figure 5.20:** Result of the rotor design process for all three devices.

Significant differences in the optimal rotor design are noticeable when comparing the three custom designs. As can be seen in figure 5.20 the twist of the ducted and open-centre rotors is similar, but significantly higher than for the bare rotor by $10^\circ - 15^\circ$ along the full blade span. This offset in twist angle is due to the higher flow velocities

through the turbine plane achieved by the ducted devices. Together with a lower λ to achieve peak performance the twist needs to be increased compared to the bare rotor in order for the rotor blade to operate close to the optimal angle of attack, $\alpha_{target} = 7^\circ$.

The results of blade solidity derive from the requirement to resist the flow by the given $C_{T,loc, target}$, which is dependent on both σ_r and λ . The open-centre turbine is designed at a lower λ but for a higher $C_{T,loc, target}$, compared to the ducted turbine. Therefore in order to achieve $C_{T,loc, target}$, σ_r must increase significantly compared to the ducted turbine, as seen in figure 5.20.

5.6 Axial inflow

After obtaining the rotor designs for the turbine devices, the designs are employed in a variety of simulations; first in uniform, axially aligned inflow, and later in yawed flow condition.

Examining the results of the RANS-BEM simulations one must take into account the differences to the actuator disc simulations discussed in chapter 4. The two main differences on the flow field are the addition of a circumferential force component and the variation in force coefficients both radially and, in the case of non-axisymmetric flow, azimuthally. The circumferential force component imparts a swirl on the flow in the opposite direction of blade rotation.

Whereas for the actuator disc, turbine power is simply the product of the axial thrust applied to the flow and the axial velocity, the power extracted by a real rotor is extracted through torque - a physical mechanism captured in the RANS-BEM simulations. Therefore, compared to the actuator disc simulation, the axial thrust component now only contributes to the drag of the device, whereas the power is purely derived from the torque.

The RANS-BEM simulations include hubs, and thus more structures placing a force on the fluid, therefore more energy is removed from the flow, affecting basin efficiency. All of the forces acting in the flow direction will therefore need to be included in any basin efficiency calculation.

5.6.1 Comparison of steady and unsteady simulations

A number of unsteady simulations were conducted in order to investigate the occurrence of unsteady flow features. As a test case the ducted turbine was simulated using both steady and unsteady RANS-BEM using three time-step levels, $\Delta t = 0.1$ s,

0.05 s, and 0.01 s. The ducted turbine was chosen as a test case, as it is the least hydrodynamically efficient design investigated within this study. It exhibits more flow separation than the bare and open-centre turbines and is more likely to exhibit unsteady flow features. The tests were conducted at the maximum thrust point, $\lambda = 4$, which is also the design point.

A first indication that unsteady flow features play only a minor role in the configuration tested, is that the simulation residuals and force coefficients converge for the steady simulation case. No fluctuations were found in the result of the unsteady simulations (apart from residual numerical fluctuations also present in the steady result), further supporting this finding. Table 5.4 presents the results of the error of the thrust force, $\epsilon(T_\xi)$ of the duct and hub for the four analysed cases. The converged result of $\Delta t = 0.01$ s was used as the reference value. As no fluctuations were found, the unsteady results did not require averaging. From table 5.4 it can be seen that all of the unsteady cases converge toward the same value of drag and that the error in drag on the structures using the steady simulation is found to be negligible.

Table 5.4: Comparison of steady and unsteady simulations.

| | steady | unsteady $\Delta t = 0.1$ s | unsteady $\Delta t = 0.05$ s | unsteady $\Delta t = 0.01$ s |
|---------------------------------|--------|--------------------------------|---------------------------------|---------------------------------|
| $\epsilon(T_{\xi,\text{duct}})$ | 0.08 % | < 0.01 % | < 0.01 % | N/A |
| $\epsilon(T_{\xi,\text{hub}})$ | 0.01 % | < 0.01 % | < 0.01 % | N/A |

Next, the horizontal flow field is analysed by plotting transversal pressure profiles of the xz -plane, presented in figure 5.21. Both static (gauge) and dynamic pressure are presented for half the domain at various locations upstream and downstream of the device. Minor differences are observed in the flow field between steady and unsteady simulations, in particular in areas of large gradients.

The effect on the flow through the turbine disc is analysed by plotting values of velocity, angle of attack, and local thrust coefficient as a function of disc radius.

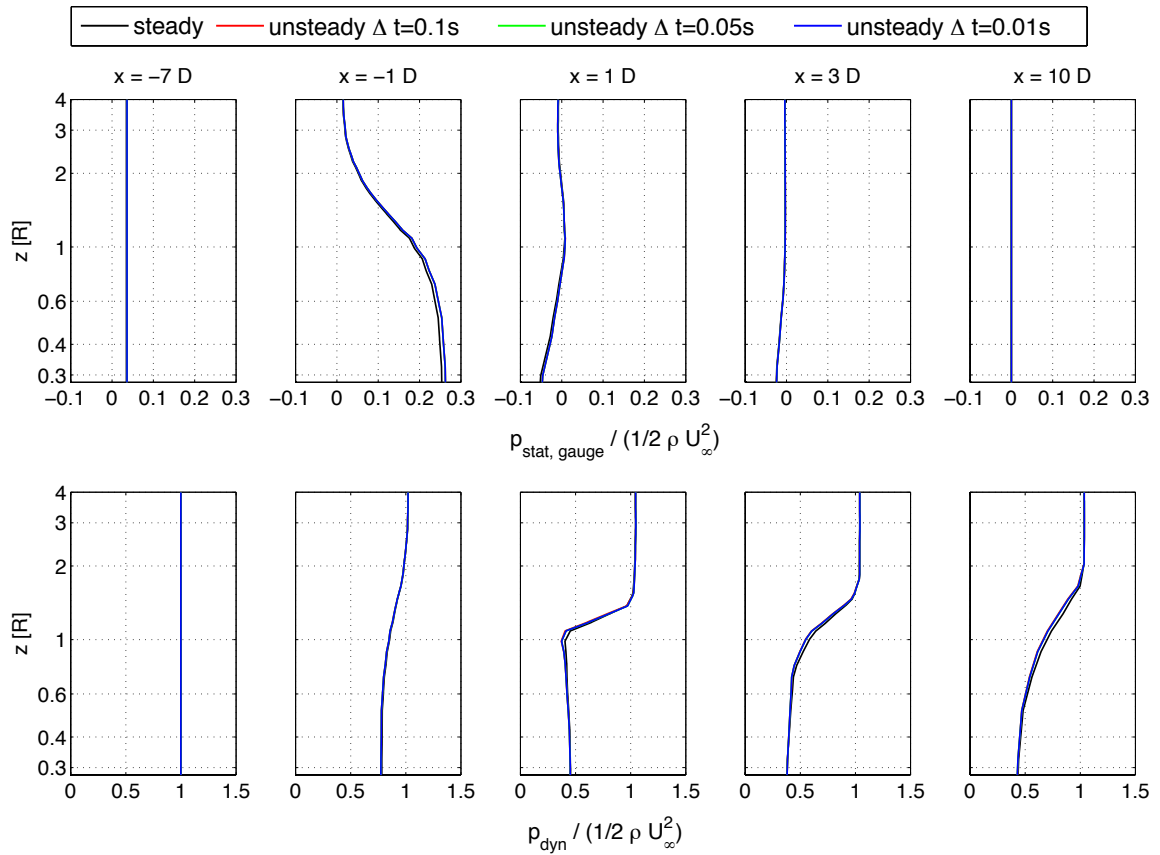


Figure 5.21: Pressure field of the ducted turbine using steady and unsteady simulation. Note vertical axis uses a base 10 logarithmic scale.

As can be seen from figure 5.22, no visible differences in these flow parameters are observed at the turbine disc between steady and unsteady simulations.

No fluctuations were found for the converged unsteady simulation cases. Minor variations are visible in the flow field, however, no effect is found on the rotor disc or the mean forces acting on the duct. The error in power produced by the disc was less than 0.1% for the steady simulation case. The simulations in this chapter are therefore conducted using steady simulations. Simulating the devices in yawed flow leads to larger separation regions on the duct and the hub. Test cases were therefore also conducted in yawed flow, and indicated that steady simulations could also be applied for the devices in yawed inflow.

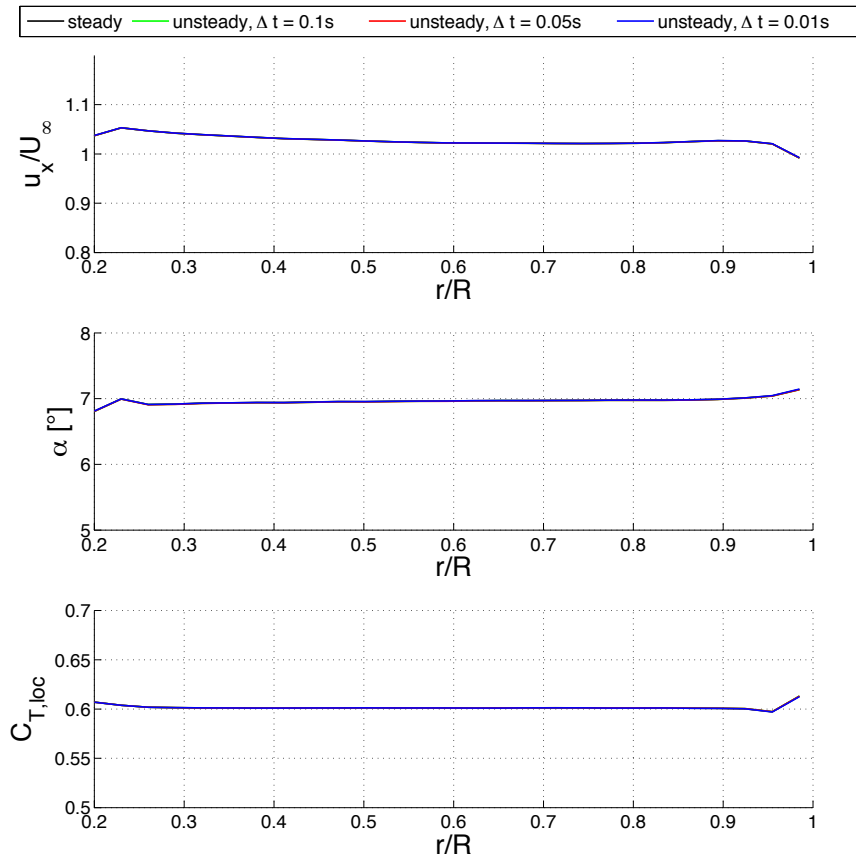


Figure 5.22: Radial distribution of axial velocity, angle of attack and local thrust coefficient presented for steady and unsteady simulations.

5.6.2 Bare turbine in axial inflow

The bare turbine configuration presented in section 5.5.3.1 is analysed in axial flow and the analysis methodology is presented. The analysis outline follows that of the actuator disc, discussing first the flow field, then the thrust acting on the turbine and finally the performance of the turbine.

5.6.2.1 Flow field of the bare turbine in axial inflow

Fig 5.23 presents the streamlines and velocity contours in a horizontal cut-plane of the bare turbine simulations for various levels of λ , including the design point at $\lambda = 5$. As λ is increased, the thrust acting on the fluid increases, and hence, as observed

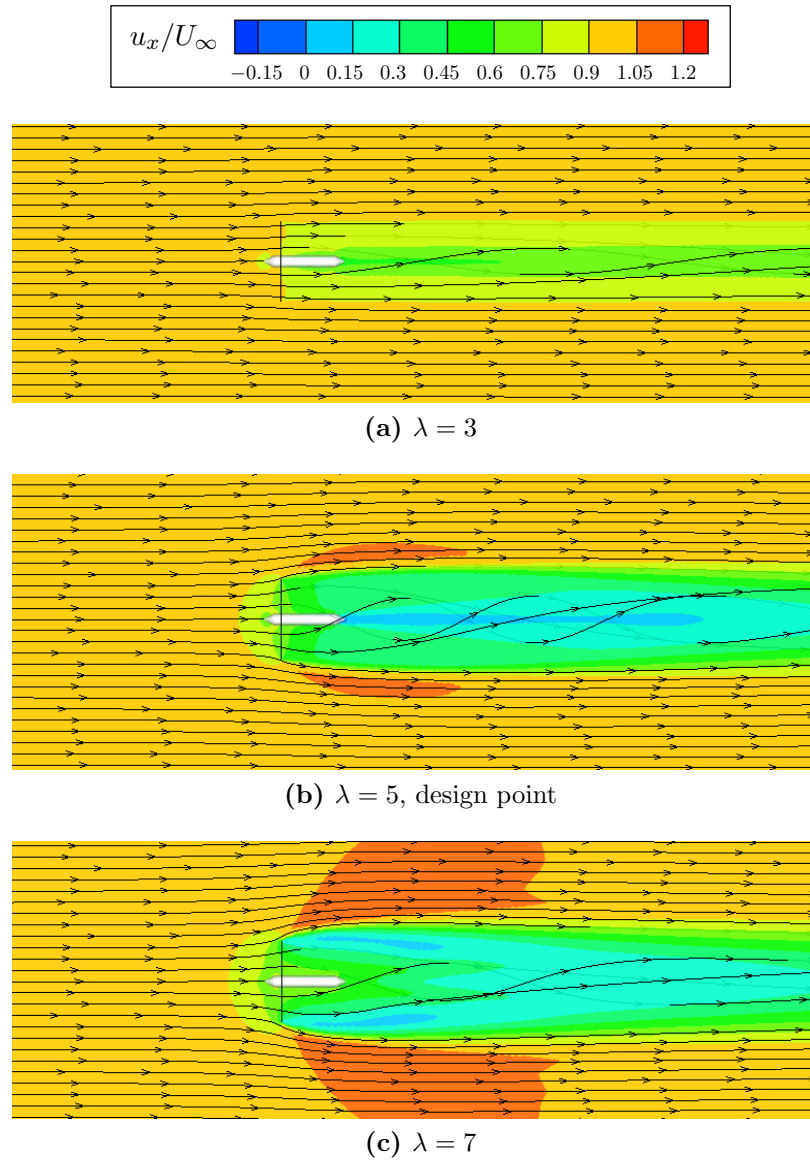


Figure 5.23: Flow field of the bare turbine shown in the horizontal cut-plane for various levels of λ . The rotor plane is shown by a straight vertical line.

for the actuator disc simulations, the approaching streamtube widens. A number of differences are visible compared to the actuator disc flow field. The hub is explicitly modelled and therefore generates a wake within the rotor wake. Swirl is generated at the rotor plane and is clearly visible in the wake. Further, radial variation in velocity through the disc is observed.

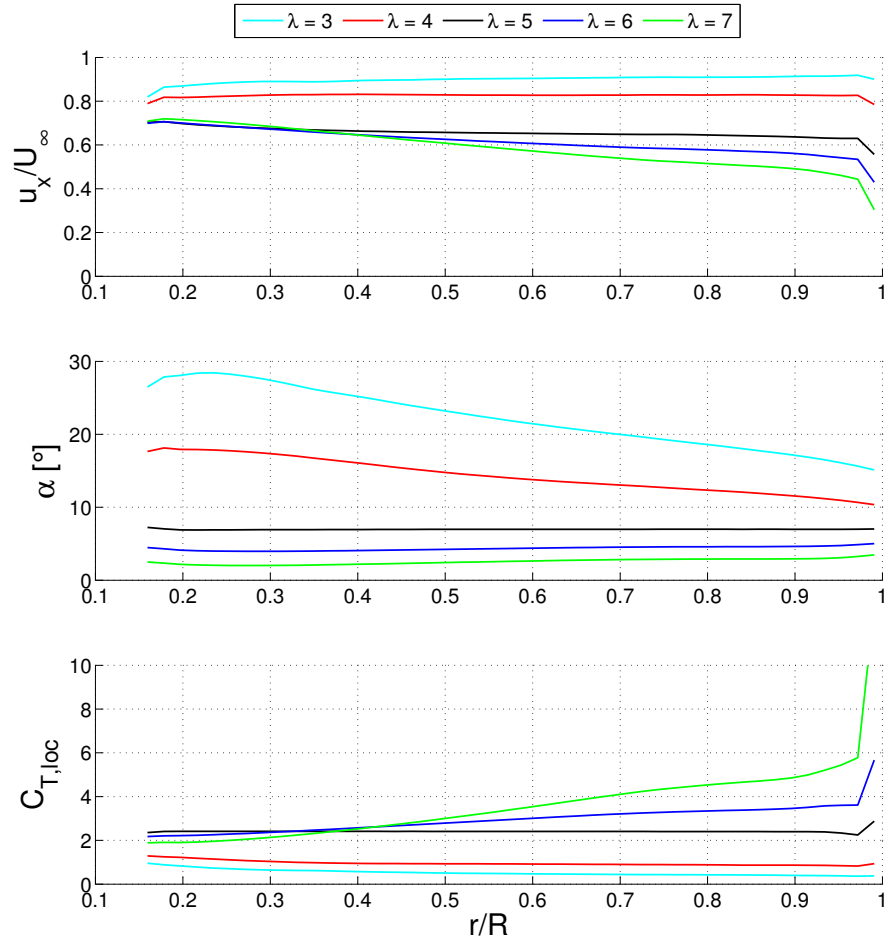


Figure 5.24: Azimuthally averaged flow results of the bare turbine for $3 \leq \lambda \leq 7$.

As the flow is axisymmetric around the rotation axis, it is convenient to present the flow data at the rotor plane as a function of radial position and thus more easily compare the data of design and off-design operation. Azimuthal averaging is applied to remove numerical scatter. The results for velocity, angle of attack and local thrust coefficient are presented in figure 5.24.

At the design point, $\lambda = 5$, the values of α and $C_{T,loc}$ are nearly constant across the span, as per design target, as is the axial velocity at the rotor. For low tip-speed ratio operation ($\lambda = 3, 4$) the flow induction is reduced and u_x therefore increased. The angle of attack increases at the hub, leading to stall on the aerofoil. $C_{T,loc}$ is

significantly reduced across the whole span. For high tip-speed ratio operation, a drop in axial velocity occurs towards the tip of the blade due to the increase in the radial velocity component. As the rotational velocity is increased ($\lambda = 6, 7$), the angle of attack decreases across the whole span relative to the lower tip-speed ratios, with a lesser reduction in the tip region due to the reduced axial flow component. Though the thrust values only change moderately, the local thrust coefficient increases sharply in the tip region due to the drop in local axial velocity in this region (note that u_x is used for normalisation in $C_{T, loc}$).

5.6.2.2 Thrust of the bare turbine in axial inflow

The thrust on the bare turbine is split into two components, the thrust on the hub and the thrust on the rotor. In general, each of these thrust components is described by a force vector, but in the case of axial flow the non-axial components are zero due to flow symmetry. The force on the rotor results directly from the BEM calculation within the code (see equation (5.18)) while the force on the hub is obtained through integration of surface pressure and wall shear stress, as introduced for the duct in section 4.5.2. Figure 5.25 presents the results of this thrust analysis. Both the thrust on the rotor and the hub are normalised using $1/2 \rho U_\infty^2 A_{device}$ in order to present the quantitative difference in thrust posed by the elements of the device.

It can be seen from figure 5.25 that for the aligned flow case the thrust of the hub is very small compared to that of the rotor. Although small compared to the rotor thrust, the thrust of the hub more than doubles over the range of λ investigated. The thrust on the rotor also increases with increasing λ and reaches a thrust coefficient of $C_T = 0.98$ at design point.

In order to validate the results obtained above, an alternative method for calculating the overall thrust on the flow is used. It is possible to perform a momentum balance

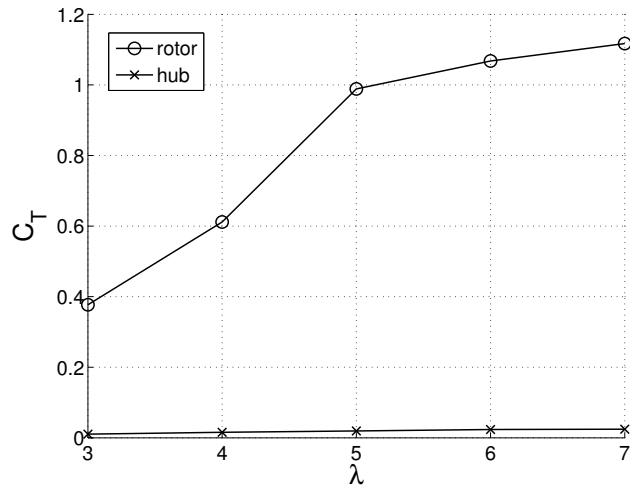


Figure 5.25: Thrust components of the bare turbine at various λ .

on the simulation domain using surface integrals on the inlet and outlet of the domain and thus determine the total thrust exerted on the flow by the device. The result of the overall thrust in x direction is the same (error < 1 %) as for the above method.

5.6.2.3 Performance of the bare turbine in axial inflow

The same approach to performance analysis is taken, as previously employed for the actuator disc simulations. The main difference to the actuator disc simulations is the method in which power is computed. In RANS-BEM, the circumferential blade forces are used according to equation (5.21). A further difference between RANS-BEM and the actuator disc simulations is a reduced reference area for the power density ($A_{\text{ref, PD}} = A_{\text{rotor}}$) due to the inclusion of the hub for the former. In order to calculate the power extracted from the flow, the axial forces in x -direction (see previous section) are employed according to the definitions in section 4.4.4.3.

For the bare turbine simulated with RANS-BEM all three measures of performance reach their peak at the design point, $\lambda = 5$. The power coefficient increases steeply until it reaches a value of $C_{P,\text{max}} = 0.6$, after which it drops off moderately for higher

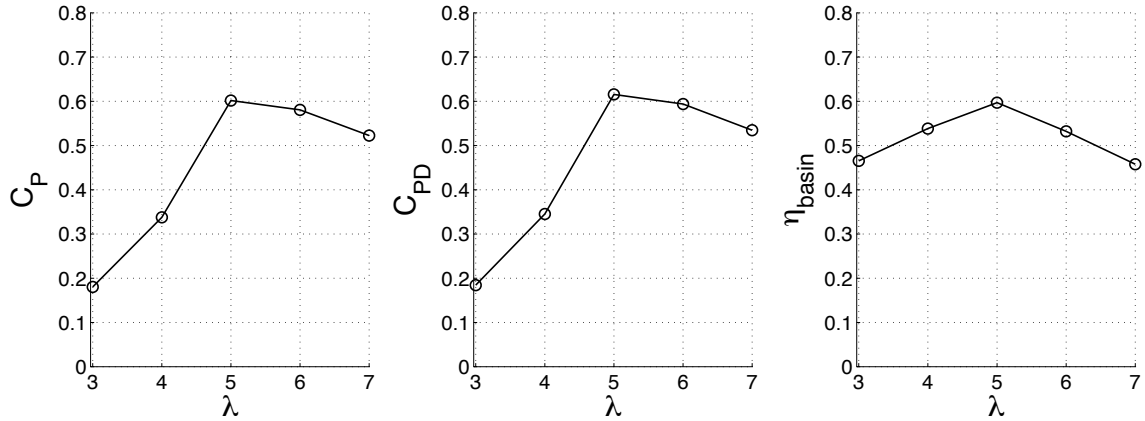


Figure 5.26: Performance of the bare turbine at various λ .

λ . The inclusion of the hub means that the power and power density differ slightly, however the difference is marginal, with $C_{PD,\text{max}} = 0.62$. For the basin efficiency the rise and drop off is comparatively flat and almost symmetrically centred around the maximum of $\eta_{\text{basin}} = 0.6$. For low λ , the moderate increase of η_{basin} is due to the power increasing more steeply than the thrust. For $\lambda > \lambda_{\text{design}}$, power decreases slightly, while the thrust of the device increases further, thus leading to a decrease in basin efficiency.

5.6.3 Ducted turbine in axial inflow

The ducted turbine is analysed in axial flow using the same metrics as described in the previous section. Various operating points are examined through a variation of tip-speed ratio, mimicking changes in rotational velocity for a given inflow velocity.

5.6.3.1 Flow field of the ducted turbine in axial inflow

Figure 5.27 presents the flow field results for the ducted turbine in axial flow for $2 \leq \lambda \leq 6$. For comparison the contour levels are the same as in Fig 5.23 and also the same as those used for the actuator disc analysis.

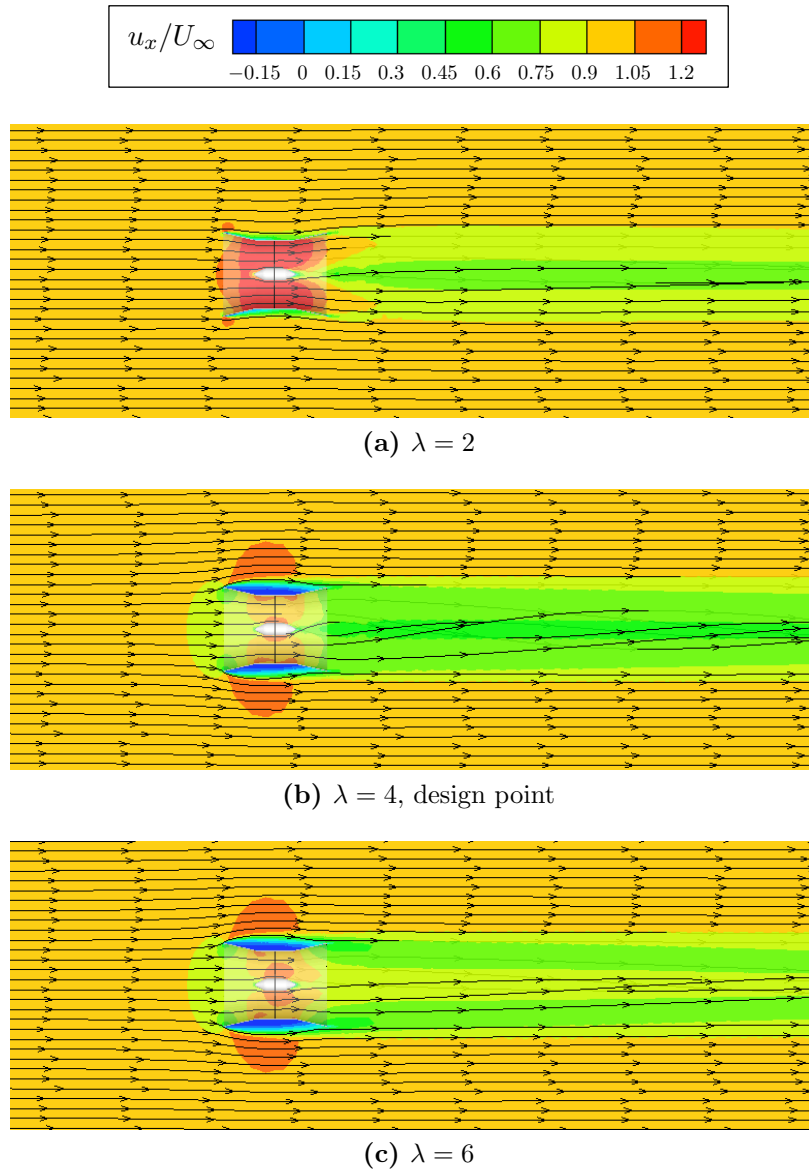


Figure 5.27: Flow field of the ducted turbine for various levels of λ .

The general flow features on the duct show the same features observed for the actuator disc simulations. For low λ , and therefore low flow resistance within the duct, the flow stays attached to the duct exterior (nozzle-contoured flow) and a significant velocity increase is visible within the duct, with the highest velocity reached in the region of the rotor plane. When moving to higher λ , separation occurs on the outer surface of the duct as described in section 4.5.1. Though not pictured here, the separation

bubble starts to form at $\lambda = 3$ and is fully developed at $\lambda = 4$. No separation is observed on the duct interior surface, as in the actuator disc simulations.

As the resistance within the duct is increased, the flow velocity is reduced approaching the duct, before accelerating within the duct. At $\lambda = 4$ (design point) this effect balances, so that the flow velocity at the rotor is approximately equal to the free-stream velocity. Moving past the design point, the rotor within the ducted turbine applies less thrust to the flow (see figure 5.29 in following section) such that the axial flow velocity at the rotor plane increases slightly again. The swirl velocity is also reduced, following a reduction in torque. A radial variation in velocity through the rotor can be observed, most pronounced at $\lambda = 6$.

Azimuthally averaged flow data is presented in figure 5.28 for five levels of λ , with the design point, $\lambda = 4$, presented in black. As seen in figure 5.27, the increase in velocity inside the duct is substantial for tip-speed ratios below the design point. At the design point the axial velocity at the rotor is fairly constant at $u_x/U_\infty \approx 1$, with slight increases for higher λ as discussed above. This variation in axial velocity, combined with the decreased / increased rotational velocities compared to the design point, leads to a substantial increase in α for low λ and a moderate drop in α for high λ . While these changes in axial velocity and angle of attack lead to low local thrust coefficients across the whole blade span for low tip-speed ratios, the result for high tip-speed ratios is more varied. Though the increase in α across the span is marginal, the local thrust coefficient increases significantly across the blade span to the tips. This can partially be attributed to the increase in blade incident velocity, U_{rel} , which affects the blade thrust quadratically, partially to the variation in α , leading to a variation in C_l and hence to a variation in axial blade force, and partially to the slight drop in axial velocity towards the tip region, which affects the normalisation quadratically.

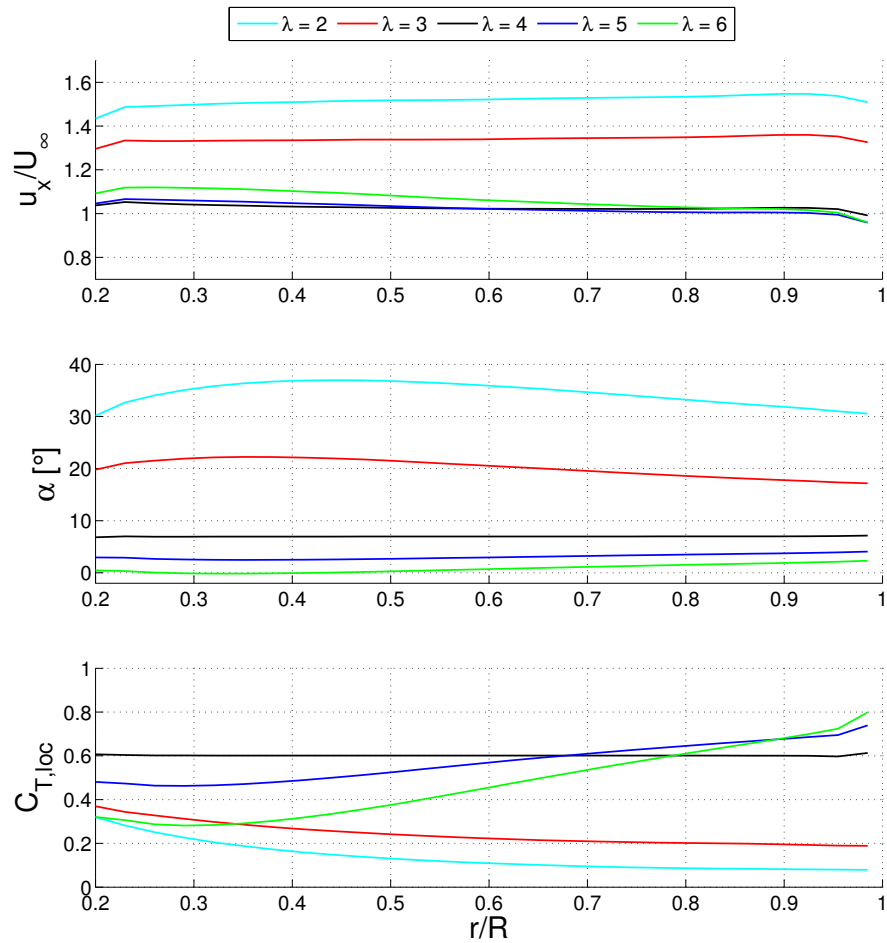


Figure 5.28: Azimuthally averaged flow results of the ducted turbine at $2 \leq \lambda \leq 6$.

5.6.3.2 Thrust of the ducted turbine in axial inflow

The axial thrust on the ducted turbine is obtained in the same way as for the bare turbine, with the thrust on the duct being obtained in the same manner as for the hub. Figure 5.29 presents the results for a range of λ with the thrust split into three components; the rotor, duct and hub.

The qualitative results compare well to those obtained with the actuator disc simulation. As for the actuator disc, rotor and duct thrust are of a similar magnitude. The thrust on the duct reaches its maximum when the flow on the outer duct surface is

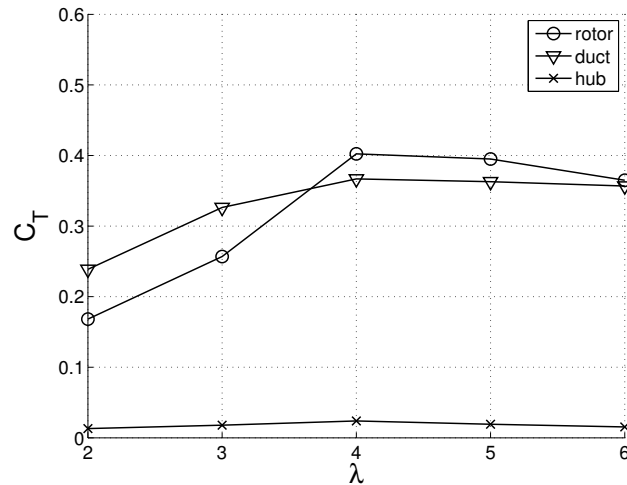


Figure 5.29: Thrust components of the ducted turbine at various λ .

fully separated, at $\lambda = 4$. The thrust on the hub is small in comparison and reaches a maximum at the design point. The total thrust of the device at the design point is $C_{T,\text{tot, duct}} = 0.79$ and thus lower than that of the bare turbine at the design point ($C_{T,\text{tot, bare}} = 0.98$), in line with the actuator disc simulations.

The main difference to the actuator disc simulations is that the rotor thrust does not increase past the design point, but actually decreases slightly for higher tip-speed ratios, a feature that can also be observed in the results of a ducted turbine presented by McIntosh *et al.* (2011).

5.6.3.3 Performance of the ducted turbine in axial inflow

The performance of the ducted turbine is presented in figure 5.30. The overall performance peak, applicable to all measures of performance, is reached at the design point of $\lambda = 4$. The maximum power coefficient and power density coefficient are $C_{P,\text{max}} = 0.39$ and $C_{PD,\text{max}} = 0.59$ respectively, which are roughly 10% lower than the values reached with actuator disc simulations, also given here. For the basin

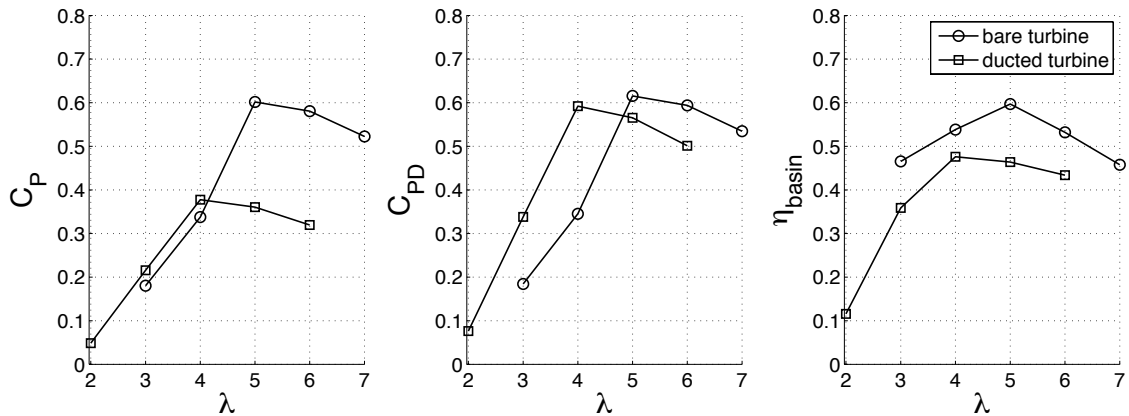


Figure 5.30: Performance of the ducted turbine.

efficiency the peak occurs at the design point, with a value of $\eta_{\text{basin, max}} = 0.48$, which is 15% lower than that of the actuator disc simulations at maximum power.

Compared to the bare turbine, $\eta_{\text{basin, max}}$ is reduced by 15%. For $\lambda < \lambda_{\text{design}}$, the significant duct drag leads to further reductions in efficiencies compared to the bare turbine. For $\lambda > \lambda_{\text{design}}$ the ducted rotor unloads, leading to a reduced power extraction from the flow, and therefore a result in η_{basin} closer to that of the bare turbine.

5.6.4 Open-centre turbine in axial inflow

The same analysis method is now applied to the open-centre turbine. As presented in section 5.5.3.3, a single aperture size is studied.

5.6.4.1 Flow field of the open-centre turbine in axial inflow

The flow field of the open-centre turbine is presented in figure 5.31. The flow features on the outer surface of the duct are comparable to the results presented for the actuator disc. For all but the lowest λ investigated, a small separation bubble forms

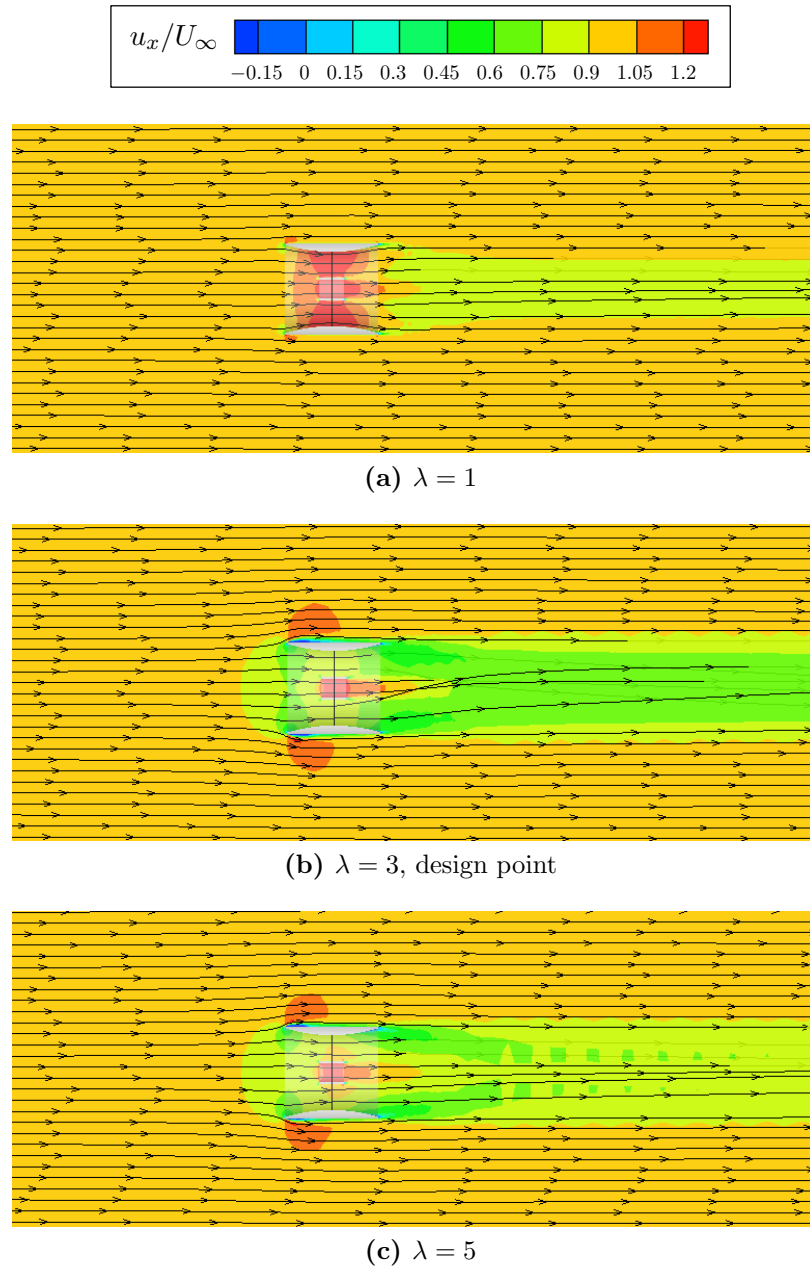


Figure 5.31: Flow field of the open-centre turbine for three levels of λ .

at the outer surface of the duct near the leading edge. For $\lambda = 5$ some separation is visible on the duct interior near the diffuser exit.

A ring-shaped hub has been placed around the aperture in order to simulate a blade support at the root, as has been suggested by the industry (see O'Rourke *et al.* (2010)). Although the hub ring introduces further flow features on its inner and

outer surfaces, the general flow feature of the aperture – flow jetting – is clearly visible at all levels of λ . In general, it seems that the jetting flow helps the wake mixing process due to the additional mixing layer present at the interior of the wake, thus leading to faster wake recovery than for the ducted turbine.

Both the flow velocity at the rotor plane and the swirl in the wake vary with λ much in the same way as the ducted turbine. A significant velocity increase is visible through the rotor plane at low tip-speed ratios. As the tip-speed ratio increases towards the design point, $\lambda = 3$, this effect is balanced by the flow expansion close to the duct inlet. For $\lambda > 3$ thrust exerted by the rotor drops, as previously observed in figure 5.27 and thus the velocity at the rotor plane again increases. Maximum swirl is observed at the design point, where maximum torque is achieved.

The azimuthally averaged rotor data for the open-centre turbine (figure 5.32) follows the same trends discussed for the ducted turbine, presented in figure 5.28. As for the ducted turbine, strong radial variations in $C_{T,loc}$ are observed, and more moderate radial variations of α and u_x . For $\lambda < 3$, α is very high, leading to stalled operation.

5.6.4.2 Thrust of the open-centre turbine in axial inflow

The results of the thrust analysis of the forces in the flow direction are presented in figure 5.33. As before, the force components are split into rotor, duct and hub ring. Immediately noticeable is significantly reduced loading on the duct compared to the ducted turbine (see figure 5.29). This can be attributed to the more streamlined exterior duct shape which results in only a small separation on the leading edge outer surface. The thrust variation of the rotor is comparable to that of the ducted turbine, with a steep increase for low λ until the design point and then a slight drop off for higher λ . In a similar manner to the other devices, the thrust on the hub ring is an

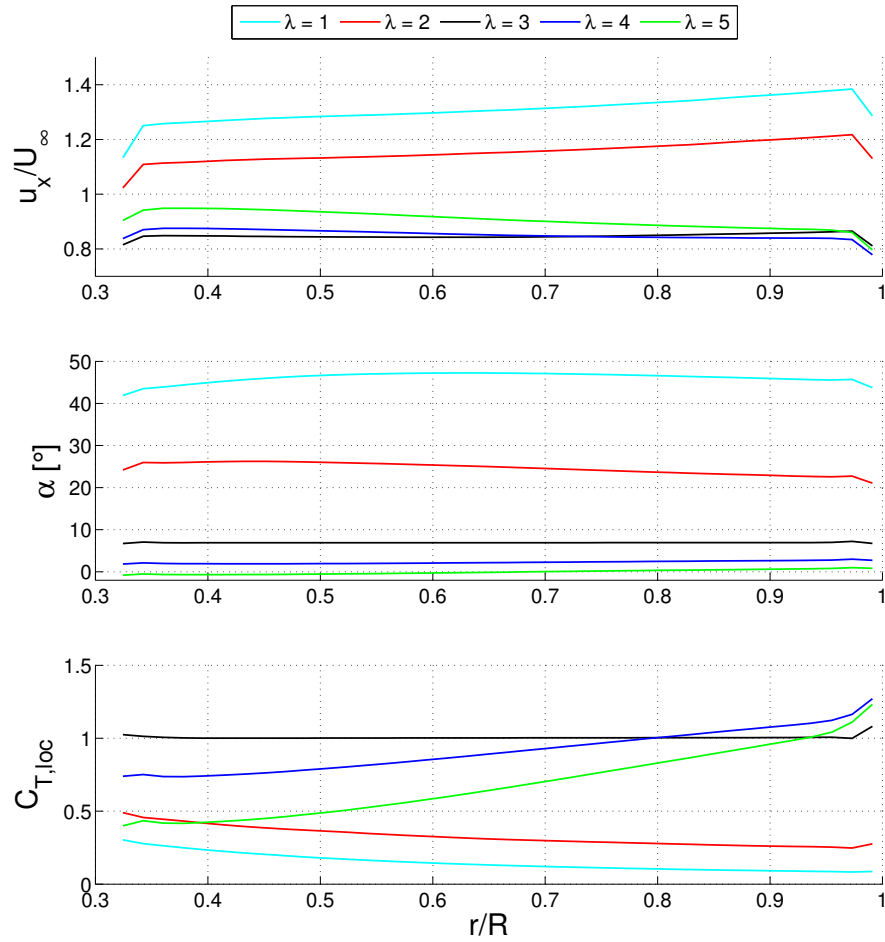


Figure 5.32: Azimuthally averaged flow results of the open-centre turbine at various λ .

order of magnitude smaller than that of rotor and duct. Minimal variation with λ is observed for $C_{T, \text{hub ring}}$, as the hub ring presents little frontal area for pressure forces to act on. The total thrust of the device at design point is $C_{T, \text{tot}} = 0.63$, significantly lower than both bare and ducted turbines.

5.6.4.3 Performance of the open-centre turbine in axial inflow

The three measures of performance for the open-centre turbine are presented in figure 5.34. All of the maximum performance values in figure 5.34 lie roughly 10–15% below those of the open-centre turbine actuator disc simulations. While the perfor-

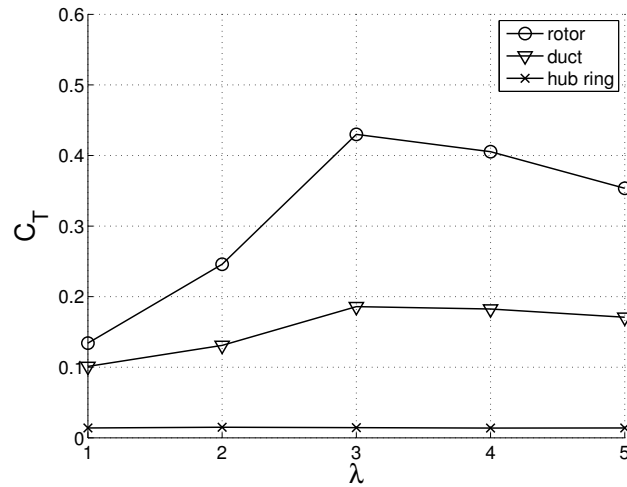


Figure 5.33: Thrust components of the open-centre turbine at various λ .

mance coefficients follow the same trend as the ducted turbine, the maximum values differ. The open-centre turbine reaches lower values of $C_{P,\max}$ and $C_{PD,\max}$, while reaching a higher value of $\eta_{\text{basin},\max} = 0.53$. The latter is a direct result of the lower thrust levels reported in figure 5.33, leading to lower parasitic power extraction compared to the ducted turbine. From this it can be concluded that the streamlined duct shape used for the open-centre turbine is better able to convert axial thrust to power.

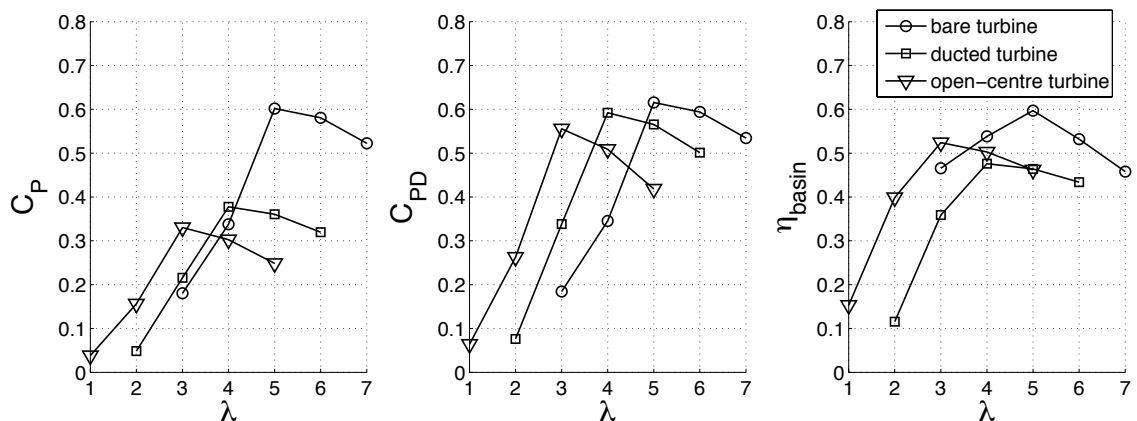


Figure 5.34: Performance of the open-centre turbine at various λ , compared to the bare and ducted turbines.

5.6.5 Comparison of RANS-BEM and actuator disc simulations

In order to facilitate comparison of the three devices, figure 5.35 summarises the results of all three device types. Both the results of actuator disc and RANS-BEM method are presented as a function of the induction factor, a . For the actuator disc simulations of the open-centre turbine, the results obtained for an aperture of $R_{ap} = 3$ m are presented.

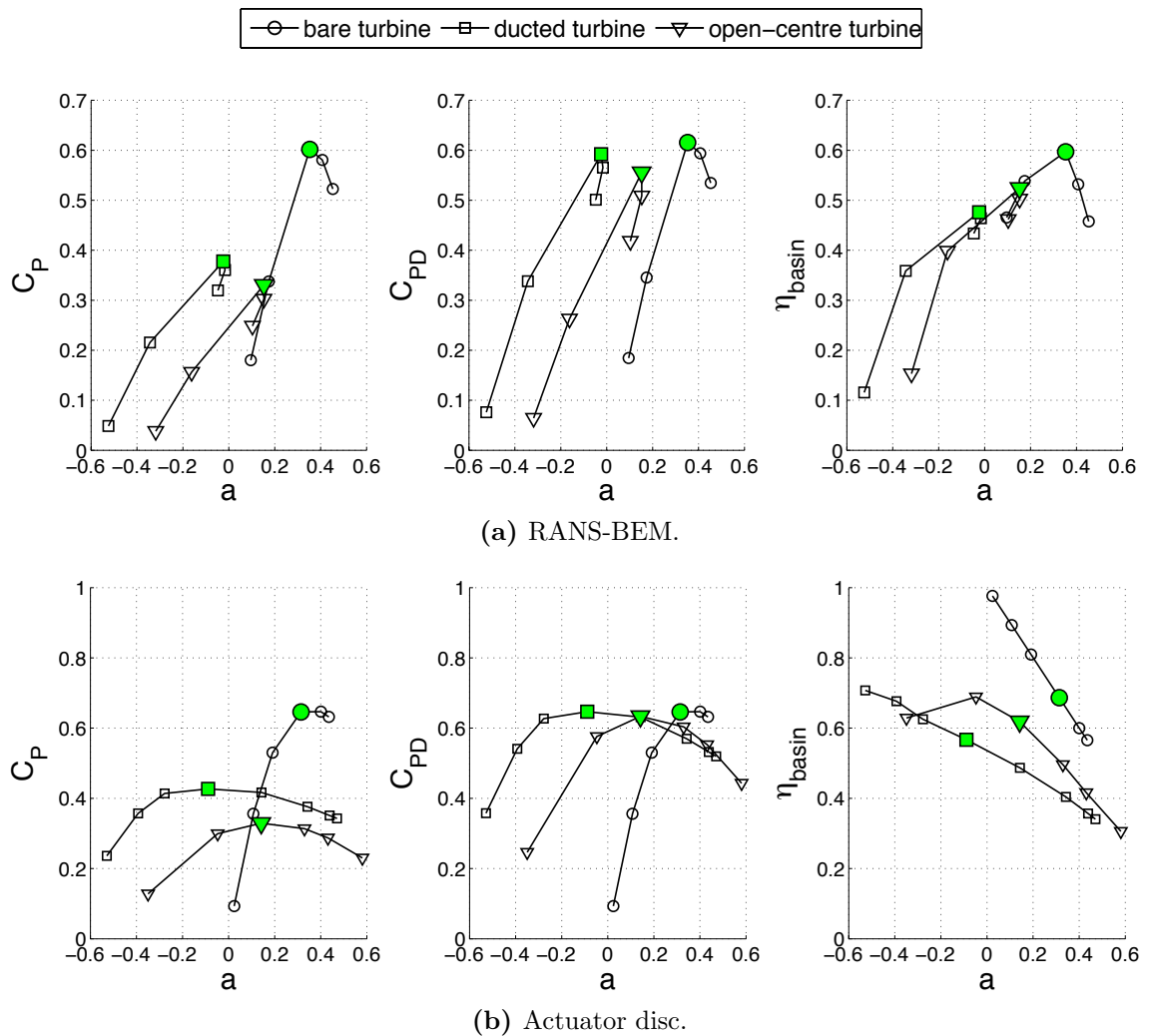


Figure 5.35: Performance of the bare, ducted, and open-centre turbines, modelled using RANS-BEM and actuator discs. Design points are marked in green.

For the RANS-BEM simulations, presenting the performance as a function of a clearly shows an interesting feature of the ducted and open-centre turbines when operated at high λ . At $\lambda > \lambda_{\text{design}}$ the flow velocity at the rotor increases again, leading to a reduction in a . This, together with the thrust analysis presented in figures 5.29 and 5.33, suggests that, for the two ducted devices a limit to the thrust on the rotor and the induction factor exists. For the actuator disc simulations, a steadily increases with increasing disc thrust setting, however, for RANS-BEM simulations, employing a fixed rotor design, a limit to both a and C_T is found close to the design point. For tip-speed ratios higher than the design point the ducted rotor imparts less axial thrust on the flow, combined with less swirl, leading to an increase in the velocity at the disc plane.

The overall performance penalty (measured at the design point) observed in the RANS-BEM simulations is 8 – 15 %, compared to the actuator disc simulations. The sources of this drop in performance can be found in several features of the real turbine, which are captured by the RANS-BEM simulations, but not by the actuator disc simulations.

Real blade data is employed for the RANS-BEM simulations, and hence blade drag losses are modelled. These drag losses lead to a reduction in power extracted by the rotor and account for the bulk power reduction compared to the drag free actuator disc simulations. Blade tip effects, another feature of the real rotor blade in free-stream, are modelled for the bare turbine, leading to performance increases at the blade tips. This local performance increase partly balances the losses deriving from blade drag, hence leading to a lower overall power penalty for this type of device of 8 %. A further difference of the RANS-BEM simulations presented here is the inclusion of hub structures. The hub exerts drag on the flow, removing additional

power from the flow, thus negatively affecting the basin efficiency, while also reducing the overall rotor area.

Another difference between actuator disc and RANS-BEM simulations is the location of the design point within the basin efficiency distribution. For the RANS-BEM results, the design point (peak power) coincides with a peak in basin efficiency, which is not the case for actuator disc simulations. This can be attributed to the fact that the actuator disc simulations assume all loss of axial momentum at the disc is converted into rotor power. In the limit, as seen for the bare turbine, the actuator disc tends to $\eta_{\text{basin}} = 1$ for no power removal.

From this comparison of modelling techniques a conclusion about the applicability of actuator disc models may be drawn. Actuator disc models are an appropriate tool for modelling the performance of a turbine at the design point, where a real rotor is designed to efficiently convert thrust to power. However, when operated off the design point, where rotors are less efficient thrust to power converters, actuator disc models are poor substitutes for real turbine behaviour. As a result, for actuator disc models, η_{basin} exhibits little variation over the C_T space, whereas η_{basin} has a much bigger variation for RANS-BEM.

5.7 Yawed inflow

Using the actuator disc simulation technique, significant changes in performance have been observed in yawed flow operation. Thus it is of interest to examine whether these changes in performance hold when an actual rotor is placed in yawed flow. All yawed simulations were performed using the yawed inflow approach described in section 4.7.1, where the alignment of domain and device are kept fixed and only the flow is yawed by the yaw angle, γ . The sides of the domain are modelled as periodic boundaries. For yawed flow problems, it is often easier to analyse the results in an alternative coordinate system that is dependent on the rotation defined by the yaw angle, see figure 5.36.

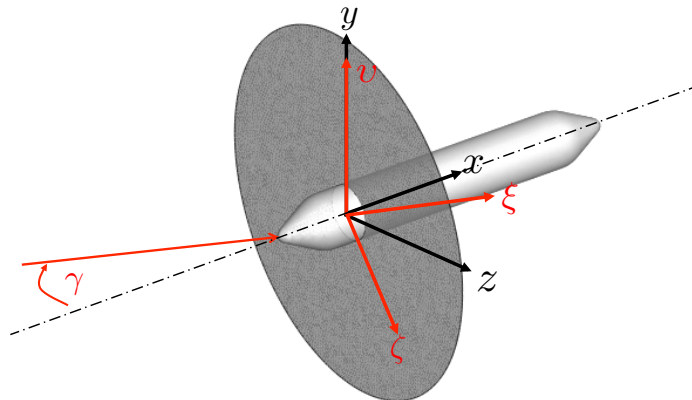


Figure 5.36: Illustration of the coordinate systems in axial and yawed flow.

As yawed inflow is introduced, the simulation becomes an asymmetric flow problem. For the majority of the simulations the rotor is loaded non-uniformly and thus an azimuthally averaged analysis is not appropriate. Therefore a more detailed flow representation of the rotor plane is introduced in this section. Furthermore, as the resulting forces on the components of the turbine are also asymmetric, the force vector must be considered.

5.7.1 Bare turbine in yawed inflow

The bare turbine has been simulated at three levels of yaw, low ($\gamma = 10^\circ$), moderate ($\gamma = 20^\circ$) and high ($\gamma = 30^\circ$) yaw. Results of the flow field are displayed through velocity contour plots both of the horizontal cut-plane and the rotor disc. A detailed force component analysis is introduced as are the resulting effects on the basin efficiency calculation.

5.7.1.1 Flow field of the bare turbine in yawed inflow

The flow field is presented as a contour plot of a horizontal cut-plane through the simulation domain, as in previous sections. The velocity contours show values for ξ -velocity, which is the velocity in the inflow direction. As before, the contour plots are overlaid with streamlines. While these streamlines each have a starting point within the cut-plane, they move in and out of the cut-plane depending on the local flow features of the streamline. Figure 5.37 presents this type of flow field contour plot for the bare turbine at four yaw angles ($\gamma = 0^\circ, 10^\circ, 20^\circ$, and 30°) for a tip-speed ratio of $\lambda = 5$.

The overall flow features of the bare turbine in yaw are not significantly different to the bare turbine in axial flow. The main difference is the flow separation at the hub. While some level of flow separation are always observed on the hub surface, at $\gamma > 20^\circ$ this separation increases significantly.

In order to capture the azimuthally asymmetric features contour plots of the rotor plane are displayed in figure 5.38. Six flow and performance parameters are presented: u_x , the velocity in x -direction; U_{rel} , the rotor blade inflow velocity; α , the angle of attack; T , the thrust in x -direction; F_θ , the circumferential force; and P , the power generated. The velocities are normalised by U_∞ , while the forces and power are

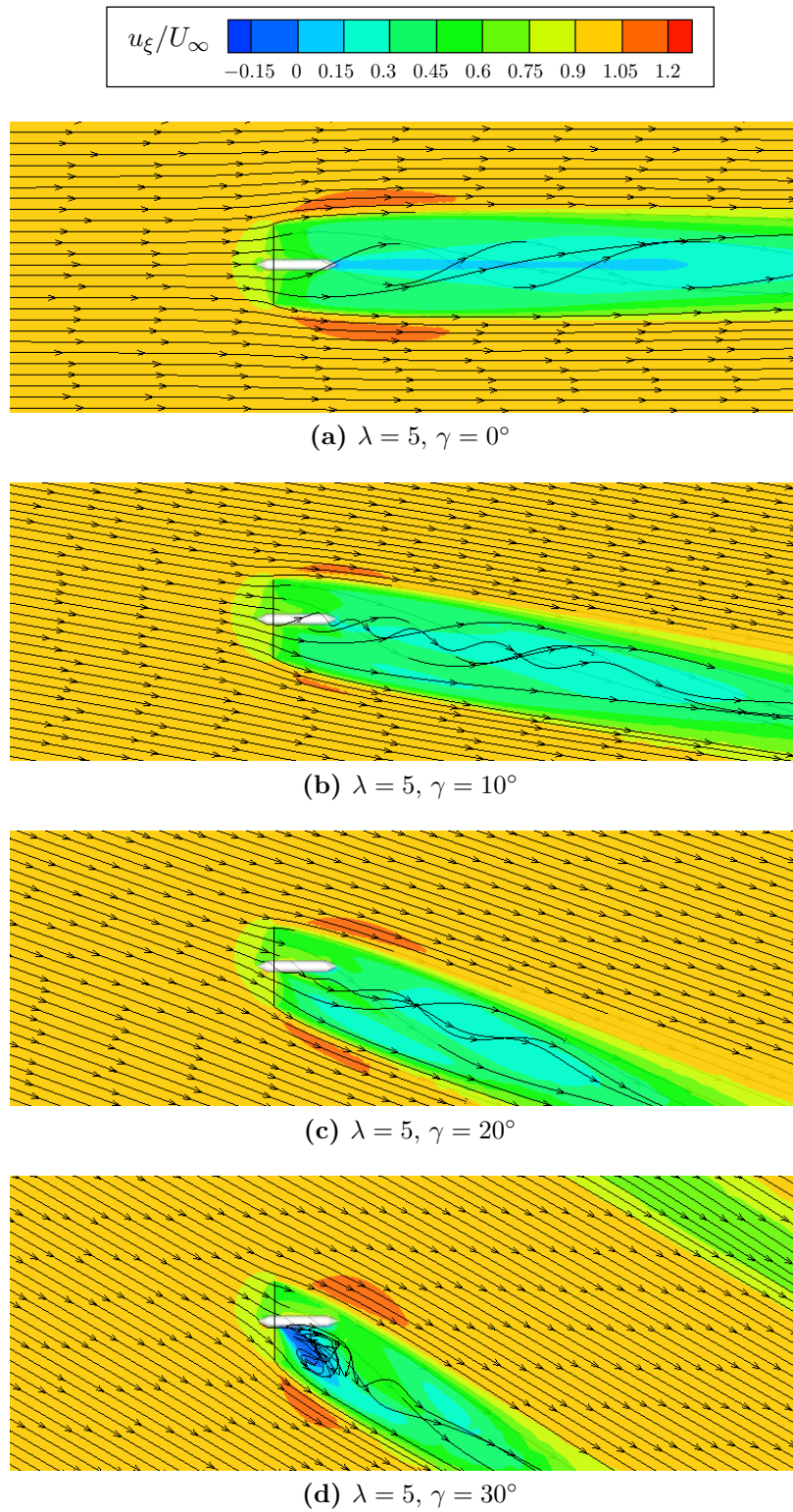


Figure 5.37: Flow field of the bare turbine at $\lambda = 5$ and for four levels of γ . The contours show the relative velocity in inflow direction, u_ξ/U_∞ .

presented as coefficients. The coefficients are defined using the incremental value of force/power acting on an incremental rotor area, A_{cell} , and are therefore referred to as density coefficients in the following. For an incremental rotor element the performance coefficients are therefore:

$$\text{thrust density coefficient:} \quad C_{TD} = \frac{T_{\text{cell}}}{1/2 \rho U_{\infty}^2 A_{\text{cell}}}, \quad (5.29)$$

$$\text{circumferential force density coefficient:} \quad C_{F_{\theta D}} = \frac{F_{\theta, \text{cell}}}{1/2 \rho U_{\infty}^2 A_{\text{cell}}}, \quad (5.30)$$

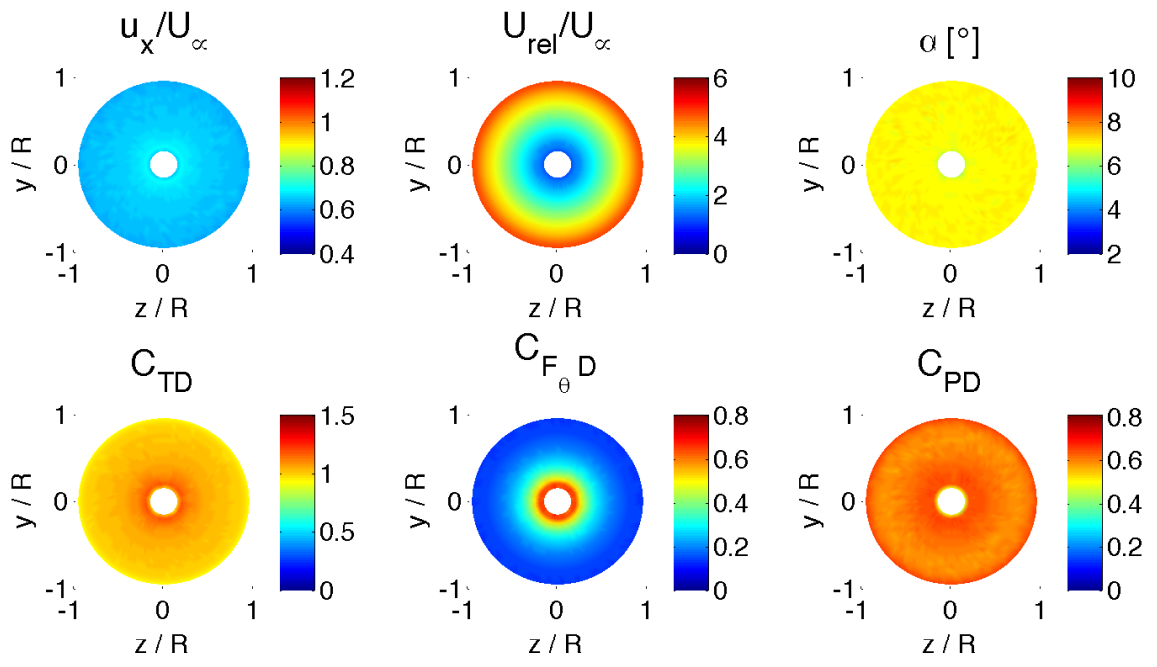
$$\text{power density coefficient:} \quad C_{PD} = \frac{P_{\text{cell}}}{1/2 \rho U_{\infty}^3 A_{\text{cell}}}. \quad (5.31)$$

For reference, both the design point ($\lambda = 5$, $\gamma = 0$) and one yawed flow case are presented ($\lambda = 5$, $\gamma = 20^\circ$) in figure 5.38.

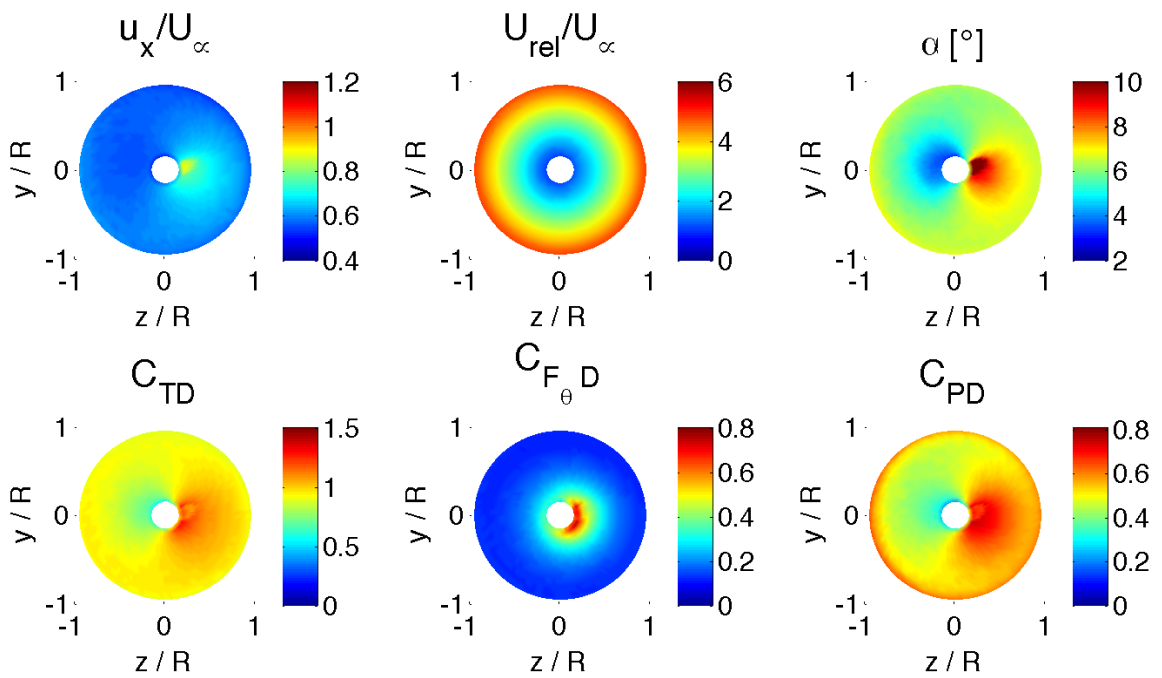
The plot of the velocity in x -direction shows a variation in velocity across the rotor plane, with a pronounced velocity increase to the right of the hub. This azimuthal variation is only barely visible in the $U_{\text{rel}}/U_{\infty}$ plot due to the strong radial variations of U_{rel} masking this effect. However, the changes in velocity are significant enough to lead to changes in the angle of attack with a magnitude of $\Delta\alpha \pm 3^\circ$. Since the forces acting on the blade are directly related to the angle of attack, the asymmetry is reflected in the force and performance results (C_{TD} , $C_{F_{\theta D}}$, and C_{PD}). An increased velocity leads to higher α which leads to higher axial thrust and circumferential force which in turn leads to a higher value of power. The opposite is the case for reduced velocity regions. A slight vertical asymmetry is present in the results as well, which is attributed to the swirl present in the flow.

5.7.1.2 Forces of the bare turbine in yawed inflow

As the forces on the turbine in yawed inflow are no longer axisymmetric, the resulting forces of the turbine are significant in all three directional components. In figure 5.39



(a) $\lambda = 5, \gamma = 0^\circ$.



(b) $\lambda = 5, \gamma = 20^\circ$.

Figure 5.38: Rotor plane flow and performance of the bare turbine for both axial and yawed flow, viewed front on.

the resulting forces on the device components are presented as a function of λ . The forces are split into the device component, rotor and hub, and the coordinate components x, y, z as well as the inflow direction ξ (from top to bottom). The force components are displayed as coefficients, e.g.

$$C_{F_{x,\text{rotor}}} = \frac{\sum F_{x,\text{rotor}}}{1/2 \rho U_\infty^2 A_{\text{ref}}}, \quad (5.32)$$

where $\sum F_{x,\text{rotor}}$ is the sum of forces on the rotor in x -direction. A_{ref} is uniformly A_{device} for all coefficients.

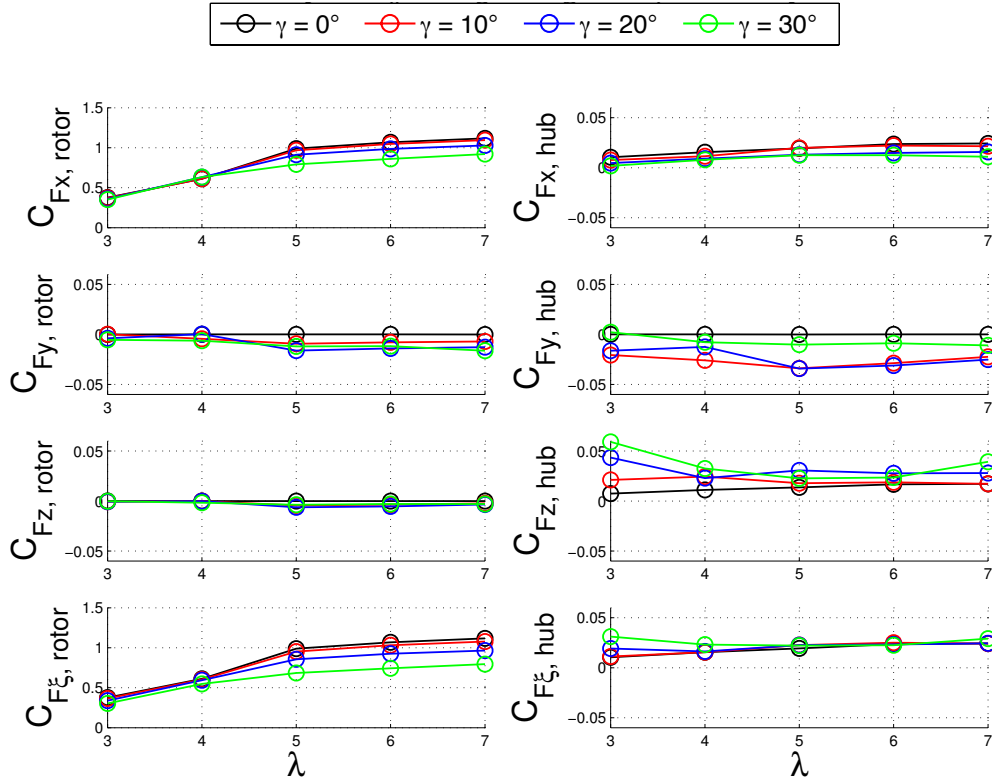


Figure 5.39: Force coefficients for the components of the bare turbine at various λ and γ .

Overall, the force component of the rotor in x - or ξ -direction is one to two orders of magnitude larger than any of the other force components. In the un-yawed condition, $\gamma = 0$, the resulting y and z force components are negligible, both for the hub as well as for the rotor. Even though circumferential blade force components are acting in

both these directions, in uniform axial flow these components integrate out such that the resulting forces $F_{y,\text{rotor}} = 0$ and $F_{z,\text{rotor}} = 0$.

For the yawed flow cases a general drop in $F_{x,\text{rotor}}$ and $F_{x,\text{hub}}$ is visible for increasing yaw angles, which is in line with the reduction of the x -velocity component. On the rotor, the horizontal asymmetry seen in figure 5.38 results in a negative vertical force, $F_{y,\text{rotor}}$, shown in figure 5.39: The high velocity region on the right side of the hub leads to high angles of attack, and consequently increased circumferential forces which here act parallel to the y -axis in negative y -direction (the rotor blade spins clockwise). Similarly, regions of decreased α on the left side of the hub result in decreased circumferential forces which are here acting in positive y -direction. The vertical asymmetry in figure 5.38 is small, as is the variation of the horizontal rotor force, $F_{z,\text{rotor}}$, shown in figure 5.39. The force in the inflow-direction, $F_{\xi,\text{rotor}}$, drops for increased γ , partly due to the decrease in axial velocity and hence decrease in $F_{x,\text{rotor}}$, and partly due to the change of ξ in relation to the main axis of thrust, x .

On the hub, the yawed flow leads to a negative vertical force, $F_{y,\text{hub}}$ and a positive horizontal force, $F_{z,\text{hub}}$, which acts in the direction towards the side of the flow separation. $F_{\xi,\text{hub}}$ shows little variation (apart from low at λ), resulting from the decrease in $F_{x,\text{hub}}$ and increase in $F_{z,\text{hub}}$, as γ increases.

5.7.1.3 Performance of the bare turbine in yawed inflow

The performance analysis of the bare turbine in yawed flow is performed using the same metrics as for axial flow. Note that the basin efficiency is calculated using the sum of forces in the inflow direction, $\sum F_{\xi}$, see section 4.4.4.3.

Figure 5.40 presents the performance results for the bare turbine in axial as well as yawed inflow. The results are similar to those obtained using yawed actuator disc simulations: the power and power density drop significantly with increasing γ , while

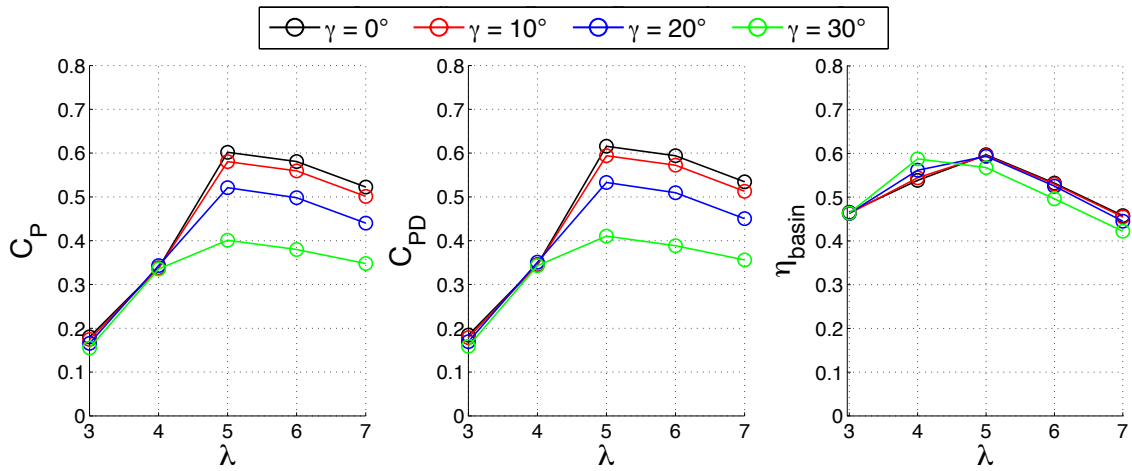


Figure 5.40: Performance of the bare turbine at various λ and γ .

η_{basin} is nearly unaffected, as the thrust also decreases. The main difference to the actuator disc simulations can be found at high γ , where large flow separations occur on the hub surface, see figure 5.37d. Such large scale flow separations have a visible negative impact on η_{basin} .

5.7.2 Ducted turbine in yawed inflow

In this section the ducted turbine is analysed in yawed inflow. The ducted turbine has been simulated at three levels of yaw, low ($\gamma = 10^\circ$), moderate ($\gamma = 20^\circ$) and high ($\gamma = 30^\circ$) yaw.

5.7.2.1 Flow field of the ducted turbine in yawed inflow

The flow field is displayed by the horizontal cross-section of ξ -velocity contours in figure 5.41. The tip-speed ratio is chosen as $\lambda = 5 = \lambda_{\text{design}} + 1$, as the performance analysis in section 5.7.2.3 shows that the highest performance of the yawed turbine occurs at this higher tip-speed ratio.

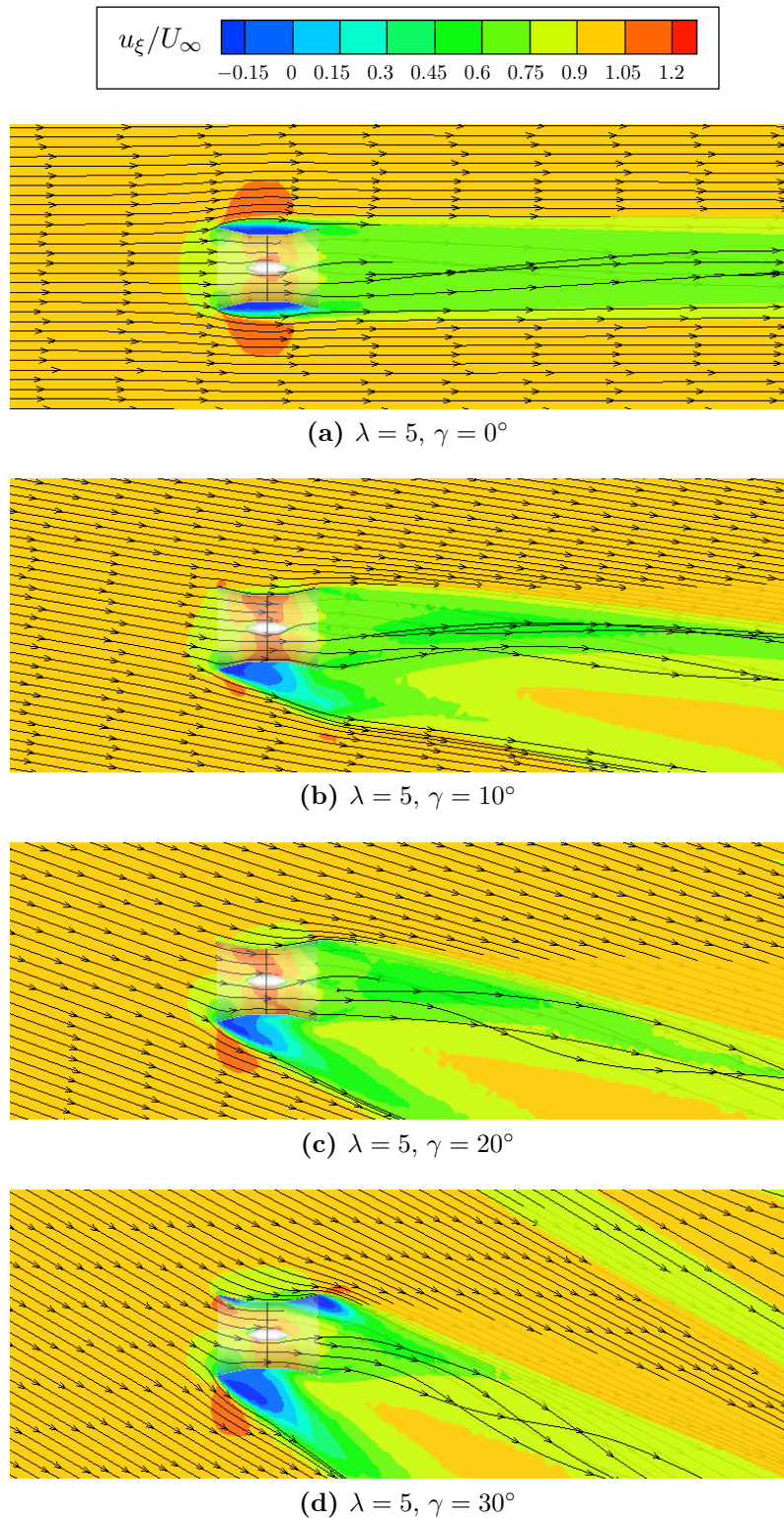


Figure 5.41: Horizontal cross-sections of the flow field of the ducted turbine at $\lambda = 5$ and for $0^\circ \leq \gamma \leq 30^\circ$, represented by velocity contours and streamlines. The contours show the relative flow velocity in the inflow direction, u_ξ/U_∞ .

Two main flow features of the duct in yawed flow become apparent in figure 5.41: flow alignment by the duct and a shift to asymmetric separation on the duct exterior. While for axial flow the separation encompasses the full duct exterior (figure 5.41a), for yawed flow parts of the duct exterior now feature attached flow, while others exhibit large scale flow separation. The size of the separation area is dependent on the yaw angle and increases with increasing yaw angle. For low to moderate yaw angles (figures 5.41b, 5.41c) flow alignment by the duct leads to flow acceleration around the inlet lip and to near axisymmetric velocities through the duct. For higher yaw angles, separation occurs on the interior surface, both in the nozzle and diffuser sections (figure 5.41d).

Figure 5.42 presents the flow and local performance parameters directly at the rotor plane for $\lambda = 5$ and $\gamma = 20^\circ, 30^\circ$. In comparison to figure 5.38 the flow field through the duct is much more evenly distributed circumferentially, thus it is evident from this plot type that the duct performs very well as a flow straightening device. The first two plots of figure 5.42a show the axial and blade inflow velocities through the ducted rotor. The axial velocity is increased compared to the free-stream velocity, $u_x/U_\infty > 1$, which means that the duct is working very efficiently at this operating point. As a result, the relative blade inflow velocity, U_{rel}/U_∞ , is also significantly increased compared to that of the bare turbine. The angle of attack is evenly distributed at $4^\circ < \alpha < 5^\circ$, which is lower than α_{design} and therefore not operating at optimal lift to drag ratio. However, due to the significantly increased blade inflow velocity, the performance parameters C_{TD} , $C_{F_\theta D}$ and C_{PD} show high values and outperform those of the ducted un-yawed device (recalling that the coefficients are defined based on U_∞).

Figure 5.42b presents the rotor flow field for a higher yaw angle, $\gamma = 30^\circ$. As shown in figure 5.41d, for such high yaw angles internal separation occurs in the nozzle section

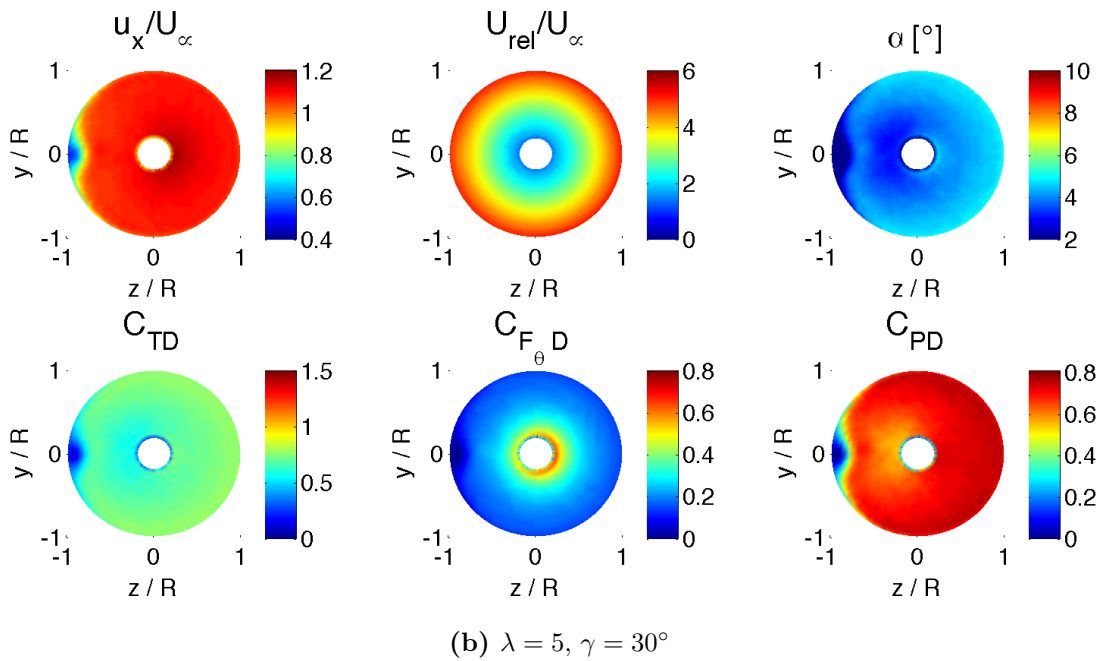
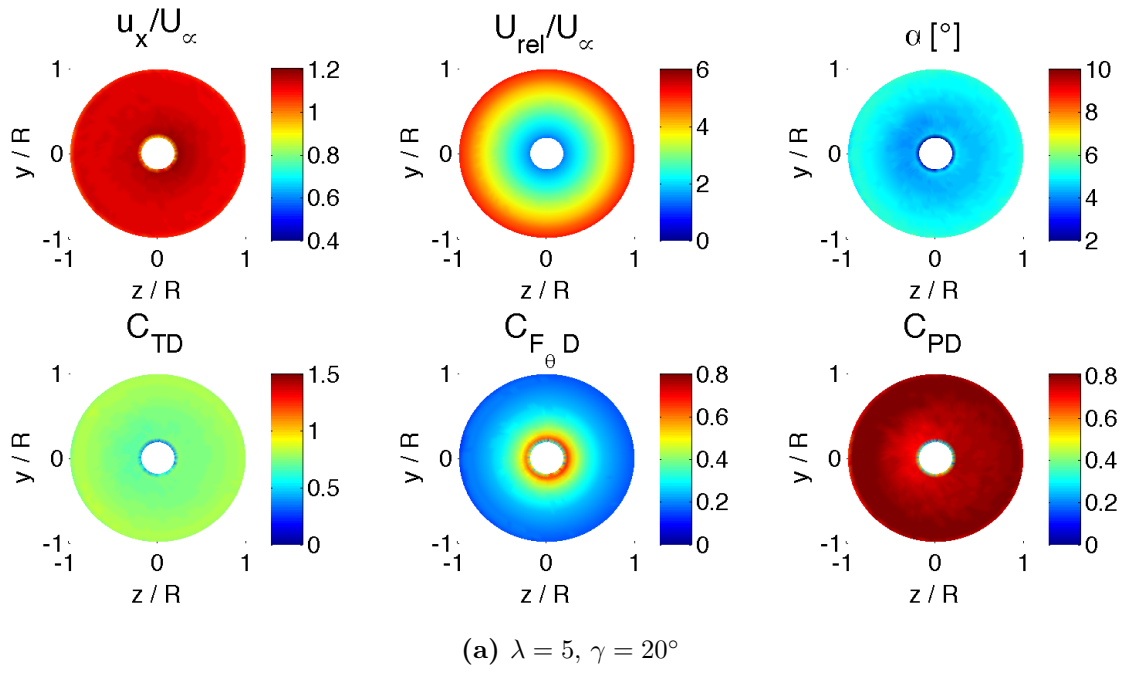


Figure 5.42: Rotor plane flow and performance of the ducted turbine at $\lambda = 5$ and two levels of γ .

of the duct. This separation progresses into the rotor plane, as clearly visible in figure 5.42b, resulting in reduced performance (as well as cyclical blade loading).

As figure 5.42a shows, the distribution of the parameters across the rotor disc is nearly axisymmetric for $\gamma = 20^\circ$. Therefore, in figure 5.43 the flow field is further analysed using azimuthally averaged data for easier comparison.

Figure 5.43 displays the rotor flow parameters for 5 different operating points:

- $\lambda = 4, \gamma = 0^\circ$, design point to which data is compared
- $\lambda = 5, \gamma = 0^\circ$ unyawed case at increased rotational velocity
- $\lambda = 5, 10^\circ \leq \gamma \leq 30^\circ$ various yawed flow cases at increased rotational velocity

These operating points were chosen based on the increase in performance for the yawed turbine seen at $\lambda = 5$, see section 5.7.2.3. Some azimuthal variation occurs in the rotor tip region for inflow angles $\gamma > 20^\circ$, see Figure 5.42b. In the azimuthally averaged presentation of flow data this low velocity region is averaged with higher flow velocities within the tip blade region, and results for this region must be treated with caution.

The top three plots in figure 5.43 present the results of velocity and angle of attack at the rotor plane. All of the yawed flow results (in colour) presented here exhibit a higher u_x through the rotor compared to the design point ($\lambda = 4, \gamma = 0^\circ$, dashed line), with the maximum velocity achieved for $\gamma = 20^\circ$. An explanation for this increase is that in yawed conditions the inlet angle of the duct is more closely aligned with the inflow over one half of the device inlet. Due to the particular alignment in the case of $\gamma = 20^\circ$, the duct nozzle section is effectively acting as a cambered aerofoil, therefore increasing the flow velocity into the duct. At the same time, the flow on the leeward side of the duct, that now sees a stronger angle between duct inlet and inflow, is only moderately reduced compared to the axial flow case. In sum, the overall flow passing through the device is increased, leading to higher flow velocities.

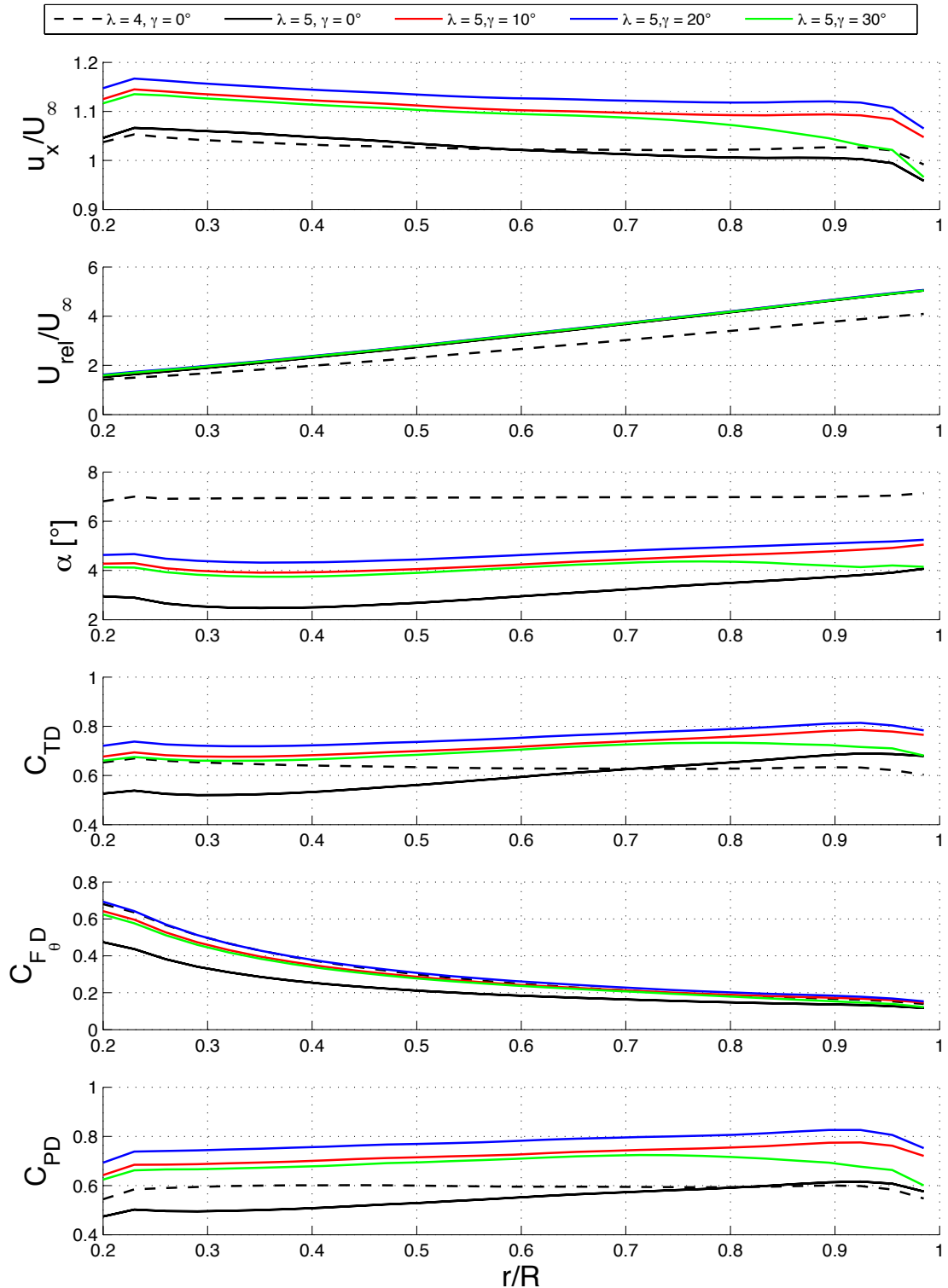


Figure 5.43: Azimuthally averaged rotor flow parameters of the ducted turbine in yawed and unyawed inflow conditions. Results are displayed for the design point, $\lambda = 4$, $\gamma = 0^\circ$, as well as for various yaw angles at $\lambda = 5$.

The blade inflow velocity is dominated by the tip-speed ratio and as such one can observe an increase in $U_{\text{rel}}/U_{\infty}$ when moving from $\lambda = 4$ to $\lambda = 5$. The changes in U_{rel} and u_x directly result in changes in α . For instance, whilst the operating point of $\lambda = 5$, $\gamma = 0^\circ$ shows nearly the same axial flow velocity as the design point, due to higher rotor speed, α is significantly reduced. The yawed flow cases at $\lambda = 5$ have a more moderate drop in α as the axial and blade inflow velocities are increased.

Both α and U_{rel} directly influence the forces generated by the blade, which in turn define the axial and circumferential forces on the rotor. Recalling the aerofoil force coefficients in figure 5.7 we see that for the region of $\alpha \leq 8^\circ$ the lift coefficient, C_l , drops off linearly, while the drag coefficient remains constant at $C_d \approx 0.025$. The region of α spanned by the cases under investigation lies within $2^\circ \leq \alpha \leq 8^\circ$, where $C_l \gg C_d$, hence the lift is the main force acting both circumferentially as well as axially.

The bottom three plots in figure 5.43 present the result of the forces acting on the rotor blade and, subsequently, the power generated by each blade section. Compared to the design point, the axial force, represented by C_{TD} , is increased across the whole blade span as a result of a trade-off in moderately lower α but significantly increased U_{rel} . The increase in C_{TD} is more pronounced towards the outboard blade sections, nearly following the slope of α . The unyawed case at higher rotational velocity ($\lambda = 5$, $\gamma = 0^\circ$) leads to a lower axial thrust for the inboard stations close to the blade root, but a higher axial thrust close to the tips, again very much dependent on the radial variation of α .

For the circumferential force component, little variation is seen between the yawed flow cases and the design point, whereas for the unyawed high rotational velocity case a reduction by roughly 50% is seen. Together with the rotational velocity, Ω , the circumferential force component directly translates into the power produced by

each annular section, thus for the same circumferential force, the cases with higher rotational velocity produce more power.

Note that for all flow and performance parameters analysed, the tip region for $\gamma = 30^\circ$ shows a significant drop. This can be attributed to the separation inside the duct which leads to a significant reduction in flow velocity in the tip region, see figure 5.41d. Due to the azimuthal averaging this effect is less pronounced in the results shown in figure 5.43.

5.7.2.2 Forces on the ducted turbine in yawed inflow

The resultant forces in x, y, z, ξ on the device components rotor, duct and hub are analysed for a range of λ and γ , see figure 5.44. All forces are displayed as force coefficients, as defined in equation (5.32).

As can be seen from the rotor force components (left column of figure 5.44), the forces in horizontal and vertical directions are minimal. This is a result of the flow alignment achieved by the duct, as already discussed in the previous section. With increasing yaw angle, the duct (middle column) sees a strong increase in horizontal force, $F_{z,\text{duct}}$, up to three times that of the axial force, $F_{x,\text{duct}}$, and half that of the force in the flow direction, $F_{\xi,\text{duct}}$. Vertical forces are minimal in all cases, as are the forces on the hub. Hence, it can be concluded that, the duct absorbs nearly all additional asymmetric loading caused by the yawed flow impinging the device, a significant advantage over the bare turbine in yawed flow.

5.7.2.3 Performance of the ducted turbine in yawed inflow

In the flow field and force analysis it has been shown that the duct performs well in terms of flow straightening of the core flow, at least up to yaw angles of $\gamma = 20^\circ$. At the same time, large scale asymmetric separation occurs on the outer duct surface

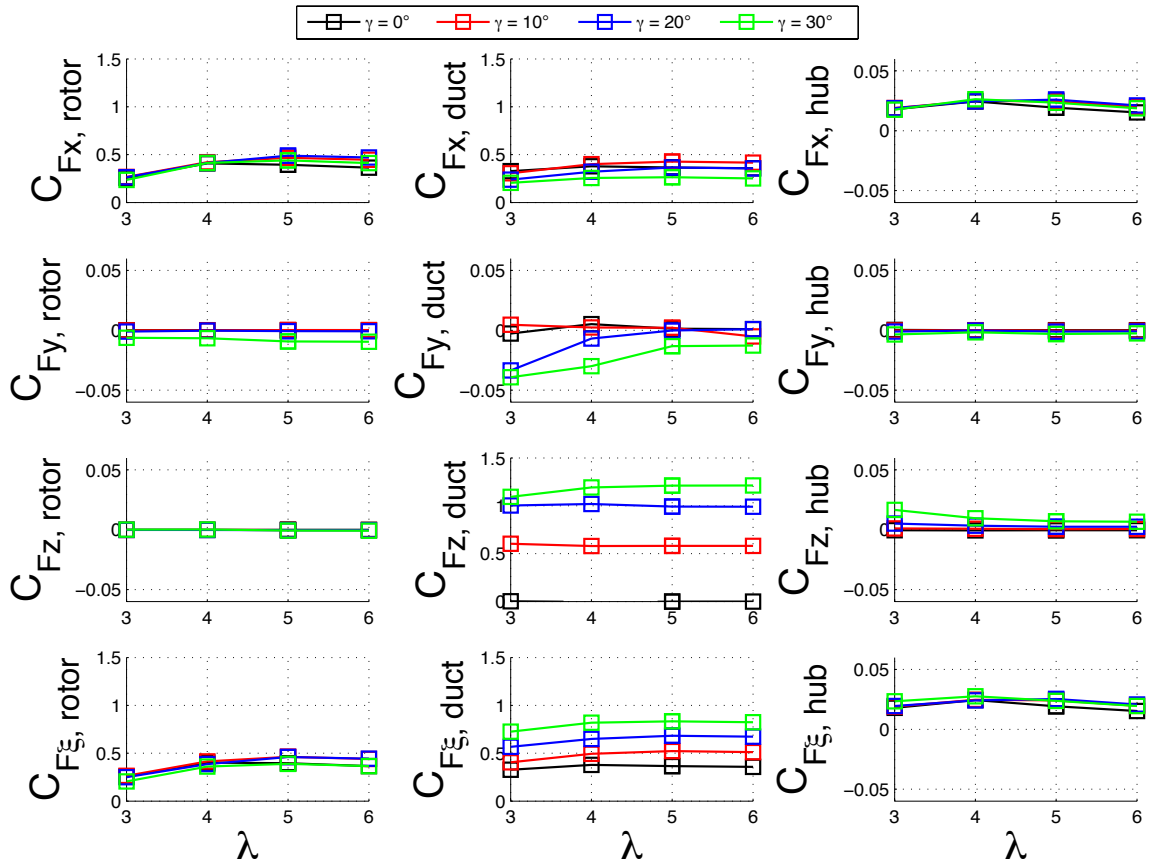


Figure 5.44: Force coefficients for the components of the ducted turbine at various λ and γ .

and therefore large resultant forces act in the horizontal cross-stream direction. The results of power production are given in figure 5.45.

Overall, the results are in line with those found using actuator disc simulations. For both C_P and C_{PD} the ducted device performs better when placed in yawed flow compared to axial flow. The maximum power is reached at a $\lambda = 5$, which is higher than the design point of $\lambda = 4$. Of the yaw angles tested with the given duct geometry (with a nozzle contraction angle of 13.5°), the yaw angle yielding the highest power is $\gamma = 20^\circ$. The maximum power is increased by 30% compared to the design point, leading to an equal increase in both C_P and C_{PD} .

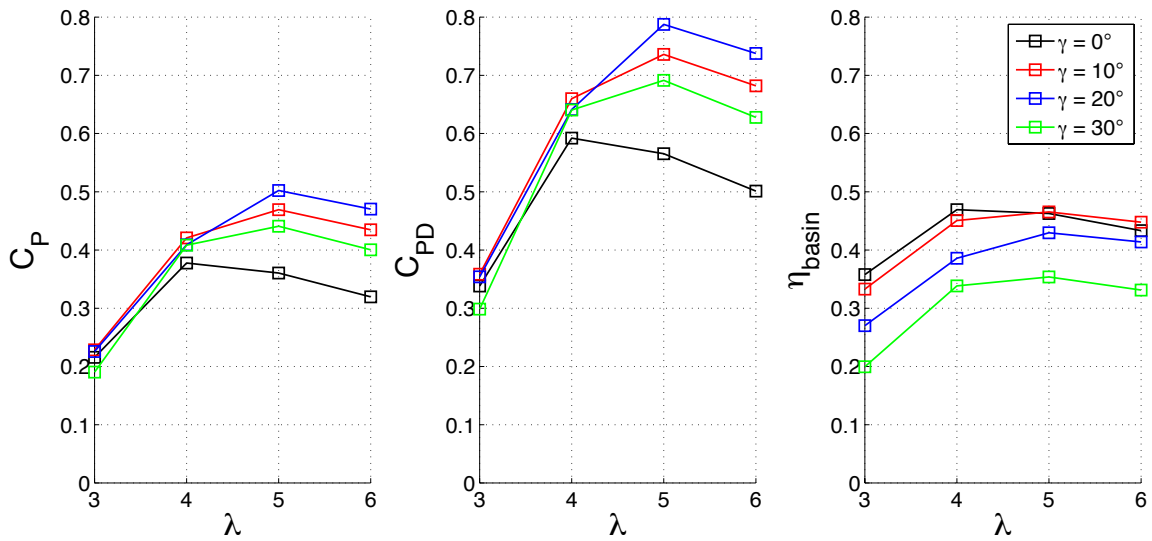


Figure 5.45: Performance of the ducted turbine at various λ and γ .

In terms of basin efficiency the turbines in yawed flow exhibit decreases in particular for $\gamma \geq 20^\circ$. For $\gamma = 10^\circ$ the asymmetric separation is not as pronounced and thus the added thrust in flow direction (see $F_{\xi, \text{duct}}$ in figure 5.44) is offset by the significantly increased power produced by the rotor. For $\gamma = 20^\circ$, the additional power gain at the rotor is not large enough to offset the strong increase in thrust on the duct, therefore the basin efficiency drops moderately to $\eta_{\text{basin}} = 0.43$, a drop of approximately 9% compared to the design point. As the power drops for higher yaw angles whereas the thrust on the duct increases further, the basin efficiency for $\gamma = 30^\circ$ is significantly lower than for all the other cases.

5.7.3 Open-centre turbine in yawed inflow

The following section discusses the results of the yawed flow simulations for the open-centre turbine. The analysis methods used are the same as for the ducted turbine yawed flow.

5.7.3.1 Flow field of the open-centre turbine in yawed inflow

Figure 5.46 presents the horizontal flow field cross-section for yaw angles of $0^\circ \leq \gamma \leq 40^\circ$. The range of yaw angles is extended to $\gamma = 40^\circ$ as the power peak for the open-centre turbine lies at a higher yaw angle than for the ducted turbine.

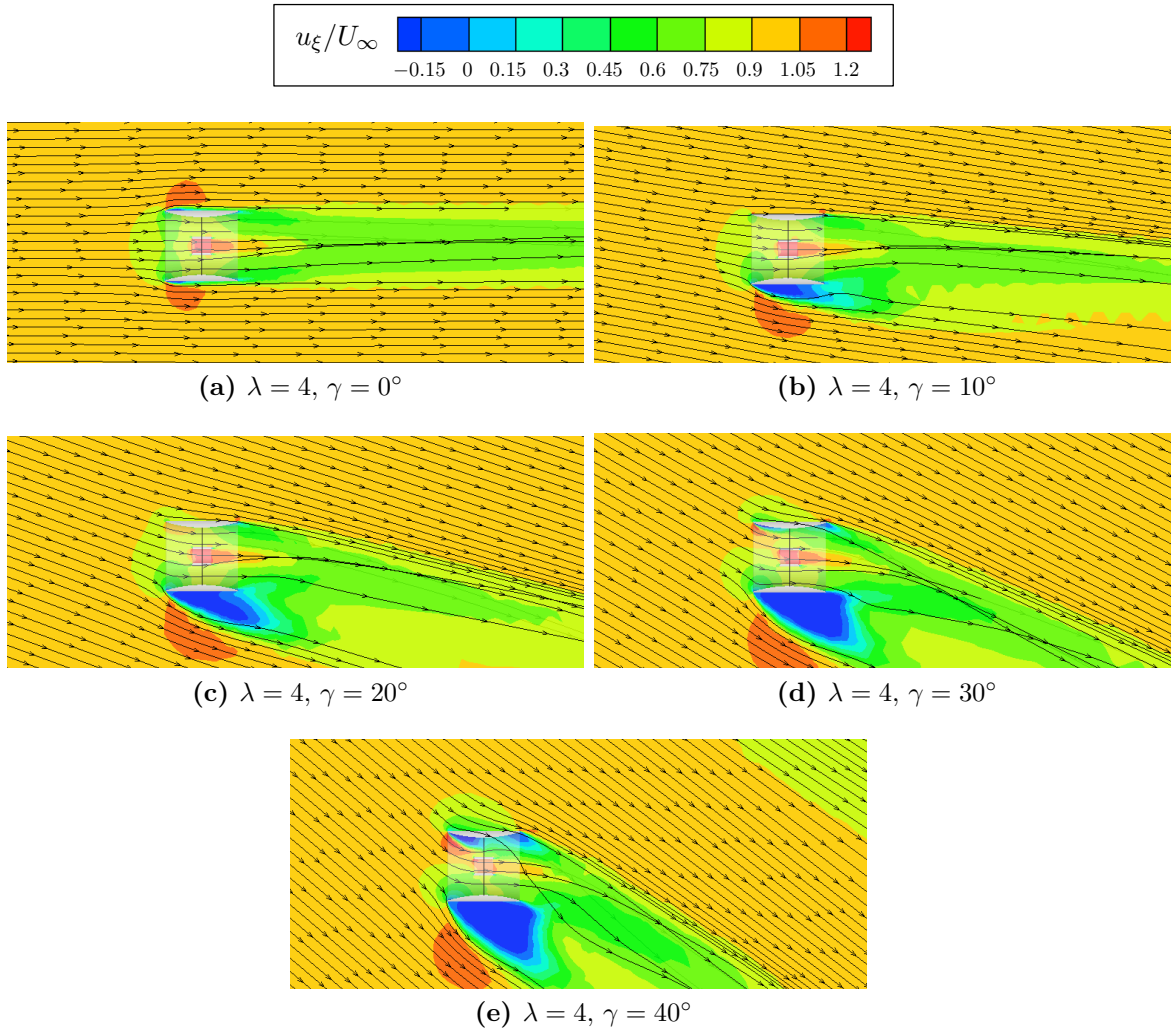


Figure 5.46: Horizontal cross-section of the flow field of the open-centre turbine at $\lambda = 4$ and for various γ , represented by velocity contours and streamlines. The contours show the relative flow velocity in the inflow direction, u_ξ/U_∞ .

The main difference to the ducted turbine, see figure 5.41, is the lack of accelerated velocity through the disc plane. Though a high velocity jet is formed in the central aperture, the velocity through the disc is lower than the free-stream in all cases of γ

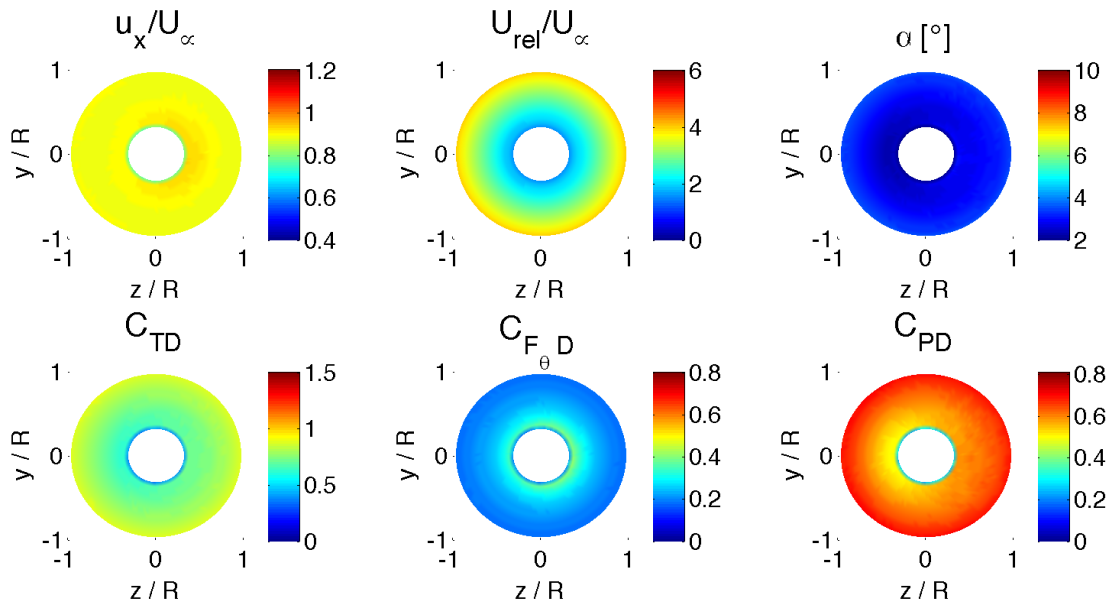
and λ . The axial flow case does not exhibit significant separation on the duct outer surface, however for all yawed flow cases an external asymmetric separation develops, its size depending on the magnitude of γ . For $\gamma \geq 20^\circ$, separation occurs on the duct interior surface as well, first in the diffuser section and for higher yaw angles also in the nozzle section. However, the small internal separation seen for $20^\circ \leq \gamma \leq 30^\circ$ does not appear to have a negative impact in terms of performance as shown in section 5.7.3.3. For $\gamma = 40^\circ$, the internal separation extends further into the rotor plain, thereby negatively impacting the performance.

The rotor flow fields for the cases of $\lambda = 4$ and $\gamma = 20^\circ$, $\gamma = 30^\circ$ are further investigated in figure 5.47. Though some flow separation occurs inside the diffuser section for $\lambda = 4$, $\gamma = 20^\circ$, the rotor flow field is largely uniform, see figure 5.47a. For a higher yaw angle of $\gamma = 30^\circ$ the rotor flow field is visibly affected by the internal separation, see figure 5.47b. Nonetheless, the remaining rotor area sees a higher axial velocity and angle of attack, leading to higher force and power coefficients compared to the cleaner flow field of figure 5.47a. One source for this effect might be the considerably extended separation area forming on the duct exterior at $\gamma = 30^\circ$ and thus the increased effective blockage.

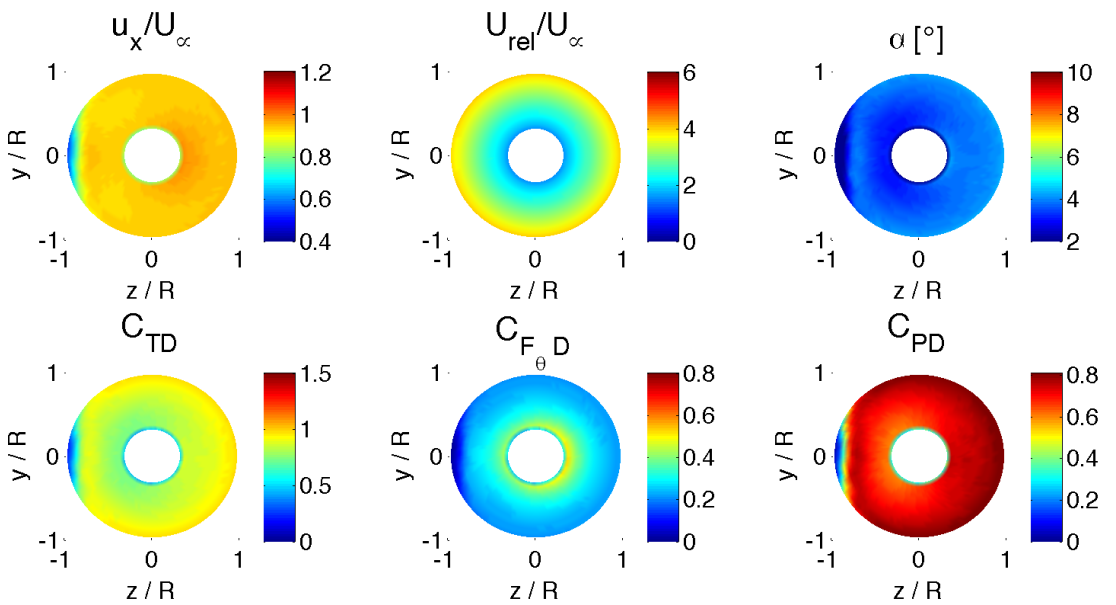
The duct of the open-centre turbine efficiently aligns the flow in yawed flow conditions, as seen for the ducted turbine. The rotor plane flow field may therefore be further investigated by employing azimuthally averaged data. Figure 5.48 displays the rotor flow parameters for 5 different operating points:

- $\lambda = 3$, $\gamma = 0$, design point to which data is compared,
- $\lambda = 4$, $\gamma = 0^\circ$ unyawed case at increased rotational velocity,
- $\lambda = 4$, $10^\circ \leq \gamma \leq 30^\circ$ various yawed flow cases at increased rotational velocity.

The operating points were chosen based on the performance increase of the open-centre turbine for higher rotational velocity, $\lambda = 4$. As for the ducted turbine, for



(a) $\lambda = 4, \gamma = 20^\circ$



(b) $\lambda = 4, \gamma = 30^\circ$

Figure 5.47: Rotor plane flow and performance of the open-centre turbine for two levels of γ .

yaw angles of $\gamma > 20^\circ$ the separation on the duct interior leads to an azimuthal variation in the tip region of the rotor flow field, that is averaged across the annulus in the azimuthally averaged plots.

The trends presented in figure 5.48 follow those of the ducted turbine discussed in section 5.7.2.1 and figure 5.43. The axial velocity, u_x , through the rotor disc is increased for higher yaw angles due to the change in duct alignment with the incoming yawed flow. As a sum of increased axial and rotational velocity, the incident blade velocity, U_{rel} , increases as well. The angle of attack drops due to increased rotational velocity, but less so for high γ (and resulting high u_x) such that the lift coefficient is only moderately decreased at high yaw angles. Together with the increase in U_{rel} , this leads to higher power and axial thrust for yaw angles of $\gamma = 20^\circ, 30^\circ$, while for lower yaw angles the disc average of these values is roughly the same as the design point. Compared to the ducted turbine, for which maximum power occurs at $\gamma = 20^\circ$, the operational point leading to maximum power in yawed flow, is found at a higher yaw angle ($\gamma = 30^\circ$).

5.7.3.2 Forces of the open-centre turbine in yawed inflow

The results of the force analysis of the open-centre turbine are presented in figure 5.49. Though the flow field of the open-centre turbine looks distinctly different to that of the ducted turbine, for $\gamma \leq 20^\circ$ the overall trends are the same. The main resultant force components are found in x - and ξ -direction for the rotor and in x -, z -, and ξ -direction for the duct. As for the ducted turbine, for all highly yawed cases, $F_{z,\text{duct}}$ is the dominant component of the force vector on the duct. The resultant hub forces are again small, as are the other directional components of rotor and duct forces.

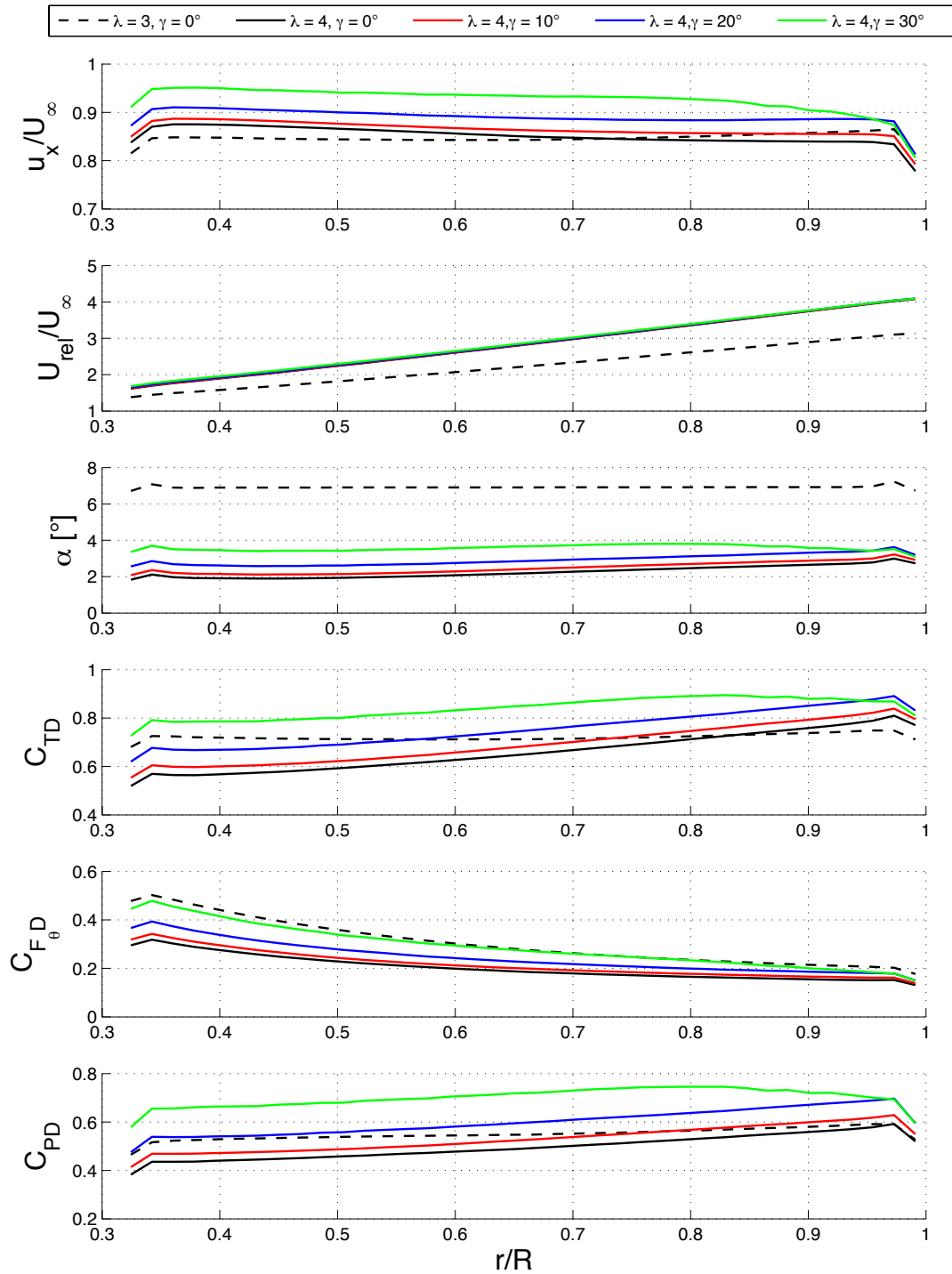


Figure 5.48: Azimuthally averaged rotor flow and performance parameters of the open-centre turbine in yawed and unyawed inflow conditions. Results are displayed for the design point, $\lambda = 3, \gamma = 0^\circ$, as well as for various yaw angles at $\lambda = 4$.

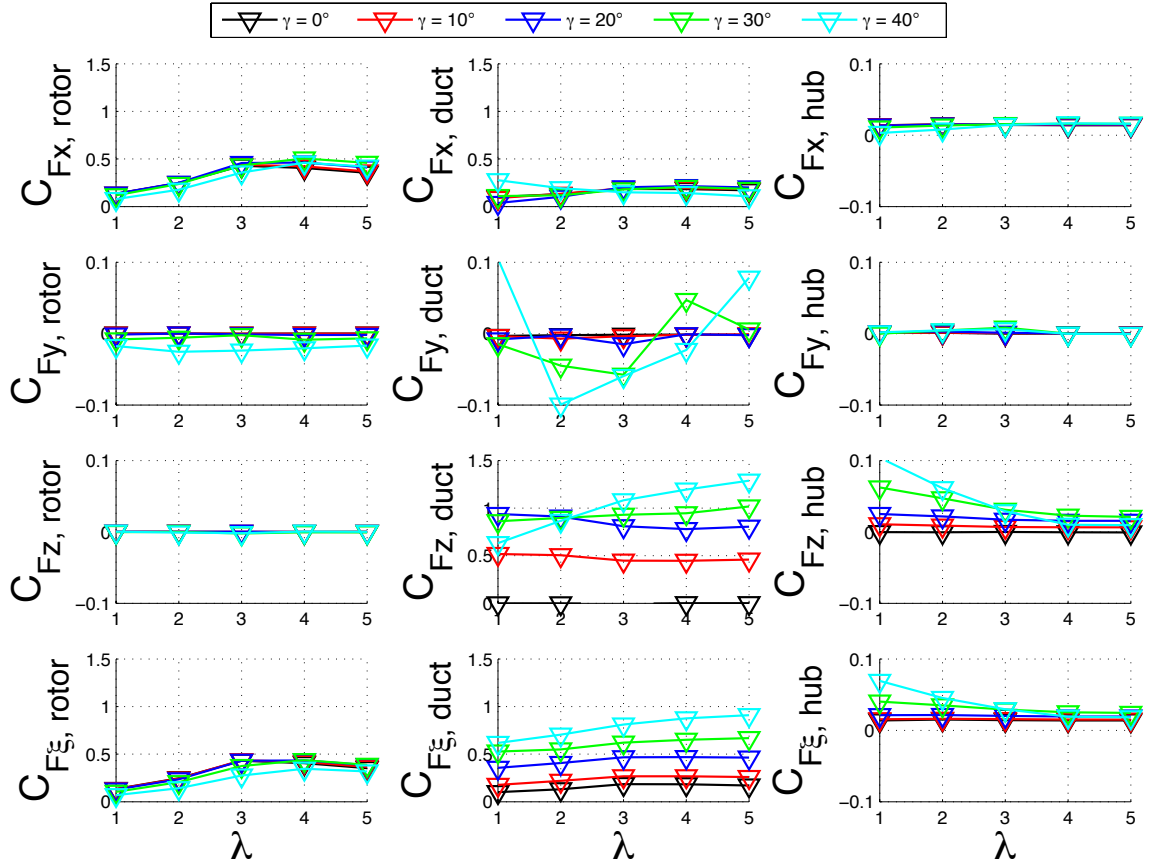


Figure 5.49: Force coefficients for the components of the open-centre turbine at various λ and γ .

For $\gamma \geq 30^\circ$, multiple separation regions lead to further imbalances in the resultant forces and stronger variation dependent on λ . The duct vertical force component ($F_{y,\text{duct}}$) becomes significant, as does the hub horizontal force component $F_{z,\text{hub}}$.

5.7.3.3 Performance of the open-centre turbine in yawed inflow

The performance of the open-centre turbine in yawed flow is given in figure 5.50. Maximum power is found at $\lambda = 4$, $\gamma = 30^\circ$, with $C_{P,\text{max}} = 0.43$ and $C_{PD,\text{max}} = 0.70$. Though not as high a value as for the ducted turbine, compared to the design point the power has increased by $\Delta P = 30\%$, which is a similar increase to that seen for the ducted turbine ($\Delta P = 31\%$). As for the ducted turbine, the duct inlet design acts as a cambered aerofoil, accelerating and turning the flow, and hence increasing

the mass flow that enters the duct. Interestingly, maximum power is achieved at an operating point displaying moderate internal flow separation.

The drop in basin efficiency is uniform across all values of λ and γ . Compared to the ducted turbine, a drop is visible even for $\gamma = 10^\circ$ and becomes more pronounced for each increase in yaw angle. For the maximum power point the efficiency is reduced by $\Delta\eta_{\text{basin}} = 30\%$ compared to the design point.

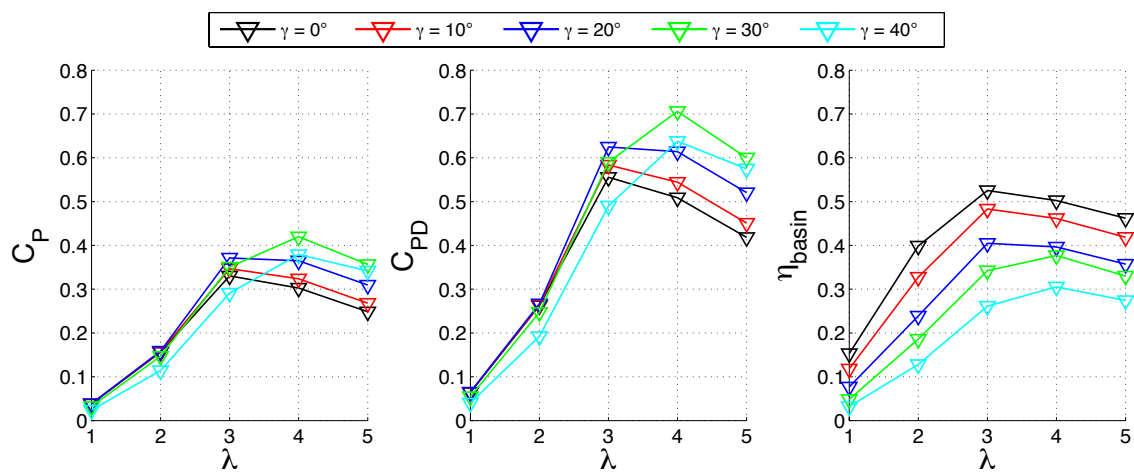


Figure 5.50: Performance of the open-centre turbine at various λ and γ .

5.8 Summary of results of the RANS-BEM simulations

A RANS-implemented BEM code has been presented and validated using the bare turbine in nearly unconstrained flow. The code compares well to analytical BEM, with some differences for high solidity rotors.

Rotor designs for the three devices, bare, ducted and open-centre turbines, have been generated using a RANS-BEM-integrated rotor design tool following a constant local thrust design approach. The design iterations were conducted for a range of tip-speed ratios and thrust settings and the designs with highest yielding power were chosen. The designs for the three devices include hub structures modelled approximately on existing devices proposed by the industry.

The chosen rotor designs were applied to their respective devices and simulated in both axial and yawed inflow for various tip-speed ratios. In general, the performance trends measured at the design point follow those of the actuator disc simulations. However, there are distinct differences in the flow field, the forces on the devices as well as off-design operation.

In all RANS-BEM simulations the circumferential force exerted by the turbine on the flow is clearly visible in the swirling motion of the wake. Together with the inclusion of the hub, they form the two main differences to the actuator disc flow field, giving a much more realistic representation of a turbine wake.

For all three devices analysed, the thrust exerted by the hub structures are small compared to the rotor thrust and thus only have a small impact on the turbine performance. The duct, as already shown in the actuator disc simulations, takes on

almost 50 % of the total axial thrust loading for the ducted turbine and slightly less for the more streamlined duct of the open-centre turbine studied.

Both ducted and open-centre devices exhibit a limit to the thrust on the rotor and the induction factor close to the design point. At tip-speed ratios higher than the design point, the rotors placed within a duct impart less axial and circumferential thrust on the flow, leading to an increasing velocity at the disc plane.

For axial flow, the performance of the devices modelled employing RANS-BEM lies roughly 8 – 15 % lower than for the actuator disc simulations, when comparing the devices at their respective design points. This reduction in performance is mostly due to the blade drag captured by the RANS-BEM model, which is not modelled by the actuator disc. The bare turbine sees a lower performance penalty than the other two devices, which may be attributed to tip-effects modelled in RANS-BEM which were not applied to the rotors operating in a duct. The overall performance trends remain the same as those observed for the actuator disc simulations. The bare turbine significantly outperforms the ducted and open-centre turbines in terms of C_P and moderately in terms of η_{basin} , while all three devices perform similarly in terms of C_{PD} . The open-centre turbine exhibits a lower C_P than the ducted turbine while exhibiting a higher η_{basin} .

When placed in yawed flow, a significant portion of the duct inlet of both open-centre and ducted turbine acts as a cambered aerofoil, accelerating and turning the flow. This, together with the increased effective blockage, leads to an increase in axial flow velocity at the rotor plane and a higher resulting blade inflow velocity. The power produced by ducted and open-centre turbines therefore increases significantly (up to 30 %), in line with the findings of the actuator disc simulations. Note that maximum power occurs at increased λ , due to the fact that, with increased axial velocity, the rotational velocity must be increased in order to maintain a near-optimal α .

As shown by the actuator disc simulations, the power increase of the ducted and open-centre devices comes at a cost of η_{basin} as large scale separation on the duct leads to drastically increased power removal from the flow. The power and power density of the bare turbine in yawed flow drop significantly with increasing γ , while η_{basin} is nearly unaffected, as the thrust also decreases.

For the yawed flow cases, a detailed force analysis of rotor, hub, and duct has been conducted in order to analyse the asymmetric loading of the rotor. It has been shown that while the bare turbine is loaded asymmetrically for all yaw angles, a bidirectional duct straightens the flow such that the velocities at the rotor plane are nearly axisymmetric. Thus, by employing a duct, asymmetry in the rotor loading for both the ducted and open-centre turbines can be significantly reduced for yaw angles up to $\gamma = 30^\circ$. For real rotors, the more evenly distributed loads would lead to significantly decreased cyclical loading on the blades of the ducted rotor.

The results presented in this and the previous chapter have been achieved for two particular bidirectional duct geometries. The geometries chosen are based on designs proposed by the industry and were therefore deemed representative for this analysis. Due to the low number of duct shapes analysed, however the question of general applicability of the results arises. A parametric study of interior and exterior bidirectional duct shapes was conducted by Fleming *et al.* (2011). Fleming *et al.* analysed eight duct shapes including a straight pipe, providing evidence that the axial flow trends presented here also hold for a broad range of bidirectional duct shapes. In terms of yawed inflow, the present study shows very similar trends for the two different duct shapes presented here. These trends are based on a variety of flow effects, some of which are duct geometry dependent, and as such the general applicability of the yawed flow result must be treated with care.

Chapter 6

Conclusions and future work

Section 6.1 presents a summary of the main conclusions drawn from the analyses presented in chapters 4 and 5. Suggestions for future work are given in section 6.2. Section 6.3 summarises the contribution made by the thesis to the tidal energy research community.

6.1 Conclusions

As tidal energy has progressively gained momentum, several ducted tidal turbine devices have been proposed by the tidal energy industry. Most of the ducted devices proposed for large scale tidal energy extraction are designed as bidirectional turbines, some of which feature a central aperture instead of a closed hub. The manufacturers of these ducted devices claim substantial increases in power delivery, by comparison to bare devices, as well as other advantages such as better performance in yawed flow conditions and lower maintenance costs. However, no independent scientific publications supporting these claims were available at the outset of this research. Hence a thorough analysis of the hydrodynamics of bidirectional ducted tidal turbines, both with and without an aperture, was chosen as the topic for this study.

The analysis was performed using numerical simulation, employing two different methods for representing the turbine rotor. The first uses a numerical actuator disc, applying an axial resistance to the flow, and thus modelling the extraction of linear momentum. The second method employs a CFD-embedded blade element momentum model, modelling both extraction of linear momentum as well as the

introduction of swirl to the flow, based on real rotor geometry and blade aerodynamic coefficients.

Both methods were applied to the bare, ducted, and open-centre turbines in order to study the flow field, forces and performance of each device. The main conclusions drawn from the RANS-BEM simulations support the findings obtained through the actuator disc simulations and are summarised here.

In axial flow:

1. The power delivered per rotor area (power density) is similar for all three devices. The duct nozzle accelerates the flow through the rotor plane, aided by increased effective blockage due to external separation (ducted turbine) and flow entrainment due to the central jet through the aperture (open-centre turbine). The accelerated flow at the rotor plane is however balanced by the reduced thrust loading of the rotor.
2. The power delivered by the ducted and open-centre turbines studied here is significantly less than that by a bare turbine of equal outer device diameter (reduction of 37% and 45%, respectively). Although the power per rotor area is the same, the rotor area per device, and therefore the power generating area, is significantly reduced for the ducted and open-centre turbines.
3. Increasing the size of the aperture of the open-centre turbine decreases the overall power generated per device (further reduction in rotor area), but increases the power density (increased central jet).
4. The power delivered per total power removed from the flow (basin efficiency) is dependent on the amount of thrust imparted on the flow by the entire device. Employing real rotors, modelled with a minimal amount of structure (hubs, ducts), the basin efficiency at design point (peak power point) is highest for the bare turbine and lowest for the ducted turbine with concave duct exterior.

5. Blockage affects the bare, ducted and open-centre turbines similarly; even moderate increases in blockage significantly increase the power extracted by a tidal turbine device.
6. For a turbine with a duct, the thrust force acting on the rotor at design point is significantly lower than that for a bare turbine, as the duct takes a large portion of the total thrust loading. For the geometries analysed, the combined thrust loading of duct and rotor are lower for the ducted devices than for the bare turbine, compared at their respective design (peak power) points.
7. The thrust acting on the duct is highly dependent on the exterior duct shape. Large scale external separation increases the thrust loading significantly. A streamlined duct exterior minimised the thrust on the duct as well as the overall device thrust, as seen for the open-centre turbine studied here.
8. For a duct of concave exterior, as employed for the ducted turbine, two flow regimes form on the duct exterior: nozzle contoured flow at low disc thrust and separation dominated flow at high disc thrust. The associated thrust force of the duct increases with increasing separation and reaches a maximum for a fully separated duct exterior. Maximum power of the ducted turbine is achieved at separation dominated flow due to an increase in effective blockage formed by the separation.

In yawed flow:

9. For both ducted devices, large asymmetric separation regions develop on the duct exterior, leading to asymmetric loading of the duct. At high yaw angles internal separation starts to form, both in the nozzle and the diffuser sections.
10. A portion of the duct inlet area acts as a cambered aerofoil, accelerating and turning the approaching flow into the duct, thereby increasing the velocity through the rotor plane for a range of yaw angles.

11. The duct interior shape acts as a flow conditioning device and straightens the flow such that the ducted turbine rotor is approached nearly uniformly for a broad range of yaw angles. Due to the uniform rotor inflow, the loading of the ducted and open-centre turbine rotors remains predominantly axisymmetric in yawed flow. In contrast, the loading of the bare turbine rotor is highly asymmetric, leading to cyclical blade loading for real turbine rotors.
12. For the bare turbine, the power decreases monotonically with increased yaw angles, while the power produced by the ducted and open-centre turbines increases significantly (maximum increase found at yaw angles of $20 - 30^\circ$). This power increase is attributed in part to an increased effective blockage, as the projected frontal area of the duct increases substantially, and in part to the flow acceleration at the duct inlet.
13. The basin efficiency of the bare turbine is not significantly affected by yaw. For the ducted and open-centre turbines, the large scale asymmetric separation on the duct, and associated drag force, leads to significant drops in basin efficiency due to yaw, increasing with increased yaw angles.

Comparison of actuator disc and RANS-BEM simulations:

14. Numerical actuator disc models are a useful tool for comparing devices qualitatively at their respective design points. However, actuator disc models perform poorly in predicting real turbine behaviour.

When judging whether to pursue the development of bare, ducted or open-centre turbines, the results of this study are not fully conclusive, as each device exhibits certain advantages. Further, this study purely analyses the hydrodynamic performance of these devices, while other factors such as reliability, manufacturing, and maintenance costs play important roles.

6.2 Future work

Based on the results obtained from this study the following future analyses are suggested.

Structural requirements of bare, ducted, and open-centre turbines: This study has shown that, while the performance of ducted and open-centre turbines in axial flow is lower than that of bare turbines, the forces acting on the rotor are also significantly lower. This is even more so the case for yawed inflow. Therefore the structural requirements for the rotor blades are quite different, and could constitute one of the advantages from employing a duct. For the open-centre turbine, which supports the rotor blades at the tips, the advantage is expected to be even larger.

Impact of shear and non-uniform flow on bare and ducted devices: The simulations presented in this thesis were conducted using uniform steady inflow. A realistic offshore environment exhibits time-dependent turbulent and sheared flow (Milne *et al.*, 2013). As the duct has been shown to condition the flow efficiently for yawed uniform inflow, it would be of interest to investigate to what extent flow conditioning is possible for non-uniform inflow.

Comparison of tidal fence configurations: As has been confirmed by the present study, blockage highly influences the performance of all tidal devices analysed. It is therefore a goal to make use of this blockage effect and install turbines in tidal fences (Daly *et al.*, 2010; Draper *et al.*, 2013; Nishino and Willden, 2013). Bare axial-flow devices, when aligned in a tidal fence configuration, do not make full use of the available cross-sectional area due to their circular cross-section. Using a ducted structure could enable devices to cover fully the defined cross-sectional area, and potentially boost the performance of the tidal fence. The author therefore suggests a comparison of bare and ducted tidal fences of same outer cross-sectional area.

6.3 Contribution of thesis

The main contributions of this thesis are:

Analysis of bidirectional ducted turbines:

This study is the first to deliver a detailed hydrodynamic analysis of bidirectional ducted turbines, both with and without an aperture. While unidirectional ducts have been analysed in detail, this study is the first to analyse bidirectional ducts with turbine representation, directly addressing industry needs. The present work analyses the hydrodynamics of bidirectional ducted turbines in axial and yawed flow and presents a detailed performance comparison of three types of devices: bare, ducted, and open-centre turbines.

Introduction of three measures of performance:

Typically the performance of a tidal energy device is given as the power coefficient based on the rotor area. This, however, fails to portray the whole picture, in particular when discussing ducted devices. This study employs three measures of performance including the term of basin efficiency which relates the power produced to the overall power removed from the flow.

Effect of blockage on ducted turbines:

The positive effect of increased blockage on the performance of tidal turbines has been covered extensively in the literature. This thesis presents the first analysis of blockage variation on ducted devices. Due to the known significant impact of blockage, the blockage ratio is kept constant throughout comparisons of devices. This is a novel approach for ducted turbines, notwithstanding that the standard approach of maintaining a constant rotor area fails to acknowledge the effect of blockage and therefore penalises the bare turbine.

Appendix A

Publications

Belloni, C.S.K., Willden, R.H.J. and Houlsby, G.T. (2013). A numerical analysis of bidirectional ducted tidal turbines in yawed flow. *Marine Technology Society Journal*, Vol. 47, No. 4, pp. 23-35.

Belloni, C.S.K. and Willden, R.H.J. (2011). Flow field and performance analysis of bidirectional and open-centre ducted tidal turbines. *In Proc. 9th European Wave and Tidal Energy Conference (EWTEC)*, Southampton, UK.

Belloni, C.S.K. and Willden, R.H.J. (2010). A computational study of a bidirectional ducted tidal turbine. *In Proc. 3rd International Conference on Ocean Energy (ICOE)*, Bilbao, Spain.

Bibliography

- Abbott, I. and von Doenhoff, A., eds (1959), *Theory of Wing Sections: Including a Summary of Airfoil Data*, Courier Dover Publications.
- Afgan, I., McNaughton, J., Rolfo, S., Apsley, D., Stallard, T. and Stansby, P. (2013), ‘Turbulent flow and loading on a tidal stream turbine by LES and RANS’, *International Journal of Heat and Fluid Flow* .
- Ahmed, M. R. (2012), ‘Blade sections for wind turbine and tidal current turbine applications – current status and future challenges’, *International Journal on Energy Research* **36**.
- Alidadi, M. (2009), Duct optimization for a ducted vertical axis hydro current turbine, PhD thesis, University of British Columbia.
- Anderson, J. D., ed. (1995), *Computational Fluid Dynamics. The basics with applications*, McGraw-Hill, Inc.
- Andritz Hydro Hammerfest (2013), ‘AHH Technologies’, <http://www.hammerfeststrom.com/>. Accessed August 20, 2013.
- ANSYS Inc. (2009a), ‘ANSYS FLUENT 12.0 Theory Guide’.
- ANSYS Inc. (2009b), ‘ANSYS FLUENT 12.0 User Guide’.
- ANSYS Inc. (2009c), ‘ANSYS ICEM CFD 12.1 User Manual’.
- Apsley, D. D. and Leschzinger, M. A. (1999), ‘Advanced turbulence modelling of separated flow in a diffuser’, *Flow, Turbulence and Combustion* **63**, 81–112.
- Atlantis Resources Corporation Pte Ltd (2013), ‘Atlantis Technologies’, <http://www.atlantisresourcescorporation.com/marine-power/atlantis-technologies.html>. Accessed April 4, 2013.
- Autodesk (2012), ‘AutoCAD 2013 User’s Guide’.

- Bahaj, A., Batten, W. and McCann, G. (2007), ‘Experimental verifications of numerical predictions for the hydrodynamic performance of horizontal axis marine current turbines’, *Renewable Energy* **32**.
- Bahaj, A., Myers, L., Thomson, M. and Jorge, N. (2007), Characterising the wake of horizontal axis marine current turbines, in ‘Proc. 7th European Wave and Tidal Energy Conference’.
- Batten, W., Bahaj, A., Molland, A. and Chaplin, J. (2008), ‘The prediction of the hydrodynamic performance of marine current turbines’, *Renewable Energy* **33**.
- Batten, W., Harrison, M. and Bahaj, A. (2013), ‘The accuracy of the actuator disc-RANS approach for predicting the performance and far wake of a horizontal axis tidal stream turbine’, *Philosophical Transactions of the Royal Society A* **371**.
- Belloni, C. and Willden, R. (2011), Flow field and performance analysis of bidirectional and open-centre ducted tidal turbines, in ‘Proc. 9th European Wave and Tidal Energy Conference’.
- Bertagnolio, F., Sørensen, N., Johansen, J. and Fuglsang, P. (2001), ‘Wind turbine airfoil catalogue’.
- Betz, A. (1920), ‘Das Maximum der theoretisch möglichen Ausnutzung des Windes durch Windmotoren’, *Zeitschrift für das gesamte Turbinenwesen* .
- Boussinesq, J. (1878), ‘Essai sur la théorie des eaux courantes’, *Journal de mathématiques pures et appliquées*, 3^e série **4**, 335–376.
- Bredberg, J. (2001), On two-equation eddy-viscosity models, Technical Report 01/8, Chalmers University of Technology.
- Burton, T., Sharpe, D., Jenkins, N. and Bossanyi, E., eds (2011), *Wind Energy Handbook*, John Wiley & Sons Ltd.
- Carbon Trust (2011a), ‘Accelerating marine energy’.
- Carbon Trust (2011b), ‘UK Tidal Current Resource & Economics’.
- Churchfield, M., Li, Y. and Moriarty, P. (2013), ‘A large-eddy simulation study of wake propagation and power production in an array of tidal-current turbines’, *Philosophical Transactions of the Royal Society A* **371**.
- Clean Current Power Systems Inc. (2013), ‘Clean current tidal turbines’, <http://www.cleancurrent.com/tidal-turbines>. Accessed April 4, 2013.

- Consul, C. A. (2011), Hydrodynamic Analysis of a Tidal Cross-Flow Turbine, DPhil thesis, University of Oxford.
- Consul, C. A., Willden, R. H. J. and McIntosh, S. C. (2013), 'Blockage effects on the hydrodynamic performance of a marine cross-flow turbine', *Philosophical Transactions of the Royal Society A* **371**.
- Daly, T., Myers, L. E. and Bahaj, A. S. (2010), Experimental analysis of the local flow effects around single row tidal turbine arrays, in 'Proc. 3rd International Conference on Ocean Energy'.
- Davis, B. V., Grillos, E. and Allison, S. (2011), 'Underwater ducted turbine', Patent. **URL:** http://www.patentlens.net/patentlens/patent/US_8022567/en/
- Draper, S., Borthwick, A. G. L. and Housby, G. T. (2013), 'Energy potential of a tidal fence deployed near a coastal headland', *Philosophical Transactions of the Royal Society A* **371**.
- Drela, M. (1989), XFOIL: An analysis and design system for low Reynolds number airfoils, in 'Conference on Low Reynolds Number Airfoil Aerodynamics'.
- Elemental Energy Technologies Ltd. (2013), 'EET SeaUrchin', <http://www.eettidal.com/>. Accessed January 9, 2013.
- Engineering Business Ltd. (2005), 'Stingray tidal energy stream device - Phase 3', Report for DTI New and Renewable Energy Programme.
- E.ON UK (2007), 'E.ON and Lunar Energy announce proposal to build one of the worlds largest tidal stream power stations off the Welsh coast', <http://pressreleases.eon-uk.com/blogs/eonukpressreleases/archive/2007/10/25/1135.aspx>. Accessed August 25, 2013.
- European Commission (1996), The exploitation of tidal marine currents, Technical Report EUR16683EN, European Commission.
- European Marine Energy Centre Ltd. (2013a), 'European Marine Energy Centre', <http://www.emec.org.uk>. Accessed April 4, 2013.
- European Marine Energy Centre Ltd. (2013b), 'Tidal developers', <http://www.emec.org.uk/marine-energy/tidal-developers/>. Accessed August 25, 2013.
- Feistauer, M., Felcman, J. and Straškraba, I., eds (2004), *Mathematical and Computational Methods for Compressible Flow*, Clarendon Press, Oxford.

- Fleming, C., McIntosh, S. and Willden, R. (2011), Design and analysis of a bi-directional ducted tidal turbine, *in* ‘Proc. 9th European Wave and Tidal Energy Conference’.
- Fleming, C., McIntosh, S. and Willden, R. (2012), Performance and wake structure of a model horizontal axis axial flow turbine, Technical Report RE-585, University of Oxford.
- Fleming, C., McIntosh, S. and Willden, R. (2013), Tidal turbine performance in sheared flow, *in* ‘Proc. 10th European Wave and Tidal Energy Conference’.
- Foreman, K., Gilbert, B. and Oman, R. A. (1978), ‘Further investigations of diffuser augmented wind turbines’, *Solar Energy* **20**, 305–311.
- Froude, R. (1889), ‘On the part played in propulsion by differences of fluid pressure’, *Transactions of the Institute of Naval Architects* **30**.
- Fuglsang, P., Dahl, K. S. and Antoniou, I. (1999), Wind tunnel tests of the Risø-A1-18, Risø-A1-21 and Risø-A1-24 airfoils, Technical Report R-1112(EN), Risø.
- Gaden, D. (2007), An investigation of river kinetic turbines: Performance enhancements, turbine modelling techniques, and an assessment of turbulence models, MSc thesis, University of Manitoba.
- Gaden, D. and Bibeau, E. (2010), ‘A numerical investigation into the effect of diffusers on the performance of hydro kinetic turbines using a validated momentum source turbine model’, *Renewable Energy* **35**.
- Gant, S. and Stallard, T. (2008), Design and performance assessment of a tidal ducted turbine, *in* ‘Proc. 18th International Offshore and Polar Engineering Conference’.
- Garrett, C. and Cummins, P. (2007), ‘The efficiency of a turbine in a tidal channel’, *Journal of Fluid Mechanics* **588**.
- Gerber, A. G., Jeans, T., Culina, J. and Holloway, A. G. L. (2013), Turbulent tidal flow in Minas Passage using high-fidelity CFD simulation, *in* ‘Proc. 10th European Wave and Tidal Energy Conference’.
- Glauert, H. (1935), Airplane propellers, *in* W. Durand, ed., ‘Aerodynamic Theory, Vol. IV, Section L’, Julius Springer, Berlin.

- Grassmann, H., Bet, F., Cabras, G., Ceschia, M., Cobai, D. and DelPapa, C. (2003), 'A partially static turbine – first experimental results. Technical note.', *Renewable Energy* **28**, 1779 –1785.
- Grassmann, H., Bet, F., Ceschia, M. and Ganis, M. (2003), 'On the physics of partially static turbines', *Renewable Energy* **29**, 491 – 499.
- Grasso, F. (2011), Design and optimization of tidal turbine airfoil, in 'Proc. 29th Applied Aerodynamics Conference'.
- Green-Tide Turbines Ltd (2013), 'Green-Tide Turbines: Technology', <http://www.green-tide.com/technology>. Accessed September 20, 2013.
- Guinard Energies (2013), 'BluStream: Innovative second-generation high-output turbine', <http://www.pole-mer-bretagne.com/blustreamr-innovative-second-generation-high-output-turbine.php>. Accessed September 20, 2013.
- Hallanger, A. and Sand, I. Ø. (2013), 'CFD wake modelling with a BEM wind turbine sub-model', *Modeling, Identification and Control* **34**.
- Hansen, A. C. (1992), Yaw dynamics of horizontal axis wind turbines, Technical Report 442-4822, NREL.
- Hansen, M. O. L., ed. (2008), *Aerodynamics of Wind Turbines*, Earthscan.
- Hansen, M., Sørensen, N. and Flay, R. (2000), 'Effect of placing a diffuser around a wind turbine', *Wind Energy* **3**.
- Harrison, M. E., Batten, W. M. J., Myers, L. E. and Bahaj, A. S. (2009), A comparison between CFD simulations and experiments for predicting the far wake of horizontal axis tidal turbines, in 'Proc. 8th European Wave and Tidal Energy Conference'.
- Houlsby, G. T., Draper, S. and Oldfield, M. L. G. (2008), Application of linear momentum actuator disc theory to open channel flow, Technical Report OUEL 2296/08, University of Oxford.
- Houlsby, G. T., Oldfield, M. L. G. and Draper, S. (2008), The Betz limit and tidal turbines, Technical Report commissioned by Lunar Energy, University of Oxford.
- Hyman, J. M. (1984), 'Numerical methods for tracking interfaces', *Physica D* **12**, 396–407.

- Jamieson, P. M. (2008), 'Generalized limits for energy extraction in a linear constant velocity flow field', *Wind Energy* **11**.
- Jamieson, P. M. (2009), 'Beating Betz: Energy extraction limits in a constrained flow field', *Journal of Solar Engineering* **131**.
- Khunthongjan, P. and Janyalertadun, A. (2012), 'A study of diffuser angle effect on ducted water current turbine performance using CFD', *Songklanakarinn Journal of Science and Technology* **34 (1)**, 61–67.
- Kirke, B. (2005), 'Developments in ducted water current turbines', Technical Report. University of South Australia.
- Klaptocz, V. R., Rawlings, G. W., Nabavi, Y., Alidadi, M., Li, Y. and Calisa, S. M. (2007), Numerical and experimental investigation of a ducted vertical axis tidal current turbine, in 'Proc. 7th European Wave and Tidal Energy Conference'.
- Kracht, P., Giebardt, J., Lutz, M.-A., Vecchio, M., Moroso, A. and Bard, J. (2012), Implementation of a vertical axis marine current turbine for off-grid village electrification in indonesia, in 'Proc. 4th International Conference on Ocean Energy'.
- Labroquère, J., Duvigneau, R. and Guilmineau, E. (2013), Impact of turbulence closures and numerical errors for the optimization of flow control devices, in 'Proc. 21st AIAA Computational Fluid Dynamics Conference'.
- Lanzafame, R. and Messina, M. (2007), 'Fluid dynamics wind turbine design: Critical analysis, optimization and application of BEM theory', *Renewable Energy* **32**.
- Lawn, C. J. (2003), 'Optimization of the power output from ducted turbines', *Journal of Power and Energy* **217**.
- Lilley, G. M. and Rainbird, W. J. (1956), A preliminary report on the design and performance of ducted windmills, Technical Report 102, College of Aeronautics, Cranfield University.
- Lokocz, T. A. (2012), Testing of a ducted axial flow tidal turbine, MSc thesis, University of Maine.
- Lunar Energy Ltd. (2013), 'The Rotech Tidal Turbine', <http://www.lunarenergy.co.uk/productOverview.htm>. Accessed April 4, 2013.

- Luquet, R., Bellevre, D., Fréchet, D., Perdon, P. and Guinard, P. (2013), 'Design and model testing of an optimized ducted marine current turbine', *International Journal of Marine Energy* **2**.
- MacLeod, A., Barnes, S., Rados, K. and Bryden, I. (2002), Wake effects in tidal current turbine farms, in 'Proc. International Conference on Marine Renewable Energy'.
- Malki, R., Williams, A., Croft, T., Togneri, M. and Masters, I. (2013), 'A coupled blade element momentum - computational fluid dynamics model for evaluating tidal stream turbine performance', *Applied Mathematical Modelling* **37**(5), 3006 – 3020.
- Marine Current Turbines Ltd. (2013), 'SeaGen Technology', <http://www.marineturbines.com/Seagen-Technology>. Accessed April 4, 2013.
- Massey, B. S., ed. (1968), *Mechanics of Fluids*, Chapman & Hall.
- Masters, I., Malki, R., Williams, A. and Croft, T. (2013), 'The influence of flow acceleration on tidal stream turbine wake dynamics: A numerical study using a coupled BEM-CFD model', *Applied Mathematical Modeling* **38**.
- Masters, I., Orme, J. and Chapman, J. (2007), Towards realistic marine flow conditions for tidal stream turbines, in 'Proc. 7th European Wave and Tidal Energy Conference'.
- McAdam, R., Houlsby, G. and Oldfield, M. (2013), 'Experimental measurements of the hydrodynamic performance and structural loading of the Transverse Horizontal Axis Water Turbine: Part 1', *Renewable Energy* **59**.
- McIntosh, S., Fleming, C. and Willden, R. (2011), Embedded RANS-BEM tidal turbine design, in 'Proc. 9th European Wave and Tidal Energy Conference'.
- McNaughton, J., Rolfo, S., Apsley, D., Stallard, T. and Stansby, P. (2013), CFD power and load prediction on a 1MW tidal stream turbine with typical velocity profiles from the EMEC test site, in 'Proc. 10th European Wave and Tidal Energy Conference'.
- Mehmood, N., Liang, Z. and Khan, J. (2012a), 'CFD study of NACA 0018 for diffuser design of tidal current turbines', *Research Journal of Applied Sciences, Engineering and Technology* **4**(21).

- Mehmood, N., Liang, Z. and Khan, J. (2012b), ‘Harnessing ocean energy by tidal current technologies’, *Research Journal of Applied Sciences, Engineering and Technology* **4(18)**.
- Menter, F. R. (1993), ‘Zonal two-equation $k-\omega$ turbulence model for aerodynamic flows’, *AIAA Paper* (1993-2906).
- Menter, F. R., Kuntz, M. and Langtry, R. (2003), Ten years of industrial experience with the SST turbulence model, *in* ‘Proc. 4th Symposium on Turbulence, Heat and Mass Transfer’.
- MeyGen Ltd. (2013), ‘MeyGen secures consent for 86 MW tidal energy project’, <http://www.meygen.com/2013/09/meygen-secures-consent-for-86mw-tidal-energy-project/>. Accessed September 19, 2013.
- Mikkelsen, R. (2003), Actuator Disc Methods Applied to Wind Turbines, PhD thesis, Technical University of Denmark.
- Miley, S. (1982), ‘A catalogue of low Reynolds number airfoil data for wind turbine applications’.
- Milne, I. A., Sharma, R. N., Flay, R. G. J. and Bickerton, S. (2013), ‘Characteristics of the turbulence in the flow at a tidal stream power site’, *Philosophical Transactions of the Royal Society A* **371**.
- Moriarty, P. and Hansen, A. (2005), AeroDyn Theory Manual, Technical report, National Renewable Energy Laboratory.
- Münch, C., Vonlanthen, M., Gomes, J., Luquet, R., Guinard, P. and Avellan, F. (2009), Design and performance assessment of a tidal ducted turbine, *in* ‘Proc. 3rd IAHR International Meeting of the Workgroup on Cavitation and Dynamic Problems in Hydraulic Machinery and Systems’.
- Myers, L. E. and Bahaj, A. S. (2009), ‘Experimental analysis of the flow field around horizontal axis tidal turbines by use of scale mesh disk rotor simulators’, *Ocean Engineering* **37**.
- Nishino, T. and Willden, R. H. J. (2012), ‘Effects of 3-D channel blockage and turbulent wake mixing on the limit of power extraction by tidal turbines’, *International Journal of Heat and Fluid Flow* **37**, 123–135.

- Nishino, T. and Willden, R. H. J. (2013), The efficiency of tidal fences: A brief review and further discussion on the effect of wake mixing, *in* ‘Proc. ASME 2013 32nd International Conference on Ocean, Offshore and Arctic Engineering’.
- Ocean Renewable Power Company (2013), ‘TidGen Power System’, http://www.orpc.co/orpcpowersystem_tidgenpowersystem.aspx. Accessed April 4, 2013.
- Ohya, Y., Karasudani, T., Sakurai, A., Abe, K. and Inoue, M. (2008), ‘Development of a shrouded wind turbine with a flanged diffuser’, *Journal of Wind Engineering and Industrial Aerodynamics* **96**.
- OpenHydro Group Ltd. (2013), ‘The Open-Centre Turbine’, <http://www.openhydro.com/technology.html>. Accessed June 20, 2013.
- O’Rourke, F., Boyle, F. and Reynolds, A. (2010), ‘Tidal energy update 2009’, *Applied Energy* **87**(2), 398 – 409.
- Phillips, D. (2003), An Investigation on diffuser augmented wind turbine design, PhD thesis, University of Auckland.
- Phillips, D., Richards, P. and Flay, R. (2005), ‘Diffuser development for a diffuser augmented wind turbine using computational fluid dynamics’, Technical Report. University of Auckland.
- Ponte di Archimede S.p.A. (2013), ‘The Kobold Turbine’, http://www.pontediarchimede.it/language_us/. Accessed January 18, 2013.
- Pope, S. B., ed. (2000), *Turbulent flows*, Cambridge University Press.
- Prandtl, L. and Betz, A. (1927), Vier Abhandlungen zur Hydrodynamik und Aerodynamik, Technical report, Göttinger Kaiser-Wilhelm-Instituts für Strömungsforschung.
- Pulse Tidal Ltd. (2013), ‘Pulse Tidal, Powered by Nature’, <http://pulsetidal.com/our-technology.html>. Accessed April 4, 2013.
- Ray, B., Bhaskaran, R. and Collins, L. R. (2012), ‘Introduction to CFD basics’, Cornell University.
- Reinecke, J., von Backstrm, T. and Venter, G. (2011), Effect of a diffuser on the performance of an ocean current turbine, *in* ‘Proc. 9th European Wave and Tidal Energy Conference’.

- Sale, D., Jonkman, J. and Musial, W. (2009), Hydrodynamic optimization method and design code for stall-regulated hydrokinetic turbine rotors, *in* ‘Proc. 28th International Conference on Ocean, Offshore, and Arctic Engineering’.
- Salter, S. H. and Taylor, J. R. M. (2007), ‘Vertical-axis tidal-current generators and the Pentland Firth’, *Journal of Power and Energy* **221**(2), 181–199.
- Sant, T. (2007), Improving BEM-based aerodynamic models in wind turbine design codes, PhD thesis, Technical University Delft.
- Savage, A. (2007), ‘Tidal power in the UK. Research report 2 - Tidal technologies overview. An evidence-based report by Entec for the Sustainable Development Commission’.
- Schluntz, J. (2014), Numerical methods for tidal turbine array modelling, DPhil thesis, in preparation, University of Oxford.
- Schluntz, J. and Willden, R. (2012), Development of an actuator line model for tidal turbine simulations, *in* ‘Proc. Oxford Tidal Energy Workshop’.
- Schluntz, J. and Willden, R. (2013), The effect of rotor design on the power output of closely packed tidal turbines, *in* ‘Proc. 10th European Wave and Tidal Energy Conference’.
- Schmitt, F. G. (2007), ‘About Boussinesq’s turbulent viscosity hypothesis: historical remarks and a direct evaluation of its validity’, *Comptes Rendus Mécanique* **335**, **9-10**, 617–627.
- Setoguchi, T., Shiomi, N. and Kaneko, K. (2004), ‘Development of two-way diffuser for fluid energy conversion system’, *Renewable Energy* **29**.
- Shields, K. (2008), ‘Harnessing tidal power’, *Enterprising Scotland* pp. 39–40.
- Shives, M. (2011), Hydrodynamic Modeling, Optimization and Performance Assessment for Ducted and Non-ducted Tidal Turbines, MSc thesis, University of Victoria.
- Shives, M. and Crawford, C. (2010), Overall efficiency of ducted tidal current turbines, *in* ‘Proc. OCEANS 2010 Conference’.
- Shives, M. and Crawford, C. (2011), ‘Developing an empirical model for ducted tidal turbine performance using numerical simulation results’, *Journal of Power and Energy* **226**, 112–125.

- Skywolf Wind Turbine Corporation (2013), ‘Skywolf Wind Turbines’, <http://www.skywolfwindturbines.com>. Accessed September 20, 2013.
- Sørensen, J. and Myken, A. (1992), ‘Unsteady actuator disc model for horizontal axis wind turbines’, *Journal of Wind Engineering and Industrial Aerodynamics* **39**, 139–149.
- Sørensen, J. and Shen, W. (2002), ‘Numerical modelling of wind turbine wakes’, *Journal of Fluid Mechanics* **124**, 393–399.
- Spalart, P. R. and Allmaras, S. R. (1992), ‘A one-equation turbulence model for aerodynamic flows’, *AIAA Paper 92-0439*.
- Spera, D. A. (2008), Models of lift and drag coefficients of stalled and unstalled airfoils in wind turbines and wind tunnels, Technical Report NASA/CR2008-215434, NASA.
- Sun, H. and Kyojuka, Y. (2012), Analysis of performances of a shrouded horizontal axis tidal turbine, *in* ‘Proc. OCEANS 2012 Conference’.
- Sun, X. (2008), Numerical and experimental investigation of tidal current energy extraction, PhD thesis, University of Edinburgh.
- Sun, X., Chick, J. and Bryden, I. (2008), ‘Laboratory-scale simulation of energy extraction from tidal currents’, *Renewable Energy* **33**.
- Tangler, J. L. (1987), ‘A horizontal axis wind turbine performance prediction code for personal computers’, User’s Guide, Solar Energy Research Institute.
- Tangler, J. L. and Kocurek, J. D. (2005), Wind turbine post-stall airfoil performance characteristics guidelines for blade-element momentum methods, *in* ‘Proc. 43rd AIAA Aerospace Sciences Meeting and Exhibit’.
- Thorpe, T. (2005), The advantages of ducted over unducted turbines, *in* ‘Proc. 6th European Wave and Tidal Energy Conference’.
- Tidal Energy Pty Ltd. (2013), ‘The world’s most powerful water turbine’, <http://www.tidalenergy.net.au/index.html>. Accessed April 4, 2013.
- Turner, N. and Owen, A. (2009), The effect of boundary conditions on performance prediction model results for tidal turbines, *in* ‘Proc. 8th European Wave and Tidal Energy Conference’.

- Turnock, S., Phillips, A., Banks, J. and Nicholls-Lee, R. (2011), ‘Modelling tidal current turbine wakes using a coupled RANS-BEMT approach as a tool for analysing power capture of arrays of turbines’, *Ocean Engineering* **38**.
- UEK Corporation (2013), ‘Underwater electric kite’, <http://uekus.com/>. Accessed September 20, 2013.
- van Bussel, G. J. W. (2007), ‘The science of making more torque from wind: Diffuser experiments and theory revisited’, *Journal of Physics: Conference Series* **75**.
- van Drentham Susman, H. F. A., Stewart, K. R. and Stewart, D. (2011), ‘Power generator and turbine unit’, Patent.
- Verdant Power (2013), ‘Verdant Power: The RITE project’, <http://verdantpower.com/what-initiative/>. Accessed April 4, 2013.
- Versteeg, H. K. and Malalasekera, W., eds (1995), *An introduction to computational fluid dynamics. The finite volume method.*, Pearson Prentice Hall.
- Visser, K. D. (2009), Wind Tamer Turbine Performance Report, Technical Report 11, Clarkson University.
- Viterna, L. A. and Corrigan, R. D. (1981), Fixed pitch rotor performance of large horizontal axis wind turbines, Technical Report No. 83 19233, NASA Lewis Research Center.
- Voith Ocean Current Technologies (2013), ‘Tidal current power stations’, <http://www.voith.com/en/products-services/hydro-power/ocean-energies/tidal-current-power-stations--591.html>. Accessed August 20, 2013.
- Whelan, J., Graham, J. M. R. and Peiró, J. (2009), ‘A free-surface and blockage correction for tidal turbines’, *Journal of Fluid Mechanics* **629**, 281 – 291.
- Wilcox, D. C., ed. (1993), *Turbulence Modeling for CFD*, DCW Industries, Inc.